



**HAL**  
open science

# Beta and neutron imaging with an optical readout Micromegas detector

Antoine Cools

► **To cite this version:**

Antoine Cools. Beta and neutron imaging with an optical readout Micromegas detector. High Energy Physics - Experiment [hep-ex]. Université Paris-Saclay, 2024. English. NNT : 2024UPASP090 . tel-04804807

**HAL Id: tel-04804807**

**<https://theses.hal.science/tel-04804807v1>**

Submitted on 26 Nov 2024

**HAL** is a multi-disciplinary open access archive for the deposit and dissemination of scientific research documents, whether they are published or not. The documents may come from teaching and research institutions in France or abroad, or from public or private research centers.

L'archive ouverte pluridisciplinaire **HAL**, est destinée au dépôt et à la diffusion de documents scientifiques de niveau recherche, publiés ou non, émanant des établissements d'enseignement et de recherche français ou étrangers, des laboratoires publics ou privés.

Beta and neutron imaging with an  
optical readout Micromegas detector  
*Imagerie beta et neutron à l'aide d'un détecteur  
Micromegas à lecture optique*

Thèse de doctorat de l'université Paris-Saclay

École doctorale n°576, Particules, hadrons, énergie et noyau : instrumentation,  
imagerie, cosmos et simulation (PHENIICS)  
Spécialité de doctorat: Physique des particules  
Graduate School : Physique. Référent : Faculté des sciences d'Orsay

Thèse préparée dans l'unité de recherche : **Département d'Electronique des  
Détecteurs et d'Informatique pour la Physique** (Université Paris-Saclay, CEA),  
sous la direction de **Esther FERRER RIBAS**, directrice de recherche,  
le co-encadrement de **Thomas PAPADEVANGELOU**, ingénieur chercheur

Thèse soutenue à Paris-Saclay, le 20 Septembre 2024, par

**Antoine COOLS**

**Composition du jury**

Membres du jury avec voix délibérative

<b>Laurent SERIN</b> Directeur de recherche, Université Paris-Saclay	Président
<b>Konstantinos NIKOLOPOULOS</b> Professeur, Université de Hambourg	Rapporteur & Examineur
<b>Dominique THERS</b> Professeur, Nantes Université	Rapporteur & Examineur
<b>Maria DIAKAKI</b> Professeure assistant, National Technical University of Athens	Examinatrice
<b>Pawel MAJEWSKI</b> Professeur, Institut Rutherford Appleton Laboratory	Examineur

**Titre:** Imagerie beta et neutron à l'aide d'un détecteur Micromegas à lecture optique

**Mots clés:** Détecteurs gazeux, Micromegas, Détecteurs à lecture optique, Détecteurs de rayons-X, Radiographie neutron, Autoradiographie beta

**Résumé:** Les détecteurs gazeux ont démontré, au cours de ces dernières décennies, leur haute performance pour l'imagerie de particules radioactives, atteignant des résolutions spatiales inférieures à  $100\ \mu\text{m}$ . Les propriétés scintillantes de certains mélanges gazeux, combinées au gain important des détecteurs gazeux et à l'usage d'une caméra à bas bruit électronique, ont permis d'utiliser la lumière scintillée pour l'imagerie. Cette approche permet d'obtenir une large surface de détection et une haute résolution spatiale tout en réalisant l'imagerie en temps réel à un coût par pixel réduit, avec une faible complexité d'analyse des données. Les principaux objectifs de cette thèse sont d'optimiser la résolution spatiale ainsi que la sensibilité du détecteur, soit par une méthode d'acquisition "événement par événement" avec des temps d'acquisition d'image courts, soit par "intégration" avec des temps d'acquisition longs.

Un détecteur Micromegas en verre innovant pour la lecture optique a été développé, tirant parti de la haute résolution spatiale inhérente au détecteur Micromegas. L'adaptabilité du gain du détecteur Micromegas liée au mécanisme d'amplification par avalanche, lui permet de couvrir une large gamme de flux et d'énergies de particules. Durant cette thèse, des mesures d'imagerie ont été réalisées à l'aide de sources avec des niveaux de radioactivité inférieurs à un Becquerel et des énergies de quelques keV, jusqu'à des flux caractéristiques d'un synchrotron et d'une source de spallation, avec des énergies dépassant le MeV.

Le rendement lumineux du détecteur a été étudié pour différents mélanges gazeux et pour diverses valeurs de gain sous irradiation aux rayons-X afin d'optimiser la sensibilité du détecteur. L'homogénéité et la précision de la réponse du détecteur ont été

caractérisées par radiographie à rayons-X. La Fonction d'Étalement du Point (PSF) du Micromegas à lecture optique a été mesurée à l'aide d'un faisceau de rayons-X parallèles de quelques microns d'épaisseur, générés par le rayonnement synchrotron. Cette mesure a permis de déterminer la résolution spatiale du détecteur pour différentes configurations et d'identifier et de quantifier les effets qui rentrent en jeu. L'impact de la microgrille et des piliers sur la réponse en scintillation du détecteur a également été observé et quantifié.

Deux applications ont été choisies afin d'illustrer le potentiel du Micromegas à lecture optique: l'autoradiographie pour la quantification d'échantillons tritiés de très faible activité et la radiographie neutronique à haute résolution en environnement hautement radioactif.

L'autoradiographie et le comptage radioactif de rayonnements beta faiblement énergétiques ont été réalisés avec des échantillons de glucose tritié. Des activités inférieures à un Becquerel ont été mesurées avec précision et simultanément sur un grand nombre d'échantillons tout en assurant une reconstruction précise de leur position. Ce travail valide la possibilité de quantifier la concentration de médicaments anticancéreux à l'échelle de cellules tumorales uniques.

Enfin, l'utilisation du Micromegas à lecture optique pour la neutronographie a été démontrée en utilisant une source de spallation produisant des neutrons thermiques à un flux d'environ  $10^8\ \text{n} \cdot \text{s}^{-1}\text{cm}^{-2}\text{mA}^{-1}$ . L'uniformité de la réponse du détecteur a été étudiée, et les effets de la diffusion et du parcours moyen des particules dans le gaz sur la netteté de l'image ont été mesurés et comparés à une simulation. Une résolution spatiale de l'ordre de  $400\ \mu\text{m}$  a été obtenue en utilisant une amplification à double étages au sein du détecteur Micromegas.

**Title:** Beta and neutron imaging with an optical readout Micromegas detector

**Keywords:** Gaseous detectors, Micromegas, Optical readout detectors, X-ray detectors, Neutron radiography, Beta autoradiography

**Abstract:** Gaseous detectors have demonstrated, over the past decades, their high performance for imaging radioactive particles, achieving spatial resolutions below  $100\ \mu\text{m}$ . The scintillating properties of certain gas mixtures, combined with the significant gain of gaseous detectors and the use of a low-noise camera, have enabled the use of scintillation light for imaging. This approach allows for a large detection surface and high spatial resolution while achieving real-time imaging at a low cost per pixel, with low data analysis complexity. The main objectives of this thesis are to optimize the spatial resolution and sensitivity of the detector, either by an "event-by-event" acquisition method with short image acquisition times or by "integration" with long acquisition times.

An innovative glass Micromegas detector for optical readout has been developed, taking advantage of the inherently high spatial resolution of the Micromegas detector. The adaptability of the Micromegas detector's gain, due to the avalanche amplification mechanism, allows it to cover a wide range of particle fluxes and energies. During this thesis, imaging measurements were performed using sources with radioactivity levels below one Becquerel and energies of a few keV, up to fluxes characteristic of a synchrotron and a spallation source, with energies exceeding one MeV.

The light yield of the detector was studied for different gas mixtures and various gain values under X-ray irradiation to optimize the detector's sensitivity. The homogeneity and precision of the detector's response were characterized by X-ray radiography. The Point Spread Function (PSF) of the optical readout

Micromegas was measured using a parallel X-ray beam a few microns thick, generated by synchrotron radiation. This measurement allowed us to determine the detector's spatial resolution for different configurations, and to identify and quantify the effects involved. The impact of the micro-mesh and pillars on the detector's scintillation response was also observed and quantified.

Two applications were chosen to illustrate the potential of the optical readout Micromegas: autoradiography, for the quantification of very low-activity tritiated samples and high-resolution neutron radiography in highly radioactive environments.

Autoradiography and radioactive counting of low-energy beta radiation were performed with tritiated glucose samples. Activities below one Becquerel were measured accurately and simultaneously on a large number of samples, while ensuring precise reconstruction of their position. This work validates the possibility of quantifying the concentration of anticancer drugs at the scale of single tumor cells.

Finally, the use of the optical readout Micromegas for neutron imaging was demonstrated using a spallation source which produces thermal neutrons with a flux of approximately  $10^8\ \text{n} \cdot \text{s}^{-1}\text{cm}^{-2}\text{mA}^{-1}$ . The uniformity of the detector's response was studied, and the effects of the diffusion and the mean free path of particles in the gas on image sharpness were measured and compared to a simulation. A spatial resolution on the order of  $400\ \mu\text{m}$  was achieved using double-stage amplification within the Micromegas detector.



# Acknowledgements

The entirety of my work over the past three years is reflected in this thesis, but the people who enabled me to complete it and the support they provided are underrepresented. I would like to take a moment in these few lines to acknowledge that my colleagues from CEA, from other institutes, my family, and my friends have been indispensable in helping me carry out this research.

First, I would like to thank the members of my jury for their interest, curiosity, and expertise regarding my work. I am grateful to Laurent Serin for his valuable feedback and his consideration of my research. I extend my deepest thanks to Dominique Thers, who first introduced me to instrumentation and sparked my passion for it through his courses in Nantes and his guidance throughout my education. His expertise and evaluation of my thesis have been crucial. I would also like to express my gratitude to Konstantinos Nikolopoulos, who dedicated precious time to evaluating and improving my thesis with his suggestions and through our valuable exchanges. I also wish to thank Maria Diakaki for evaluating my thesis and for her enthusiasm and curiosity about my work. My sincere thanks to Pawel Majewski for his many suggestions, which significantly enhanced the quality of my thesis, and with whom I greatly enjoyed discussing the subject.

Above all, it is thanks to my supervisors that my thesis has been such a rewarding and enjoyable experience. All the moments we spent together in the lab, at beam tests, conferences, and outside of work will remain etched in my memory.

First, I am deeply grateful to Esther and so glad to have had her as my thesis advisor. Her kindness, attentiveness, trust, and passion for her work have always inspired and motivated me. It is also her balance of conviviality and rigor that makes her the ideal mentor, someone I loved working with and sharing life moments, such as meals with her family and trips.

I have also been fortunate to have a second supervisor, Thomas, who trained me in experimentation and analysis with dedication, always creating a light and fun atmosphere. Σας ευχαριστώ με όλη μου την καρδιά Thomas, for being a great teacher, for trusting me early on, and for encouraging inventiveness and creativity. We still need to go skiing on powdery slopes and enjoy a fondue together!

Lolly is like a kind mad scientist and a mentor to me. He generates quirky ideas at a frantic pace (and often they turn out to be brilliant!), is full of energy and positivity, and lights up the lab whenever he arrives. He is also deeply kind and considerate, and I thank him for his support over these past few years.

Thanks to Maxence, who taught me a lot, was always ready to help, and whose frankness I have always appreciated. Without a doubt, the best happiness manager and, sometimes, even partner in crime.

I am grateful to Olivier, who has always given me excellent advice, has been an precious help with my manuscript and thesis defense, and with whom I enjoyed discussing and learning about his projects, astronomy, and brainstorming together.

Many thanks to Fabien, who has accompanied me since the beginning of my thesis, always showing great interest in my work and helping me substantially with the writing. I would like to especially thank Laura and David for their help throughout my thesis and with the writing, as well as Frank, Kostas Aivazelis, Stephan, Jacques, Caroline, Ioannis Giomataris, Rémy, and Georgios for the time we

spent together, which made me love life in the lab so much.

I would like to express my deep gratitude to Florian, whose work has been very inspiring for me. From CERN to SOLEIL and the GDD lab, he has always helped and advised me, and I have always enjoyed working and exchanging ideas with him.

Thanks to Fabrice, without whom an important part of my thesis would not have been possible, and for the passionate and friendly moments we shared. Thanks also to Carole, Florent, Laurent, Zakariya, and Melissa for their kindness and their crucial contributions to my thesis.

I am infinitely grateful to Ioannis and Ourania, who are incredible people and who allowed me to experience unforgettable moments at PSI.

Thanks to Paco, who has supported me since the start of my thesis. He has always been available to help and is the origin of key tests at SOLEIL, which were crucial to my work and enriching personally. Thanks to Paulo and Pascal, who made those essential tests for my thesis possible.

Thanks to Mayeul, who dedicated his precious time to carry out major tests at SPRE. I am also grateful to Frédéric Ott for his help and our thrilling discussions about neutron imaging.

I would like to thank Alexandra, Ana, Marta, Felipe, Abel, Maël, and Dylan, who supported me at different points during my thesis, with whom I shared an office (or rather the "chitchat room" for all the members of the building) and some great life moments.

Thanks to my friends from La Celle and Noisy for all the time we spent together and for being there for me for so long.

Thanks to my parents, my brother and my grandparents for encouraging and supporting me in my choices, for your trust, and for giving me the strength to reach my goals. Thanks to H el ene, Jean-Philippe, Iris, L'or Iman, and Guy Karim for always being there for me. Thanks to the entire Renaudin Rault family and the brothers-in-law for the joyful moments we spent together before and during my thesis.

Finally, thanks to Alix for supporting me every day, for being by my side in my projects, and for helping me accomplish the things that matter to me. Thank you for your kindness, attentiveness, and enthusiasm. Thanks for making the difficult moments gentler and the good moments even more beautiful.

# Contents

<b>1</b>	<b>Introduction</b>	<b>11</b>
<b>2</b>	<b>Radiation interaction with matter</b>	<b>13</b>
2.1	Interaction of charged particles with matter . . . . .	13
2.1.1	Ionization and excitation . . . . .	13
2.1.2	Electrons energy loss . . . . .	15
2.2	Interaction of photons with matter . . . . .	16
2.2.1	Photoelectric effect . . . . .	16
2.2.2	Compton scattering . . . . .	18
2.2.3	Pair production . . . . .	18
2.3	Nuclear processes and interaction of neutrons with matter . . . . .	19
2.3.1	Alpha decay . . . . .	19
2.3.2	Beta decay . . . . .	19
2.3.3	Electron capture . . . . .	19
2.3.4	Gamma decay . . . . .	20
2.3.5	Neutron production . . . . .	20
	Nuclear reaction . . . . .	20
	Spallation . . . . .	21
2.3.6	Neutron capture and moderation . . . . .	21
<b>3</b>	<b>Gaseous detectors</b>	<b>23</b>
3.1	Charge production and transport in gas . . . . .	23
3.1.1	Particle conversion in gas . . . . .	23
3.1.2	Transport of charges in gas . . . . .	24
3.2	Charge amplification . . . . .	25
3.2.1	Avalanche amplification . . . . .	25
3.2.2	Instabilities and gas choice . . . . .	28
3.2.3	Induced signals . . . . .	29
3.3	MPGD and Micromegas detectors . . . . .	30
3.3.1	Micro Pattern Gaseous Detectors . . . . .	30
3.3.2	The Micromegas detector . . . . .	31
<b>4</b>	<b>Optical readout</b>	<b>35</b>
4.1	MPGDs: from charge to optical readout . . . . .	35
4.2	Light production mechanisms . . . . .	36
4.2.1	Argon scintillation . . . . .	36
4.2.2	CF <sub>4</sub> scintillation . . . . .	37
4.2.3	Argon - CF <sub>4</sub> mixture scintillation . . . . .	38
4.2.4	TMEA and TEA scintillation . . . . .	38



4.3	Visible light detection . . . . .	40
4.3.1	Light detection devices . . . . .	40
	Photomultiplier tube (PMT) . . . . .	41
	CCD and CMOS sensor . . . . .	42
4.4	Geometrical optics and lens . . . . .	43
4.5	Optical effects . . . . .	46
<b>5</b>	<b>The glass Micromegas concept</b> . . . . .	<b>49</b>
5.1	Micromegas on a glass . . . . .	49
5.2	Glass Micromegas characterisation . . . . .	52
5.2.1	Gain and energy resolution measurement . . . . .	52
5.2.2	Light yield measurement . . . . .	55
5.3	Optical elements . . . . .	61
5.3.1	Camera . . . . .	61
5.3.2	Lens . . . . .	62
5.3.3	Dark chamber . . . . .	63
5.4	Acquisition modes and imaging processing . . . . .	64
5.4.1	Events integration . . . . .	64
5.4.2	Single event detection . . . . .	66
5.5	Conclusion . . . . .	67
<b>6</b>	<b>X-ray imaging</b> . . . . .	<b>69</b>
6.1	Detector characterization with an X-ray tube . . . . .	69
6.1.1	X-ray tube measurements . . . . .	70
6.1.2	Flat X-ray radiography . . . . .	70
6.1.3	X-ray radiography . . . . .	71
6.1.4	Deconvolution . . . . .	72
6.2	Measurements at the SOLEIL synchrotron . . . . .	74
6.2.1	The SOLEIL synchrotron and set-up description . . . . .	75
6.2.2	Glass Micromegas signal uniformity . . . . .	77
6.2.3	Optical aberrations . . . . .	80
6.2.4	Light reflection . . . . .	81
6.2.5	PSF 2D modelization . . . . .	83
6.2.6	Comparison of the blurring contributions and electron diffusion . . . . .	84
6.2.7	Electron range . . . . .	89
6.2.8	Simulation of the electrons range and diffusion . . . . .	91
	Diffusion . . . . .	92
	Mean range . . . . .	92
6.2.9	set-up configurations comparison . . . . .	95
6.2.10	Study of the Micromegas pillar and mesh effects . . . . .	96
6.2.11	Conclusion . . . . .	99
<b>7</b>	<b><math>\beta</math> imaging</b> . . . . .	<b>101</b>
7.1	Biological context and autoradiography . . . . .	101
7.2	Setups description and samples preparation . . . . .	103
7.3	Autoradiography simulation . . . . .	105
7.3.1	Energy spectrum simulation . . . . .	105
7.3.2	Electron range simulation . . . . .	105
7.4	$\beta$ detection with charge readout . . . . .	106

7.5	$\beta$ detection with optical readout . . . . .	108
7.5.1	Single event mode . . . . .	110
7.5.2	Integration mode . . . . .	112
7.6	Comparison with other $\beta$ imagers . . . . .	113
7.6.1	Biospace $\beta$ Imager 2000 comparison to Micromegas . . . . .	115
7.6.2	The PIMager . . . . .	117
7.7	Conclusion . . . . .	118
<b>8</b>	<b>Neutron radiography</b>	<b>119</b>
8.1	Context and applications . . . . .	119
8.2	Setup description and $^{10}\text{B}_4\text{C}$ converter . . . . .	121
8.3	Single event study . . . . .	123
8.3.1	Fragments length measurement . . . . .	123
8.3.2	Fragments width measurement . . . . .	125
8.4	Test at PSI . . . . .	125
8.4.1	Reduced drift gap and pre-amplification . . . . .	126
8.4.2	Flat beam irradiation . . . . .	127
8.4.3	Spatial resolution measurement . . . . .	129
	Line Spread Function fit . . . . .	129
	MTF measurement with the slit target . . . . .	130
	MTF by contrast measurement . . . . .	130
	Methods and amplification modes comparison . . . . .	132
8.4.4	Fragments energy loss simulation . . . . .	135
8.4.5	Radiography . . . . .	139
8.5	Conclusion . . . . .	140
<b>9</b>	<b>Conclusion and perspectives</b>	<b>143</b>
<b>A</b>	<b>Appendices</b>	<b>147</b>
A.1	Extended tritiated source . . . . .	147
A.2	Solid wavelength shifter: towards the mitigation of greenhouse gases . . . . .	148
	<b>Résumé en français</b>	<b>153</b>
	<b>Bibliography</b>	<b>157</b>



# 1 - Introduction

Imaging began with photography, where photons induce a signal on a silver film through the photoelectric effect. An image of the luminous sources is then printed on the film by multiple chemical processes. This foundational concept evolved, leading to the development of imaging devices for various types of particles, including X-rays, beta particles, neutrons, and more. Imaging detectors come in a large variety, with solid and gaseous states being the most widespread. Films, for instance, offer excellent spatial resolution for both X-rays and neutrons. Semiconductors are commonly used in medical imaging and astrophysics, allowing for high spatial resolution, time resolution and efficiency.

Scintillators coupled to a digital camera provide real-time imaging with high spatial resolution and efficiency. Solid-state detectors are highly efficient due to the particle conversion in solid-state, providing excellent spatial resolution through high localization of particle conversion in the detection medium. However, they are very sensitive to radiation and are not particularly radiation hard; they either saturate, or are subject to aging or damaging in high particle flux environment. Additionally, the cost per pixel increases rapidly with the surface of the active region.

On the other hand, gaseous detectors are radiation hard because of typical lower cross-section values of particle interactions with gas, while the signal is amplified through an avalanche structure. They can also cover large active areas with low material budgets. Over the last 30 years, these detectors have achieved high energy, time and spatial resolution and can be tuned for various applications, including the detection of X-rays, beta particles, muons, alpha particles, neutrons, and neutrinos. However, achieving a large detection surface with high spatial resolution requires a significant number of readout and electronics channels, along with extensive off-line data analysis. The complexity and cost increase rapidly with the number of pixels.

At the early stages of gaseous detectors, a new concept emerged, based on the use of the scintillated light from the excitation of gas molecules as an information carrier. A large amount of light is generated during the avalanche amplification process, and the choice of specific gas mixture (e.g.,  $\text{CF}_4$  and Argon) allows for emission across various wavelengths. In recent decades, CCD and CMOS sensors have improved, offering cameras with a large number of pixels and low noise. By coupling gaseous detectors with a camera and a magnifying lens, one can achieve a full 2D pixelized readout with high granularity, large active area, and low cost per pixel. Due to the low complexity and cost of Micro Pattern Gaseous Detector (MPGD) production, the primary investment lies in the camera. The cost of the camera can be significantly reduced, depending on the application. This setup exploits the camera's ability to integrate light, providing an average distribution of particles' position and flux. There is no need for timing resolution or clustering algorithms in this case, as overlapping events allow for imaging despite high particle flux. Cameras can also be used with short integration times to record single particle interactions, providing tracking capabilities, energy measurement, and suitability for time projection chambers when coupled with a time-resolved device (e.g. PMT, transparent readout strips).

The Micromegas detector geometry has been adapted for optical readout: it consists of a bulk Micromegas detector integrated on a glass substrate coated with Indium Tin Oxide (ITO), which is conductive and transparent to visible light. The visible light produced in the avalanche amplification crosses the Micromegas substrate and the chamber windows before reaching the camera sensor. This thesis focuses primarily on the ability of the detector to integrate consecutive events, which provides a user-friendly instrument, easy data handling, and eliminates the need for complex algorithms for event reconstruction. While the glass Micromegas detector fulfills gaseous detectors' main properties (radiation hardness, low material budget, unlimited particle flux dynamic range, high gain and energy resolution), it also offers high spatial resolution and sensitivity for real-time imaging with a large active area and at low cost per pixel. The Micromegas detector is particularly well-suited for light integration imaging due to its intrinsic properties and geometry. The micro-mesh structure ensures an almost uniform response, due to its small holes pitch and wire width, unlike other MPGD technologies.

Its simple geometry, consisting of one drift region and one amplification region, results in low charge diffusion. It results in better inherent spatial resolution compared to multiple amplification structure detectors.

In Chapter 2, the physical principles of particles interacting with matter are described. The processes of particles converting into charges, electron transport, and amplification in gaseous detectors are detailed in Chapter 3. Scintillation light is generated when gas molecules are ionized and excited after particle interaction. The scintillation mechanisms in Argon/CF<sub>4</sub> gas mixtures are depicted in Chapter 4. An overview of light detection devices and optics involved in optical readout Micromegas detectors is also provided.

During this thesis, the glass Micromegas design is optimized to achieve high spatial resolution and sensitivity imaging for X-rays, beta particles, and neutrons. Due to the high availability of X-ray sources and the high cross-section of soft and hard X-rays with gas via the photoelectric effect, X-ray imaging is an efficient tool to characterize new gaseous detector prototypes. In Chapter 5, the energy resolution and gain of glass Micromegas detectors are measured with different glass substrates and mesh geometries, both in charge and light readout using a <sup>55</sup>Fe source, charge readout modules and a photomultiplier tube. In Chapter 6, the light response uniformity of the glass Micromegas detector was examined at the CERN Gas Detector Development (GDD) laboratory, using an X-ray tube. X-ray radiography was performed on a small deceased animal and on a lead target to render the detector's spatial resolution.

The detector's light response is further studied in Section 6.2 by measuring the detector's Point Spread Function (PSF) at the SOLEIL synchrotron facility. The detector's response to a point-like signal provides a detailed description of the factors that affect the spatial resolution. The PSF is described as a convolution of distinct physical effects, each studied individually. The weight of their contribution to the PSF was assessed, providing a detailed strategy for spatial resolution improvement.

In Chapter 7, the potential of the glass Micromegas detector to detect, quantify, and localize tritiated samples is studied in collaboration with biologists and microfluidics experts in the context of oncology research.

The Chapter 8 is dedicated to the glass Micromegas detector upgrade for high spatial resolution neutron radiography. Coupling the glass Micromegas detector with a <sup>10</sup>B neutron-to-charge converter provides high sensitivity of neutron detection and real-time imaging capability in high particle flux environment. The imager spatial resolution was characterized at the Paul Scherrer Institut (PSI).

Finally, the main results of this thesis are highlighted and possible future directions and perspectives are outlined in Chapter 9.

## 2 - Radiation interaction with matter

The interaction of radiation with matter is governed by a large diversity of processes that depend on the particle and on the medium of interaction. The detection of radiation relies on the energy deposition of the incident particle in matter. Charged particles, photons or neutrons strongly differ in their interaction processes with matter. Within these categories, the energy, mass, type of particle (hadron, electron, etc) as well as the detection medium's matter state and elements involve a wide range of the interaction principles.

Full understanding of these mechanisms is necessary to reconstruct the incident particle properties (energy, type, position, momentum, spin, etc) or to identify non-desirable particles (from natural or experimental background). For charged particles, the interaction occurs by collision with the electronic structure of matter, leading either to the ionization or excitation of atoms. The charges (electron-ion pairs) or photons resulting from these interactions are generally the information carriers of the incident particle. As for incident photons, complementary mechanisms like the photoelectric effect, scattering or pair production lead to their detection. Since neutrons have no charge, they mainly interact with the nucleus. Their detection involves specific mechanisms based on neutron scattering or neutron capture, which lead to nuclear recoil and to the emission of charged particles, photons, neutrons, etc.

### 2.1 . Interaction of charged particles with matter

The electromagnetic interaction is involved in the interaction of charged particles with the atomic charges of the target. Charged particles can either interact through collision (elastic or inelastic) or radiative processes (Bremsstrahlung, Cherenkov, transition radiation, etc.). The charged particle can be fully absorbed or scattered, depending on the target material, the particle mass and energy. In this section, the ionization and excitation processes as well as photon emission reactions are described for heavy charged particles, electrons and positrons.

#### 2.1.1 . Ionization and excitation

Matter at ground state is formed of atoms with electrons bound to the nucleus, which can be removed by ionization. For charged particles with a kinetic energy above the ionization threshold, the target atom converts into an electron-ion pair, releasing electrons from their attachment. Below the ionization threshold, the atom transits to an excited state that leads to the emission of one or several photons, after the atom de-excitation and the potential return to its ground state. This process, known as fluorescence, causes the emission of photon in the entire range of the electromagnetic spectrum, including visible light and X-ray emission.

Charged particles mostly interact by inelastic collision with matter. A fraction of the kinetic energy of the charged particle is deposited in the medium, and the particle is either absorbed or scattered. If it is scattered, additional collisions occur until it is absorbed and most of its energy is released. When the kinetic energy of the charged particle is high, the produced electron from the electron-ion pair carries enough energy to undergo secondary ionization processes. These electrons are known as  $\delta$ -rays and contribute to the spreading of the deposited energy in a medium. The energy of the charged particle is usually larger than the minimum energy required to ionize matter (ionization potential). Hence, it goes through multiple ionizing collisions before all its energy is released. The number of collisions per unit length being large, the ionization and excitation mechanisms are described by the average deposited energy per unit length. Also called stopping power, it is well described for heavy charged particles by the Bethe-Bloch formula for a relativistic speed  $\beta\gamma \geq 0.05$  with  $\beta = \frac{v}{c}$ ,  $v$  the particle speed and  $c$  the speed of light. The Bethe-Bloch formula is given by:

$$\left\langle -\frac{dE}{dx} \right\rangle = K \rho \frac{Z}{A} \frac{z^2}{\beta^2} \left[ \ln \left( \frac{2m_e c^2 \beta^2 \gamma^2 T_{\max}}{I^2} \right) - 2\beta^2 \right] \quad (2.1)$$

where:

- $\left\langle -\frac{dE}{dx} \right\rangle$  is the mean energy loss per unit distance,
- $K = 2\pi N_A r_e^2 m_e c^2 = 0.1535 \text{ MeV cm}^2/\text{g}$ , where:
  - $\rho$  is the density of the material,
  - $A$  is the atomic mass of the material,
  - $Z$  is the atomic number of the material,
  - $N_A$  is Avogadro's number ( $6.022 \times 10^{23} \text{ mol}^{-1}$ ),
  - $r_e$  is the classical electron radius ( $2.817 \times 10^{-13} \text{ cm}$ ),
  - $m_e$  is the electron mass ( $0.511 \text{ MeV}/c^2$ ),
  - $c$  is the speed of light in vacuum ( $3 \times 10^{10} \text{ cm/s}$ ),
- $z$  is the charge of the incident particle in units of the electron charge,
- $\gamma = \frac{1}{\sqrt{1-\beta^2}}$  is the Lorentz factor,
- $T_{\max}$  is the maximum kinetic energy transfer to a free electron,
- $I$  is the mean excitation potential of the material,

For particles of relativistic speeds  $\beta\gamma \leq 0.1$  and  $\beta\gamma \geq 100$ , corrections have to be added to the formula. As an approximation, the term  $1/\beta^2$  dominates and the average energy loss per unit length decreases as the particle energy increases (Figure 2.1, left). This trend is valid until the limit  $\beta\gamma = 3$ . These particles are called the Minimum Ionizing Particles. As a heavy charged particle travels in matter it loses energy and its stopping power increases. Hence, the deposited energy increases with the penetration in matter and the major part of its energy is released at the end of its path. This is illustrated by the so-called Bragg curve shown in Figure 2.1 (right).

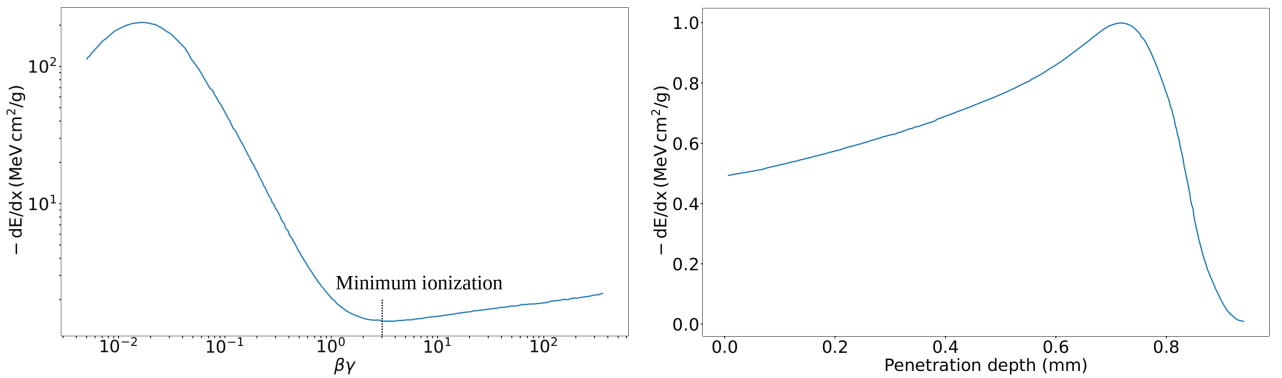


Figure 2.1: Stopping power for positive muons in copper as a function of  $\beta\gamma$  (left). Extracted from [1]. For  $0.05 \geq \beta\gamma \geq 100$ , the stopping power is well described by the Bethe-Bloch formula with corrections. Below  $\beta\gamma = 0.05$ , the stopping power is described by semi-empirical models [2, 3]. Stopping power as a function of the penetration depth of the particle inside matter (right). The so-called Bragg curve shows that more energy is deposited in the medium by the heavy charged particle at the end of its path.

The distance that the particle travels can be derived from this formula. The range of the particle is defined by the distance at which all its energy is released. Even for identical particles in the same

conditions and in the same medium, the range fluctuates. The mean of the ranges distribution is called the mean range,  $R$ , and corresponds to the average range weighted by the energy loss.

The mean range can be expressed as the integration of the inverse of the  $dE/dx$  over the energy. Since  $\beta^2 \propto T$  with  $T$  the kinetic energy,

$$\frac{dE}{dx} \propto \frac{1}{T} \text{ and } R \propto \int_0^{T_0} \left( \frac{dE}{dx} \right)^{-1} dE \propto T^2 \quad (2.2)$$

with  $T_0$  the initial particle kinetic energy. A more accurate computation of the range gives the relation  $R \propto T^{1.75}$ . This relation is issued from models and experimental data and must take into account the multiple Coulomb scattering of low-energy charged particles. The nuclei mass being usually much larger than the charged particle, at low energy it scatters elastically following a zigzag trajectory and strongly deviates from its original straight direction.

### 2.1.2 . Electrons energy loss

The Bethe-Bloch formula is no longer valid for electrons because of their much smaller mass. In addition, these low mass particles are sensitive to the electric field of a nucleus, which deflects them while passing through matter. The charged particles accelerate (or decelerate) producing a radiative loss of energy called Bremsstrahlung. At low energy, the ionization collision dominates, while at high energy it is the bremsstrahlung effect (Figure 2.2). The energy at which both effects contribute equally corresponds to the critical energy. The total stopping power for electrons is thus:

$$\left( \frac{dE}{dx} \right)_{tot} = \left( \frac{dE}{dx} \right)_{brem} + \left( \frac{dE}{dx} \right)_{coll} \quad (2.3)$$

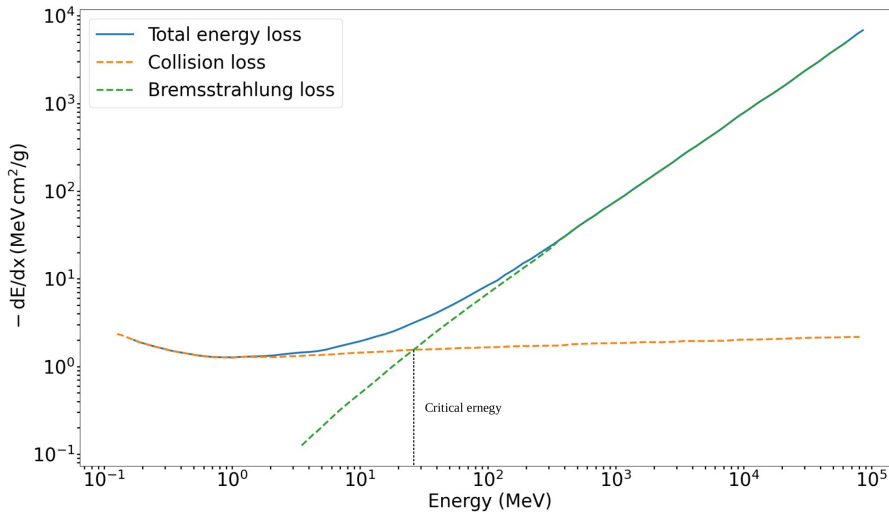


Figure 2.2: Stopping power in copper for electrons by ionization energy loss or radiative loss (Bremsstrahlung). Extracted from [4]. Energy loss by collision dominates for  $E \leq E_c$  and the Bremsstrahlung radiative effect dominates for  $E \geq E_c$  with  $E_c$  the critical energy.



The stopping power by ionizing collision loss of energy is similar to the Bethe-Bloch formula with a few modifications. First, the electron is frequently deflected by inelastic collisions and Coulomb scattering and its trajectory is not straight. The main exception is that collisions occur between identical particles. The maximum kinetic energy transfer to a free electron becomes  $T_{max} = T_e/2$  with  $T_e$  the incident electron kinetic energy. As mentioned earlier, the motion of electrons is hardly theorized and requires empirical data to be modelled. The mean range of electrons highly differs from the mean range computed from the integration of the Bethe-Bloch formula for heavy charged particles.

Radiation by the Bremsstrahlung effect only occurs in the presence of electrons and positrons. The probability of this effect indeed scales with the inverse square of the particle mass. The electric field of the nucleus is screened by the atomic electrons. Larger atomic number atoms will then involve a lower probability of radiative loss of energy. The energy loss by radiation is proportional to  $E/m^2$  with  $E$  and  $m$  the energy and the mass of the charged particle. This effect is involved in X-ray tubes that produce high-energy X-rays after accelerating electrons under an electric field of few tens of kV and decelerating them through matter (Copper, silver or tungsten mostly). The energy spectrum from an X-ray tube is composed of an extended energy band from Bremsstrahlung X-rays and energy peaks that correspond to the target excitation levels (K-shell  $\approx 8$  keV for copper).

Charged particles might also be accelerated perpendicularly to their velocity by a magnetic field. Similarly to the Bremsstrahlung effect, the acceleration is radiative, with the emission of light in the opposite direction to the electron deflection due to the Lorentz force. For relativistic charged particles, the radiative process is called the synchrotron radiation. This process is utilized in synchrotron facilities to produce X-rays by accelerating electrons in a circular accelerator to relativistic speeds.

## 2.2 . Interaction of photons with matter

Unlike heavy charged particles,  $\gamma$ -rays and X-rays do not cross matter by losing energy and being undeflected from the beam axis. Photons either cross matter without being affected, are scattered or absorbed. They can undergo either elastic or inelastic scattering, absorption that leads to photon or charge particle production. A given probability of interaction is attributed to each channel  $i$  by the cross-section  $\sigma_i$ . The attenuation of a photon beam is directly related to the processes' cross-section and to the density  $\rho$  of the traversed medium by the relation:

$$\mu = \frac{N_A \rho}{A} \sum_i \sigma_i \quad (2.4)$$

where  $\mu$  is the attenuation coefficient,  $N_A$  the Avogadro number and  $A$  the atomic mass. The attenuation of the beam induced by all the processes after a distance  $x$  in the material is given by the relation:

$$I(x) = I_0 e^{-\mu x} \quad (2.5)$$

The main interaction mechanisms of  $\gamma$ -rays and X-rays in matter are the photoelectric effect, scattering and pair production. The attenuation coefficient as a function of the photon energies is displayed on Figure 2.3 for each reaction.

### 2.2.1 . Photoelectric effect

The photoelectric process consists in the absorption of a photon by an electron bound to an atom. Free electrons can not be subject to the photoelectric effect because the photon momentum is conserved by the absorption of the momentum by the nucleus. The incident photon must have enough energy to extract the electron from the atom. Following the ionization of the atom, the ejected electron has an energy:

$$T_e = h\nu - E_b \quad (2.6)$$

where  $T_e$  is the emitted electron kinetic energy after ionization,  $h\nu$  the photon energy and  $E_b$  the binding energy of an electronic shell. A photon will preferably eject an electron from a shell of binding

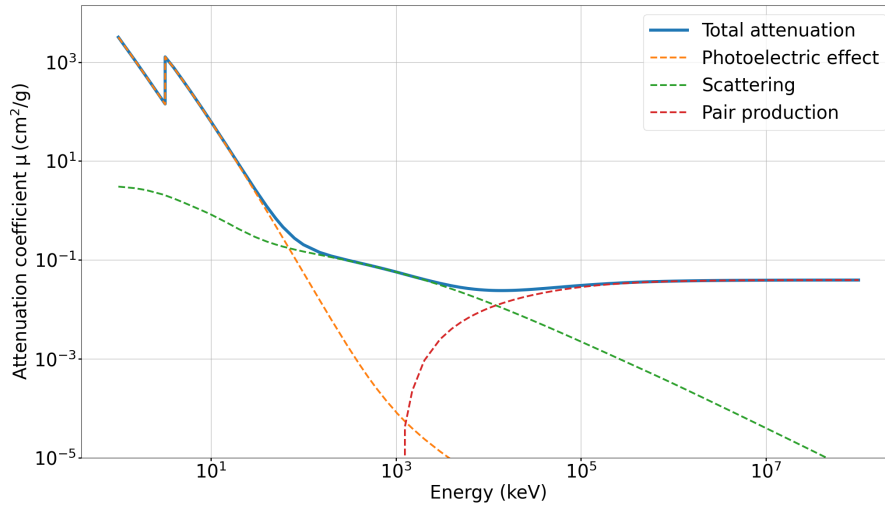


Figure 2.3: Attenuation coefficient as a function of the incident photon energy in keV, in Argon. The photoelectric effect dominates a low energy, then the scattering effect is dominant at intermediate energies and the pair production effect is prevailing at high energies. Compiled with data from [5].

energy close to the photon energy. For photons of energy larger than the highest binding energy, there is a higher cross-section for the ionization of the innermost shell (K-shell). As shown in Figure 2.3 (orange dotted line), the cross-section increases as the photon energy decreases until the photon energy becomes lower than the K-shell binding energy. Thus, the cross-section drastically drops, which is known as the K absorption edge. As the photon energy further decreases, the cross-section for the interaction with outer shells increases and the same phenomenon repeats.

As a consequence of the ionization by the photoelectric effect, a vacancy is left in the electronic structure of the atom and can be filled by an electron from an outer shell. The rearrangement of the atom leads either to a photon emission or to an Auger electron emission through a radiationless transition. For fluorescence, the emitted photon has an energy equal to the difference  $\Delta E$  between the inner and shallower shells binding energies. The Auger electron has an energy  $\Delta E - E_{b2}$  with  $E_{b2}$  the binding energy of an outer shell.

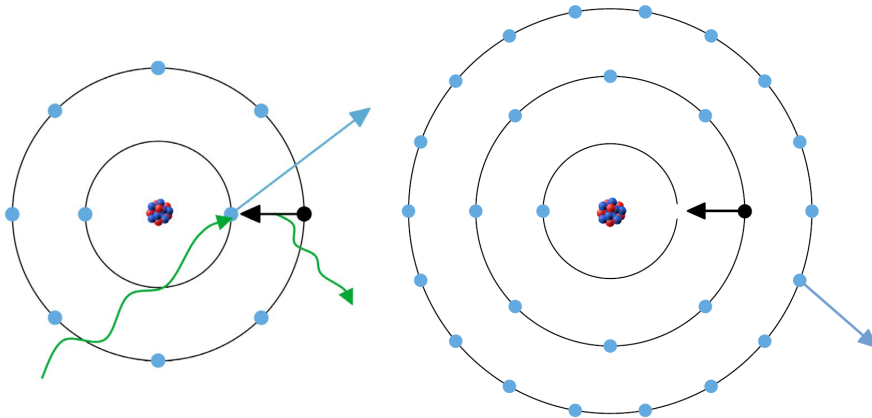


Figure 2.4: Cartoon illustrating the photoelectric effect. On the left, a photon is absorbed by the innermost shell of the atom and an electron from the same shell is ejected. An electron from an outer shell fills the hole and a photon is emitted. On the right, the transition is radiationless and the energy balance is removed by direct ejection of a third electron from an outer shell. An Auger electron is ejected from the atom. The green, blue and black arrows represent respectively a photon, an ejected electron from the atom and an electron transitioning to an inner shell.

The Auger electron and photon emissions, which follow the rearrangement of an atom after ion-

ization, are competitive processes. At low atomic numbers (below 30 approximately) the Auger effect dominates while the photon emission dominates at large atomic number.

### 2.2.2 . Compton scattering

At medium energies in Figure 2.3, the Compton scattering interaction dominates. This inelastic process involves a high-energy photon that is deflected by a weakly bound electron to the atom. The photon wavelength is shifted during the scattering reaction and the electron is ejected from the atom. The loss of energy of the photon is given by the formula:

$$\lambda - \lambda' = \frac{h}{m_e c} (1 - \cos \theta) \quad (2.7)$$

where  $\lambda$  and  $\lambda'$  are the photon wavelength before and after the scattering.  $h$  is the Planck constant and  $\theta$  is the deflection angle illustrated in Figure 2.5 (left).

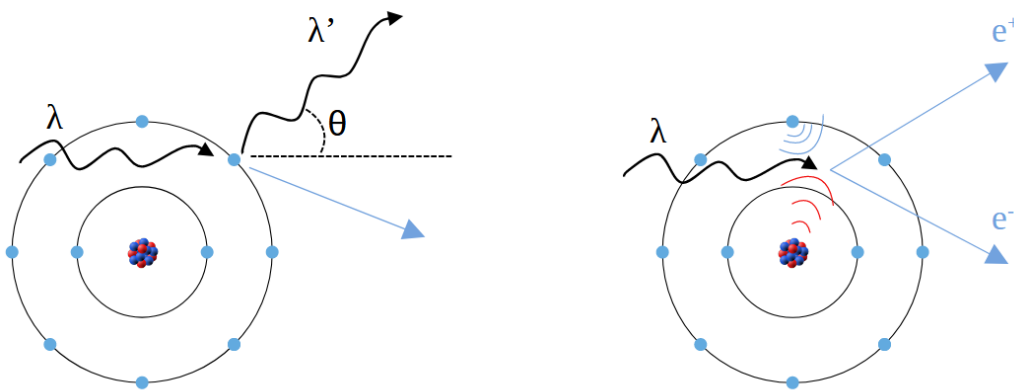


Figure 2.5: Cartoon illustrating the Compton effect (left). The incident photon of wavelength  $\lambda$  scatters on an outer shell electron of the atom. The photon scatters with an angle  $\theta$  and its wavelength shifts to  $\lambda'$ . Illustration of the pair production reaction (right). The photon converts in a electron-positron pair in the presence of the nucleus (or electron) electric field.

Photons might also scatter elastically on an atom while no energy is transferred to the medium. At low-energy photons, the photon bounces by Thomson scattering on a electron of the atom. At intermediate energy, Rayleigh scattering happens, involving all the electrons coherently in the scattering of the photon.

### 2.2.3 . Pair production

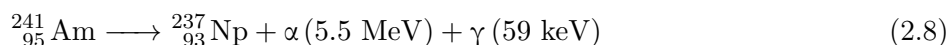
At high photon energy, while the cross-section for the two previous effects drops, the pair production mechanism is enabled. In fact, an electron and a positron are produced when the photon enter the vicinity of an atom. By energy conservation, the energy of the photon must be higher than the mass energy of the two products:  $E_\gamma \geq E_{e^-} + E_{e^+} = 2 \times 511 \text{ keV} = 1022 \text{ keV}$  where  $E_{e^+}$  and  $E_{e^-}$  are the rest mass energies of the positron and electron respectively. The momentum is conserved by the nucleus decay. The remaining energy is transferred to the electron and positron kinetic energies. The process is usually triggered by the nucleus electric field but can also happen because of the electron electric field, although it is less probable because of their smaller charge. The cross-section of these mechanisms rapidly stagnates as the photon energy increases. However, the cross-section mostly depends on the electric field, hence on the atomic number. The pair production process is illustrated in Figure 2.5 (right).

## 2.3 . Nuclear processes and interaction of neutrons with matter

Many sources of radiation are based on nuclear processes that lead to the emission of  $\gamma$ -rays or X-rays,  $\beta$  or neutron particles. While some isotopes naturally decay over time and emit particles repeatedly, others are involved in scattering processes towards the emission of neutrons, for example. The neutron interaction with matter differ from previous reactions because it has no charge. Neutrons cover a large range of energies and as their energy decreases, they are called fast, thermal or cold neutrons. The production, moderation and detection mechanisms of neutrons are details in this section.

### 2.3.1 . Alpha decay

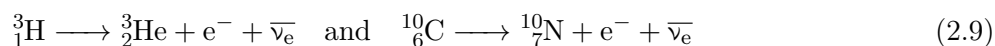
Alpha decay results from the spontaneous fission of a heavy nucleus. An alpha particle is a Helium nucleus  ${}^4_2\text{He}^{2+}$  of charge +2 with two protons and two neutrons. The decay of a parent atom produces a daughter atom with an alpha particle and a gamma emission eventually. For example, the alpha decay of Americium is:



Only heavy nucleus are inclined to alpha decay because of their instability. In fact, the strong interaction that holds a nucleus together has a short range and fades away for large size nucleus that breaks under the electromagnetic repulsion between protons. A helium nucleus is produced because of its large binding energy per nucleus, thus stability. Most of the energy becomes the  $\alpha$  particle kinetic energy and a small fraction goes to the daughter nucleus recoil because of momentum conservation.  $\alpha$  particles have an energy of the order of few MeV and have a large stopping power because of their important charge (two positrons). Their range in dense matter is of the order of few microns. Converters that produce  $\alpha$  particles are usually very thin (smaller than the  $\alpha$  range) to minimize the  $\alpha$  energy loss in the converter while maximizing its energy loss in the detection medium.

### 2.3.2 . Beta decay

The beta decay results in the emission of an electron or a positron from an unstable nucleus that has an excess of neutron or proton. After beta decay, the nucleus turns into a more stable state and gains in binding energy per nucleon. In the case of  $\beta^-$  decay, a neutron transforms into a proton by the weak-interaction.  ${}^3\text{H}$  and  ${}^{14}\text{C}$  are  $\beta^-$  radioactive isotopes and decay following the reactions:



In the case of  $\beta^+$  decay, a proton transforms into a neutron which leads to the decay of  ${}^{23}_{12}\text{Mg}$  following the reactions:



For the conservation of the lepton number, an electron antineutrino is emitted in the  $\beta^-$  decay and an electron neutrino in the  $\beta^+$  decay. Because of the neutrino or antineutrino production, the energy is shared between the electron (or positron) and the antineutrino (or neutrino) kinetic energies, and the nucleus recoil. While the antineutrino is almost never detected, the  $\beta$  particle detection spectrum is continuous. The energy spectrum from the  ${}^3\text{H}$  and  ${}^{14}\text{C}$  beta decay is shown in Figure 2.6. Tritium is particularly difficult to detect due of its low-energy spectrum and because of the short penetration depth of electrons.

### 2.3.3 . Electron capture

The electron capture (EC) process is similar to the  $\beta^+$  decay, where a nucleus with an excess of protons has a proton converted into a neutron. However, for the charge conservation, an electron is absorbed by the nucleus instead of having the emission of a positron. For  ${}^{55}\text{Fe}$ , its decay follows the reaction:



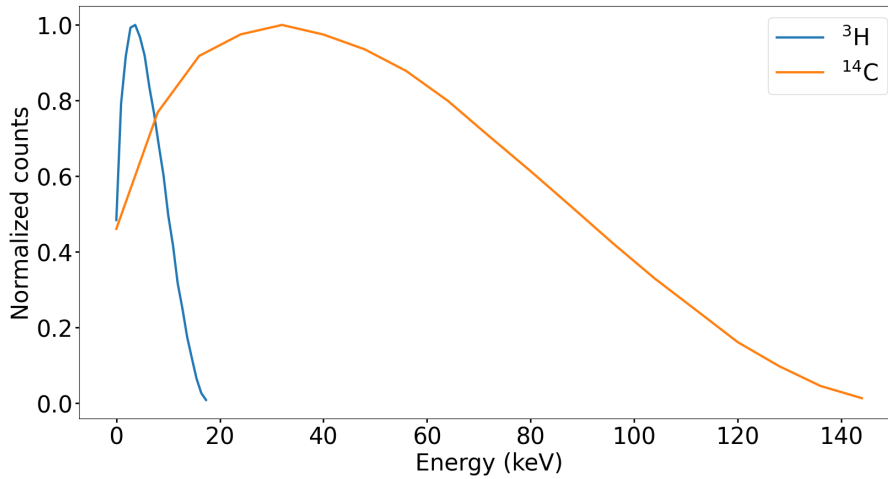


Figure 2.6: Energy spectrum from the beta decay of  $^3\text{H}$  (blue line) and  $^{14}\text{C}$  (orange line). The maximum energy of the  $\beta$  electrons is about 18 keV and 160 keV for the  $^3\text{H}$  and  $^{14}\text{C}$  respectively. Simulated on Geant4 [6].

Most of the time, an electron from the K-shell is absorbed, leading to a rearrangement of the electronic structure. To fill the hole left by the electron, an electron from an outer shell replaces it, emitting an X-ray photon. Its energy is the difference between the shells' binding energy. An Auger electron might be emitted depending on the atomic number of the atom. The EC energy spectrum from  $^{55}\text{Fe}$  is studied in details in Sec. 5.2.1. X-ray sources such as  $^{55}\text{Fe}$  are often used to characterize detectors because of their well-defined energy peak.

### 2.3.4 . Gamma decay

Similarly to electrons that are bound to the nucleus by the electromagnetic force, nucleons are bound together by a larger binding energy forming the nucleus. The nucleus can reach an excited state and often emits  $\gamma$ -rays when nucleons transit between the nuclear shell levels. The large energy of the  $\gamma$ -rays is due to the large binding energies involved in the nucleus. The excitation of the nucleus is commonly a consequence of other decay processes like the beta decay, alpha decay or nuclear reactions such as neutron capture, fission or fusion.

### 2.3.5 . Neutron production

Neutrons can be produced by different mechanisms, such as spontaneous fission or nuclear reactions. Spontaneous fission mainly occurs for large atomic mass elements. The electromagnetic repulsion between protons overcomes the strong interaction for heavy elements that compels the nucleus to split into more stable nuclei. Several neutrons are, in general, emitted in the process, with a continuous energy spectrum ranging from about 0 to 10 MeV. However, neutron sources based on nuclear reactions are often preferred because of their larger half-life ( 2.645 years for the spontaneous fission source  $^{252}\text{Cf}$  against 432 years for a AmBe nuclear reaction-based source).

## Nuclear reaction

Nuclear reactions that lead to the emission of neutrons can be triggered by alpha particles or  $\gamma$ -rays. The neutron sources are thus made of a mixture of a neutron emitter such as  $^9\text{Be}$  and an alpha or gamma source. Nuclear reactions induced by gammas occur when the  $\gamma$  particle energy is higher than the binding energy of a bound neutron to the nucleus. Several reactions are required to reject a neutron after that an  $\alpha$  particle has hit the nucleus. The most common neutron sources are based on alpha decay rather than gamma decay because of their larger neutron yield. For example, the AmBe source produces neutrons by the reaction  $^9\text{Be}(\alpha, n)^{12}\text{C}$ . The alpha production from the  $^{241}_{95}\text{Am}$  is also accompanied by a gamma emission. The neutron source is often shielded to diminish the gamma background to which

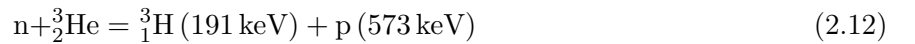
the detector is exposed. The neutron energy spectrum shows a continuum: because of  $\alpha$  particles rapid loss of energy in matter, the energy transmitted to the neutron is randomized. On the contrary, gamma induced nuclear reaction such as  ${}^9\text{Be}(\gamma, n){}^8\text{Be}$  shows a more sharpen energy spectrum due to the non attenuation of  $\gamma$  particles. In this case, the shielding of the source to contain the remaining gammas is even more appropriate.

## Spallation

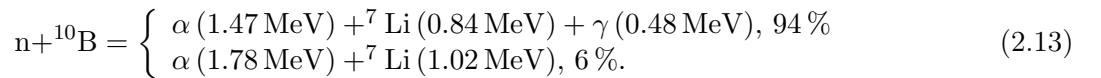
Spallation is a process where nuclear reactions such as fission are generated by a high-energy and high flux particle beam that hits a target made of heavy elements. Protons are mainly used in spallation sources and can be accelerated to about 1 GeV by a linear accelerator. Heavy elements such as Tungsten are used as a target because of their high density and melting point and are favorable to fission when they enter a highly excited state. While some neutrons are emitted when the proton hits a nucleus, a larger amount of neutrons is rejected during the evaporation: the nucleus has been heated up to a high excited state and undergoes several fission reactions. No chain reaction is involved in the spallation process in opposition to fission reactors, which constitutes an advantage regarding nuclear safety. The neutron source can also be pulsed.

### 2.3.6 . Neutron capture and moderation

Similarly to photons, neutrons do not have charge and rarely interact with matter. Mostly at low energy, they can interact via several processes, among which are the neutron capture and scattering reactions. A cross-section is associated to each one of these channels, and the total probability of interaction can be described by the attenuation coefficient (2.4). A neutron beam will be attenuated following a negative exponential decrease of the beam intensity (2.5). Neutron capture is the result of the absorption of a neutron by the nucleus that leads to the rearrangement of the nucleus and occasionally relaxation and gamma emission. A wide range of products exist for the neutron capture, involving the emission of photons, charged particles or fission fragments. In gaseous detectors, neutron captures leading to the emission of charged particles such as  $\alpha$  particles or protons are preferred for their more convenient detection. The isotopes  ${}^3\text{He}$  and  ${}^{10}\text{B}$  are commonly preferred as converters for their charged daughter particles and high neutron capture cross-section. The charged fragments also have large kinetic energies, facilitating their detection. The neutron captures reactions of these isotopes are:



and



The cross-sections of the two nuclear reactions are shown in Figure 2.7. The neutron energy is also expressed in wavelength by the relation  $\lambda (\text{\AA}) = 0.28601 / \sqrt{E (\text{eV})}$ . The cross-section is significant for thermal ( $E = 25 \text{ meV}$ ) and cold ( $E \leq 25 \text{ meV}$ ) neutrons and rapidly decreases with the neutron energy in  $1/v$  with  $v$  the neutron velocity. Proportional counters using  ${}^3\text{He}$  as a neutron converter and a detection medium show a high detection efficiency. Other detectors use  ${}^{10}\text{B}$  as a solid converter deposited in a very thin layer to prevent the reabsorption of the fragments by the converter layer.

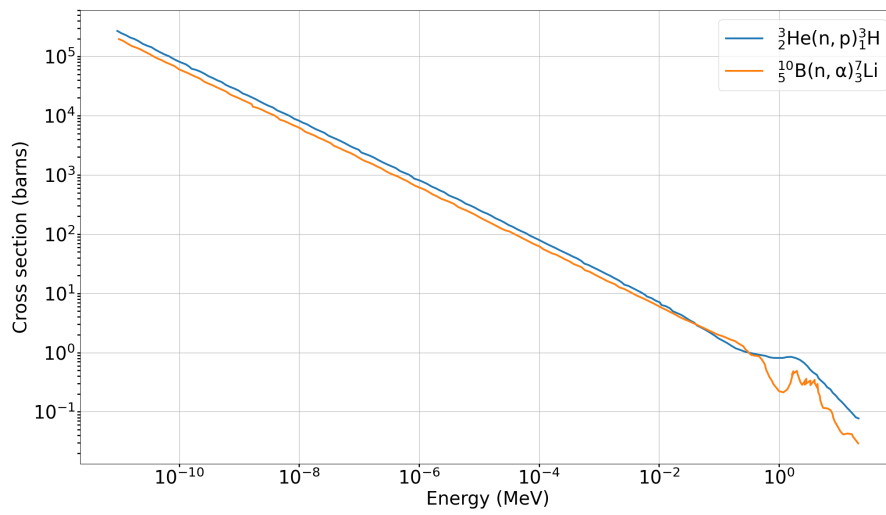


Figure 2.7: Neutron capture cross-section as a function of the neutron energy for the reactions  ${}^3_2\text{He}(n, p){}^3_1\text{H}$  (blue plot) and  ${}^{10}_5\text{B}(n, \alpha){}^7_3\text{Li}$  (orange plot). Extracted from [7]

## 3 - Gaseous detectors

As seen in the previous chapter, radiation detectors mainly rely on the property of matter to be ionized or excited by charged particles. In the case of neutral particles (photons, neutrons, etc), intermediate processes such as the photoelectric effect or neutron capture are necessary to end with charged particles carrying the neutral particle information. Different types of detectors exist and are specifically designed to extract the desired radiation information with optimum performances. Solid-state detectors such as scintillators, semi-conductors or radiographic films show high detection efficiency because of the detection medium high density. However, gaseous detectors generally exhibit lower detection efficiency but are competitive regarding the time, energy and spatial resolution. Their main advantages are their scalability to large detection areas at a low material budget, thanks to the detection medium gas state. The low interaction rate of particles with gas, however, constitutes a major benefit regarding the radiation hardness. In high-radiation environments, it enables the discrimination of parasitic radiation such as gamma radiation from heavy charged particles. Finally, the wide array of existing gaseous detector designs underscores their versatility in adapting to diverse conditions, objectives, and constraints in radiation detection.

Gaseous particle detection is based on several phenomena such as the particle conversion to free electrons in gas, the movement of the electrons in an electric field through drifting and diffusion or the avalanche multiplication process. This work focuses on the properties of gas mixtures based on Argon, Carbon Tetrafluoride ( $\text{CF}_4$ ) and Isobutane.

### 3.1 . Charge production and transport in gas

This section describes the conversion of charged particles by gas atom ionization followed by the production of free electrons and ions pairs. The transport of charges in an electric field is also described.

#### 3.1.1 . Particle conversion in gas

Charged particles crossing a detector's gas medium convert their kinetic energy into multiple ionization and excitation reactions, as detailed in Sec. 2.1. The average number of free electrons from gas ionization, also called primary electrons, is proportional to the charged particle energy loss. The mean number of primary electrons is then

$$\langle N \rangle = \frac{\Delta E_{Loss}}{W} \quad (3.1)$$

where  $\Delta E_{Loss}$  is the energy loss and  $W$  the mean energy required to produce an ion-electron pair, which depends only on the gas properties.  $W$  takes into account the energy converted in both the excitation and ionization mechanisms, unlike the ionization potential. The use of noble gases in gaseous detectors promotes the energy loss via ionization processes rather than further excitation channels like vibrational or rotational excitation.

By measuring the number of primary electrons, it is possible to reconstruct the incident particle energy with a given error. This error contributes to the energy resolution and derives from the uncertainty on the number of ionizations. The actual number of ionizations,  $N$ , follows the Poisson statistics, such that its standard deviation is  $\sigma_N^2 = \langle N \rangle$ . However, the variable  $N$  follows a distribution that slightly differs from the Poisson distribution. In fact,  $N$  is constrained by the incident particle's finite energy and the individual ionization collisions are not independent. The variance is then corrected by a factor  $F$  called the Fano factor that considers all the energy deposition mechanisms. Since  $F \leq 1$ , the variance is improved such that  $\sigma_N^2 = F \langle N \rangle$ . The energy resolution is defined as

$$\frac{\Delta E(\text{FWHM})}{\Delta E_{Loss}} \quad (3.2)$$



where  $\Delta E(\text{FWHM}) \approx 2.335 \sigma_E$  is the Full Width at Half Maximum (FWHM) and  $\sigma_E$  is a convolution of  $\sigma_N$  and the error involved by other processes such as the detector gain.

The primary electrons and ions must be transferred to an electrode for readout or to an amplification region. An electric field is thus implemented in the gas medium to drift the charges and additionally limiting their recombination or attachment with the gas atoms.

### 3.1.2 . Transport of charges in gas

The transport of charges constitutes one of the main parameters of a gaseous detector, involving for instance the signal spread both in time and space. The charges' transport is involved by an electric field implemented by a difference of potential between the cathode and the anode such that  $E = \Delta V/d$  with  $E$  defining the electric field norm,  $\Delta V$  the difference of voltages and  $d$  the distance between the two electrodes. Electrons are thus drifting towards the anode and ions towards the cathode at a much slower speed because of their larger mass. The drift of charges is defined by the average velocity, also called drift velocity  $w$  instead of the instant velocity  $v$ . In fact, the instant speed of electrons fluctuates considerably, switching from acceleration and deceleration phases due to the electric field and scattering with the gas molecules respectively. The electron drift velocity  $w^-$  thus depends on the mean time between collisions  $\tau$  and is written by Townsend as

$$w^- = k \frac{eE}{m} \tau \quad (3.3)$$

where  $k$  is a constant between 1 and 0.75 related to the electron energy distribution,  $m$  and  $e$  the electron mass and charge. The electron drift velocity is thus the result of the competition between the electric field's induced acceleration and the collision rate  $1/\tau$ . While the acceleration from the drift field increases the particle instant speed, it also increases the probability to scatter elastically with gas molecules (Figure 3.1, left). The electron recurring scattering involves a growth of its deviation from its original path and thus implies a reduced drift velocity. To increase further the drift velocity, the electron kinetic energy must be drained by another process than elastic scattering that does not deviate the electron. While the electron kinetic energy is too low for ionization or excitation at this stage, loss of energy via vibrational and rotational excitation are inaccessible to monatomic noble gases. Hence, adding a molecular element in the gas mixture allows to unlock these excitation channels and promotes the electrons' loss of energy by other ways than elastic scattering. In fact,  $\text{CF}_4$  shows high cross-section values for the inelastic scattering of electrons with the gas molecules at smaller energies than for Argon by one order of magnitude (Figure 3.1, right). The drift velocity for several gas mixtures is shown in Figure 3.2 (left). The drift velocity is, in fact, higher for gas mixtures with a fraction of a molecular element than for pure Argon gas mixture.

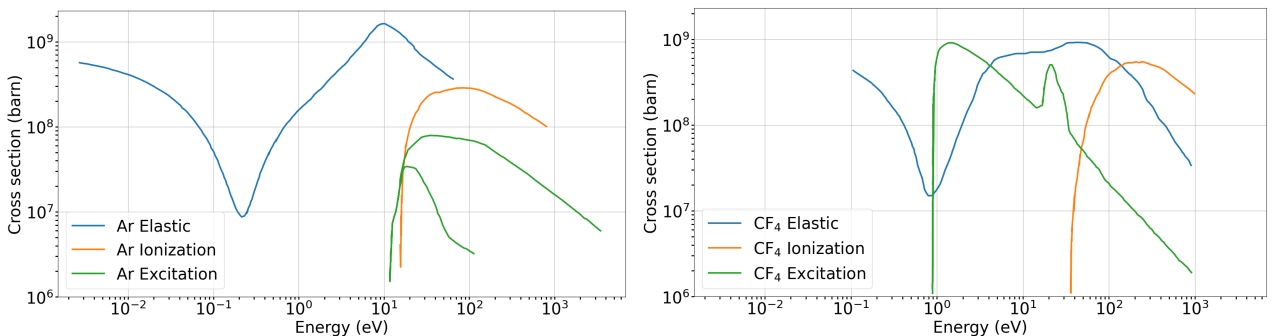


Figure 3.1: Electron–molecule cross section for Argon (left) and  $\text{CF}_4$  (right). In noble gas like Argon, elastic scattering is the only available channel until energies of about 10 eV where excitation and ionization become likely. In polyatomic gas like  $\text{CF}_4$ , inelastic scattering by excitation dominates at smaller energies of about 1 eV. Extracted from [8].

For both electrons and ions, the drift velocity is related to the electric field by the relation

$$w = \mu E \quad (3.4)$$

where  $\mu$  is the mobility.

Either because of the charges' thermal energy or movement induced by an electric field, charges diffuse from their original position because of multiple collisions with the gas molecules. The fraction of particles in a portion of space  $dx$  and at a distance  $x$  from their original position after a time  $t$  follows a Gaussian distribution:

$$\frac{dN}{N} = \frac{1}{\sqrt{4\pi Dt}} e^{-\frac{x^2}{4Dt}} dx \quad (3.5)$$

with  $D$  the diffusion coefficient that mainly characterizes the diffusion for a given gas mixture, temperature and pressure. One can deduce from it the standard deviation of the particle position distribution in 1D along the axis  $x$  and in 3D in a volume  $v$ :

$$\sigma_T = \sqrt{2Dt} \quad \text{and} \quad \sigma_v = \sqrt{6Dt} \quad (3.6)$$

In the presence of an electric field, the diffusion is inversely proportional to the electric field strength according to the modified Nernst–Townsend formula:

$$\frac{D}{\mu} = \frac{\epsilon_k}{e} \quad (3.7)$$

The characteristic energy  $\epsilon_k$  is a phenomenological number including the additional electron energy due to the electric field. For ions and thermal electrons, the minimum diffusion is reached and  $\epsilon_k = kT$  with  $k$  the Boltzmann's constant and  $kT$  the thermal energy. From the relations 3.6 and 3.7, the diffusion standard deviation is given by the space dependent relation:

$$\sigma_T = \sqrt{\frac{2\epsilon_k x}{eE}} \quad (3.8)$$

The transverse diffusion standard deviation  $\sigma_T$  has been plotted in Figure 3.2 (right) for pure Argon and for several gas mixtures. The diffusion is much larger for pure Argon gas than for a mixture of Argon and a polyatomic gas, such as Isobutane. For  $CF_4$  based gas mixtures, the maximum of drift velocity matches a minimum of diffusion. After this minimum, the diffusion increases because the excitation cross-section of  $CF_4$  drops at larger energy. At even larger field of about 10 kV/cm, the diffusion starts to decline again because of the increased probability of energy loss by ionization. In addition, the gas pressure and temperature significantly affects the diffusion. These effects have not been studied in this thesis, while it is well reported in the literature [8].

The diffusion involves an enlargement of the charge density distribution. In addition, the longitudinal diffusion, that spreads the electrons cloud in the direction parallel to their drifting direction, brings timing uncertainty. In fact, the difference between the arrival times of the first and last electrons reaching the anode is widened by the diffusion. Moreover, the transverse diffusion, that spreads the electron cloud perpendicularly to their drifting direction, brings an uncertainty on the reconstruction of the primary electron position. This has direct consequences on the spatial resolution of the detector.

## 3.2 . Charge amplification

As explained previously, the electric field between two electrodes allows the drift of the electrons towards the anode. At higher electric field strength, other mechanisms such as electron multiplication take place, known as the proportional counter regime.

### 3.2.1 . Avalanche amplification

In a proportional counter, after the drift of the primary electrons towards the anode, they reach a region of much higher electric field for amplification. Under the acceleration of the electric field, electrons gain sufficient kinetic energy to trigger atomic excitation and ionization. As seen in Figure 3.1,

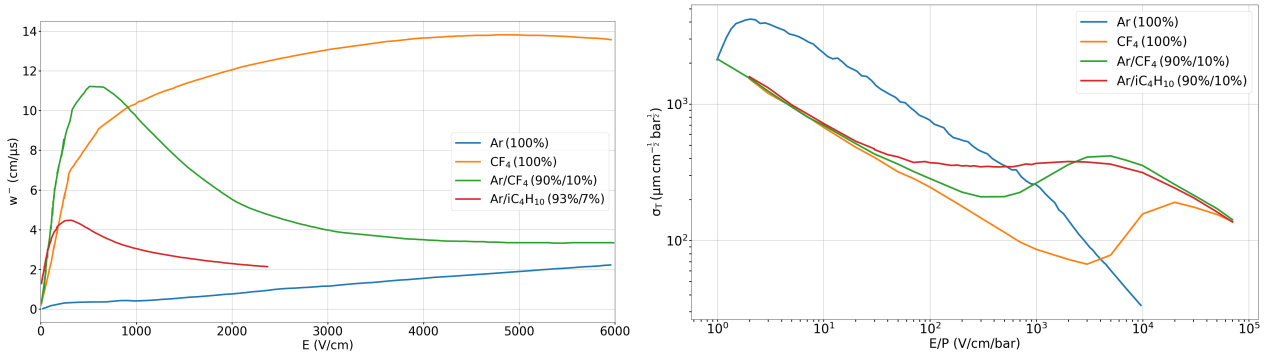


Figure 3.2: Drift velocity  $w^-$  as a function of the electric field for different gas mixtures (left). Polyatomic gases such as  $\text{CF}_4$  or  $\text{C}_4\text{H}_{10}$  considerably increases the drift velocity, even in small proportion. Extracted from [9]. Transverse diffusion standard deviation  $\sigma_T$  for different gas mixtures (right) computed with Magboltz. The addition of a polyatomic gas decreases the diffusion.

energy loss via ionization and excitation begins at 10 eV for Argon. The ionization from the acceleration of a primary electron hence leads to the production of a secondary electron following the reaction



with A the gas species. The secondary electrons are further accelerated to the required kinetic energy to enable ionization and again produce an electron-ion pair. As long as the electrons drift in the gap between the electrodes, they undergo an exponential multiplication of the number of secondary electrons. The number of electron-ion pairs produced per unit length in such amplification process is defined by the first Townsend coefficient  $\alpha$  and is directly related to the ionization cross-section through the expression:

$$\alpha = N\sigma_i \quad (3.10)$$

with  $N$  the number of molecules per unit volume. The increase of the number of secondary electrons  $n$  in a portion of space  $dx$  is given by the formula:

$$dn = \alpha n dx \quad (3.11)$$

Hence, the number of secondary electrons produced by the amplification process from a number  $n_0$  of primary electrons in a distance  $x$  leads to the relations:

$$n = n_0 e^{\alpha x}, \quad M = \frac{n}{n_0} = e^{\alpha x} \quad (3.12)$$

$M$  is the multiplication factor, also called gain of the gaseous detector. In a non ideal-case, the electric field is not uniform in space and the electron multiplication should then be computed in any location in depth from a point  $x_1$  to  $x_2$  such that

$$M = e^{\int_{x_1}^{x_2} \alpha(x) dx} \quad (3.13)$$

The multiplication process is illustrated in Figure 3.3. A electron is duplicated when it crosses a distance larger than the ionization mean free path  $\lambda = \alpha^{-1}$ , decreasing as the electric field increases. While the ions drift in the electrons opposite direction with a much lower velocity, the avalanche gets a drop like shape (Figure 3.3).

The Townsend coefficient dependence on the electric field and gas pressure is established by the Korff formula.

$$\frac{\alpha}{P} = A e^{-\frac{BP}{E}} \quad (3.14)$$

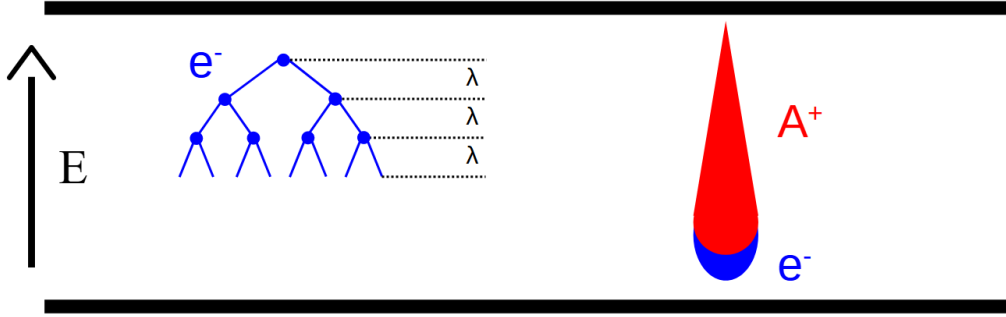


Figure 3.3: Scheme of the multiplication process of the electrons with  $\lambda = 1/\alpha$  the mean free path for ionization. The avalanche with a drop shape is represented, having a long ion tail because of their long drift velocity.

where A and B are phenomenological parameters depending on the gas mixture.

The category of gaseous detectors operating in the avalanche multiplication mode is called proportional counter. Indeed, the number of secondary electrons is proportional to the number of primary electrons through the formula (3.12). This regime is stable in a wide range of electric field values as shown in Figure 3.5. According to Sec. 3.1, the energy loss in the gas by the incident particle is related to the number of primary electrons. The error associated is  $\sigma_N^2 = F \langle N \rangle$ . The error on the incident particle energy that defines the energy resolution also takes into account the multiplication factor such that

$$\left(\frac{\sigma_S}{S}\right)^2 = \left(\frac{\sigma_N}{N}\right)^2 + \left(\frac{\sigma_M}{M}\right)^2$$

with  $S$  the measured signal energy. The error on the gain  $\left(\frac{\sigma_M}{M}\right)^2$  is the dominant term and increases with the absolute gain. At low gain, the electronic noise afflicts the energy resolution. The optimum energy resolution hence is found at an intermediate amplifying electric field.

In  $\text{CF}_4$  based gas mixture, electron capture, or attachment, significantly affects the energy resolution at high electric field [10]. The inelastic scattering cross-section for  $\text{CF}_4$  shows a peak at about 25 eV in Figure 3.1 that corresponds to an increase of the electron attachment with the gas positive ions. The number of primary electrons hence diminishes and its proportionality with the incident particle energy is affected. For  $\text{CF}_4$  based gas mixtures, the attachment coefficient  $\eta$  (probability of attachment per unit length) must be taken into account in the gain formula such that

$$M = e^{\bar{\alpha}x} \quad (3.15)$$

where  $\bar{\alpha} = \alpha - \eta$  is the effective ionization coefficient. The Townsend and attachment coefficients have been simulated on Magboltz [11] for an Ar/ $\text{CF}_4$  (90%/10%) gas mixture, and are represented on Figure 3.4 as a function of the electric field. The effective ionization coefficient is negative at an electric field from around  $10^4$  V/cm and down to  $10^3$  V/cm, involving a significant loss of primary electrons. However, at higher field values, the attachment is largely compensated by the electrons multiplication. At electric field values below  $10^3$ , which is typical for the ionization chamber regime where electrons are drifting without amplification, the attachment probability becomes null. Electron capture is also triggered by gas impurities such as electronegative species ( $\text{O}_2, \text{H}_2\text{O}$ ).

At lower electric field, gaseous detectors operate in the ionization chamber regime (Figure 3.5). No amplification takes place in this mode: the primary charges are directly collected by the electrodes. Without amplification, the electric signal induced in the electrodes is often very low and difficult to monitor with standard electronics. At even smaller electric field (few tens of kV/cm), the primary charges are poorly accelerated by the field and are prone to recombination with positive ions (Figure 3.5). The amount of collected charges is too low for particle detection.

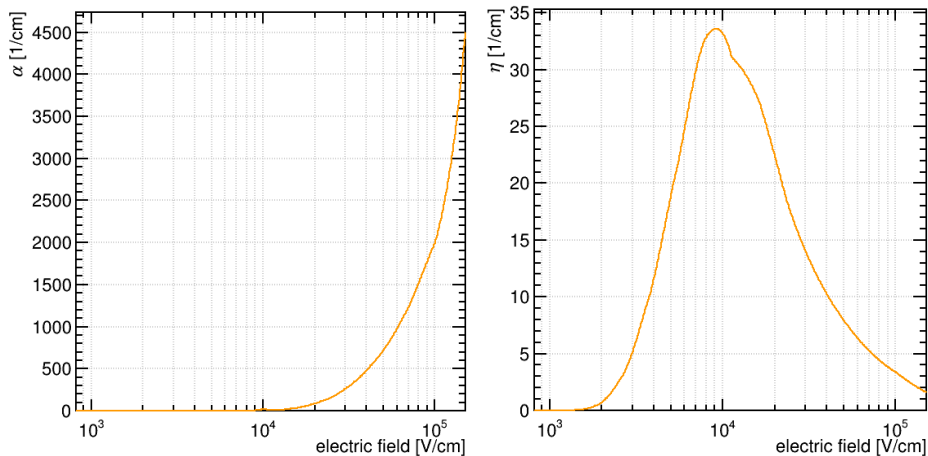


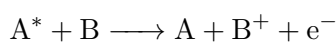
Figure 3.4: Townsend coefficient (left) and attachment coefficient (right) as a function of the electric field in an Ar/CF<sub>4</sub> (90%/10%) gas mixture.

### 3.2.2 . Instabilities and gas choice

The maximum achievable gain is given by the so-called Raether limit and corresponds to a phenomenological limit:  $\alpha x < 20$  which is equivalent to a gain of about  $10^8$  [12]. However, in most detectors this limit is reached at gains lower than the Raether limit because of instabilities such as streamers or discharges. At electron energies where the inelastic scattering by ionization or excitation is enabled, de-excitation by photon emission is also possible. The energy of these photons might be high enough to generate photo-ionization and to produce secondary photoelectrons. In the case of Argon, secondary scintillation photons are emitted in the UV region ( $\lambda \approx 120$  nm) [8]. The secondary electrons from photo-ionization lead to the formation of secondary avalanches. If the secondary avalanches develop in extension of the first avalanche, the proportional multiplication process turns into a streamer [12]. The number of secondary electrons is no longer proportional to the number of primary electrons: this corresponds to the limited proportional regime on Figure 3.5. At even higher electric field, the streamers generate very high charge density in the gas volume, which leads to a breakdown and a continuous flow of charges between the electrodes. This operation mode corresponds to the Geiger-Müller mode [13] where the number of secondary electrons is independent of the number of primary electrons. While this mode is not applicable to proportional detection, it is well suited for counting applications. Increasing further the electric field generates discharges independently of the primary electrons. Events from  $\beta$  particles have been recorded with the optical readout MPGD detector that has been developed in this thesis and will be described in Chapter 5. Events captured under the proportional, streamer and discharge modes are shown in Figure 3.6.

In order to push back the proportional limit, the use of polyatomic species called quenchers are of very common use for proportional counters. The quencher is mixed with the noble gas, even in a low proportion to absorb the secondary photons. The polyatomic species de-excite through vibrational or rotational modes and even dissociation or scintillation in wavelengths above the UV region that does not trigger ionization. Organic species such as CH<sub>4</sub>, C<sub>2</sub>H<sub>6</sub> or iC<sub>4</sub>H<sub>10</sub> are known as efficient quenchers because of their large number of atoms. Inorganic species such as CO<sub>2</sub> or CF<sub>4</sub> also provide quenching properties but are less efficient. The de-excitation of CF<sub>4</sub> by scintillation in visible wavelengths is reviewed in detail in Sec 4.2. The addition of a quencher increases the operation voltage while staying in the proportional counter mode and allows reaching gains of the order of  $10^5 - 10^6$  [8].

Moreover, the addition of a quencher allows increasing substantially the ionization yield by the Penning effect. If the ionization potential of the species is lower than the excitation potential of the other, additional ionization by charge transfer is enabled:



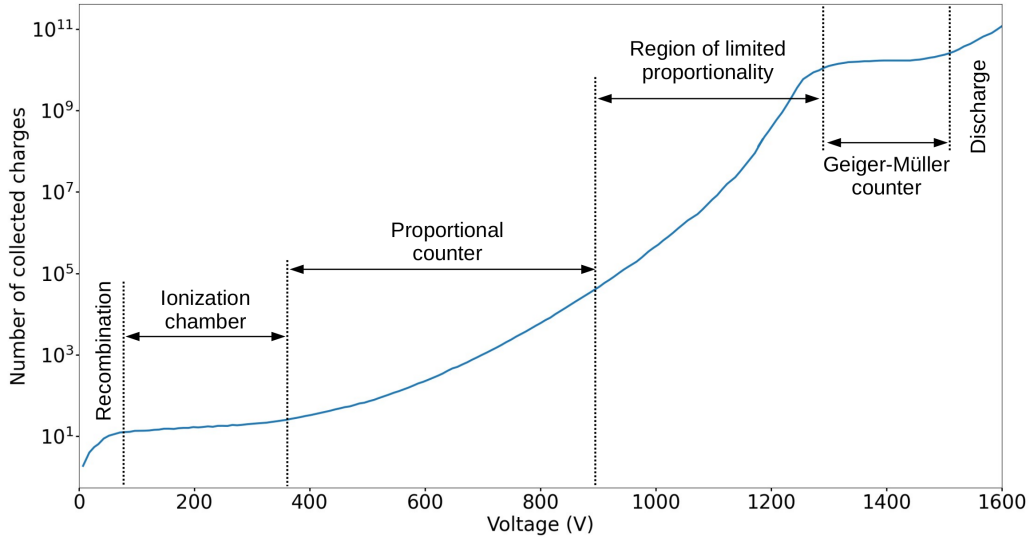


Figure 3.5: Illustration of the regimes of operation of a gaseous detector. Dependency of the number of collected charges as a function of a proportional counter voltage of operation. Extracted from [8]

For example, Argon with Isobutane is one of the best Penning mixture. The lowest exciting state of Argon is at 11.55 eV and the ionization potential of isobutane is 10.7 eV. Argon in metastable state does not instantly de-excite through radiative processes but undergoes charge transfer through collision, ionizing Isobutane [4].

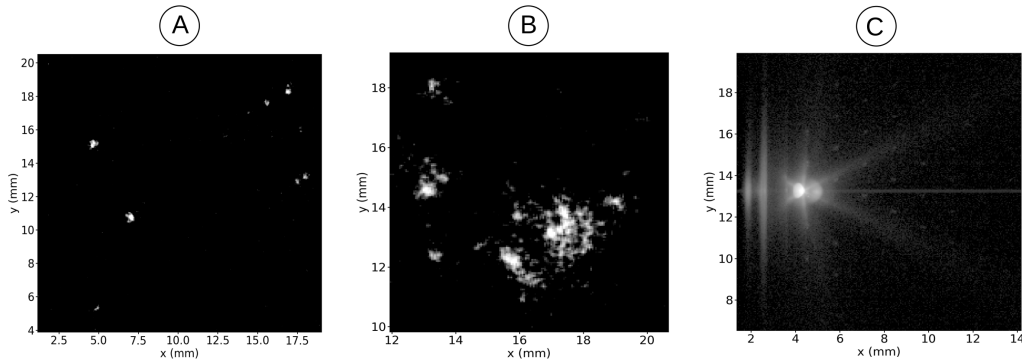


Figure 3.6: Recorded images of beta events from a tritium sample with a glass Micromegas detector with optical readout. Images were acquired under the proportional counter regime (A), limited proportionality regime with streamers production (B) and the discharge mode (C).

### 3.2.3 . Induced signals

One of the main reasons to amplify the charges is to obtain a signal amplitude above the noise of the readout electronics. The induction process of charges drifting between two parallel electrodes is similar for simple charge drifting or avalanche multiplication. However, the signal induced on the electrodes depends indeed on the amount of charges. The Ramo theorem [14] gives the current induced on a electrode from a single charge at a given time:

$$i = E_v q v(t) \quad (3.16)$$

with  $E_v$  the weighted field in the direction of the electric field,  $q$  the charge of the drifting electron or ion and  $v(t)$  the charge velocity at a time  $t$ . The weighted field is a hypothetical field, constant and independent of the movement of the charges, measured considering that one electrode is at a potential

of 1 V and the others at the ground. which depends only on the geometry of the field geometry such that of Since the current is the variation of the charge in time, the total charge induced on the electrode is given by the formula:

$$Q = Q_I + Q_e = \int_0^{t_I} i_I(t)dt + \int_0^{t_e} i_e(t)dt \quad (3.17)$$

with  $Q_I$ ,  $Q_e$  and  $i_I(t)$ ,  $i_e(t)$  the total charge induced and the current at a time  $t$  of all the ions and electrons respectively. Since the drift velocity of the ion is much smaller than the electron velocity,  $t_I \gg t_e$  with  $t_I$  and  $t_e$  the maximum time of drift before collection of an ion and electron respectively. In the case of parallel electrodes with electrons drifting from the cathode towards the anode, electrons induce a negative charge signal on the anode and a positive charge signal on the cathode. On the contrary, ions have the opposite charge of electrons but are drifting in the opposite direction. Hence, the charge signal induced by ions is also positive on the cathode and negative on the anode. In the equation (3.17), the total charge induced on an electrode by the electrons and ions are indeed adding up.

Charge induction is also established on more complex electrodes geometries. Among the existing designs, the division of the electrode in an array of conductive strips or pixels are one of the main geometry to obtain spatial information on the charges positions in the gas. Since the drifting charges derive from the incident particle ionization of the gas, these geometries allow reconstructing the position of the incident particle. In cases where good spatial resolution or large detection area is required, the number of pixels or strips rapidly increases. The signals readout, shaping and analysis thus involve an important complexity and cost. This thesis is dedicated to the development of an alternative to the charge readout process which provides the readout of a large detection area with high spatial resolution. More details will be given in Chapter 4.

### 3.3 . MPGD and Micromegas detectors

The capability of detecting particles with high gain was first achieved with a cylindrical gas-filled chamber. At this time, the anode was made of a thin metal wire and around it the cathode was made of a cylindrical metallic plate in axial symmetry with the wire (Figure 3.7). The electric field between the electrodes follows a  $1/r^2$  distribution with  $r$  the radial distance of the particle from the wire. The primary electrons are slowly drifting towards the wire at large  $r$  values while avalanche multiplication occurs at small  $r$  values. Known as the first proportional chamber, the amount of charge collected by the anode was proportional to the initial energy of the particle. The so-called Geiger-Müller counter [13] was designed with this principle of operation, allowing the detection of single electrons in discharge mode.

Tracking capability was first accomplished with large area proportional chambers coupled with a photographic imaging device. The scintillated light produced during the sparks or streamers was pictured, allowing to reconstruct the particle track in 3D. The triggered spark chamber [15] and then the streamer chamber [16] allowed to select specific events and to capture multiple tracks events. The multi-wire proportional chamber (MWPC), was invented in 1967 by Georges Charpak [17], allowing large detection area with better spatial resolution and detection rate than any comparable technology at this time. The MWPC consists of an array of wires in proportional counter mode (Figure 3.7), achieving a gain of about  $10^5$ . Large size experiments in high-energy physics were made possible thanks to the MWPC, providing particle tracking capability in magnetic field environment. The idea of parallel electrodes with the implementation of multiple drift and amplification regions came with the Parallel Plate Chamber [18] developed by Georges Charpak.

#### 3.3.1 . Micro Pattern Gaseous Detectors

The limited rate capability and spatial resolution of the MWPC was solved by the Micro Pattern Gaseous Detectors (MPGD) technology based on parallel plate electrodes and small electrode structure. MPGD detectors are based on dual electric field regions:

- The conversion region is generally large (few mm to meters) to allow a maximum number of conversions of incident particles into primary charges (Figure 3.7). The electric field is uniform and at typically low field strength to avoid amplification: the amount of charges produced in this gap is proportional to the particle energy. For example, the detection of X-ray photons is more efficient at a large conversion gap of about one centimeter, depending on the photon energy. The field is strong enough to avoid charges recombination and leads to the drift of the charges towards the second region.
- The amplification region hosts a much larger electric field to generate an avalanche multiplication of the charges in proportional counter mode. All the charges issued from the conversion region are amplified along the same distance. The electrodes structure of this region is at the microscopic scale, assuring the stability of the high electric field and requiring low applied voltages (Figure 3.7). The multiplication factor is thus quasi uniform, providing good energy resolution.

The stability of the electric field allows in particular to reach high detector gain while operating in high radiation flux environment and represented a significant advantage for high-energy and luminosity experiments. The Micro-Strip Gas Counter (MSGC), developed by A. Oed. [19], was the first MPGD detector to be developed. Metal strips spaced by about  $100\ \mu\text{m}$  are implemented on a Printed Circuit Board (PCB) insulating substrate by photolithography techniques. The strips constitute successive electrodes with opposite polarities. The intense electric field between the electrodes generates charge multiplication with small charge mobility. This detector evolved into the Micro Pixel Chamber (Micro PIC) [20] with electrodes with a dot shape instead of strips. These detectors suffered from instabilities and discharges at high gain values. Novel detector geometries were then studied aiming at sustaining high gain in high-radiation environment while the spatial resolution, the cost and simplicity of fabrication should remain competitive. The Micro-Mesh Gaseous Structure (MicroMeGas) [21] was invented by I. Giomataris at Saclay and at the same time, F. Sauli [22] designed the Gas Electron Multiplier (GEM) detector at CERN (Figure 3.7). The Micromegas detector consists in three parallel electrodes and two regions separated by a micro-mesh. The conversion gap is defined between the cathode and the mesh while amplification occurs in a gap ranging from  $50\ \mu\text{m}$  to  $150\ \mu\text{m}$  between the micro-mesh and the anode.

The GEM is based on an insulating foil perforated by multiple holes crossed by an intense electric field where the avalanche takes place. The foil has a typical thickness of  $50\ \mu\text{m}$  with  $5\ \mu\text{m}$  thick copper layers on each side constituting the cathode and anode. The holes have a  $70\ \mu\text{m}$  diameter with a pitch of  $140\ \mu\text{m}$  and are distributed in a hexagonal pattern. The GEM is generally coupled with a top plane electrode defining the conversion gap border and a bottom electrode with electronic readout by charge induction. One strength of the GEM detector is the decoupling between the induction field and the amplification field. If a discharge occurs in the amplification field between the two GEM sides, it most probably does not reach the readout structure that is on the bottom electrode. A structure with multiple GEMs is often implemented to spread the amplification and avoid field instabilities and discharges. The triple GEM generally reaches maximum gain values of the order of  $10^6$ . The GEM detector has been intensively used in high-energy physics experiments and implemented in Time Projection Chamber (TPC) for 3D particle tracking. The use of GEM in Optical TPC is detailed in Sec. 4.1.

### 3.3.2 . The Micromegas detector

The Micromegas detector is based on the association of a low electric field and a large electric field regions separated by a thin micro-mesh ( $\sim 30\ \mu\text{m}$  thickness). The dimension of the amplification gap being of the order of few hundred microns, high field stability is achieved, allowing high gain. Moreover, the amplifying electric field existing between the two parallel electrodes is highly uniform and good energy resolution of the order of 15% is obtained with 6 keV photons [24]. The readout of the fast signal induced by the electrons on the electrode is rather challenging and optimized fast electronics is required. The signal induced by the ions is much longer and easier to read out, involving better



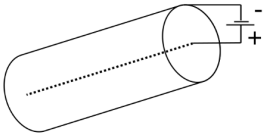
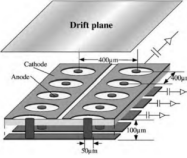

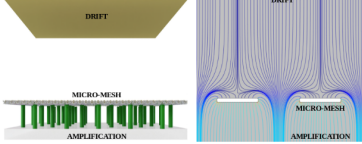
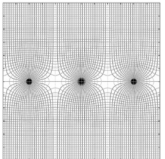
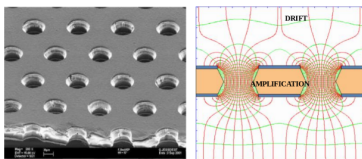
Proportional counters - trackers		MPGDs	
	Geiger Müller		MSGC & μ-PIC
	Spark chamber		Micromegas
	MWPC		GEM

Figure 3.7: Illustration of the proportional counters, trackers and MPGD technologies [23, 15, 17, 22, 21].

sensitivity and energy resolution. Good spatial resolution of the order of  $12 \mu\text{m}$  [25] has been achieved with a standard Micromegas detector in low diffusion  $\text{CF}_4$  based gas mixture. The Micromegas detector can also maintain high gain in a high particle flux environment as large as  $10^9 \text{s}^{-1}\text{mm}^{-2}$  thanks to the fast evacuation of ions and mitigated space-charge effect.

The Micromegas detector has the specificity that the drift region and the amplification regions are physically separated by a micro-mesh (Figure 3.8, left). The micro-mesh is generally made of stainless-steel with a  $45 \mu\text{m}$  aperture,  $18 \mu\text{m}$  wire width and  $30 \mu\text{m}$  thickness at the wire intersection. While the optical transmission of the mesh is about 60%, the curvature of the field lines at the level of the mesh allows most electrons to go through the mesh holes (Figure 3.8, center). Total electron transmission is nevertheless obtained only at specific drift and amplification fields ratio. Figure 3.8 (right) represents a transmission plot: the relative signal amplitude is represented as a function of the fields ratio. At low drift field values, recombination occurs and primary charges are lost in the drift gap before reaching the mesh. At large field ratio, a fraction of the primary electrons end absorbed by the mesh and the transmission drops. Absolute mesh transmission was confirmed by simulations according to [26]. The Micromegas detectors were also built using thinner meshes down to  $10 \mu\text{m}$ , with holes made with electroforming or chemical etching techniques [24], improving the stability of the amplification field.

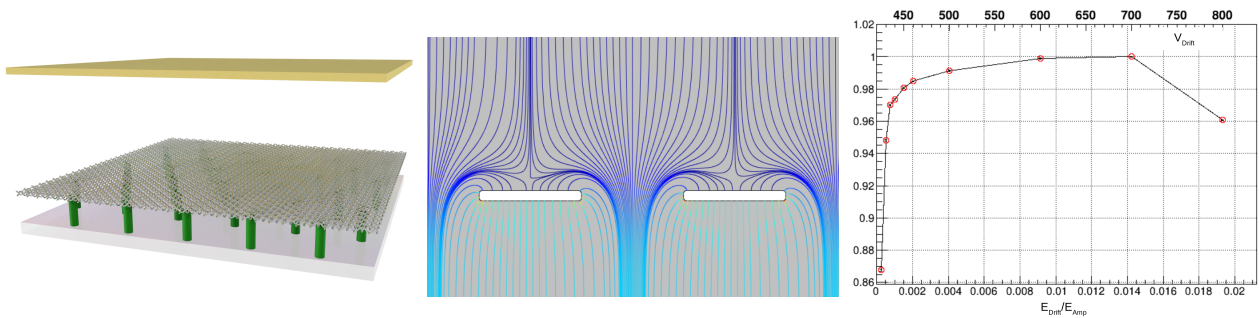


Figure 3.8: Drawing of a Micromegas detector with a woven mesh (left). Measurement of the transmission of a Micromegas detector integrated on a quartz glass substrate with a standard woven stainless-steel mesh ( $45 \mu\text{m}$  aperture,  $18 \mu\text{m}$  wire width and  $30 \mu\text{m}$  thickness). Slice of the electric field lines in the mesh vicinity simulated on Comsol [27] (center). Transmission plot measured with a glass Micromegas detector with a standard mesh (right).

To maintain the gap between the mesh and the anode constant, insulating spacers must be implemented. Insulating pillars with a cylindrical shape of about  $300\ \mu\text{m}$  diameter are spread among the anode, supporting the mesh with a minimum reduction of the active area. The pillars are made of photoresistive foils and are printed on the anode by photolithography techniques. For the standard Micromegas, the mesh is thereafter stretched, glued on a metallic frame and superposed on the pillars. A high electric field is applied between the mesh and the anode, pulling down the mesh on the pillar and defining the gap as the height of the pillars. This method is particularly well suited for large detection area of few  $\text{m}^2$  and was used for the ATLAS New Small Wheels detector [28].

The fabrication process of the Micromegas detector was optimized and simplified, improving the robustness. The elements are all integrated and stuck together in a bulk [29]. The woven mesh is encapsulated in the pillar, ensuring gap thickness stability. The fabrication for glass Micromegas is detailed in Figure 3.9. The pillars obviously affect the detection efficiency of the detector although it has been shown that the pillars does not significantly affect the efficiency and spatial resolution of trackers [30].

The bulk process allows to adapt the Micromegas detector to a wide diversity of geometries and readout, structures. Bulk Micromegas detectors are produced in the CERN Micro Pattern Technologies laboratory at CERN and in the MPGD Bulk laboratory at IRFU/DEDIP. It has been implemented on a resistive readout ensuring a protection from discharges [31] and is widely used in large TPC detectors for high-energy physics experiments such as T2K [32], CLAS12 [33] with a cylindrical detector or COMPASS [34]. Other type of Micromegas is the Microbulk Micromegas, using a  $5\ \mu\text{m}$ -Copper-thin mesh with Kapton pillars featuring a very uniform amplification structure, allowing high-energy resolution [35] and high radiopurity for the axion searches in the CAST experiment [36]. Finally, the GridPix detector implements a  $1\ \mu\text{m}$ -Aluminium-thin grid with a pixel readout, allowing high granularity and single electron detection efficiency [37].

The bulk process has been adapted to the glass Micromegas detector, using a piece of glass ( $\text{SiO}_2$  or quartz) coated with a  $150\ \text{nm}$  thick ITO (Indium Tin Oxide) layer instead of PCB for the anode. The use of thin  $1.1\ \text{mm}$  thick glass anode required to adapt the lamination process to prevent from the break of the glass.

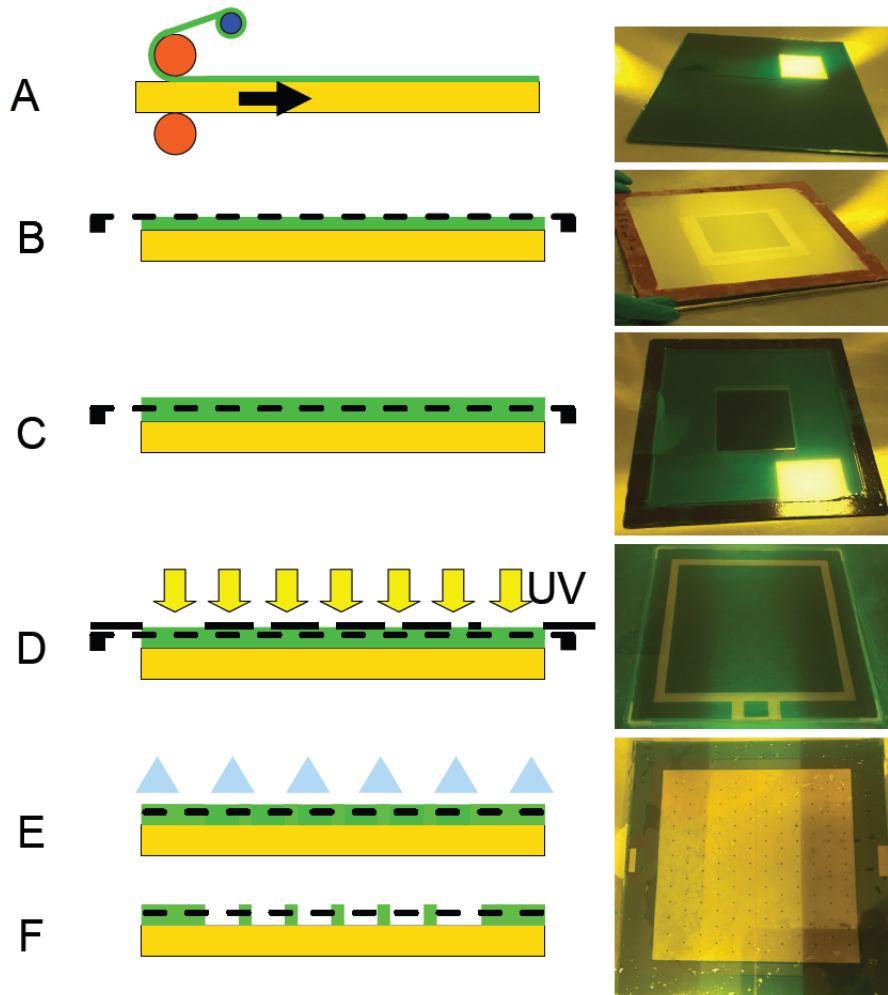


Figure 3.9: Cartoons and pictures illustrating the bulk process on a 1.1 mm thick glass substrate. A) The PCB board (yellow), or in this case, the glass piece with ITO coating for optical readout, is first laminated by an insulating polyimide material, such as Pyralux ( $64\ \mu\text{m}$  thick) or Vacrel ( $50\ \mu\text{m}$  thick). It is usually laminated twice for an amplification gap of  $128\ \mu\text{m}$  in the case of Pyralux ( $100\ \mu\text{m}$  for Vacrel). B) The mesh is stretched on a metallic frame and layed down on the insulating layers. Here the standard mesh is woven but the process is valid for other meshes such as thin electroformed meshes. C) The bulk is laminated a third time, encapsulating the mesh. D) An opaque mask with holes defining the pillars geometry overshadows the bulk during the UV insolation process. The power and time of insulation required to be adapted for glass anode substrate that has different optical characteristics compared to a PCB substrate, altering the pillars polymerisation. E) The insulating material that has not been illuminated is removed with a basic solution during the development phase. F) Finally, the bulk Micromegas is ready and baked to remove any trace of humidity. Adapted from [24].

## 4 - Optical readout

The ionization of gas molecules is accompanied by their excitation, which is often followed by the emission of photons [38]. The charge multiplication taking place in MPGDs results in the emission of photons that can be used to compute information about the time, energy and position of the particles' interaction with the gas medium. By optimizing the light production mechanism, better performances can be achieved compared to standard charge readout detectors, improving the spatial resolution, active area size, data acquisition and processing speed and simplicity, and cost per pixel. An overview of these detectors is given at the beginning of this chapter and is followed by a summary of the physical mechanisms involved in light production in gaseous detectors. Finally, the technologies and processes involved in the detection of visible light are reviewed.

### 4.1 . MPGDs: from charge to optical readout

MPGD technologies have demonstrated the capability to reconstruct the position of incident particles with high accuracy using standard charge readout. Spatial resolution of few tens of microns was achieved with a Micromegas detector using conductive strips with a pitch of  $100\ \mu\text{m}$  [39]. A spatial resolution lower than  $100\ \mu\text{m}$  has been reached with X and Y strips allowing 2D reconstruction of the incident particle using resistive strips [40]. The crossed strips are integrated in an insulating layer and share the signal induced by resistive layers. Using strips with perpendicular orientations involves a much lower amount of channels than using pixels, although multiplexing and expensive electronics might be required for large amount of strips. Multiplexing can be used to decrease the number of channels in applications where the occupation rate is low[41]. Pixel readout has been achieved by hybridation of a resistive Micromegas with a CMOS pixelized chip (Gridpix), achieving a spatial resolution lower than  $10\ \mu\text{m}$  [37].

Large volume coverage is often required and involves either to increase strips pitch and their width or the amount of strips. Small strip width is required to maintain high spatial resolution while the number of channels must be increased to cover a large volume. Optical readout engages a much lower cost-per-channel and has become a first-rate choice for large detection area with high spatial resolution. In fact, Charge-Coupled Devices (CCD) or Complementary Metal-Oxide-Semiconductor (CMOS) cameras provide a granularity of several megapixel with a field of view of tens of centimeters at reduced cost. In the early development of the optical readout of gaseous detectors, the CCD cameras exhibited a large noise and were coupled with a Microchannel plate (MCP) [42] to intensify the scintillated light [43].

The scintillation light signal is also used for the reconstruction of the depth of the signal in Time Projection Chambers (TPCs). Photomultiplier tubes (PMTs), showing high time resolution, are indeed able to measure the time lag between ionization processes within a single track. The tracks' depth is measured and the vertexes are reconstructed using this method in the XENON100 experiment [44]. Neutron imaging has been performed using the scintillation light in a He/CF<sub>4</sub> gas mixture with the exclusive use of an array of PMTs [45]. PMTs are also widely used to detect Cherenkov light at the Super-Kamiokande neutrino observatory [46].

Optical TPCs (OTPCs) nowadays are extensively used for dark matter searches. A MPGD technology was coupled with a PMT in low pressure gas mixtures that scintillates in the visible range while scoring low cost-per-pixel for dark matter search [47]. Directional dark matter searches rely on the property of Weakly Interacting Massive Particles (WIMPs) to generate nucleus recoils when interacting with the gas medium. The energy and direction of the recoil allow to identify both the energy and the direction of the incoming dark matter (DM) particle. A large detection volume is necessary to improve the probability of interaction of the DM particle with the active volume. The triple-GEM detector is able to reach high gain values and is well suited to generate high amount of scintillation light. It has

been integrated in the Lime OTPC for directional dark matter search in the Cygnus collaboration [48]. The optical GEM detector is also embedded in a proton spectroscopy detector based on the OTPC technology [49]. Transparent charge readout strips have been integrated to an OTPC to help dark matter searches in the MIGDAL experiment [50], to enhance the 3D position reconstruction capability [51]. These instruments are well suited for low rate particle experiments, although they are subject to events overlapping at high rate, due to the camera frame rate limitation. Additionally, the energy threshold of optically read out detectors is higher compare to charge readout detectors, limiting their use for very low energy particle detection.

Lately, the glass Micromegas detector built on a glass substrate has been developed for optical readout, benefiting from its higher energy resolution and intrinsic spatial resolution compared to other MPGD technologies [52]. In addition, an optical readout Micromegas device has been applied to proton beam monitoring [53].

## 4.2 . Light production mechanisms

In a radiation detector, atoms or molecules might be ionized or excited by the collision of free electrons. The ionization or excitation happens with a given probability that depends on the energy of the electron as shown in Figure 3.1. While ionization leads the production of ion pairs, excitation is followed either by the de-excitation of the species, or by its dissociation in the case of molecules. The de-excitation might occur by vibrational or rotational radiation-less modes. However, de-excitation might also trigger light emission by scintillation. The energy of the radiated photons thus corresponds to the difference of energy between an upper excited state and lower excited state of the atom or molecule. The prompt emission of light by de-excitation is known as fluorescence while the delayed emission of light that might persist hours after the excitation is known as phosphorescence. In gaseous detectors, scintillation leads to the emission of light, which is synchronized with the incident particle crossing the active gas volume with a delay of few nanoseconds. Radiative de-excitation occurs for a given element through a wide range of channels with different energies. Even neutral atoms and ions of the same element might scintillate through different channels. These channels are also very different from one species to another, resulting in a broad diversity of radiative options in gaseous detectors.

In proportional counters, the scintillation occurring during primary and secondary electrons' production is dissociated. Primary scintillation is indeed associated to the incident particle interaction with the gas and secondary scintillation to the electron avalanche amplification process. The decoupling of the processes is rather meaningful, first because they occur at different locations in a gaseous detector and secondly because the light amount produced during the avalanche is much larger than the primary scintillation (Figure 4.1). In fact, the number of ionization reactions and so the amount of secondary electrons is proportional to the amount of photons.

In the perspective of having the emitted light to be read out by photon detection devices such as PMTs or cameras, the wavelength of the light must match the high quantum efficiency (QE) regions of the camera or PMT and high transmission regions of the detector windows. The QE of most CCD or CMOS cameras and the transmission of a thin ITO layer reaches significantly high values in the visible region (VIS), above 400 nm. Hence, in addition to the requirements that the gas mixture must fulfil to operate a proportional counter in optimum conditions (Sec. 3), the scintillation wavelength must be in the VIS region.

### 4.2.1 . Argon scintillation

Noble gases are prevailing in proportional counters because of their low ionization potential and their propensity to promote ionization in the presence of radiation. In particular, Argon is highly available and well-suited for radiation detectors. As any noble gas, Argon shows several emission bands in the UV region. Pure Argon shows a large emission band from 150 nm to 300 nm [54] and a narrow and intense emission around 120 nm [55] called the second and third continuums of Argon.

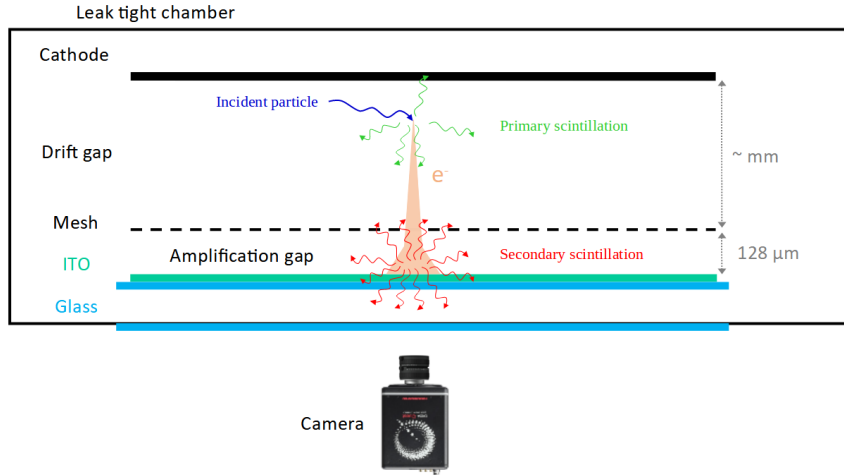
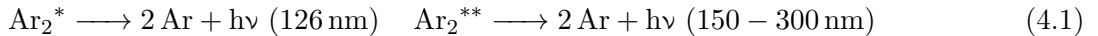
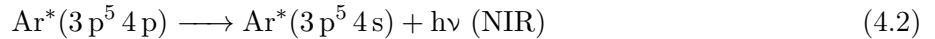


Figure 4.1: Principle of the optical readout Micromegas detector used in this thesis. The primary (green arrows) and secondary (red arrows) scintillation mechanisms are illustrated.

They are issued from the radiative de-excitation of Argon excimers according to the reactions 4.1. Excimers are dimers with two Argon atoms in this case, bound together in an excited electronic state.



Atoms of Argon also emit light in the near infrared (NIR) via de-excitation between intermediate excited states (metastable states) [38] following for example the reaction 4.2. The de-excitation of the Argon monoatomic gas produces very narrow energy peaks.

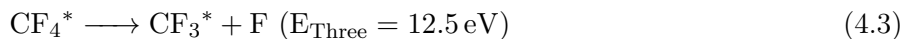


In order to produce scintillation light in the VIS range, a complementary gas such as  $\text{CF}_4$  is used, showing a large emission band in the VIS region. The UV emission of Argon could also be shifted to the visible region using a wavelength shifter (Sec. A.2) such as Tetraphenyl Butadiene (TPB).

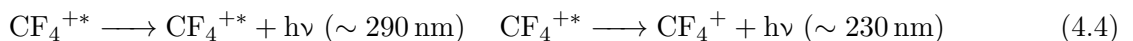
#### 4.2.2 . $\text{CF}_4$ scintillation

Being a quencher and a low diffusion gas for gaseous detector, the polyatomic gas  $\text{CF}_4$  has the specificity to emit in the visible range by scintillation around 630 nm, covering a wide emission band (Figure 4.2).  $\text{CF}_4$  also emits light in the UV region through a large variety of reactions.

In the case of  $\text{CF}_4$  ionisation by electron impact, either during the primary or secondary scintillation mechanisms, the ion  $\text{CF}_4^+$  is produced. The ion is often excited after the electron impact and is known to rapidly dissociate with high probability into different kinds of fragments. According to [56], either  $\text{CF}_4^{+*}$  dissociates into the excited ion  $\text{CF}_3^{+*}$  with an energy threshold of about 14.7 eV, or  $\text{CF}_4^*$  dissociates into the excited radical  $\text{CF}_3^*$  following the reactions:

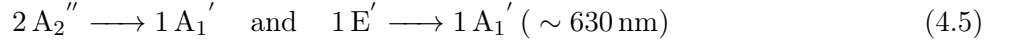


While the  $\text{CF}_3^{+*}$  ion is involved in some UV emitting relaxations [57], the UV emission band has been attributed to the predominant straight de-excitation through multiple processes of the very unstable  $\text{CF}_4^+$  ion [58] following the reactions [59]:



On the other hand, the radical  $\text{CF}_3^*$  might be excited to very high-energy levels called Rydberg states and de-excites to lower energy levels through UV and visible light emission [60]. The transitions

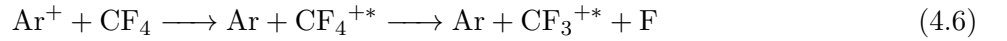
leading to the UV emission is  $2 A_1' \longrightarrow 1 A_2''$  ( $\sim 250$  nm) while the ones leading to the visible light emission are



#### 4.2.3 . Argon - CF<sub>4</sub> mixture scintillation

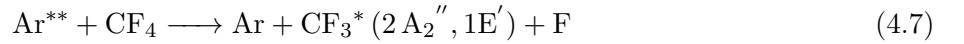
The Argon-CF<sub>4</sub> gas mixture involves the scintillation mechanisms from both species described above. However, the two gases interact with each other resulting in different relative intensities between the emission bands that depends on the elements' ratio. For example, increasing the proportion of CF<sub>4</sub> rapidly decreases the UV and NIR emissions of Argon [59]. Moreover, it has been shown that the emission intensity of CF<sub>4</sub> in the UV and VIS regions are not strictly increasing with the fraction of CF<sub>4</sub> but that the light yield reaches a maximum at ratios of CF<sub>4</sub> around 10 % [38]. The drop of visible light yield could have been attributed to the self quenching effect of CF<sub>4</sub> on the emission of CF<sub>3</sub><sup>\*</sup>. However this would have been highly dependent on the pressure, which is not the case for VIS emission [59]. In addition to direct CF<sub>4</sub> ionization, other channels of energy transfer between Argon and CF<sub>4</sub> are involved in the production of CF<sub>4</sub><sup>+\*</sup> ions (UV band) and CF<sub>4</sub><sup>\*</sup> radicals (VIS band).

The charge transfer process (CT) from Ar<sup>+</sup> ions to CF<sub>4</sub> indeed enables the production of CF<sub>4</sub><sup>+</sup> ions through the reaction [61]:



This CT process is indeed possible only because the energy released during Ar<sup>+</sup> recombination (15.76 eV) is larger than the CF<sub>3</sub><sup>+</sup> ion production (15.56 eV) [62].

Finally, the CT process between a highly excited state of Argon (Ar<sup>\*\*</sup>) and CF<sub>4</sub> feeds the emission in the VIS range following the process [59]:



The emission spectrum of a Ar/CF<sub>4</sub> (90%/10%) gas mixture is shown in Figure 4.2 (top) where the scintillation emissions in the UV, VIS and NIR regions are identified. The mechanisms described above are summarized in an energy level diagram (Figure 4.2, bottom) and the kinetics of the scintillation from the Ar/CF<sub>4</sub> (90%/10%) gas mixture are illustrated.

The sensitivity of an optical gaseous detector strongly depends on the amount of light generated per scintillation process, also called light yield. It is certainly related to the gas mixture and shows minor variations depending on the amplification field. The dynamic of the light yield has been measured with GEM detectors in previous works [38, 64] and with a glass Micromegas in this thesis in Sec. 5.2.2.

#### 4.2.4 . TMEA and TEA scintillation

Other molecules such as triethylamine (TEA) and tetrakis(dimethyl-amine)ethylene (TMAE) have been used for optical gaseous detectors, showing a scintillation emission peaking at 280 nm and 480 nm respectively [65]. In particular, the Ar/TEA gas mixture has shown high light yield emission with a GEM detector [38]. A Parallel Plate Chamber based on optical readout with Argon and vapors of TEA have been developed for high resolution imaging of beta particles [43]. However, TEA is liquid at normal conditions of pressure and temperature, toxic and flammable, involving experimental constraints. It is thus mixed with a noble gas under vapor state. TEA also exhibits chemical interactions with detector materials, potentially leading to surface contamination and affecting detector performance. Such gas mixture is unstable at high gain values. In comparison, CF<sub>4</sub> is more convenient to manipulate, as it is a better quencher and allows to reach higher gain. CF<sub>4</sub> based gas mixtures have a relatively large light yield and involve low diffusion. However CF<sub>4</sub> is a greenhouse gas contributing to global warming and making its environmental impact a significant concern.

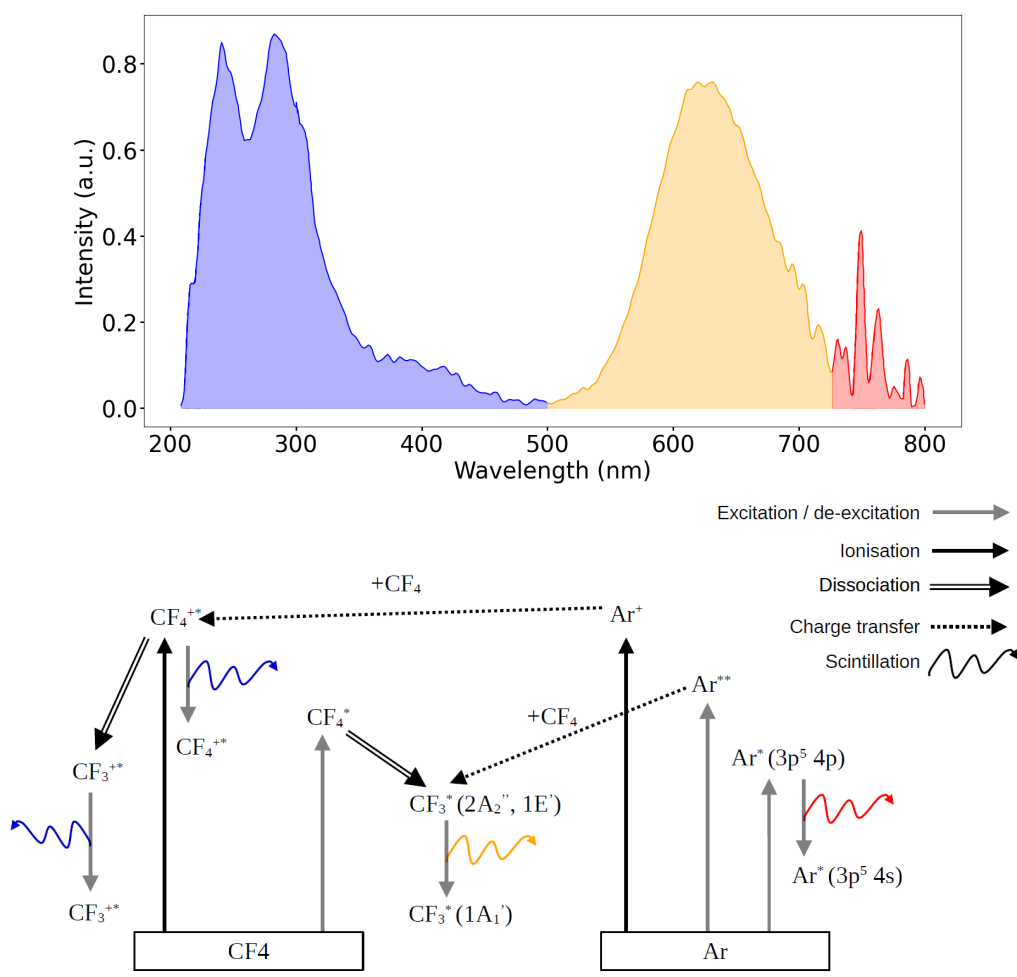


Figure 4.2: Scintillation spectrum of an Ar/CF<sub>4</sub> (90%/10%) gas mixture where the emission in UV (blue region), VIS (orange region) and NIR (red region) ranges are shown (top). Extracted from [59]. Kinetic scheme of the processes leading to the emission of scintillated light in a gas mixture of Ar/CF<sub>4</sub> (bottom). The emission of UV light is represented by the wavy blue lines and is mainly issued from the reactions (4.4) and (4.6). The UV lines from the Argon excimers (4.1) are covered by the CF<sub>4</sub><sup>+\*</sup> UV emission. The VIS light emission is illustrated by the wavy orange line and comes from the mechanisms (4.3), (4.5) and (4.7). The Argon relaxation (4.2) leads to the emission in the NIR region represented by the wavy red line. Adapted from [63, 64, 59]



### 4.3 . Visible light detection

The light issued from the scintillation process taking place in the gaseous detector is read out by light detection devices. Depending on the desired information on the photons, different types of devices can be used and integrated in the detection system at the light output window of the detector. For example, photons counting with single photon precision is enabled by PMTs while no spatial information is provided. The detection of low amounts of photons is possible thanks to the amplification of charges usually implemented in light detection devices, also known as gain. High timing precision is also ensured by PMTs, allowing to dissociate detected events even in high radiation flux. On the contrary, CCD or CMOS cameras are typically made of an array of several millions of pixels, recording the photon position of interaction in the detection plan. The use of cameras based on the semiconductor technology is widespread, allowing high granularity and sensitivity thanks to the recent progress in this field.

Cameras are often coupled with geometrical components like lenses to reconstruct the position of production of the photons. Lenses allow to obtain an image of the luminous object, based on the focusing and dispersion of light by refraction when crossing materials of different refraction indexes. However, lenses generally include an aperture stop that regulates the amount of light reaching the sensor and strongly affect the detector Signal-to-Noise Ratio (SNR). It also determines the spatial resolution of the imager, through its ability to focus all the photons into the same focal plan and might cause image blurring.

The different parameters and components that define the sensitivity of light detection devices are summarized in this section. The principle of operation of lenses and their impact on the sensitivity and spatial resolution are also depicted.

#### 4.3.1 . Light detection devices

The performance of a light detection device is mainly described by its capacity to detect a low amount of light, which depends on the sensor's QE, gain and noise. The main characteristics of photon detection devices are listed below:

- The quantum efficiency is the ratio between the number of generated photoelectrons and the number of incident photons. It basically corresponds to the magnitude of the sensor's response at a given wavelength. It depends on the transmission of the different windows of the imaging device but also on the geometry of the pixel such as the thickness of the sensor. The wavelength dependent QE of the ORCA Quest camera [66], that has been used in this thesis, is shown in Figure 5.2.
- The gain is the ratio between the number of electrons generated after the pixel readout and the number of digital counts or analog-to-digital unit (ADU) after the signal amplification. In fact, the tension signal generated after the interaction of photons with the sensor is too low to be read and must be amplified before digitalization. When the amplified signal outreaches the detection threshold, a count is recorded.
- The SNR is the ratio between the detected signal and noise contributions and it basically characterizes the sensitivity of the sensor. It includes the number of detected photons  $N_*$  after the signal processing and the error related to number of detected photons  $\sigma_*$ , to the dark current  $\sigma_D$  and to the readout noise  $\sigma_R$ . The photon noise and the dark current are both Poisson noises, issued from the statistical error on the number of photons and electrons. Hence,  $\sigma_*^2 = N_*$  and  $\sigma_D^2 = N_D$  with  $N_D$  the total number of dark current electrons per pixel. On the other hand, the readout noise does not follow a Poisson distribution and is not simplified. A simplified definition of the SNR is shown in (4.8) [67].

$$\text{SNR} = \frac{N_*}{\sqrt{\sigma_*^2 + \sigma_D^2 + \sigma_R^2}} = \frac{N_*}{\sqrt{N_* + N_D + \sigma_R^2}} \quad (4.8)$$

- The dark current  $N_D$  corresponds to the collection of electrons that have been freed by the thermal agitation instead of the interaction of a photon: the thermal agitation might randomly cause the liberation of electrons from the valence band. They are read out along with the electrons coming from the light signal. The dark current is directly related to the temperature of the sensor. It is a continuous effect that is accumulated during the exposure phase. It is thus expressed in  $e^-/\text{pixel}/\text{s}$ . The dark current is efficiently reduced by cooling down the sensor by air or liquid circulation. For a camera with an array of pixel, the heat is usually spread among the pixels and the dark current is uniform.
- The readout noise  $\sigma_R$  is a random value expressed in  $e^-/\text{pixel}$  that is added up to the signal at the readout phase. There are two main contributions to the readout noise. First, the conversion from analog to digital signal follows a statistical distribution centered around a mean value, or calibration factor. The signal is converted to a digital value according to the calibration factor with a statistical error. The second contribution is inherent to the readout electronics: electronic noise are brought by the different components of the readout electronics, such as transistors involved in the electrical signal amplification. Amplifiers indeed draw power during the amplification process. In case of short time between two readout cycles, the heat generated during the first amplification cycle affects the following cycles. High frame rate will thus increase the readout noise. The readout noise is generally the main contribution to the noise and is mitigated by lowering the acquisition rate and by implementing modern readout electronics structures as shown later in this section. For a camera, the structure of the pixels' readout electronics might bring a variation between the pixels' noise. The readout noise is thus non-uniform among the pixels and involves a pattern like noise.
- In the case of a camera, the pixel size and the amount of pixels will directly affect the noise and the spatial resolution. The treatment of a large amount of pixels through the exposure, amplification and readout phases first involves larger frame rate, limited to about 20 Hz, and also brings more power consumption, increasing the noise. The spatial resolution, or the error attributed to the reconstruction of the photon's position on a pixel is proportional to  $\sigma = \frac{d}{\sqrt{12}}$  with  $d$  the pixel size. The distribution of the photon position on a pixel is indeed uniform between the positions  $-d/2$  and  $d/2$ , and its standard deviation gives the error  $\sigma$ . The camera is coupled with a lens and the pixel size is thus magnified, affecting its size in the image plan and thus the spatial resolution. The field of view, which depends on the lens, determines the imaging surface. A large field of view involves a large pixel size and directly affects the spatial resolution. Increasing the number of pixels allows to enlarge the field of view and minimize the spatial resolution. Finally, downsizing the pixel size also reduces the solid angle of the pixel and thus the amount of light per pixel. Pixel binning provides larger light flux per pixel and improves the sensitivity.

## Photomultiplier tube (PMT)

The Photomultiplier tubes are high gain and low noise devices allowing single photon detection. The large and unique detection area involves a large solid angle and efficiency of photon detection. The incident photon is converted to an electron by a photocathode, deposited on the front glass window of the PMT. The type of the photocathode must be selected for the application to maximize the QE in the desired wavelength region. The electron drifts in vacuum in the glass tube at high speed and undergoes a multiplication process. The electron is drifting at very high speed in vacuum, involving ultra-high detection rate and time resolution. The principle of operation of a PMT is shown in Figure 4.3. The

photon is converted into a photoelectron that drifts towards the first dynode because of the electric field. The dynodes are consecutive electrodes with increasing positive potential, accelerating the electrons between each of them. Secondary electrons are produced when an electron hits a dynode with enough energy. An electron multiplication occurs, with a number of secondary electrons at the level of the anode proportional to  $2^N$  with  $N$  the number of dynodes.

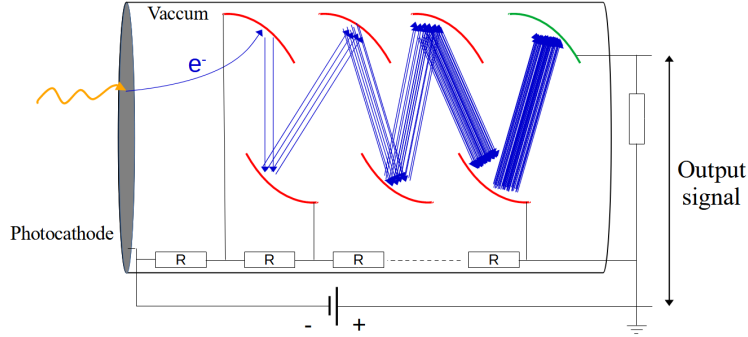


Figure 4.3: Simplified sketch of the operation of a PMT. The photon (yellow arrow) transforms into an electron by interacting with the photocathode. The electron is amplified through multiple collisions with the dynodes (red electrodes). The last dynode is the anode (green electrode). The output signal corresponds to the number of charges at the level of the anode.

PMTs are largely used in particle physics experiments as low light amount detection device or triggering device thanks to their high sensitivity and timing resolution. An array of PMTs is used in neutrino experiments to detect Cherenkov radiation [46]. They are very often used as timing reference, coupled with a scintillator to trigger the time of arrival of a charged particle. A PMT has been used in this thesis to measure the number of photons produced in a Micromegas avalanche multiplication process in Sec. 5.2.2.

## CCD and CMOS sensor

Cameras are mainly composed of a sensor which is an array of pixels, an integrated circuit for the storage, amplification and digitization of the signal, and a cooling system. Both CCD and CMOS sensors provide high resolution spatially resolved photon detection thanks to the large number of pixels. The basic principle of operation of a pixel is common to any imaging sensor, based on the interaction of a photon with a silicon active region within a pixel. The silicon is likely to free an electron by the photoelectric effect when it is hit by an incident photon in the visible wavelengths region. The principle of operation of a pixel is shown in Figure 4.4 (left). The electron-hole pair is first generated and stored in the depletion region after the photons interaction. At the beginning of the exposure of a photodiode, the depletion region is raised to a voltage called reverse voltage. When impinging photons are integrated in the photodetector, the reverse voltage is decreased. At the end of the exposure time, the remaining voltage that transcribes the number of photons is measured. The pixel voltage is then reset for the next exposure cycle [68].

The different features of a modern pixel are shown in Figure 4.4 (right). Most recent CMOS sensors are equipped with the back-illuminated technology. Previously, the wiring layer, which contains the wires guiding the signals out from the sensor's pixels, was on top of the photodetector and the photons had to cross this layer before being detected, which reduces the detection efficiency. Thanks to improved manufacturing techniques, the wiring layer is now under the photodetector and does not affect the photon detection. Moreover, in most CMOS technology, pixels are equipped with microlenses to focus photons into the semiconductor and to prevent them to be absorbed into the inter-pixel area. While increasing the depth of the depletion region increases the QE, it also allows diffusion of the photoelectrons from one pixel to another, causing cross-talking. The Deep Trench Isolation (DTI) region

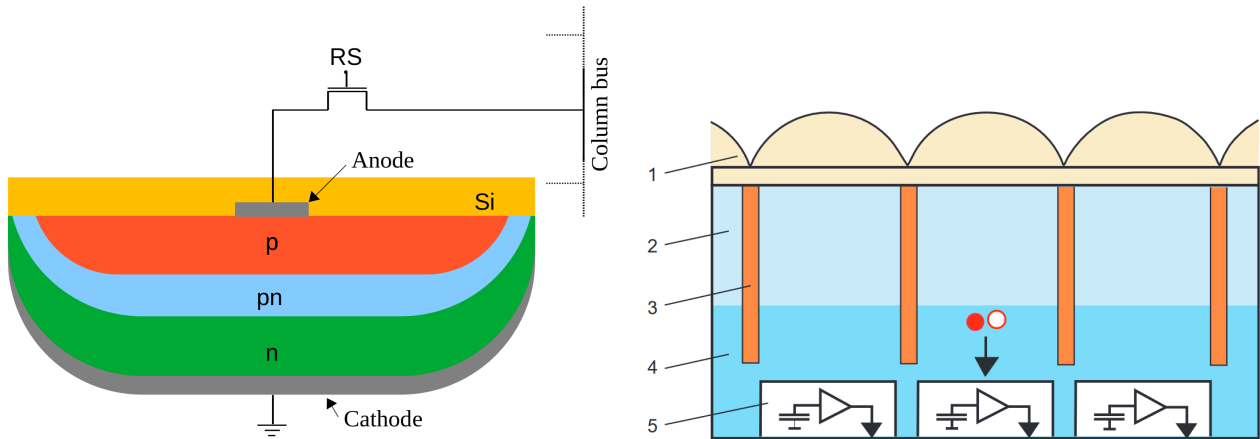


Figure 4.4: Simplified schema of a CCD passive pixel (left) [68]. The zone n is usually made of Si doped with an element which shows an excess of free electrons. The zone p is doped with an element (like boron) that has an excess of holes: its atomic electronic structure is likely to be filled with electrons. The zone pn is the depletion region. After an exposure cycle, the signal is carried to the column bus and amplified along with the other pixels signal. The transistor RS resets the pixel after the exposure cycle. In the case of CMOS sensor, the signal is amplified before being carried to the column bus. Schema of the slice of a qCMOS sensor (right), taken from [66]. 1: Microlenses, 2: Depletion region or field-free region (photocharge transport through diffusion), 3: DTI (Deep Trench Isolation) structures, 4: Electric field region (photocharge transport through drift), 5: Pixel structure for electronic photocharge detection.

avoids such effect by reflecting photons and avoiding photoelectrons migration. High QE efficiency and spatial resolution are made possible thanks to the aforementioned progresses on the pixel design.

In the case of the CCD sensor Figure 4.4 (left), the signal is directly carried through the vertical bus to be amplified by an amplifier, common for the all bus. The passive pixel suffers from large readout noise because of a significant difference between the pixel and the bus capacitance.

On the opposite, CMOS sensors are active-pixel sensors types, meaning that each pixel contains a semiconductor-based photodetector region and its own amplifier. CMOS sensors involve an active pixel technology where the signal from the photodiode is amplified right after by a field-effect transistor [69]. The CMOS sensor is a type of metal-oxide-semiconductor field-effect transistor sensor (MOSFET) that achieves low static power consumption and very low noise. The transistors of the MOSFET sensor are alternatively switched on, which allows to draw power only momentarily and to reduce the waste of heat. CMOS sensors are currently of lower fabrication cost compared to CCD sensors because of a well-mastered semiconductor manufacturing process. The signal being amplified before traveling through the vertical bus, the associated noise is significantly low. The layout of the pixels of a CMOS sensor is shown in Figure 4.5.

The pixels of a same row are being readout and reset simultaneously by the "selection" and "reset" transistors. While a pixel is in an exposure cycle, the pixel of the following row is being readout and reset. Hence, pixels of different rows are exposed to light at different consecutive moments. This mechanism is called rolling shutter effect and is prone to produce blurred images when imaging fast moving objects. This readout pattern also involves a non-uniformity of the readout noise. However, the CMOS sensor structure allows to reach high imaging rate.

#### 4.4 . Geometrical optics and lens

The light emitted from a point source behaves as rays emitted radially from the source, also described as a spherical wave. An extended object, that is either self luminous or externally illuminated, is made up of multiple point like sources that emit photons isotropically. In order to record the positions

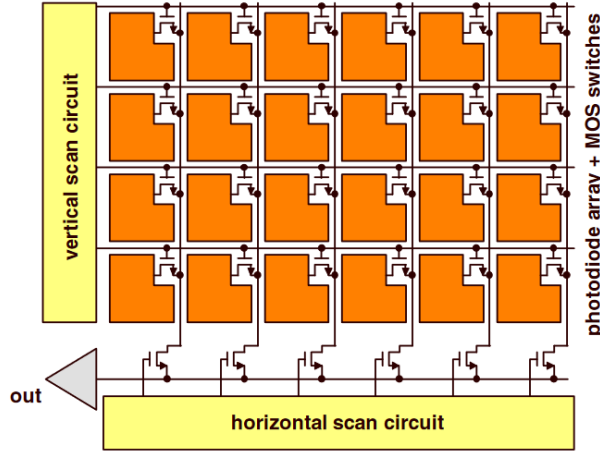


Figure 4.5: CMOS sensor schema. Each pixel has its individual amplifier and the pixels are readout by column. Taken from [68].

of light emitters and to capture the spatial distribution of an object, the rays must be focused into the imaging sensor. A lens is most commonly used to focus the rays on the image plan while preserving the integrity of the object spatial distribution. The rays focusing derives from refraction: the property of rays to change their direction of propagation while getting from one medium to another with different refraction indexes. The refraction index  $n$  depends on the photons energy and the medium and is expressed as  $n = v/c$  with  $v$  and  $c$  the speed of light in the medium and in vacuum. For example,  $n \approx 1$  in air and  $n \approx 1.46$  in  $\text{SiO}_2$  glass [70]. Thus, glass is suitable for light refraction and is the main compound of optical lenses. The relation between the variation of index between two mediums and the variation of the angle of the ray is given by the so-called Snell's Law:

$$n_1 \sin \theta_1 = n_2 \sin \theta_2 \quad (4.9)$$

with  $n_i$  and  $\theta_i$  the refraction index and angle between the ray's direction of propagation and the optical axis (which is normal to the medium surface) for the medium  $i \in \{1, 2\}$ . According to the shape of the lens, it is possible to tune the angle of emission of the rays from the optical system. A hyperbola shape has the specificity to convert a ray emission with a spherical wavefront into a parallel wavefront, and vice versa. Hence, a convex lens, which has an hyperbola shape on both sides, converges the rays from a source point to an image point. In opposition to the converging lens, a concave lens is diverging the rays. The principle of operation of a converging lens is shown in Figure 4.6.

The focal distance  $f$  is a quantity specific to an optical system which gives the focusing power of the system. The rays crossing a perfect converging lens obey a few rules that depend on the focal length: rays passing through the origin are not deflected, while rays passing through the focal point emerge being parallel to the optical axis and vice versa. The so-called Gauss lens formula gives the relation between the focal length and the distance from the object and image to the origin  $s_o$  and  $s_i$ :

$$\frac{1}{f} = \frac{1}{s_o} + \frac{1}{s_i} \quad (4.10)$$

$s_o$  is also called the working distance. Larger focal length thus involves a greater convergence of the rays. For objects at an infinite distance, for astronomy applications for example,  $f = s_i$ . In the case of finite object distance, the focal length should be chosen wisely to obtain the image at the desired position along the optical axis. The other main property of an optical system is that it enables modification of the size of the object in the image plan, also called magnification. Large magnification allows enlargement of the object and accessing small details of the object. The magnification  $M$  is given by the formula:

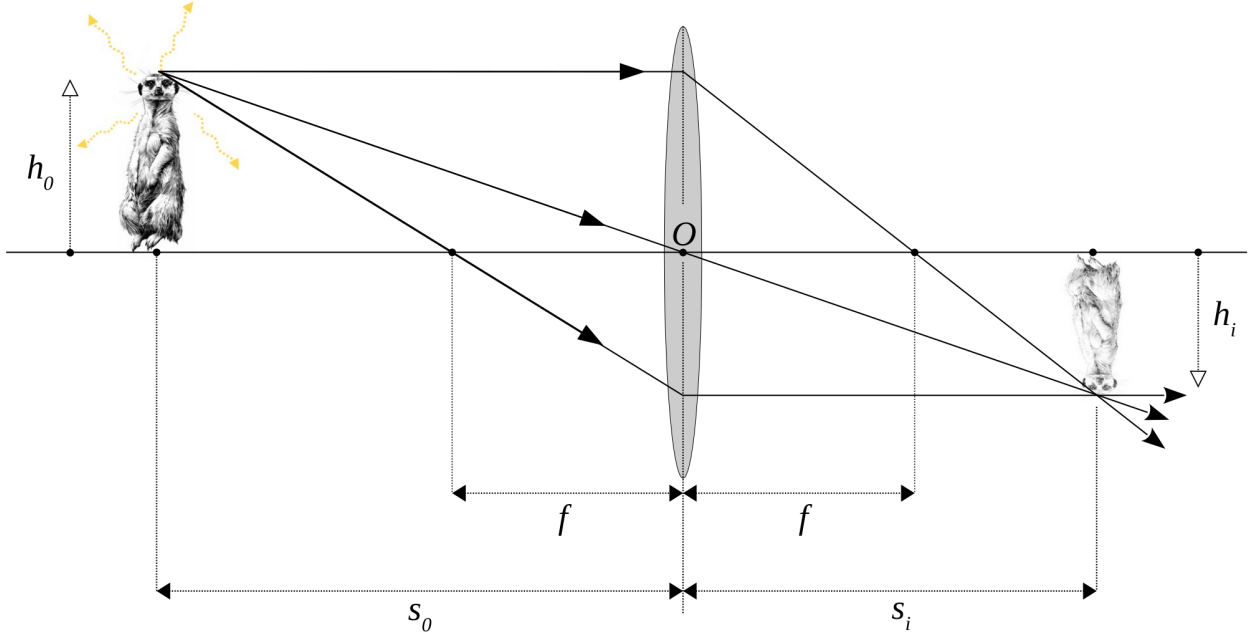


Figure 4.6: Sketch illustrating the focusing of rays emitted from an object by a converging lens. The lens is symmetric with the optical axis, centered in the origin  $O$ .  $f$  is the focal length of the lens and the focal points are on the optical axis at a distance  $f$  and  $-f$  from the origin.  $h_0$  and  $h_i$  are the height of the object and its image on the focal plan respectively.  $s_0$  and  $s_i$  are the distance from the origin of the object and the image respectively.

$$M = \frac{h_i}{h_o} = -\frac{s_i}{s_o} \quad (4.11)$$

According to the Newtonian form of this expression:

$$\frac{f}{s_0 - f} = \frac{|h_i|}{h_o} \quad \text{and} \quad M = -\frac{x_i}{f} = -\frac{f}{x_0} \quad (4.12)$$

where  $x_i = s_i - f$  and  $x_0 = s_0 - f$ . Thus, a larger focal length involves a greater magnification. In the case digital camera, the magnification is typically much lower than 1 and the size of the object is larger than the size of the image. For an object at a distance of  $s_0=300$  mm from the lens and a focal length of 25 mm,  $M = f/(s_0 - f) = 0.09$ . In the case of the qCMOS camera [66], the pixels are  $4.6\mu\text{m}$  wide. The size of the pixel on the object plan is thus  $h_0 = h_i/M = 50.6\mu\text{m}$ . According to Sec. 4.3.1, the spatial resolution is given by  $\sigma = h_0/\sqrt{12} = 14.4\mu\text{m}$  in this situation. Hence, decreasing the magnification degrades the spatial resolution, although the degradation in this case is small compared to the object size. However, decreasing the magnification also allows to image larger object. This aspect is expressed by the field of view (FOV):

$$\text{H-FOV} = 2 \arctan \left( \frac{w}{2f} \right) \quad (4.13)$$

with  $w$  the width of the sensor and H-FOV the horizontal field of view. For the qCMOS camera,  $w = 18.841$  mm and  $f = 25$  mm, thus H-FOV=41.3°. For an object at a distance  $s_0 = 300$  mm, the linear field of view in the horizontal direction is

$$\text{LH-FOV} = s_0 \times 2 \tan (\text{H-FOV}/2) = 226 \text{ mm} \quad (4.14)$$

In these conditions, the field of view is large enough to image the glass Micromegas detector while the pixel size is small enough to minimize the degradation of spatial resolution.

One other main feature of an optical system is the aperture which concerns the collimation of the rays. The collimation is achieved by a diaphragm that stops the rays going further than the diaphragm diameter  $D$ , as represented in Figure 4.7 (left). The diaphragm has two main features: to reduce the amount of light reaching the image plan and to stop the rays interacting with the lens far away from the optical axis. The light flux at the diaphragm output in fact depends on the opening area of the pupil, which varies as the square of the diameter divided by two. It has been seen that a larger focal distance increases the magnification and decreases the amount of photons per unit area, thus the flux. The light intensity flux indeed decreases as the square of the image width, which is proportional to the inverse of the square of the focal length according to (4.11) and (4.12). The light intensity on the image plan is then proportional to  $(D/f)^2$ . The aperture is often describe as the f-number:  $f/D$  also written  $f/\#$ . For example, for a lens with  $f = 25$  mm and  $D = 12.5$  mm, the f-number is  $f/2$ . The most popular values for low f-numbers are  $f/0.95$ ,  $f/1.4$ ,  $f/2$  or  $f/2.8$ . There is a factor  $\sqrt{2}$  between each value, which corresponds to a drop of the light flux by  $1/2$ .

The photon flux however is not always uniform on the image plan. As illustrated in Figure 4.7 (right), a smaller fraction of photon emitted further away from the optical axis will reach the image plan in comparison to photons emitted close to the optical axis. The result is a fading out of the light intensity on the image at the periphery. The intensity of this effect depends on the properties of the optical system can be strongly attenuated by optimizing the optical system's parameters.

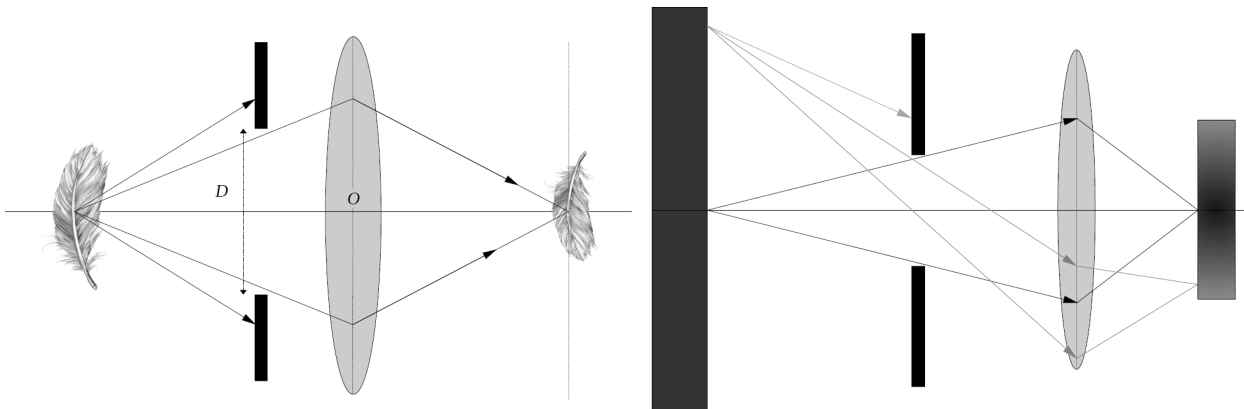


Figure 4.7: Sketch of a converging lens coupled with a diaphragm of diameter  $D$  (left). The rays with a larger angle to the optical axis are stopped by the aperture stop (left). Sketch of a optical system with rays emitted from the borders of the object (gray arrows) and from the center of the object (black arrows), illustrating the vignetting effect (right).

## 4.5 . Optical effects

Optical systems have been described in the last section in the ideal case, where the depth of the objects are not considered or the lens does not have any default. If more complex objects are considered, some of the rays emitted from the object might not converge on the image plan but before or after. This phenomenon is called unfocusing and might generate blurring of the image, which degrades the image sharpness.

Unfocusing typically happens when the object is at a distance from the lens that does not respect the Gauss lens formula (4.10). In Figure 4.8, the focal length and the position of the image plan, which corresponds to the camera sensor, are fixed. One of the objects is at the right distance from the optical system: the rays it emits are focused on the image plan and its image is well focused and sharp. The rays emitted from the other object, that is further away from the lens, are not focused on the image plan. However, the degree of unfocusing might be acceptable and the image still looks sharp for the imaging system. In this case, the depth of field is large. The depth of field is the distance between the closest and the further objects that look sharp enough.

However, the depth of field is lowered when large angle rays are accepted in the system. Large angle rays are more converged than shallow angle rays, increasing the unfocusing for objects at a distance which is different from the working distance. In the case of small depth of field, only the objects being at the right distance from the lens are sharp. This effect is often used in photography to make the background blurry. Large angle rays are accepted when the working distance is small and at large aperture; at small f-number. For example, for a focal length of 25 mm and an aperture of  $f/0.95$ , the depth of field is small and high precision focusing of the system is required to obtain sharp images. Dedicated targets are used to focus lenses with precision for applications where a large diaphragm is required, in astronomical photography for example.

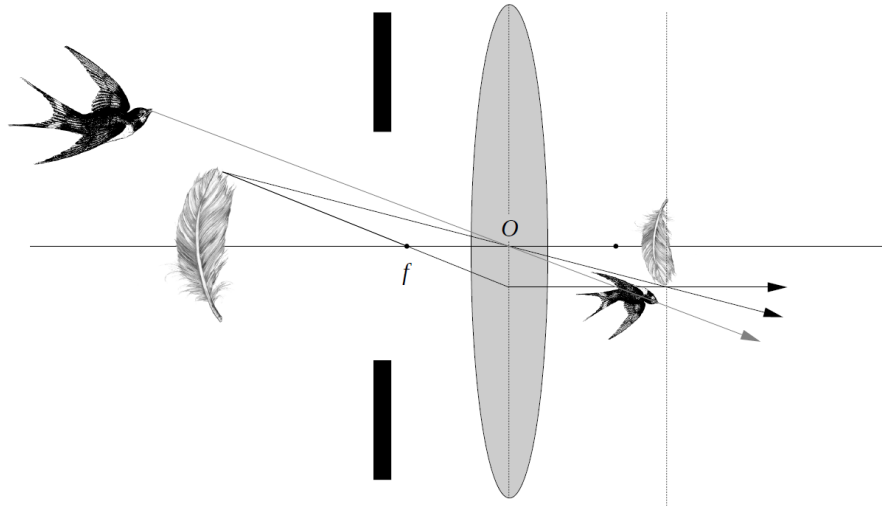


Figure 4.8: Sketch of a converging lens with two objects at different distances from the lens. One of the objects is too far away from the lens and its image is not focused on the image plane. At small depth of field, this object looks blurry.

Unwanted optical effects might be induced by the imperfections of a lens, which is not perfectly hyperbolic in reality. Because of these imperfections, all the rays emitted from a point source are not focused on the same position. These effects are called aberrations and are enhanced for rays interaction at the periphery of the lens. The ray's direction of propagation angle with the optical axis at the output of the optical system is called  $\varphi$ . The quantity  $\sin(\varphi)$  is a good description of the response of the optical system to the incident rays. The expansion in series of this quantity gives:

$$\sin(\varphi) = \varphi - \frac{\varphi^3}{3!} + \frac{\varphi^5}{5!} - \frac{\varphi^7}{7!} + \dots \quad (4.15)$$

For paraxial rays (almost parallel to the optical axis), the assumption  $\sin(\varphi) \approx \varphi$  is satisfactory. However, at the lens periphery, larger angles are observed and the term  $\varphi^3/3!$  is no longer negligible. This term describes third order effects which are called the Seidel aberrations and corresponds to the primary aberrations: spherical aberration, coma, astigmatism, field curvature, and distortion [70]. The higher orders terms are also contributing to the response of the optical system but are much weaker than the third order.

In this thesis, mainly the spherical aberration (SA) and the coma have been observed. For a converging lens, marginal rays are being excessively bent and are focused in front of the paraxial rays. The SA describes conditions with a point like source aligned with the optical axis. The marginal rays are focused in front of the image plane as shown in Figure 4.9 (left), producing concentric circles on the image plane. Lowering the diaphragm diameter significantly reduces the aberration by cutting the marginal rays.



The coma aberration also describes the over bending of the marginal rays in the lens but for a source which is away from the optical axis. The further away it is from the axis, the stronger will be the effect. The Figure 4.9 (right) illustrates the coma aberration. The rays that are the further away from the optical axis are more deflected and do not converge on the point image but further away from the axis. This shift from the main point image generates a tail, oriented away from the optical axis. The width and the length of the tail grows quadratically with the distance of the ray to the origin at the level of the lens, and thus with the diaphragm diameter. This gives a comet shape to the image of the point. In cases where imaging is performed on an extended source, this effect will be generated for all points of the object emitting light. The aberration patterns are no longer recognisable and merge all together, resulting in a blurring of the image and a drop of the spatial resolution.

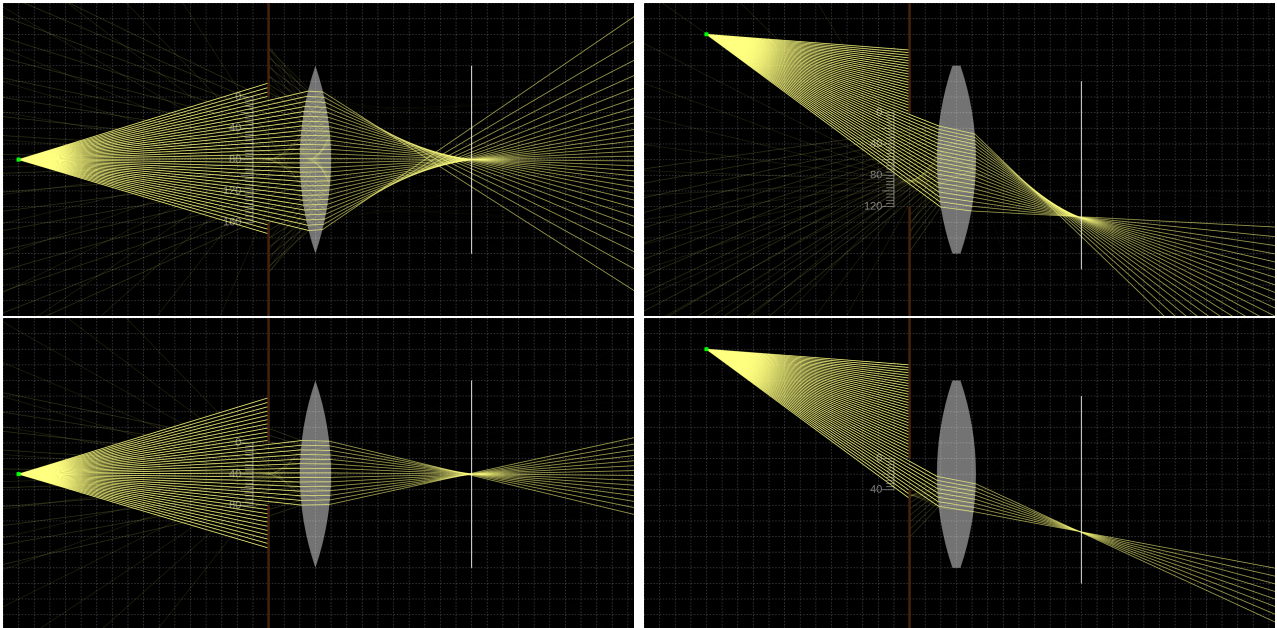


Figure 4.9: Optical simulation in 2D illustrating the spherical aberration and coma at large and small diaphragm [71]. The SA produces an over bending of the marginal rays, which focus in front of the image plan (top left). The image is composed of concentric circles. Reducing the diaphragm diameter cuts the non-paraxial rays and limits the aberration (bottom left). For a source being away from the optical axis, non-paraxial rays focus further away from the optical axis due to the coma aberration (top right). It generates a tail oriented away from the optical axis with a comet like shape. Downsizing the aperture diameter also reduces this aberration and the size of the tail (bottom right).

## 5 - The glass Micromegas concept

The possibility of optically read out the Micromegas detector has motivated the design of a new implementation of a Micromegas detector on a glass substrate. The visible light produced during the avalanche process goes through different transparent windows and is captured by a low noise camera (Figure 5.1). Different specifications of the glass Micromegas detector, such as its gain, energy resolution and light yield are presented in this section. The different elements of the imaging device and the image processing are also described.

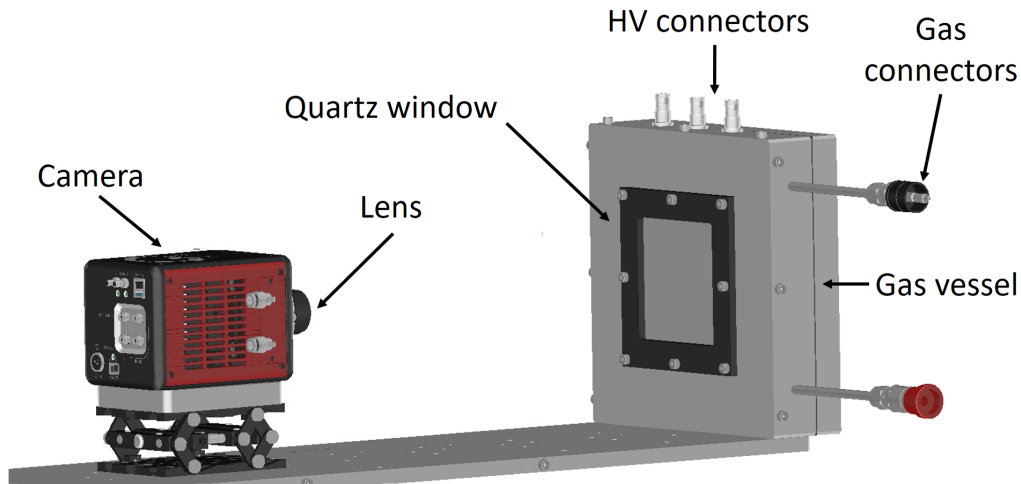


Figure 5.1: Scheme of an optically read out glass Micromegas detector. The CMOS camera faces the read-out plane of the Micromegas and captures the light exiting the gas vessel through the quartz windows.

### 5.1 . Micromegas on a glass

The new concept of a glass Micromegas detector requires an anode substrate with high optical transmission and electrical conductivity. It involves a glass anode coated with a transparent layer of metal. The light produced in the amplification gap is captured by the camera with a minimum light reflection and absorption by the glass substrate. ITO was chosen for the coating of the anode for its excellent transmission (90%) in the VIS wavelength region (Figure 5.2, green line). In addition, the electrical resistivity is low ( $100 \Omega$  from edge to edge), allowing to evacuate charges from the anode rapidly. A 3-D view of the glass Micromegas layout is illustrated in Figure 5.3.

Apart from the anode, the glass Micromegas detector shows a similar structure to standard charge readout Micromegas. The insulating pillars are made of Pyralux [73]. The combination of a minimum pitch of 6 mm and the use of a hexagonal distribution shape for the pillars allow a maximization of the active area (Figure 5.4, left). The diameter of the pillars is  $500 \mu\text{m}$ . Presently, all built detectors have an active area of  $8 \times 8 \text{ cm}^2$ . A standard woven stainless-steel mesh ( $45 \mu\text{m}$  aperture,  $18 \mu\text{m}$  wire width and  $30 \mu\text{m}$  thickness) is implemented on the detectors (Figure 5.5, left). A different type of nickel electroformed mesh called "beta mesh" has been tested to take advantage of its small thickness of  $18 \mu\text{m}$  (Figure 5.5, right). Different amplification gaps of  $128 \mu\text{m}$  and  $75 \mu\text{m}$  were used for the standard mesh and the beta mesh respectively. The structure of a glass Micromegas with a standard mesh is described in Figure 5.4 (right).

The first prototype was built on a 1.1 mm thick glass substrate coated with  $150 (\pm 10) \text{ nm}$  of ITO. This type of glass is cost effective but is likely to break during the bulk process (Figure 3.9) and easily

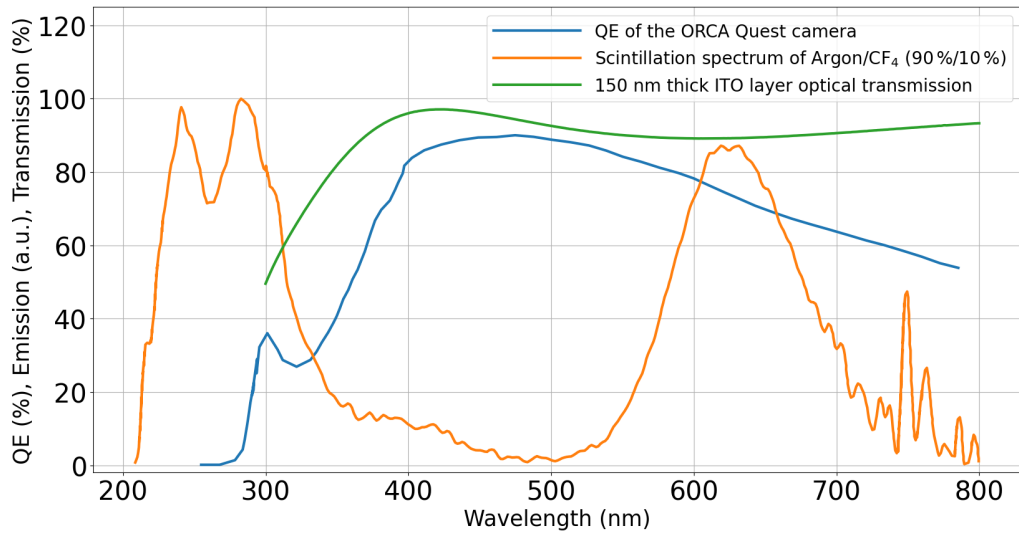


Figure 5.2: Quantum efficiency of the ORCA Quest camera, reaching 70% at 630 nm. Normalized scintillation spectrum of a Ar/CF<sub>4</sub> (90%/10%) gas mixture. Optical transmission of a 150 nm thick ITO layer, measured with a spectrometer. The transmission is around 90% in the visible. Adapted from [59, 72]

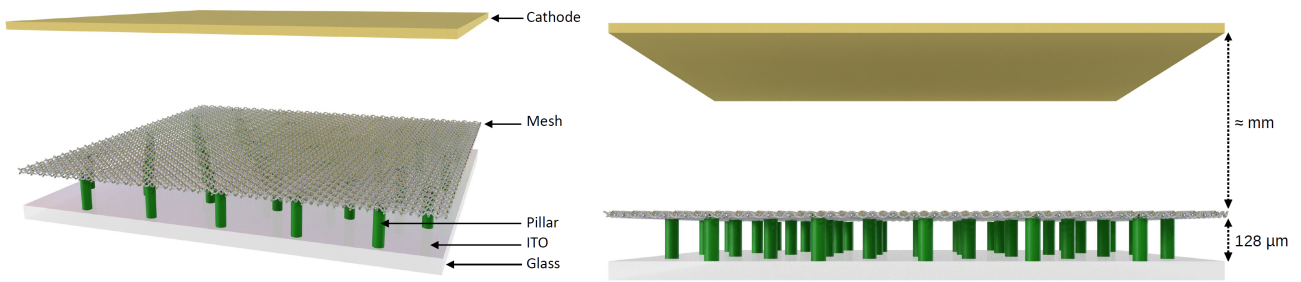


Figure 5.3: 3D drawings of the glass Micromegas detector with two view angles. The different elements of the detector, the dimension of the amplification gap (128 μm thick) and the drift gap (few millimeters thick) are shown.

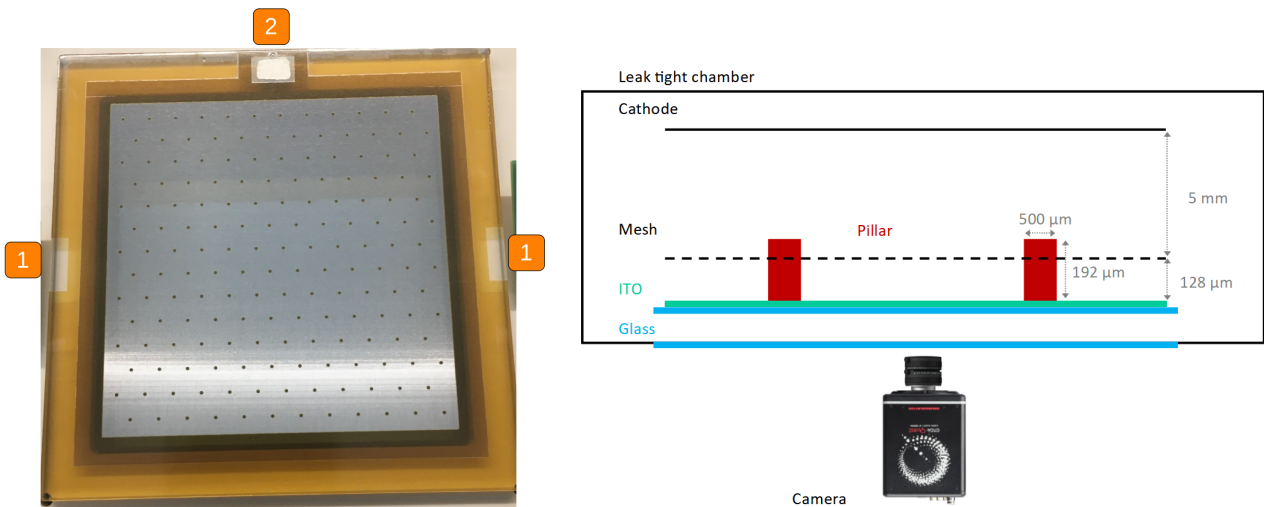


Figure 5.4: Glass Micromegas detector picture (left) with the ITO anode (1) and mesh (2) electrode contacts. Scheme of a glass Micromegas detector with a standard mesh (right). The scheme is not to scale.

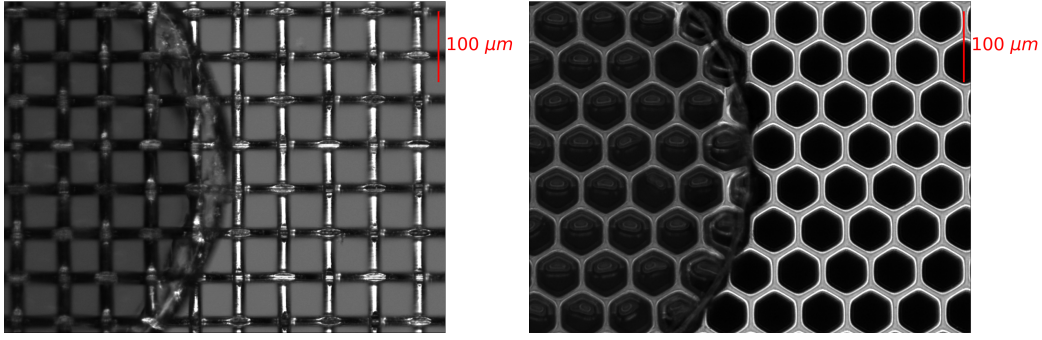


Figure 5.5: Standard woven mesh (left) and electroformed beta mesh (right). Part of the pillar is visible in each picture.

bends because of the stretched mesh, pulling the edges of the glass. This deformation of the glass leads to a non-uniformity of the gain observed by illuminating the full active area of the detector with an X-ray source (Figure 5.6 left). This figure represents the scintillation light produced in the amplification gap, which shows an intensity directly related to the gain of the Micromegas detector (Sec. 4.2). However, a Micromegas detector made of 5 mm thick pure quartz glass has been built, showing an improvement of the robustness and rigidity. This detector shows a much more uniform gain (Figure 5.6 right). The latter gain map was obtained with a high flux X-ray tube which projects X-ray photons with a 2D Gaussian shape on the detector. This shape is due to a non flat illumination from the X-ray tube rather than a non-uniform gain of the detector.

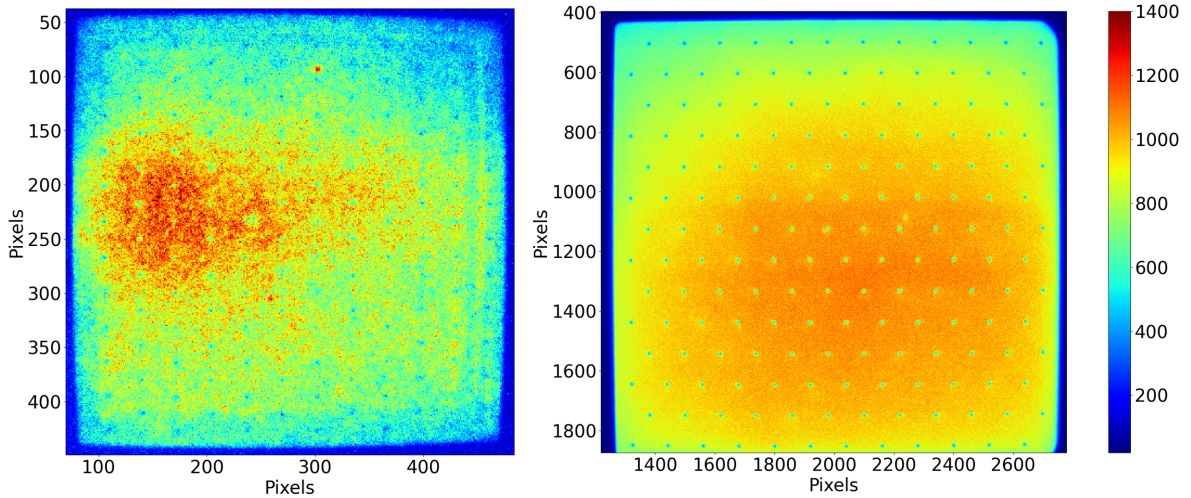


Figure 5.6: X-ray irradiation of the full active area of a 1.1 mm (left) and 5 mm (right) thick glass Micromegas detector. The colour level expresses the light intensity (a.u.). The left-hand image is obtained with a  $^{55}\text{Fe}$  source while the right-hand image is obtained with an X-ray tube with higher X-ray flux. The distance between pixels is  $192\mu\text{m}$  on the left figure and  $48\mu\text{m}$  on the right. The gas mixture is composed of 80% of Argon and 20% of  $\text{CF}_4$  and the amplification field is  $46\text{ kV/cm}$ .

These measurements were performed with the optical readout Micromegas imaging setup illustrated in Figure 5.4, right. The main components of the system are the Micromegas detector with its mechanics, the light guide, the lens and the camera. The different components of the setup are described in more details in the following part.

## 5.2 . Glass Micromegas characterisation

### 5.2.1 . Gain and energy resolution measurement

Six glass Micromegas bulk detectors were built and their performances, in terms of gain and energy resolution, were compared by reading out the charge signal from the anode. This study was led with an Argon/ $iC_4H_{10}$  (95%/5%) gas mixture at atmospheric pressure, with the gas flushing in open loop at about 1 L/h. This gas mixture is standard for the testing of Micromegas detectors, since it provides good detector stability at high gain, high energy resolution and is a Penning mixture. Both the cathode and the window of the leak tight chamber were made of a 100  $\mu\text{m}$  thick layer of aluminized polyethylene terephthalate (Mylar). An  $^{55}\text{Fe}$  source of about 100 MBq was used for this test, by irradiating the full active area of the detector with X-rays from a distance of few centimeters. The signal from the anode is integrated by a pre-amplifier ORTEC 142A before being amplified and shaped by an amplifier ORTEC 570. The signals from the amplifier have an amplitude proportional to the number of charges collected by the anode. The amplitude is measured and digitized by a Multi Channel Analyzer (MCA) over 10 bits, with a maximum input tension of 10 V. A sketch of the electronics chain is depicted in Figure 5.7.

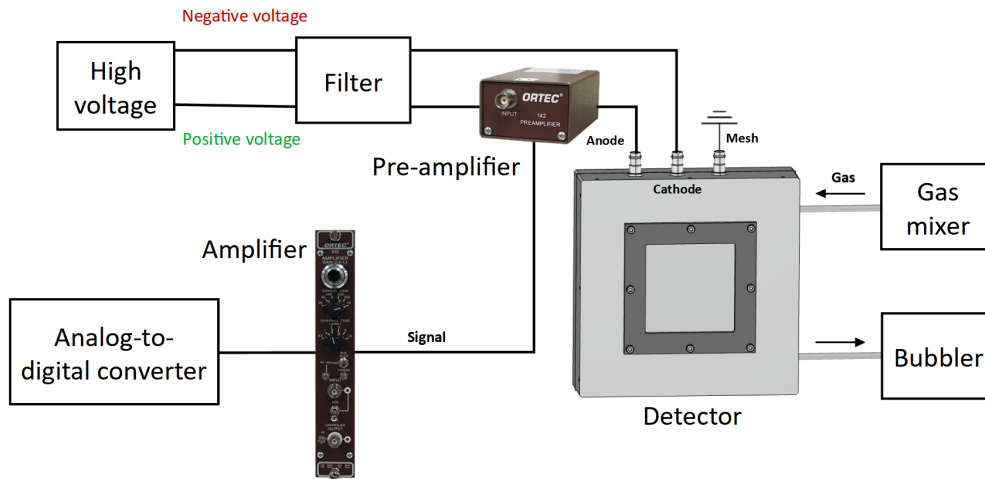


Figure 5.7: Electronics acquisition scheme where the charge signal from the anode is read out with a pre-amplifier and an amplifier. The gas system is also depicted.

The signals' amplitudes are stored in a histogram showed on Figure 5.8. Two peaks are visible: one main peak at 280 MCA channels and another one at half the value of the first peak. The large amplitude signal is known to be issued from the characteristic  $^{55}\text{Fe}$  X-rays of energy  $E_\gamma = 5.9 \text{ keV}$  produced by electron capture process (Sec. 2.3.3). X-rays interact with the gas mixture via photoelectric effect (Sec. 2.2). In the case of Argon, in most cases, an electron with an energy  $E_\gamma - E_K = 2.7 \text{ keV}$  is ejected from the K-shell, of binding energy of about  $E_K = 3.2 \text{ keV}$ . The atom returns to the ground state by emitting an energy  $E_K$  through two different processes:

- An Auger electron (Sec. 2.2) is emitted from the atom with a 85% probability [74]. At the end of the process, a photoelectron and an Auger electron produce primary electrons by ionization. All the energy of the X-ray photon is detected (Figure 5.8: large intensity peak).
- A fluorescence photon is emitted and mostly escapes the gas volume because of its large absorption length ( $\sim 4 \text{ cm}$ ). Only one photoelectron of energy  $E_\gamma - E_K$  is detected (Figure 5.8: the lower intensity peak, also called escape peak).

In order to compute the gain and the energy resolution of the detector, a specific fit of the large amplitude peak is performed. Its center of gravity and width are extracted. Regarding the  $^{55}\text{Fe}$

electron capture, several processes are involved after that an electron from the K-shell is absorbed by the nucleus and the vacancy is filled by an outer shell electron. With a 60 % probability, a 5.19 keV Auger electron is emitted (which does not reach the detector active volume), along with a 24.4 % chance of a 5.9 keV X-ray and a 2.85 % chance of a 6.49 keV X-ray. Hence, the main peak is fitted with a sum of two Gaussian functions. The first one corresponding to a 5.9 keV emission (Figure 5.8, black line). Its width ( $\sigma$ ), center of gravity ( $\mu$ ) and amplitude ( $A$ ) are free. However, the second one (Figure 5.8, pink line) has its center of gravity and width fixed by the expressions  $\frac{6.49}{5.9} \times \mu$  and  $\sqrt{\frac{6.49}{5.9}} \times \sigma$  respectively. The amplitude is set at  $\frac{2.85}{24.4} \times A$ .

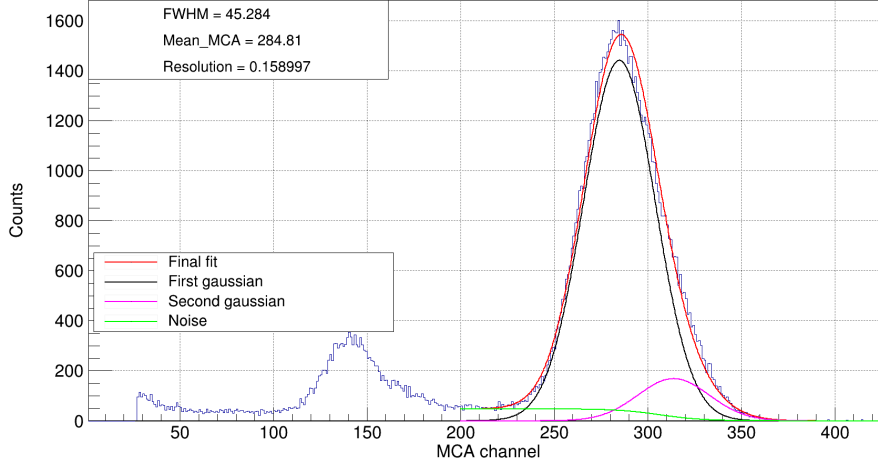


Figure 5.8:  $^{55}\text{Fe}$  spectrum (blue plot) obtained with a beta mesh Glass Micromegas detector with a 5 mm thick glass substrate. The fit of the spectrum (red plot) is the sum of two Gaussian distributions and a sigmoid function (black, pink and green plot respectively).

In addition, the main peak shows an asymmetry: on the right side, the baseline of 0 count is reached while on the left side, there is a flat plateau going on to the escape peak. This is due to the interactions at the border of the drift gap; at the vicinity of the mesh and the cathode. If an X-ray photon interacts with the gas near the drift gap borders, the produced photoelectron might hit solid materials and only a fraction of its initial energy would be deposited in the gas. This phenomenon is described by a sigmoid function (Figure 5.8, green line) centered at the main peak center of gravity. It is given by the expression (5.1) where  $B$  is the height of the plateau,  $\sigma$  and  $\mu$  are the first Gaussian function parameters. The farther the X-ray photon interacts with the gas from the borders, the weaker this effect will be.

$$B \times \left[ 1 - \frac{1}{1 + e^{-\left(\frac{x-\mu}{\sigma} + 1\right)}} \right] \quad (5.1)$$

A calibration of the electronics chain is necessary to convert the  $\mu$  value given in MCA channel into a mean number of electrons collected by the anode. A pulse generator is used to produce a signal of known amplitude. Coupled with a capacitor, this system mimics the signal which comes out from the anode of the Micromegas detector. A signal of well-known charge value can be generated through the formula  $Q = CV$  with  $Q$ ,  $C$  and  $V$  the charge, capacitance and voltage respectively. The preamplifier, the amplifier and the ADC are connected at the output of the pulse generator with a capacitor, and the pulses' amplitude (MCA channels) are measured. A linear regression then leads to a calibration factor  $K$ , converting MCA channels into an amount of measured charges.

Finally, the total amount of secondary electrons  $N_{QS}$ , produced in the avalanche and collected by the anode, are computed through the equation (5.2) with  $e$  the electron charge. The mean number of primary electrons  $\langle N \rangle$  produced in the drift gap by ionization is given by the equation (5.3), where  $\Delta E_{Loss}$  is the energy loss,  $P$  is the gas elements' ratio and  $W$  the mean energy required to produce an

ion-electron pair. The gain of the Micromegas detector at a given amplification field is given by the expression (5.4).

$$N_{QS} = \frac{1}{e} \times \mu(MCA) \times K \quad (5.2)$$

$$\langle N \rangle = \frac{\Delta E_{Loss}}{P_{Ar}W_{Ar} + P_{C_4H_{10}}W_{C_4H_{10}}} \quad (5.3)$$

$$G = \frac{N_{QS}}{\langle N \rangle} \quad (5.4)$$

As illustrated in Figure 5.9 and 5.10, both standard and beta mesh detectors successfully attained gains exceeding  $10^4$ , with only the beta mesh detectors demonstrating stability at gains surpassing  $10^5$ . The energy resolution is measured by the formula (5.5). All detectors exhibited an optimal energy resolution better than 17%. The measured energy resolution supports the argument for a uniform gain. While slightly higher gain was obtained with the beta mesh compared to the standard mesh, the price and complexity of its implementation in the glass bulk Micromegas might not be justified.

$$\text{Resolution} = \frac{\Delta E(\text{FWHM})}{E} \quad \text{and} \quad \Delta E(\text{FWHM}) = 2\sqrt{2\ln(2)} \times \sigma \approx 2.355 \times \sigma \quad (5.5)$$

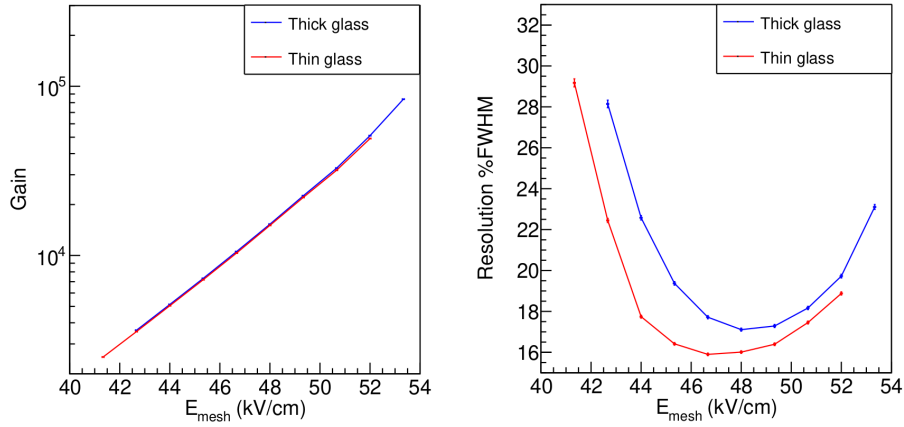


Figure 5.9: Gain (left) and energy resolution (right) in a Argon/ $iC_4H_{10}$  (95%/5%) gas mixture of glass Micromegas detectors with a beta mesh.

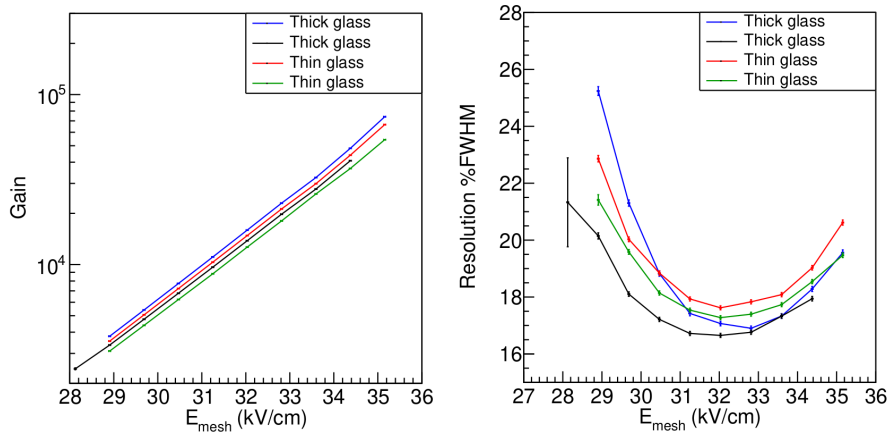


Figure 5.10: Gain (left) and energy resolution (right) in a Argon/ $iC_4H_{10}$  (95%/5%) gas mixture of glass Micromegas detectors with a standard mesh.

### 5.2.2 . Light yield measurement

Besides the gain and energy resolution obtained by charge readout, the conversion factor of electron into photons represents a critical parameter of the detector. In order to compare the amount of photons produced by the Micromegas detector for different gas mixtures, the light is recorded by a PMT while the amount of electrons after the avalanche is measured in parallel. In other words, this test allows to characterize the number of photons produced per secondary electrons, also called light yield. The detector features and the electronics chain are described in Sec. 5.2.1 and Figure 5.7. Argon based gas mixtures are used for this test with a proportion of  $\text{CF}_4$  varying from 5% to 100%. A PMT Hamamatsu R6231-01 [75] is positioned in front of the detector window while minimizing its distance from the light emission to optimize the solid angle (Figure 5.11).

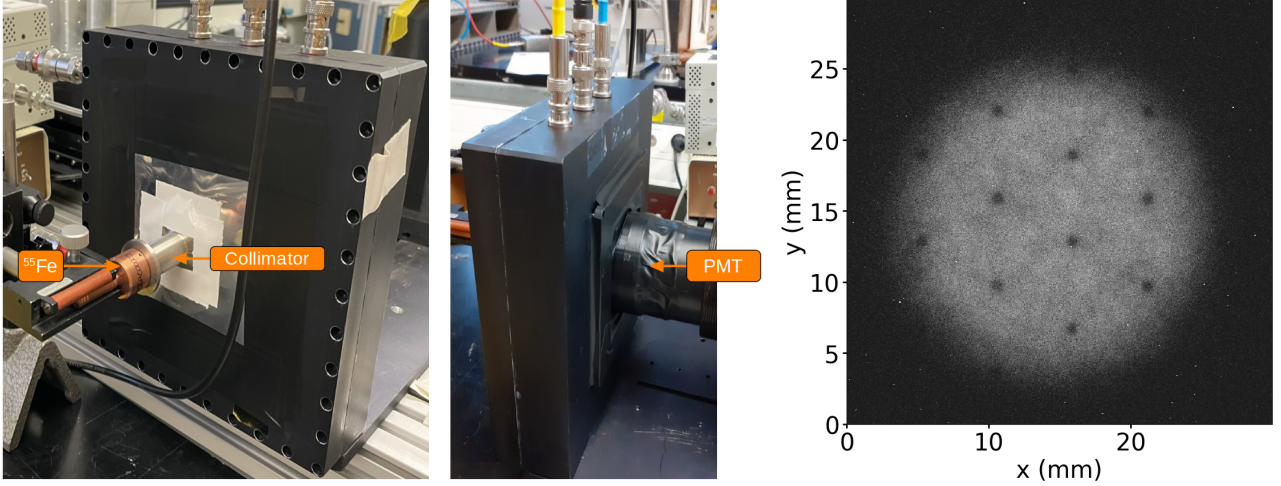


Figure 5.11: Pictures of the Micromegas detector with the collimated source and the PMT (left). Image of the light generated by the Micromegas detector being irradiated by the collimated X-ray source (right).

The correlation between the amount of photons detected by the PMT and the photons produced in the Micromegas has first to be assessed. This factor depends mainly on the solid angle of the setup and on the QE of the PMT but also on the optical transparency of the detector's windows. In fact, the detector includes one 5 mm thick quartz glass, which is the entrance window of the chamber, and an ITO coated 5 mm quartz glass, which is the Micromegas glass substrate. The two windows' transmission distribution, the PMT's quantum efficiency and the normalized scintillation spectrum of an Argon  $\text{CF}_4$  based gas mixture are depicted in Figure 5.12. The QE of the PMT is the most limiting contribution to the detection efficiency. The shift between the maximum QE of the PMT ( $\sim 400$  nm) and the maximum of light emission of the gas mixture ( $\sim 630$  nm) affects even more the detection efficiency. A detection efficiency of  $D = 1.5\%$  has been measured using the equation:

$$D = \int_{\lambda} S(\lambda) \times T(\lambda) \times \text{QE}(\lambda) d\lambda \quad (5.6)$$

with  $S(\lambda)$  the normalized secondary emission spectrum of an Argon/ $\text{CF}_4$  (80%/20%) gas mixture,  $T(\lambda)$  the wavelength dependent transmission of the glass windows and  $\text{QE}(\lambda)$  the quantum efficiency of the PMT, which also include the photocathode electron conversion efficiency.

In addition to the detection efficiency, the geometrical acceptance of the setup will be calculated. It significantly impacts the ratio between the number of detected photons and emitted photons from the avalanche. The distance between the bottom of the avalanche (ITO position) and the photocathode of the PMT is  $d = 48.6$  mm, and the photocathode half diameter is  $a = 23$  mm. The geometrical acceptance is given by the formula (5.7).



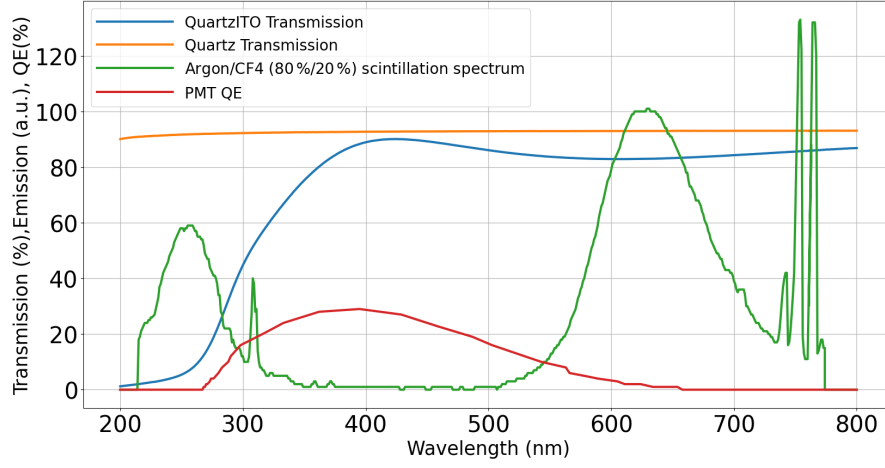


Figure 5.12: In this figure are displayed the wavelength dependent 5 mm quartz glass transmission, the 5 mm quartz glass coated with 150 nm of ITO transmission, the PMT quantum efficiency and the normalized scintillation spectrum of Argon/CF<sub>4</sub> (80%/20%) gas mixture. The total detection efficiency is 1.5%. Spectrum extracted from [52].

$$G = \frac{\Omega}{4\pi} \quad (5.7)$$

For a point-like source, the solid-angle is given by the relation (5.8).

$$\Omega = 2\pi \left( 1 - \frac{d}{\sqrt{d^2 + a^2}} \right) \quad (5.8)$$

A geometrical acceptance  $G = 4.8\%$  has been computed. However, the X-rays source has been collimated, and the total surface of light emission in the amplification gap has been shaped to a disk of 20 mm diameter and measured with the camera (Figure 5.11). It exist a more complex formula [76] for the solid angle for a source with a shape of a disk. Though, a more accurate geometrical acceptance has been computed with an optics simulation software called Apilux (Figure 5.13), assuming a uniform emission of photons in the amplification gap. A geometrical acceptance of  $G = 4.6\%$  was measured.

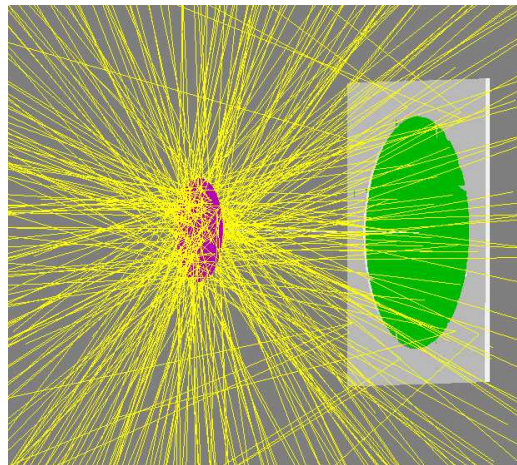


Figure 5.13: Geometry representation of the Apilux simulation software. The pink disk represents the scintillating area in the amplification gap and the green disk is the PMT photocathode. Photons (yellow lines) are emitted isotropically and the acceptance is defined as the ratio between the number of detected photons and emitted photons.

The calibration factor between the measured charge signal on the PMT and the number of photons detected by the PMT will be calculated. For this purpose, one should measure the charge signal of

the PMT from single photons. The PMT is collimated from most direct light so that only a very low amount of photons from the ambient light reaches the PMT. Thanks to the substantial time resolution of the PMT, the photons from the ambient light are well separated in time, as shown in Figure 5.14. The single photon signals are not triggered but are continuously recorded over windows of 500  $\mu\text{s}$ .

The photons from the ambient light present an almost white spectral distribution, while the expected detected wavelengths from the gas mixture scintillation are at around 300 nm and 550 nm. However, this difference only affects the QE of the PMT while the charge response of the PMT remains unchanged. In other words, the amplitude of the PMT signal from a single photon  $V_S(t)$  does not depend on its wavelength.

The integral of the tension signal over the pulse duration must be computed to access the charge signal, which is proportional to the number of photons. Figure 5.15 (left) shows the spectrum of the single photons. Three main parts are identified: the thermal noise from 0 to 5 pVs, the single photoelectron response (from 5 to 15 pVs) and the double photoelectron response (above 15 pVs). In fact, while a single photon hits the photocathode, there is a low probability that two photoelectrons, instead of one, are produced. The resulting signal has a charge signal twice as large as the single photoelectron response. These two parts are fitted with Gaussian distributions (red lines) and the sum of the distributions fits the overall distribution above the noise. The first Gaussian mean value constitutes the calibration factor of charge amount per number of photons (in  $\text{pV} \cdot \text{s/ph}$ ), given by the formula:

$$I_{ph} = \int_t V_S(t) dt \quad (5.9)$$

A calibration factor  $I_{ph} = 19.4 \text{ pV} \cdot \text{s/ph}$  has been measured for a PMT voltage of 1700 V.

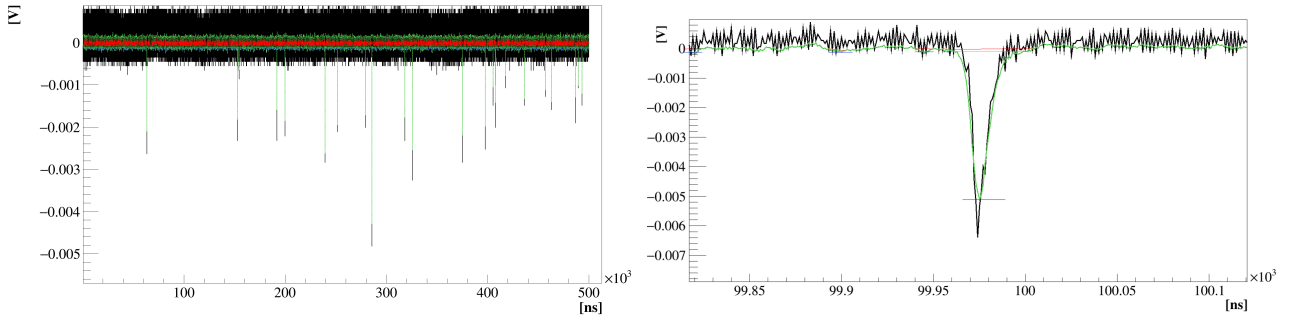


Figure 5.14: Amplitude from the PMT signal of multiple single photon events (left) and of a single photon event (right) with a time scale 1000 times smaller. The black line is the raw signal and the green plot is the smoothed signal after moving average.

One should confirm that the signals from Figure 5.14 indeed come from single photons and not from the overlap of photons. To do this, the measurement has been performed at two different photon fluxes by shielding the PMT with a 20 % transparent mesh. Even if the detection rate is not expected to diminish by exactly 20 %, this should considerably reduce it. As shown on Figure 5.15 (right), the Gaussian amplitude  $c$  of the single photoelectron has dropped by 25 % while its mean value  $\mu$  is steady (0.2 % variation). This result proves that the amount of events has decreased while the signals charge intensity is the same. In other words, there is no overlapping of events and the detected signals come from single photons instead of multiple photons.

Now that the detection efficiency, the geometrical acceptance and the single photon calibration factor have been calculated, the number of photons  $N_{ph}$  issued from secondary scintillation signals from the Micromegas detector can be computed, given the relation:

$$N_{ph} = \frac{1}{I_{ph} \times D \times G} \times \int_t V(t) dt \quad (5.10)$$

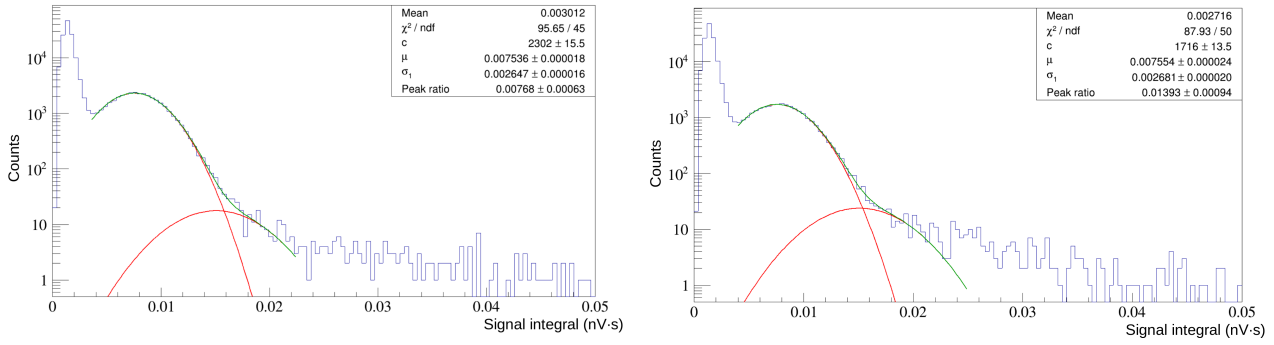


Figure 5.15: Distributions of the PMT’s charge signals from single photons for a PMT voltage of 1450 V. On the left, the PMT is collimated to reduce the photon flux and on the right, it is shielded with a 20 % optical transmission grid to further reduce the flux. The red plots represent the Gaussian fit of the single and double photoelectron responses and the green plot is the sum of the fit functions.

The PMT is now capturing the light scintillated in the Micromegas detector, and the charge signal from the mesh is simultaneously recorded. Both signals are recorded by an oscilloscope, as illustrated in Figure 5.16, triggering, on the mesh signal, the events with an amplitude above the electronic noise level. The light signal measured with the PMT, in parallel with the charge signal from the anode of the Micromegas are represented in Figure 5.17. The charge signal from the Micromegas anode being shaped by a pre-amplifier and an amplifier, it is broader and delayed by  $1 \mu\text{s}$  compared to the PMT signal.

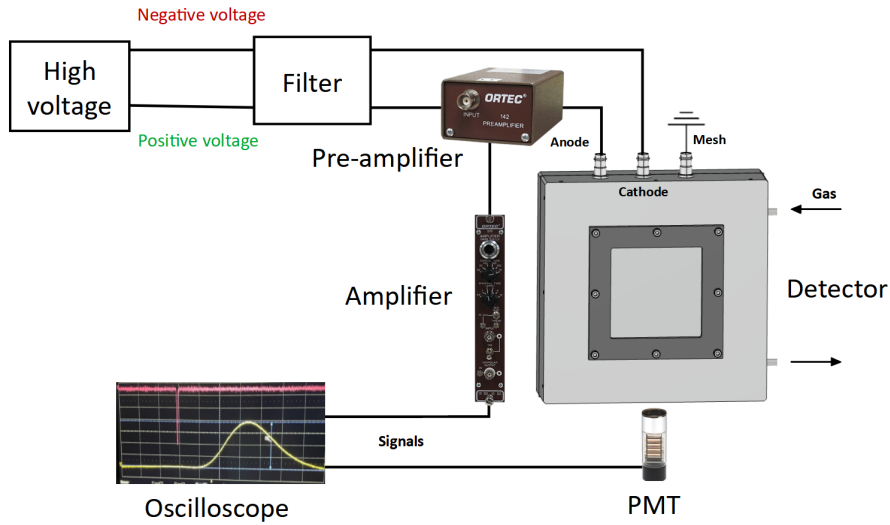


Figure 5.16: Electronics acquisition scheme where the charge signal from the anode and the signal from the PMT are read out with an oscilloscope.

To compare the charge and light signals issued from the Micromegas avalanche mechanism, the integral of the PMT signal and the amplitude of the anode signal were stored in a histogram for  $10^5$  events. The Figure 5.18 shows a clear linear correlation between the amount of secondary electrons and the amount of secondary scintillation photons.

To measure the light yield, the energy resolution and the gain with accuracy, the distribution of the light signal on one hand and the distribution of the anode charge signal of the other hand, are computed separately. These two distributions are shown on Figure 5.19.

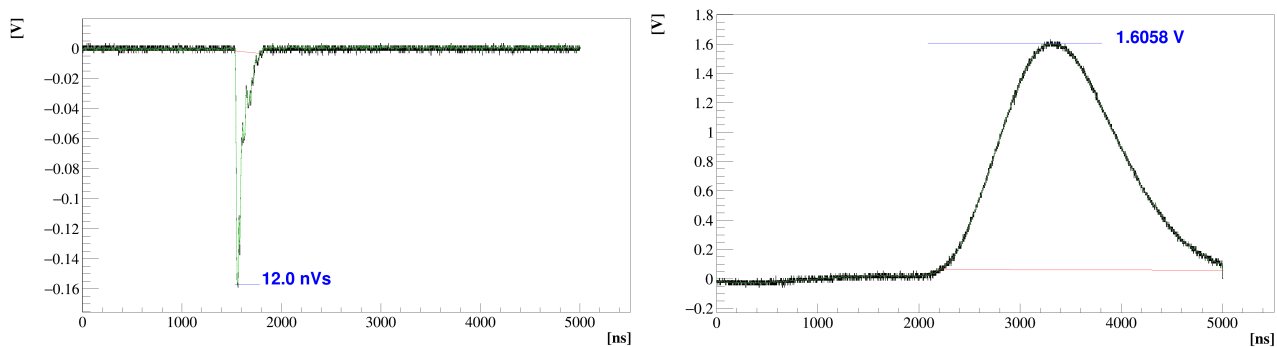


Figure 5.17: Signal from the PMT (left) and signal from the Micromegas anode (right). The green line represents the signal smoothed by moving average. The red and blue lines indicate the bottom and top of the pulse respectively. The integral of the PMT signal and the amplitude of the anode signal are written in blue.

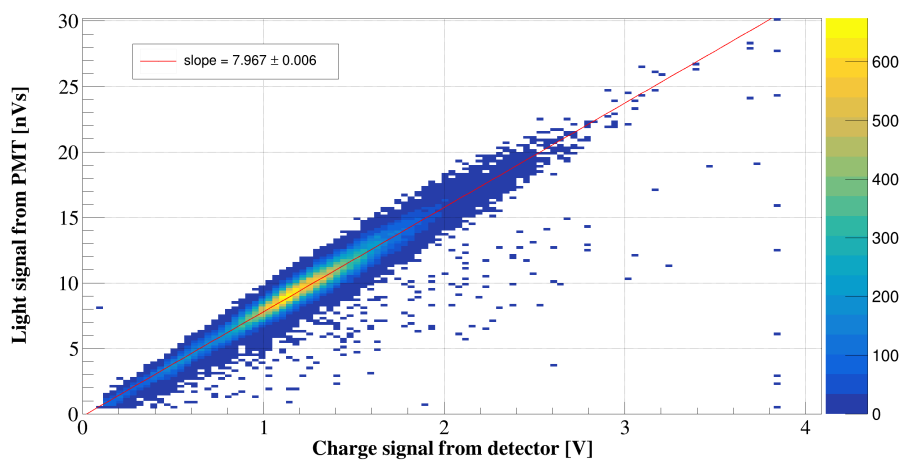


Figure 5.18: Histogram of the scintillation light signals as a function of the anode charge signals. The red line is a linear fit of the distribution and a slope of about 8 nVs/V has been measured for a gain of  $10^4$  and an Argon/ $\text{CF}_4$  (90%/10%) gas mixture.

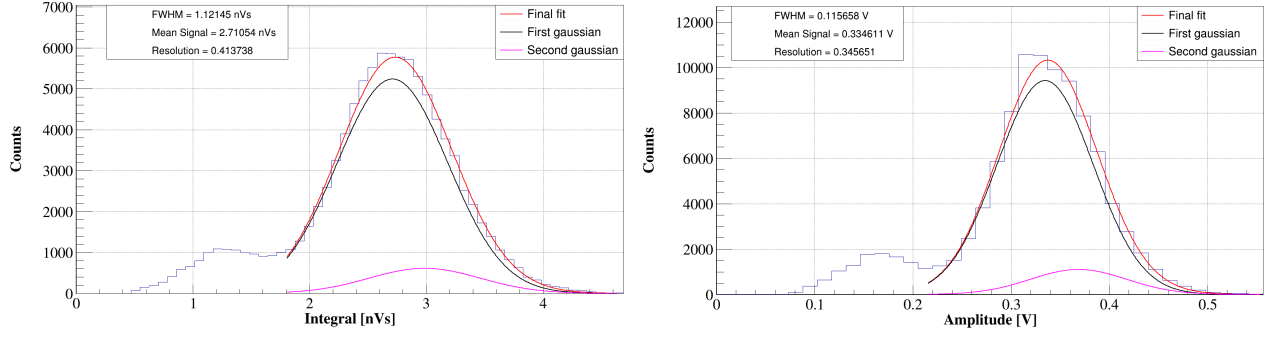


Figure 5.19: Distributions of the charge signals from the PMT (left) and the signals from the Micromegas anode (right). An optimal energy resolution of 41% is obtained for the scintillation light signal and 34% for the Micromegas charge signal for an Argon/CF<sub>4</sub> (90%/10%) gas mixture.

First, the fit of the spectrum described in Sec. 5.2.1 allows to extract the energy resolution from both charge and light readout approaches. The Figure 5.20 represents the energy resolutions (FWHM) for different gas mixtures and amplification fields. Overall, the energy resolution from the light signal is worse than the charge signal by about 5% and varies from 50% to 35% at low amount of CF<sub>4</sub>. Also, the energy resolution improves with 100% of CF<sub>4</sub>, being of about 22% and 28% with charge and light readout respectively.

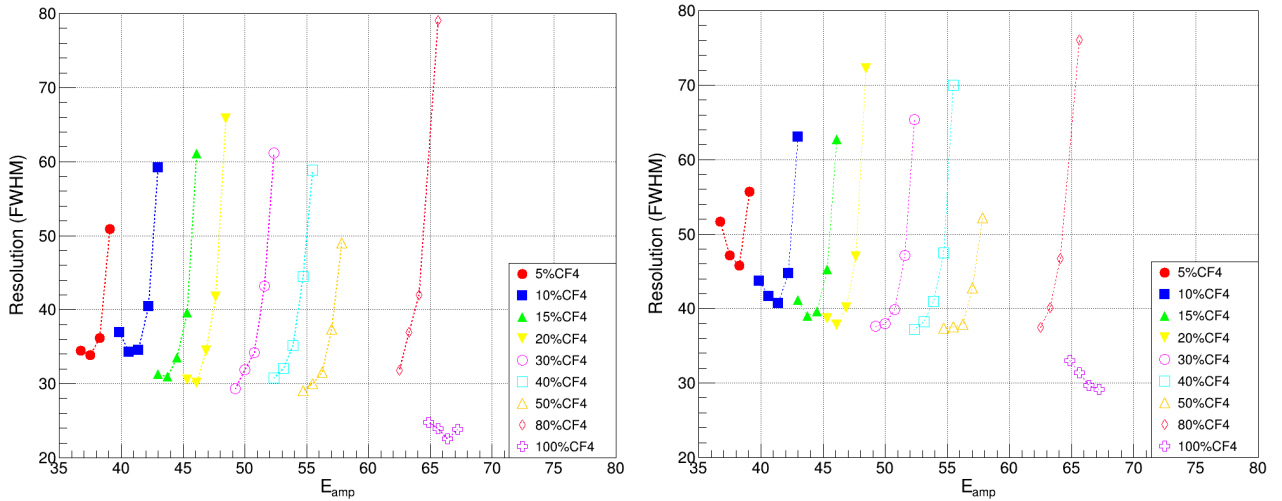


Figure 5.20: Energy resolution (FWHM) from the Micromegas charge signal (left) and from the light signal (right). Gas mixtures with a fraction of CF<sub>4</sub> from 5% to 100% have been tested. The amplification field ranges from 35 kV/cm to 70 kV/cm in a 128  $\mu$ m gap.

The fit of the spectrum also allows to extract the mean PMT charge signal  $\mu_{\text{PMT}}$  and the mean anode tension signal of the Micromegas  $\mu_{\text{Anode}}$ . Hence, the number of secondary electrons, the number of primary electrons and the gain are computed by inserting  $\mu_{\text{Anode}}$  into the equations (5.2), (5.3) and (5.4) respectively. The mean number of scintillated photons from the avalanche is obtained by averaging the equation (5.10) such as:

$$\langle N_{ph} \rangle = \frac{\mu_{\text{PMT}}}{I_{ph} \times D \times G} \quad (5.11)$$

Thus, the light yield is computed as:

$$y_L = \frac{\langle N_{ph} \rangle}{\langle N_{QS} \rangle} \quad (5.12)$$

The light yield has been represented in Figure 5.21 for different amplification fields and gas mixtures. The best light yield has been achieved for a gas mixture of Argon/CF<sub>4</sub> (80%/20%), peaking at

0.38 Ph/e<sup>-</sup>. Thus, the light yield is not proportional to the amount of CF<sub>4</sub> but reaches a maximum, as explained in Sec. 4.2.3. For fractions of CF<sub>4</sub> from 10 % to 40 %, the light yield decreases with the gain while the trend is less predictable at other amounts of CF<sub>4</sub>. Similar values and behaviour of the light yield were measured with optical GEM detectors from the literature [38, 64]. It demonstrates that the different amplification geometries of the GEM and the Micromegas detectors do not substantially affect the light production mechanism.

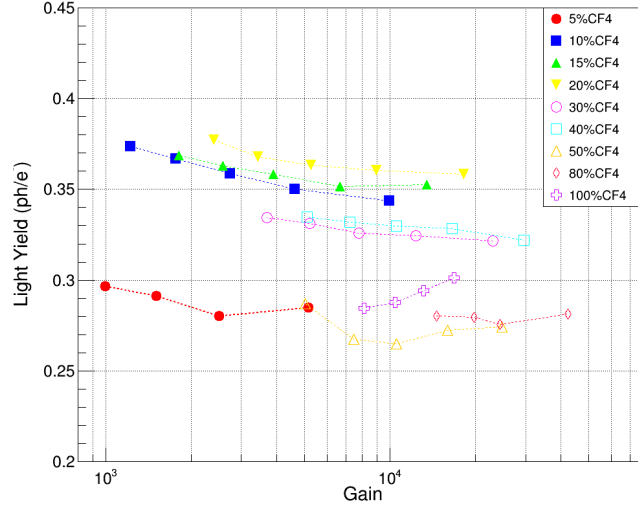


Figure 5.21: Light yield obtained from the formula (5.12) as a function of the gain. Gas mixtures with a fraction of CF<sub>4</sub> from 5 % to 100 % have been tested. The gain ranges from 1000 to 40000 in a 128  $\mu$ m amplification gap.

It is worth studying the absolute number of photons generated in the detector (Figure 5.22, left) which represents the actual amount of light emitted towards the camera and directly affects the sensitivity of the imager. Since higher gain values are reached with a high fraction of CF<sub>4</sub> (Figure 5.22, right), the maximum number of photons increases with the fraction of CF<sub>4</sub> until 80 %. However, at equal value of gain, the gas mixture with 10 % of CF<sub>4</sub> scores the highest number of photons, even larger than the mixture with 20 % of CF<sub>4</sub> that accounts for the maximum light yield. This effect comes from the lower ionization potential of Argon (26 eV) compared to CF<sub>4</sub> (54 eV). Hence, the amount of primary electrons is higher for the 10 % gas mixture than for the 20 % one and the total amount of photons increases.

### 5.3 . Optical elements

The glass Micromegas detector has shown good performances in terms of gain, energy resolution and light yield, which makes it a tailored technology for the detection of a large variety of particles with optical readout. Coupled with a low noise camera and an appropriate lens, the instrument is able to render precise information about the detected radiation, such as the position, energy and emission rate. Furthermore, this imaging system provides the capability to integrate the light in each pixel for long integration periods, and enables real-time imaging without requiring extensive data processing. The camera, the lens and the light guide, that are essential to measure the scintillation light, are described in this section.

#### 5.3.1 . Camera

The camera chosen for this project is the Hamamatsu ORCA-Quest [72], also called quantum CMOS (qCMOS) camera, with a QE of about 80 % at the gas mixture main scintillation emission wavelength (Figure 5.2). Moreover, it exhibits a 9.4 megapixel granularity with a readout noise as low as 0.27 electrons Root Mean Square (RMS). This large number of pixels is ideal for high spatial

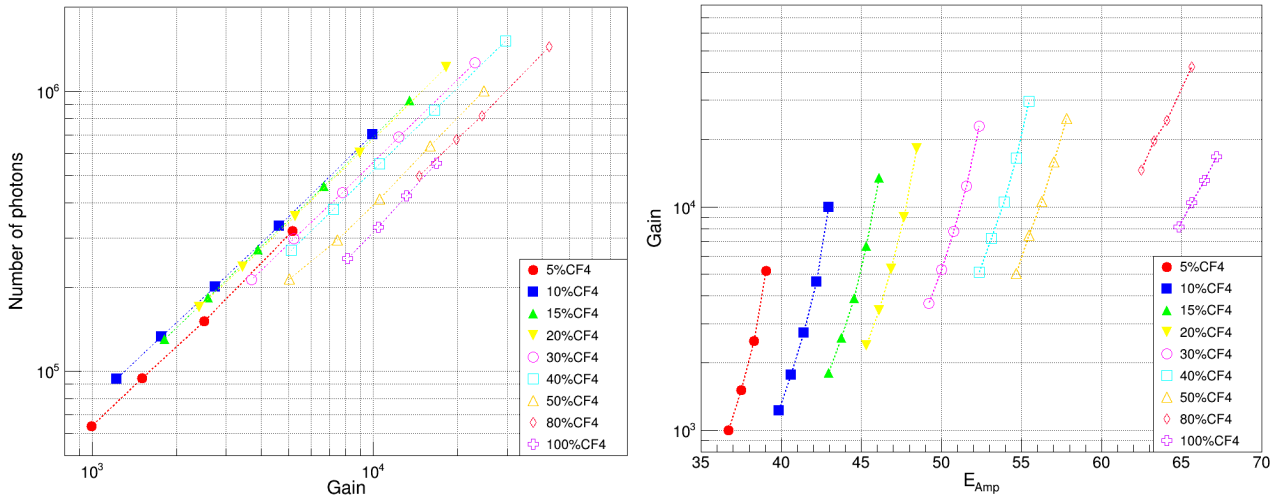


Figure 5.22: Absolute number of photons  $\langle N_{\text{ph}} \rangle$  as a function of the gain (left) and absolute gain as a function of the amplification field. Gas mixtures with a proportion of  $\text{CF}_4$  from 5% to 100% have been tested. The gain ranges from 1000 to 40000 in a  $128 \mu\text{m}$  amplification gap thickness.

resolution imaging with a large field of view while the readout noise allows to detect single photons. In the case of single event detection, while about few photons per pixel only are reaching the camera, very low noise and high QE are required to achieve proper signal-to-noise ratio.

Different features of the ORCA-Quest camera's CMOS sensor allow to reach high QE. As shows in Figure 4.4 (right), pixels are back-illuminated and microlenses focus photons into the field-free region and prevent them from ending in the Deep Trench Isolation (DTI) region (Sec. 4.3.1). Besides, the DTI region strongly prevents cross-talking between pixels by reflecting photons and avoiding photoelectrons migration. The 9.4 megapixel granularity is made possible thanks to the small pixel size of  $4.6 \times 4.6 \mu\text{m}^2$ , while the pixel is thick enough to achieve sufficient near-infrared QE.

There are two main contributions to the electrical noise: the dark current and the readout noise. At a sensor temperature of  $-20^\circ\text{C}$ , the qCMOS camera shows a dark current of  $0.016 e^-/\text{pixel}/\text{s}$ . However, the main contribution to the noise comes from the readout noise which is directly related to the individual pixel amplifier characteristics. Bias images of 0 exposure time are generally acquired to render the readout noise only. In our case, dark images of 200 ms exposure time are acquired [67], bringing down the dark current to the lowest possible value. The camera is shielded from any photon illumination. Two dark images are then subtracted to remove any dark current contribution to the noise, and the subtracted pixels distribution is displayed in Figure 5.23 (left). To render the non-uniformity of the readout noise pattern, the characteristic readout noise is defined by the RMS of the previous distribution. The RMS of the readout noise given by the camera datasheet is 0.27 electrons, and a similar value was measured. However, single photon resolution is possible for readout noise lower than 0.5 electrons RMS according to [66] and it corroborates with Figure 5.23 (right). On this figure, a clear discretization of the light amount per pixel allows to count the number of photons captured per pixel (red numbers). The previous distribution was extracted from a low light amount image similar to Figure 5.6 (left) where most pixels are exposed to few photons.

### 5.3.2 . Lens

Beside the camera, the lens is a key element of the imager, strongly affecting the sensitivity and the spatial resolution. The ONYX 0.95/25 C lens from Schneider Optics [77] was chosen for its extremely large speed ( $f/0.95$ ), which is adapted to low light amount imaging. Moreover, it provides a transmission of 90% at 630 nm. The focal length is 25 mm, implying a 200 mm minimum working distance, which is well suited for the imaging of a  $10 \times 10 \text{cm}^2$  wide object. As shown in Figure 5.1, the camera and the leak tight chamber are fixed on the same plate, ensuring a good parallelism between the lens and the detector's anode plan. The lens is focused on the Micromegas' mesh, which shows a pattern

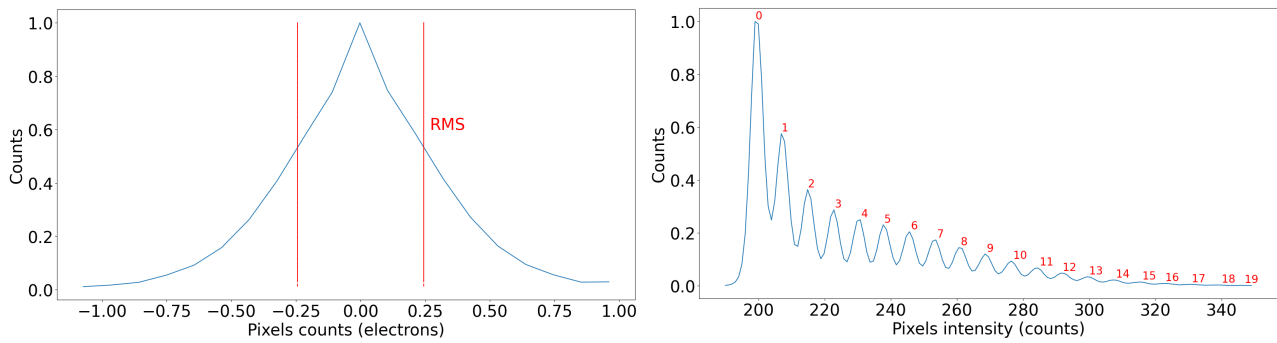


Figure 5.23: Readout noise pixel distribution centered in 0 and converted from counts (ADU) to a number of electrons (left). The RMS is represented by the red lines. Pixel intensity distribution of a low light amount image with single photon resolution (right). The number of photons corresponding to a pixel intensity is written in red.

with sharp edges, and is convenient to focus by hand. In addition, the mesh is at few tens of microns from the avalanche and from the light emission, which ensures a good focusing on the scintillation light's position of emission.

However, such large aperture involves optical effects such as aberrations (Sec. 4.5), which affect the spatial resolution. In Figure 5.24, MTF (Modular Transfer Function) values at  $f/2.8$  are much higher than  $f/0.95$ . Hence, better spatial resolution is expected for large f-number. The MTF is a method to compute the contrast of an image as a function of the spatial frequency. In the frequency domain, higher MTF values over a longer range indicates better spatial resolution. The different processes to measure the MTF are detailed in Sec. 8.4.3.

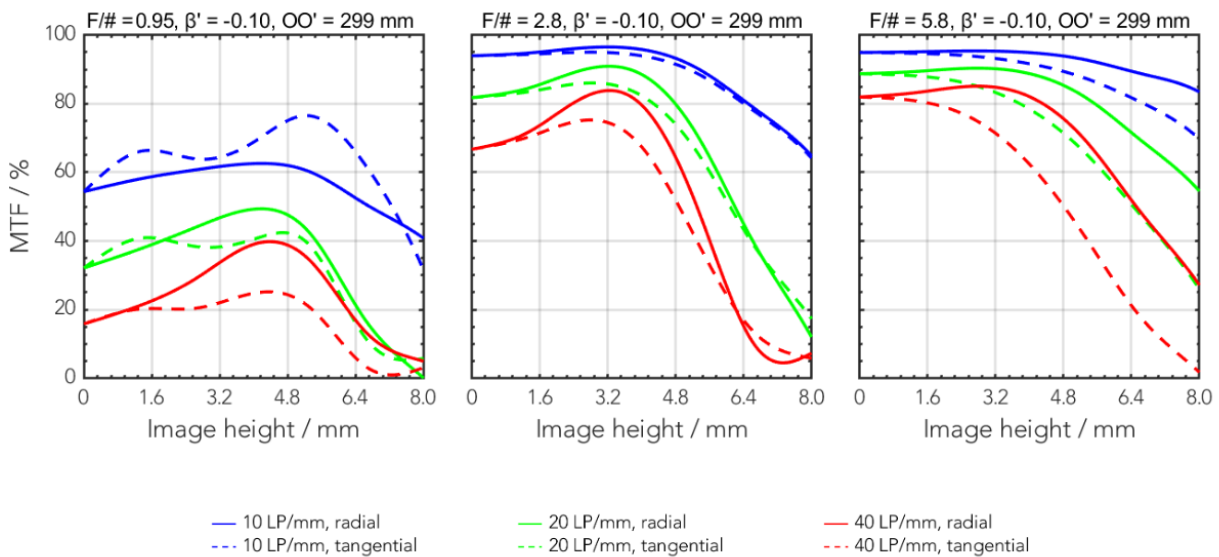


Figure 5.24: ONYX 0.95/25 C lens MTF at different lens apertures at a 299 mm working distance [77]. Three different f-numbers are shown :  $f/0.95$  (left),  $f/2.8$  (center) and  $f/5.8$  (right). For each of them, the MTF is measured as a function of the image height (distance of the object from the optical axis) for different spatial frequencies (lines per mm).

### 5.3.3 . Dark chamber

In order to prevent any light leak, which might pollute the camera, a dark chamber that links the camera to the gaseous detector has been designed. The minimum acceptable distance between the lens and the detector being of 200 mm, the dark chamber was made rigid, unlike bellows, usually preferred. Built with a 3D printer, the geometry, the robustness and the optical properties were customized,



as shown in Figure 5.25. An Ultimaker printer [78] was employed, using black mat PLA (polylactic acid) material. It was decided to cover the camera only from the lens extremity to avoid covering the camera ventilation that would warm it up. Two different pieces were designed: a straight piece for direct illumination of the camera and a right-angled piece, which includes a mirror in order that the camera is out of the particle beam axis. In fact, high-energy X-ray, gamma or neutron particle beam might be very harmful for camera sensors. Moreover, to prevent direct light reflection on the chamber walls, blades tilted by  $45^\circ$  are implemented.

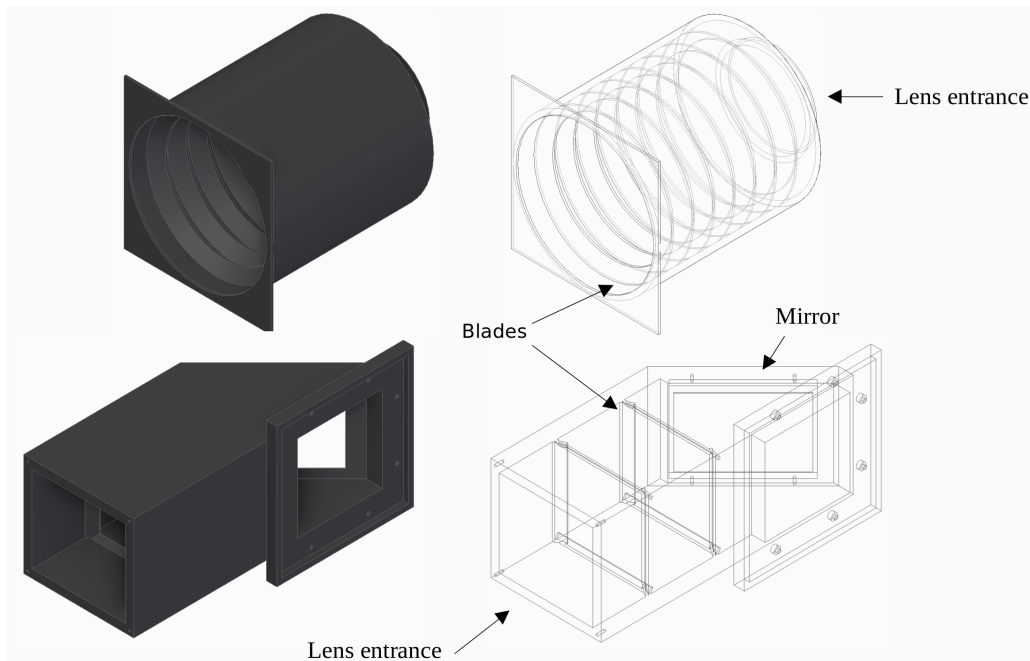


Figure 5.25: Schematics of the dark chambers, guiding the scintillation light from the Micromegas detector to the camera. The straight chamber (top) and the  $90^\circ$  chamber (bottom) are represented in solid (left) and transparent (right). There are anti-reflection blades on both designs.

## 5.4 . Acquisition modes and imaging processing

The optical readout Micromegas device aims to perform high resolution imaging of a wide variety of sources, from neutrons to beta particles, with the shortest acquisition time, data processing time and cost. From this perspective, event integration is appropriate since no timing resolution is needed and overlapping of events is allowed, which drastically simplifies the data acquisition system and the algorithmic design. However, the information about the interaction mechanism of individual particles with the gas (scattering, tracking, deposited energy, diffusion) is lost. Hence, a method for single event study has also been developed, involving different acquisition setups and data analysis approaches.

### 5.4.1 . Events integration

Two main parameters have to be optimized in the event integration mode: the SNR and the spatial resolution. The limiting factors of the SNR are the detector light yield and gain, and the background limitation. On the qCMOS camera, the two main contributions to the noise are the dark current and the readout noise. The dark current is increasing linearly with the exposure time while the readout noise is integrated once the image is recorded, at the end of an exposure cycle. Therefore, a trade-off between the integration time and the number of added images has to be chosen.

A dark image (or averaged dark images) contains both the readout noise (like bias image) and the dark current contributions. Therefore, the subtraction of dark images to the signal image helps to the reduction of the overall noise. The subtraction of dark frames also contributes to the removal of hot pixels. However, the readout noise is harder to correct and is increasing with the number of added up

frames. Hence, it is preferred to operate with a large integration time.

It is worth noting that, at a detector's gain close to  $10^5$ , there is a non-negligible probability that sparks occur, which is blinding the camera and losing the acquired frame. A long exposure time means that more frames would be unusable, which is equivalent to longer dead time in an experiment. The background treatment steps for a given exposure time are detailed:

- A number  $N$  of dark images (no radioactive source and no voltage on) are acquired, with the same exposure time. With  $B_i$  one of the dark images, an average frame  $B_\mu$  and a standard deviation frame  $B_\sigma$  of the dark images are computed so that  $B_\mu = \sum_i^N B_i/N$  and  $B_\sigma^2 = \sum_i^N (B_i - B_\mu)^2/N$ . The matrix of pixels  $B_\mu$  (Figure 5.26, left), which represents the pedestal, is preferred to be the average of several dark images, because it gives a better statistical representation of the different noises. In fact, the dark current in one frame might vary from another one because of sensor's temperature instabilities. The readout noise has a column-wise variation due to the CMOS sensor structure, and is better sampled with averaged dark images. The matrix  $B_\sigma$  is the individual pixels standard deviation and constitutes the signal common noise (Figure 5.26, right). It contains the characteristic readout noise variation of pixels.
- Signal images  $A_i$  are then acquired and accumulated through the following equation:  

$$A = \sum_i^N (A_i - B_\mu) \times I(A_i > \alpha B_\sigma)/N.$$
The term  $(A_i - B_\mu)$  stands for the pedestal subtraction while the common noise discrimination is defined by the term  $I(A_i > \alpha B_\sigma)$ . The identity function  $I(x)$  takes the value 1 if the condition  $x$  is true and 0 if not. This means that any pixel with a value lower than the common noise is set to 0. The factor  $\alpha$  is to be adapted to the experimental conditions.

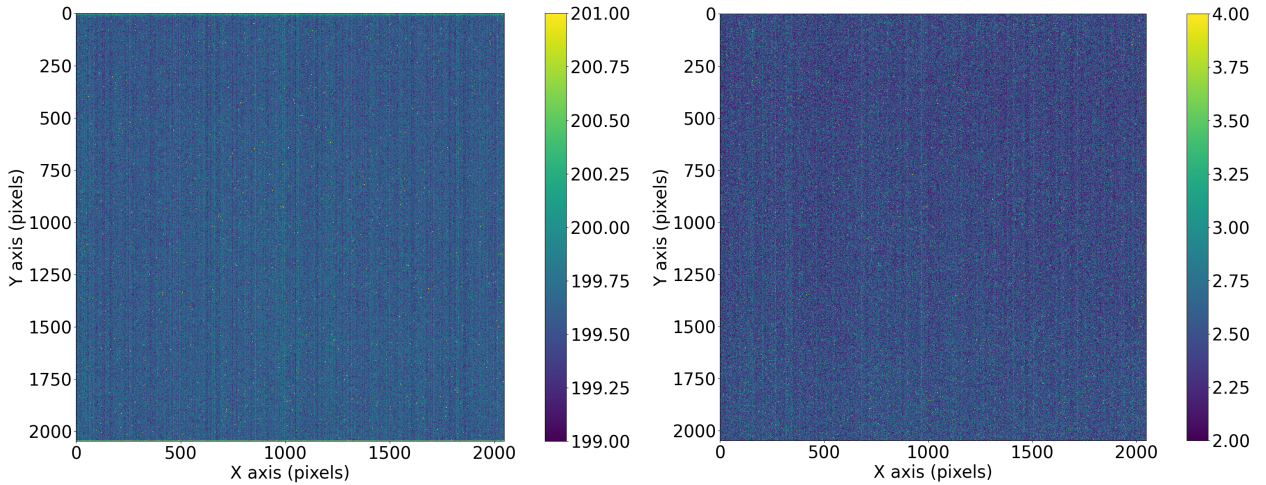


Figure 5.26: Pedestal frame (left) and common noise frame (right). These frames are extracted from 100 dark frames of 1 s exposure time without signal. At 1 s exposure time, the readout noise dominates thus the column-wise variation is well visible. While the displayed noise is very low, the colour scale has been chosen to visually reveal this variation.

The lens aperture (also called f-number) plays an important role in the maximization of the SNR. Given  $D$  the lens' diaphragm diameter and  $f$  the focal length, the light flux density on the camera sensor varies as  $(D/f)^2$  [70], which corresponds to the inverse of the f-number ( $f/\# = f/D$ ) squared. Hence, an aperture of  $f/0.95$  corresponds to a larger diaphragm than an aperture  $f/1.4$  by a factor  $\sqrt{2}$ , which correspond to a multiplication factor in flux density of one half. For this reason, a small f-number will give more light at equal exposure time. However, as seen in Sec. 4.5 and on Figure 5.24, a small f-number also means lower MTF value because of more pronounced optical aberrations. For example, a f-number of  $f/2.8$  represents a good trade-off, involving significant MTF values while the light flux density remains large enough for high-flux particle beam.

### 5.4.2 . Single event detection

In some cases, the particle energy or tracking capability are of high interest. This requires to capture single events with short exposure time frames to avoid the overlapping of events. However, high qCMOS camera sensitivity is required to record single events, which generate low light amount. The readout noise is also inversely proportional to the number of read out pixels and to the frame rate. In fact, the read noise is increasing with the sensor temperature, which depends on the number of pixels amplified per unit of time. Hence, the two ways to reduce the readout noise are to set a small frame range to reduce the amount of active pixels, or to increase the time gap between two exposure cycles, thus to increase the exposure time. The qCMOS camera provides a minimum exposure time of 200 ms at full frame ( $4096 \times 2304$  pixels<sup>2</sup>) in order to maintain the readout noise as low as  $0.27 e^-$  RMS.

Once the frame range and exposure time are settled, a  $2 \times 2$  binning is usually chosen to decrease the amount of data and increase the SNR. On CCD camera, on-chip binning is generally performed by summing 4 pixels together to a "superpixel" before readout, meaning that the SNR per pixel is reduce by a factor 4. However, the qCMOS camera performs digital binning by summing pixels after readout, which means that a "superpixel" contains also added-up noise. Thanks to the camera very low noise, the binning still increases the SNR because the background variation is averaged among the 4 pixels. After the binning, similar background treatment, described in the previous section, is operated. Additionally, smoothing based on the kernel convolution filter or the median filter are used to improve the events SNR.

Regarding the optical components, the setup is similar to what has been described earlier, while the lens aperture is set to a larger value. In fact, the optical sensitivity has to be maximized to capture low light amount from single events. Even if the lens shows smaller MTF values at such f-number, optical effects such as reflections or aberrations are negligible in very low light amount conditions (Sec. 4.5).

After the image noise processing, events are localized by the so-called Density-Based Spatial Clustering of Applications with Noise (DBSCAN) algorithm [79]. This clustering algorithm selects bunches of pixels based on their pixel density and rejects isolated pixels. It applies to a large diversity of structures, from small spots of pixels to large tracks. Two parameters only are considered and empirically chosen depending on the conditions: the cluster size  $\epsilon$  and number of points  $MinPts$ . The selection and classification of pixels respect the following rules:

- A core point is typically positioned at the center of a cluster, where there is a high density of points.
- A reachable point lies within a distance  $\epsilon$  from a core point and forms the cluster surrounding.
- A noise point cannot be reached by any other points within the distance  $\epsilon$ .
- Identified clusters are kept only if they consist of a minimum number  $MinPts$  of points.

The Figure 5.27 shows the selected clusters by DBSCAN for different kind of particles. On the right, thick tracks of alpha particles (1.47 MeV and 1.78 MeV) and <sup>7</sup>Li ions (0.84 MeV and 1.02 MeV) are visible and well defined by the algorithm. Even particles like X-rays (left) or beta particles (center) of few keV are well identified in most cases. This very simple method allows one to access the amount of light produced by single particles and to recover the total deposited energy of a particle by summing the cluster pixels intensity. It enables to compute the cluster size, the track width and orientation in the case of alpha tracks, as well as the center of gravity, which improves the spatial resolution.

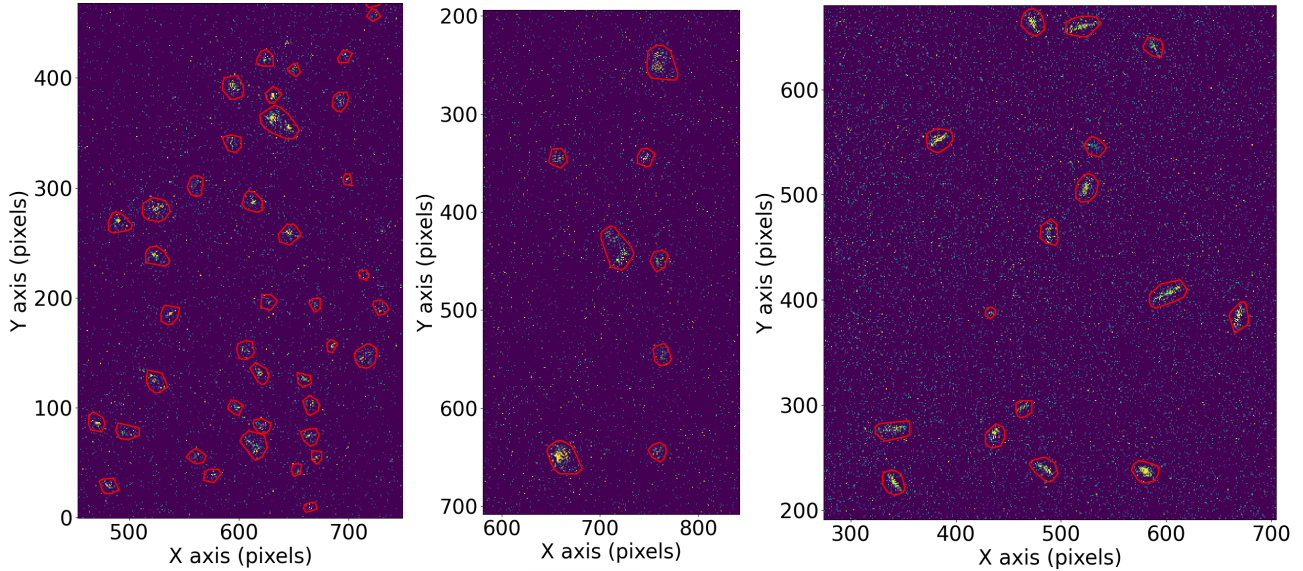


Figure 5.27: Light intensity frame of events from X-ray (left), beta (center) and neutron (right) sources. Events which have been selected by the DBSCAN clustering algorithm are encircled in red.

## 5.5 . Conclusion

The new design of a glass Micromegas detector has been optimized to achieve a uniform light response alongside high gain and energy resolution comparable to standard Micromegas detectors, in an Argon/Isobutane gas mixture. The set of measurements with the PMT were performed by Maël Jeannot, an internship student under my supervision for 5 months. These measurements led to the calculation/estimation of the glass Micromegas light yield. An optimal light yield of  $0.38 \text{ ph/e}^-$  and absolute amount of scintillated photons were obtained with 20% and 10% of  $\text{CF}_4$  respectively. Satisfactory gain and energy resolution values were measured with both light and charge readout, revealing the suitability of the glass Micromegas detector for high sensitivity imaging. The integration of a high-sensitivity qCMOS camera, capable of capturing low light signals with minimal noise, and a high-speed lens with a large aperture, underscores the potential of this detection system for precise particle imaging. Additionally, analysis routines were developed for both integration and single event imaging modes. The integration mode consists in the accumulation of signals over time, allowing real-time imaging capability at high SNR and spatial resolution. In contrast, the event-by-event mode enables detailed study of individual particle interactions, providing insights into the interaction mechanisms, positions and energy deposition profiles.



## 6 - X-ray imaging

The mechanisms involved in a gaseous detector following X-rays irradiation are governed by the photon conversion in the gas into a photoelectron, which loses energy by scattering. A cloud of secondary electrons is formed and is located close to the position of interaction of the X-ray photon (Sec. 2.2). Thus, the energy and position of the X-ray photon are recovered by the Micromegas via the avalanche and scintillation processes. The reconstruction is facilitated for low-energy X-rays that limit the photoelectron range in the gas. This makes low-energy X-ray sources a suitable tool for the characterisation of gaseous detectors. Especially, the uniformity and precision of the response of the glass Micromegas detector have been studied by X-ray radiography with an X-ray tube. The response of the detector to a point-like source has been analyzed at a synchrotron facility that provides a large flux X-ray beam with tunable size (down to  $20 \times 20 \mu\text{m}^2$ ) and energy. This test allows to characterize and quantify the different contributions that affect the spatial resolution, like the electron range, the diffusion in gas, as well as optical effects.

### 6.1 . Detector characterization with an X-ray tube

X-ray radiography is a common tool to perform examination of the inner structure of matter, and is widely used in medical imaging, in industry, or for the examination of any object intern structure. As illustrated in Figure 6.1, the imaged object is positioned between the X-ray source and the detector. The X-ray cross-section depends on the materials' density and elements' atomic mass. Going through matter, the X-ray beam is attenuated, following the Beer-Lambert law (6.1). Its solution (6.2) has a negative exponential distribution that depends on the incident beam flux  $I_0$ , the material density  $n$  (number of atoms per  $\text{cm}^{-3}$ ) and the cross section  $\sigma$ , at a given energy.

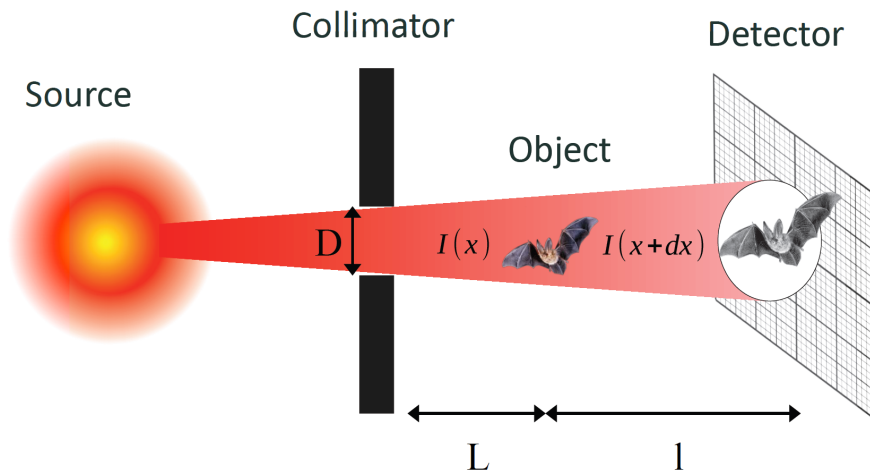


Figure 6.1: Scheme of the X-ray radiography principle with a source collimated by a pinhole of diameter  $D$ , irradiating an object at a distance  $L$  from the pinhole. The object is at a distance  $l$  from the imaging plan.

$$I(x + dx) = I(x)(1 - n\sigma dx) \quad (6.1)$$

$$I(x) = I_0 e^{-n\sigma x} \quad (6.2)$$

The optical readout Micromegas detector locates the X-ray photons' position of interaction within the gas. Hence, the detector gives a density and atomic mass distribution of the object's internal

components. High X-ray energy allows to reach greater depth of the object. X ray sources, such as X-rays tubes, are ideal for X-ray radiography, due to their high flux and beam quality, which enhance contrast and spatial resolution. For these tests, the set-up described in Sec.5.1 was used in events integration mode (Sec. 5.4.1). 1.1 mm quartz Micromegas detector was used with a 2 mm drift gap and a standard mesh.

### 6.1.1 . X-ray tube measurements

At the CERN gaseous detector development group [23], an X-ray tube has been used for this measurement, providing a high intensity flux of X-rays of few tens of keV. The X-ray beam is produced by the Bremsstrahlung effect (Sec. 2.1.2), when electrons accelerated to few tens of keV, are decelerating, in general in a copper, silver or tungsten target. The X-ray tube was located at the largest possible distance  $L = 1$  m from the detector to optimize the geometrical resolution given by (6.3), where the distance  $l$  between the detector plan and the object and the diameter of the beam collimator  $D$  are depicted in Figure 6.1. The object is put as close as possible to the imaging plan, stuck on the detector window, to minimize parallax. The gas is a mixture of Argon/CF<sub>4</sub> (80%/20%) at atmospheric pressure. The camera is the Orca-Quest and the lens' aperture is set to  $f/0.95$ .

$$U_g = \frac{l \times D}{L} \quad (6.3)$$

The parallax effect occurs when a unique point of an object is visualized at two different locations on the image plan, involving image blurring. This is often induced by non parallel particle beam as illustrated in Figure 6.2. Minimizing the geometrical resolution  $U_g$  reduces parallax.

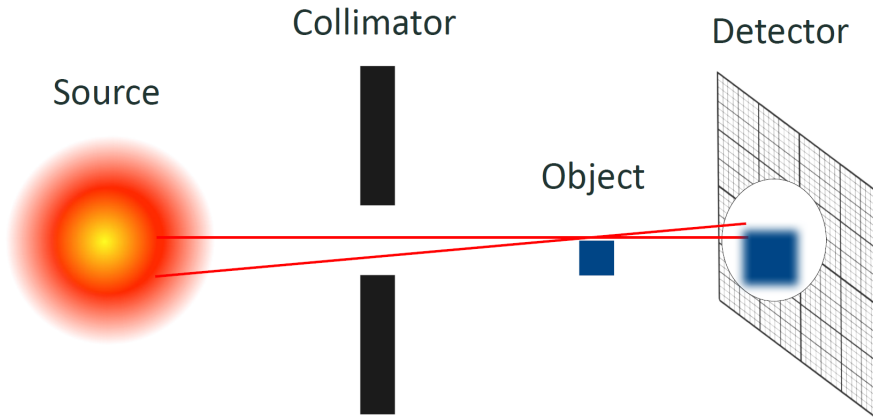


Figure 6.2: Scheme illustrating the parallax effect. Larger geometrical resolution involves more blurry images.

Images were first acquired without any object to record flat images of the detector. This allows to study the gain map uniformity and potential image deformation effects. In a second step, radiography was performed on a small animal and on a lead patterned target for contrast and spatial resolution assessment.

### 6.1.2 . Flat X-ray radiography

As a first step, the detector gain homogeneity has been characterized by irradiating the full active area, as shown in Figure 6.3. This first simple test is also an opportunity to check optical effects such as image deformation or light reflection. The non flatness and optical reflection of the cathode have been identified as factors of gain non-uniformity. At first, the cathode is made of a thin aluminized Mylar foil which is stretched on an aluminium frame. The uneven stretching of the mylar foil shows non-uniformities of the gain with "waves" pattern as shown in Figure 6.3 (left). The variation of the drift gap thickness indeed involves variations of the X-ray absorption in the gas (6.2). Improving

the flatness of the Mylar foil has solved the gain non-homogeneity has shown in Figure 6.3 (middle). However, the aluminized Mylar is quite shiny and reflects back the scintillation light emitted from the avalanche to the camera, like a mirror. On the latter image, the reflection of the pillars are clearly visible, especially on the edges. Hence, special attention should be given to the cathode material and to its reflectivity. A low resistivity Diamond-Like Carbon (DLC) layer, which is a few tens of nanometers thick, is deposited on top of a 50  $\mu\text{m}$  Kapton foil [24]. The anti-reflective foil is stretched on a aluminium frame, ensuring a uniform gain and no reflections as shown in Figure 6.3 (right).

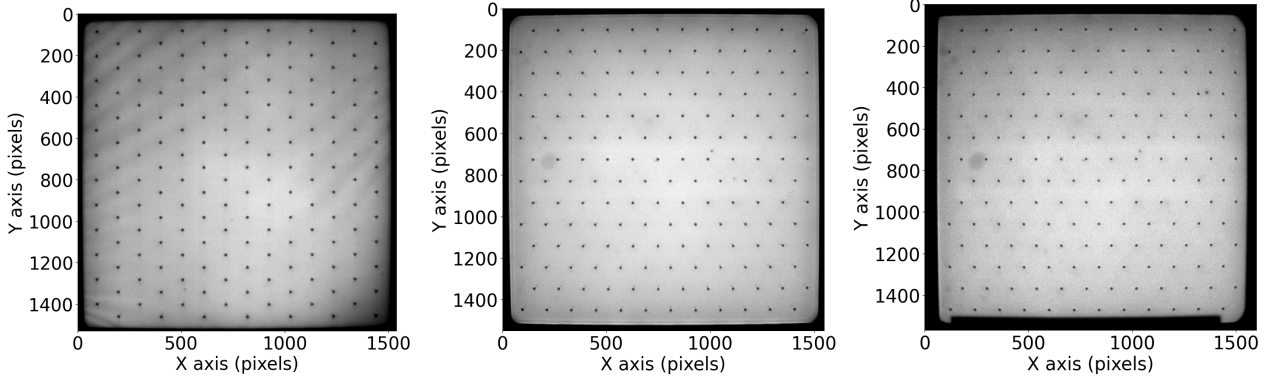


Figure 6.3: Flat images from the irradiation of the glass Micromegas detector with an X-ray beam were recorded for different cathode geometries. Images highlighting the cathode non-planarity (left), light reflectivity (middle) and light non-reflectivity (right) are shown. The pixels width is 50  $\mu\text{m}$  and the exposure time is 60 s. The current of the X-ray tube is at 0.5 mA, the voltage at 20 kV and the X-ray energy spectrum is continuous, with a maximum energy at about 20 keV. The gas is an Argon/ $\text{CF}_4$  (80%/20%) gas mixture. The detector is operated at a gain of about  $10^4$  and at the maximum transmission.

### 6.1.3 . X-ray radiography

X-ray radiography has first been performed on a deceased bat placed in front of the detector window at a distance of about  $l = 20\text{ mm}$ . For an X-ray tube collimator diameter of 10 mm, the geometrical resolution given by (6.3) is 200  $\mu\text{m}$ , which corresponds to the minimum achievable spatial resolution. The radiograph of the bat is shown in Figure 6.4 (left) and has been obtained following the acquisition routine described in Sec. 5.4.1. The characteristic shape of the X-ray beam has been flattened by Flat Fielding (FF): the radiograph is normalized by the beam flat image (Figure 6.3) in the exact same experimental conditions. This measurement is a first demonstration of the capability of the glass Micromegas detector to acquire precise radiographic images of large objects, in real time. The different densities of the object are well contrasted; in particular the bones.

In order to quantify the spatial resolution of the imager, radiography has been performed using a lead target [80] with a pattern with different spatial frequencies, as shown in Figure 6.4 (right). The pitch between the bright and dark lines is associated to a spatial frequency. Measuring the contrast between the lines allows to identify the spatial frequency at which the contrast becomes too low to discern two consecutive lines. The so-called Modular Transfer Function (MTF) provides the spatial resolution which corresponds to a contrast of 10%. The procedure to compute the MTF is described in Sec. 8.4.3. The gap between lines appears clear until a frequency of about 1.2 lines/mm, which corresponds to a spatial resolution of about 800  $\mu\text{m}$ .

The lens' aperture has been set to  $f/0.95$  in order to maximize the light intensity according to Sec. 4.4. In addition, the Micromegas detector's high gain provides a large amount of scintillation light per X-ray interaction and the camera low noise involves high SNR. Thus, highly contrasted images are recorded even with low-energy X-rays and short acquisition time. However, the lens' large aperture involves a strong degradation of the image sharpness as shown in Sec. 5.3.2.



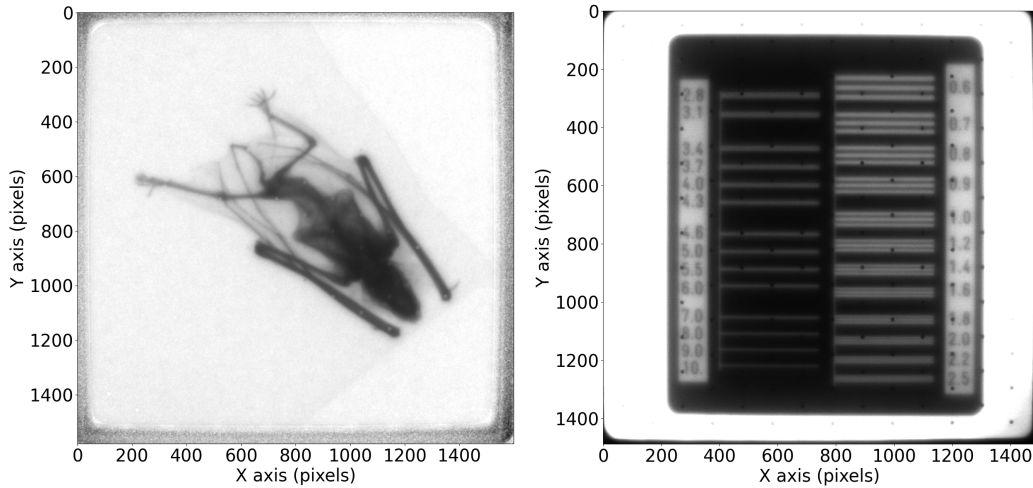


Figure 6.4: Radiographs of a deceased bat (left) and of a lead target (right). Flat fielding has been performed on the bat radiograph. The pixels width is  $50\ \mu\text{m}$  and the exposure time is 60 s. The current of the X-ray tube is at 0.5 mA, the voltage at 20 kV and the X-ray energy spectrum is continuous, with a maximum energy at about 20 keV. The gas is an Argon/ $\text{CF}_4$  (80 %/20 %) gas mixture. The detector is operated at a gain of about  $10^4$  and at the maximum mesh transmission.

#### 6.1.4 . Deconvolution

Offline image processing consists in improving the image quality with mathematical tools, like filters that treat the image noise or blurring. For example, it allows to compensate for the degradation of the image sharpness due to the electron diffusion or the lens' optical distortions. Median filters are particularly effective to remove the salt-and-pepper noise of digital images. On the other hand, Kernel filters are based on the convolution operation between the signal image and a simple matrix, usually of dimension  $3 \times 3$ , which has many applications depending on the kernel matrix. It is mostly used to sharpen or blur an image, similarly to the moving average method, which improves the SNR of the image. However, one of the most powerful method to improve the precision of an image is the deconvolution, largely used in astronomy. Deconvolution is an operation that estimates the imager' signal without its deterioration due to physical effects. In other words, given  $y$  the output signal of the imager:

$$y = \text{PSF} * x \quad (6.4)$$

with  $x$  the input signal to the imager and the Point Spread Function (PSF) of the imager. The output signal is indeed a convolution of the input signal (the ideal radiograph without any blurring) and the impulse response of the detector (PSF), which contains only the blurring signal involved by the physical effects taking place in the imager. The goal of the deconvolution is to recover the signal  $x$ . Several algorithms providing an estimation of  $x$  exist, although the Richardson–Lucy algorithm [81] is one of the most efficient. The Richardson–Lucy algorithm relies on the linearity of the system, meaning that the intensity signal from two separated objects, imaged simultaneously, could be decomposed as the sum of the two individual object signals, because of non-interacting property of photons with each other. Thus, the relation (6.4) can be rewritten for each pixel as

$$y_i = \sum_j P_{i,j} x_j \quad (6.5)$$

where  $y_i$  is the intensity of the detection pixel  $i$ ,  $x_j$  is the intensity of the input pixel  $j$  and  $P_{i,j}$  is the fraction of light from the source pixel  $j$  that is detected in pixel  $i$ , which is directly related to the PSF. This algorithm offers an iterative solution to compute an estimation  $\hat{x}_j$  of the input pixel intensity  $x_j$  given by (6.6), where  $t$  is the number of iterations.

$$\hat{x}_j^{t+1} = \hat{x}_j^t \sum_i \frac{y_i}{c_i} P_{i,j}, \quad c_i = \sum_j P_{i,j} \hat{x}_j^t \quad (6.6)$$

In comparison to other filters, this method requires to measure the response of the detector to a point-like source. The detector's PSF has been measured at a synchrotron facility in the same conditions, with an X-ray beam of dimension smaller than a pixel. The measurement of the PSF will be described in detail in this thesis in Sec. 6.2. The deconvolution method has been applied on the radiographs of the bat and the lead target as shown in Figure 6.5. Although the X-rays flux and energy are not identical but similar between the radiography and PSF measurements, the camera, lens and detector settings are the same.

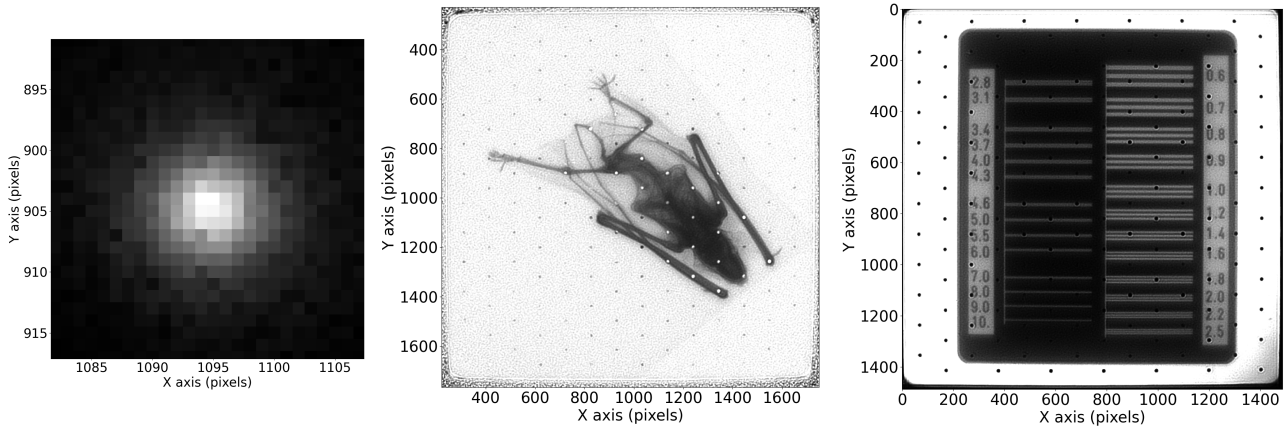


Figure 6.5: PSF of the detector measured at the SOLEIL synchrotron with a  $20 \times 20 \mu\text{m}^2$  wide 6 keV X-rays beam (left). Radiographs of the bat (middle) and of a lead target (right) using the Richardson–Lucy deconvolution algorithm with 130 iterations. The PSF has been normalized and cropped to a matrix of about  $30 \times 30 \text{ pixels}^2$ . The detector is operated at a gain of about  $10^4$  and at the maximum mesh transmission.

A clear improvement of the bat's radiography sharpness is observed, revealing more details of the bones' structure of the animal. The deconvolved lead target image also shows a better contrast between the lines, and leads to an improvement of the spatial resolution. The spatial resolution has been computed following the method described in Sec. 8.4.3 for different numbers of iteration. The Figure 6.6 represents the evolution of the spatial resolution as a function of the number of iterations. After 100 iterations, the spatial resolution has improved by about 60 % and stagnates at larger iteration numbers.

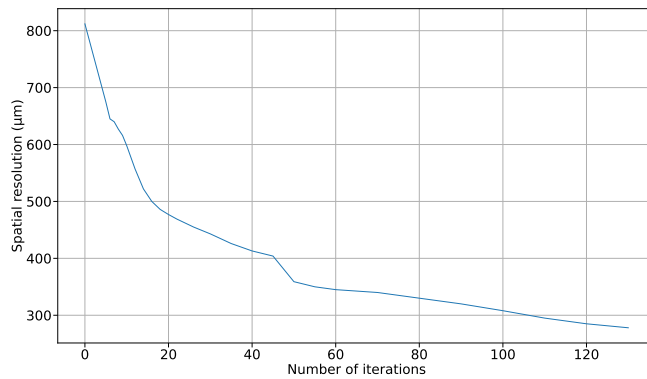


Figure 6.6: Plot of the spatial resolution as a function of the number of iterations of the Richardson–Lucy algorithm. The resolution rapidly improves at small number of iterations and the improvement slows down at large values.

## 6.2 . Measurements at the SOLEIL synchrotron

The profile of the scintillating response of the glass Micromegas detector has been thoroughly studied under X-ray illumination in [82]. To further characterize the glass Micromegas detector in terms of spatial resolution, a test at the SOLEIL synchrotron (Optimized Source of LURE Intermediary Energy Ligh) facility [83] was performed. At the Metrology beamline [84], a beam of hard X-rays of small divergence and high flux is provided. The aim of this experiment is to study the response of the glass Micromegas imaging system to a point like source. A collimation of the beam to a square shape down to 20  $\mu\text{m}$  by side allows to capture the Point Spread Function (PSF) of our device. The PSF basically gives the quality of the imaging system and is widely used in other fields like astronomy [67], microscopy or medical imaging. This measurement is also a means of comparing the spatial resolution of the system for different parameters, like the electron diffusion in the Micromegas detector or optics settings.

The PSF measurement allows to identify the different contributions to the blurring of the row images and to study how the different detector's settings affect the spatial resolution. During these tests, four main contributions to the PSF have been identified and are classified in two categories:

### 1. Electron diffusion and range in gas:

- The mean free path of photoelectrons in gas involves a broadening of the signal because the gas is being ionized away from the beam axis. Depending on the X-ray photon energy, the photoelectron range can reach several tens to hundreds of micrometers (Sec. 2.1).
- The electron diffusion spreads the secondary electrons transversally to their drift direction while they drift towards the mesh. This effect is described in Sec. 3.1.2 and depends mainly on the drift gap thickness and the drift field.

### 2. Visible light optical effects

- The response of an optical lens involves complex mechanisms explained in Sec. 4.5, such as optical aberrations. This produces a blurring of the light transmitted to the camera sensor, which depends on the lens fabrication properties and settings.
- The light being emitted isotropically from the avalanche, it is contained in the leak tight chamber and is reflected on the surfaces. Because the mesh is at few tens of microns from the avalanche, being made of shiny stainless-steel, it reflects back stray light to the sensor.

Mesh type	Standard / Beta
Drift gap	2 mm / 4mm
Lens magnification	0.1 / 1
Lens aperture ( $f/\#$ )	0.95 / 1.4 / 2.8
Camera (Read noise)	ORCA Quest (0.27 $e^-$ ) / Retiga (5.7 $e^-$ )
Beam energy	From 6 keV to 28 keV
Drift field	From 100V/cm to 2700 V/cm
Optical component	90° mirror / straight optical axis

Table 6.1: Summary table of the different configurations tested with the Micromegas set-up. While one of these parameters changes, the other settings are fixed to nominal values: beta mesh, 2 mm drift gap, 0.1 lens magnification,  $f/1.4$  lens aperture, ORCA Quest camera, 6 keV beam energy, 350 V/cm drift field, straight optical axis.

These contributions to the PSF derive from the Micromegas detector properties as well as the electric fields in the detector, the optical components and the X-ray beam. In the following study,

different glass Micromegas detectors with a beta mesh and a standard mesh (Sec. 5.1) are compared along with a  $75\ \mu\text{m}$  and  $128\ \mu\text{m}$  amplification gap respectively. Two drift gap lengths of 2 mm and 4 mm are tested. Several gain values from  $10^2$  to  $3 \times 10^3$  and drift fields from 100 V/cm to 2700 V/cm are tested. Regarding the optical components, two different lenses of magnification 0.1 and 1 are being used and different lens apertures from  $f/0.95$  to  $f/2.8$  are evaluated. The influence of a mirror on the optical axis is investigated as well. The performances of different cameras were compared, assessing the influence of the read noise on the signal sharpness. Finally, the beam size is tunable from  $20 \times 20\ \mu\text{m}^2$  to  $1 \times 1\ \text{mm}^2$  and it is possible to move the detector to adjust the beam position on the detector. A gas mixture of Argon/ $\text{CF}_4$  (90%/10%) has been used for all the measurements presented in this section, at atmospheric temperature. The different set-up configurations are summarized in Table 6.1.

### 6.2.1 . The SOLEIL synchrotron and set-up description

The SOLEIL synchrotron is a research center located in Saclay (France) consisting of 28 beamlines that provide light by synchrotron radiation (Sec.2.1.2). The synchrotron includes several parts described in Figure 6.7, which lead to a final electron beam of 2.75 GeV and to the production of synchrotron radiation. At the Metrology beamline [83], a bending magnet deviates the electrons which produces synchrotron light of tangential direction to the electron beam. The beamline then provides photons with a wide range of monochromatic energies, from 35 eV to 38 keV. The beam is tuned by different elements shown in Figure 6.8. The beam is shaped to a desired dimension down to  $20\ \mu\text{m}$  by side, by collimating slits. Ideal beam parallelism is obtained thanks to focusing mirrors and to the distance between the bending magnet and Micromegas detector of several tens of metres. A monochromator tunes the beam energy and attenuators reduce the beam flux.

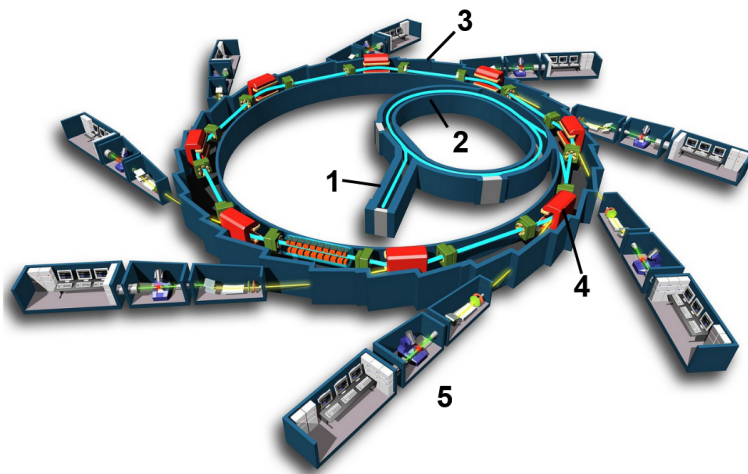


Figure 6.7: Synchrotron description scheme. 1) Electrons are first produced by an electron gun and accelerated by a Linear particle Accelerator (LINAC) to 100 MeV. 2) The electrons are conducted to the booster where they are accelerated to an energy of 2.75 GeV and focused to a RMS beam size of  $60 \times 25\ \mu\text{m}^2$ . 3) When they reach the nominal energy, they are injected in the storage ring of 354 m of circumference, and stored for several hours. 4) At the entrance of the beamlines, the beam is deviated by bending magnets and synchrotron radiation is produced. Other magnetic devices like undulators or wigglers make the electron to oscillate and produce synchrotron light. 5) The light is guided through mirrors, collimators and monochromators to the experimental area where measurements take place. Extracted from [85].

The detector is located as close as possible to the beam pipe exit (Figure 6.10 and Figure 6.9), at 1 m, to minimize the amount of photons being absorbed by the air before reaching the detector. A beam flux of  $9.43 \times 10^9\ \text{ph/s/mm}^2$  has been measured with a photodiode placed at the detector position, for a 6 keV beam.

The slits in front of the detector define the beam dimensions and must be calibrated to precisely

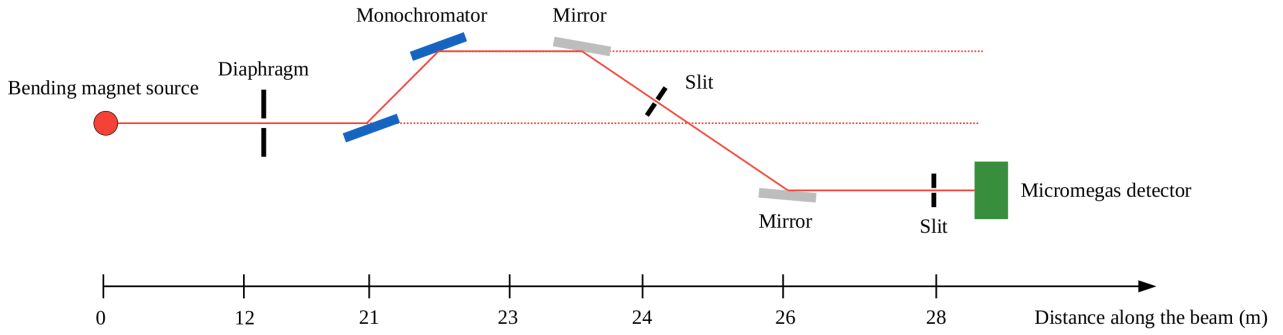


Figure 6.8: Scheme of the Metrology beamline, adapted from [84]. The experiment takes place where the focused monochromatic beam is (solid red line). The beam energy is tuned by the monochromator, focused by focusing mirrors and collimated by  $x$  and  $y$  slits. The red dotted lines represent other beamlines.

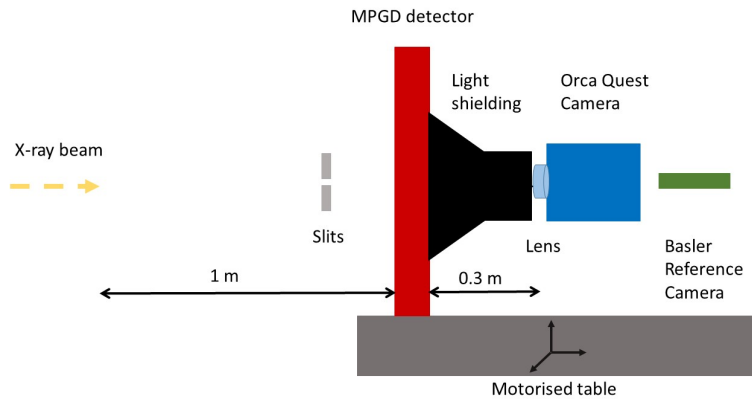


Figure 6.9: Sketch of the experimental set-up at the Metrology beamline.

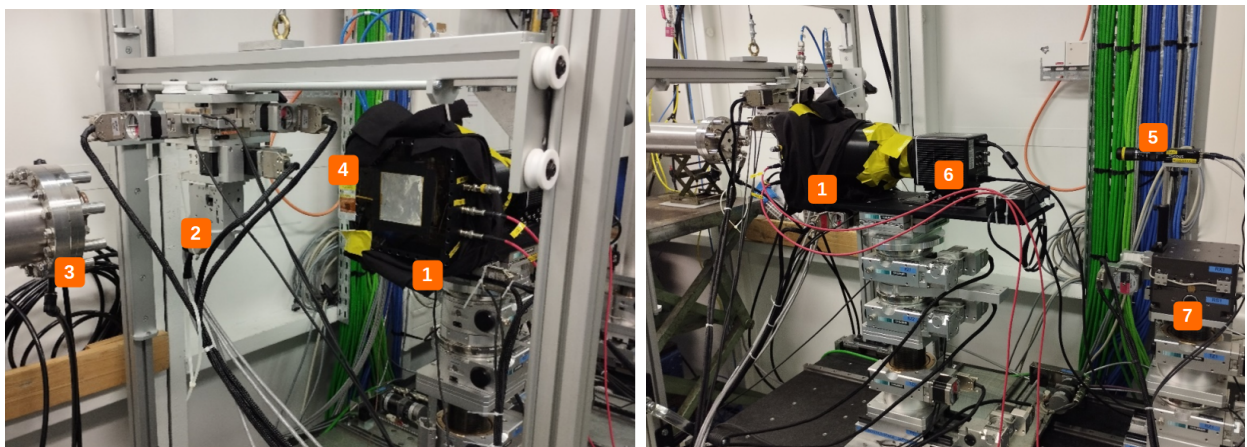


Figure 6.10: Picture of the experimental set-up at the SOLEIL synchrotron. 1) Micromegas detector 2) Vertical and horizontal slits 3) Beampipe window 4) photodiode 5) Basler camera 6) qCMOS camera 7) Moving table in X and Z axis.

assess the X-rays beam shape sent to the imaging system. A Basler camera [86], situated behind the detector, displays the 2D profile of the beam. The Basler camera includes  $1296 \times 966$  pixels of dimension  $3.75 \times 3.75 \mu\text{m}^2$ . Combining the camera with a lens of magnification of 2 and a scintillating crystal, the camera displays the beam with a  $1.88 \times 1.88 \mu\text{m}^2$  granularity. As shown on Figure 6.11 (left), for 6 keV hard X-rays, a very thin beam was captured with the Basler camera. With a simple Gaussian fit in the 2 dimensions, a FWHM of  $17 \mu\text{m}$  was measured. Since the granularity of the glass Micromegas imaging device is about  $50 \mu\text{m}$ , the beam input signal is viewed as a Dirac function of the dimension of a point.

The monochromator represents a key element of the beamline as it converts the white beam into a monochromatic beam of tunable energy. It is made of two parallel Si (111) crystals. The orientation angle  $\theta$  of the top crystal, which determines the parallelism, is adjustable with a precision of at least  $0.05 \mu\text{rad}$ . Due to diffraction, the light angle of emission from the crystal depends on its energy and tuning the parallelism of the crystals allows to refine the spectral purity of the beam. The Figure 6.11 (right) shows a Rocking Curve (RC) for a 5 keV beam, which is the measurement of the beam intensity while detuning the monochromator. At the maximum of the RC, the crystals are perfectly parallel and harmonics of much higher energy are produced with a contribution of about 10%. Detuning the crystals by  $0.05 \mu\text{rad}$  moves the high-order harmonics contribution down to less than 3% [84]. The spectral purity of the beam is a key parameter for this experiment since the signal blurring depends on the photoelectron range, which is a function of the X-rays energy.

In the next sections, the measurements performed at the Metrology beamline of the SOLEIL synchrotron are shown and described in detail.

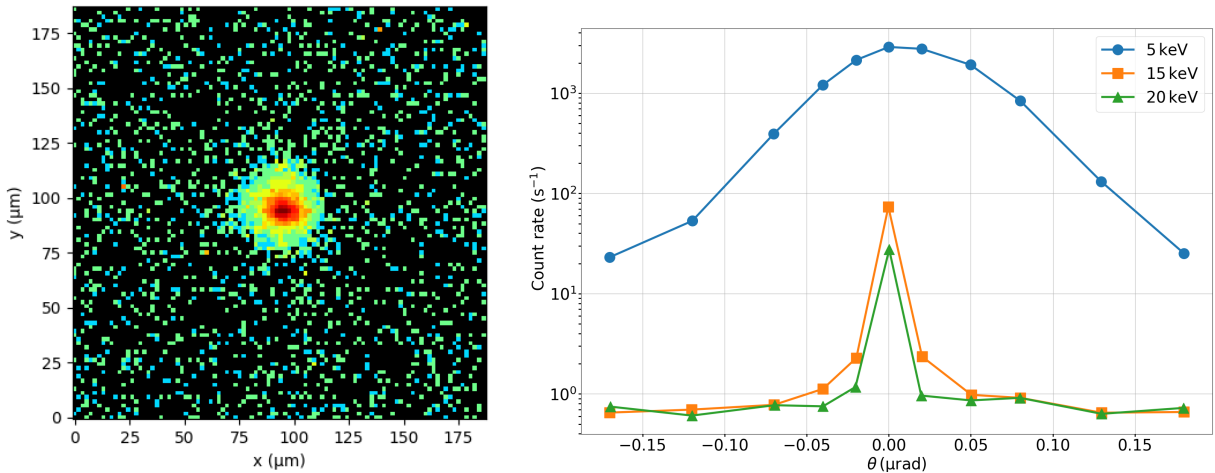


Figure 6.11: Basler camera pixel intensity frame for a 6 keV X-rays beam (left). Rocking curve for a 5 keV beam (right), extracted from [84]. The main beam energy contribution at 5 keV as well as the high-order harmonics at 10 keV and 15 keV are displayed.

### 6.2.2 . Glass Micromegas signal uniformity

The detector uniformity is the first aspect to be studied. To do so, the PSF was measured at different positions of the active area. In total, 9 positions spaced by 2 cm were picked following a square pattern of coordinates  $u v$  with  $u$  and  $v$  the line and column number respectively. The 9 beam positions on the detector are illustrated in Figure 6.12. In the first instance, the lens aperture is set to  $f/0.95$ . For each position, 5 s exposure time frames are acquired for a total of 1 min and processed through the procedure described in Sec. 5.4.1. In this set of measurements, four different drift fields are tested to study the effect of the mesh transmission on the light signal. The detector light intensity response is first evaluated by summing the total light signal. As shown on Figure 6.13, the light intensity follows a common trend for the different beam positions.

The drop of the overall light signal at the highest drift field is due to the drop of mesh transparency

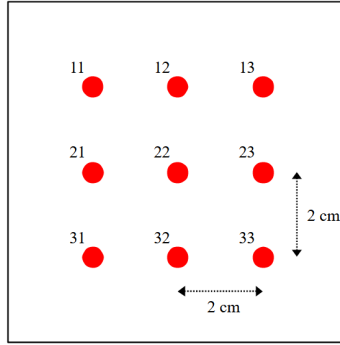


Figure 6.12: Beam positions on the detector. The red spots represent the beam and their coordinates are shown. The distance between the positions is 2 cm.

at high field ratio, as explained in Sec. 3.3.2. The Root Mean Square Percentage Error (RMSPE) [87] of the light signal among the different positions is shown in Figure 6.13. The RMSPE is obtained by the formula:

$$\text{RMSPE} = \sqrt{\frac{1}{N} \sum_i^N \left( \frac{S_i - \mu}{\mu} \right)^2} \cdot 100\% \quad (6.7)$$

where  $S_i$ ,  $\mu$  and  $N$  are the light intensity at the position  $i$ , the average light intensity and the number of positions respectively. The detector presents a RMSPE lower than 10 % meaning that the detector light intensity signal is uniform in space. Similar uniformity has been computed with large area standard Micromegas detectors according [88, 89]. It also confirms the homogeneity of the gain map showed in Figure 5.6. The drift field does not substantially impact the evenness of the light intensity response while it is shown later in this chapter that the electron diffusion, function of the drift field, is characteristic of the signal spreading.

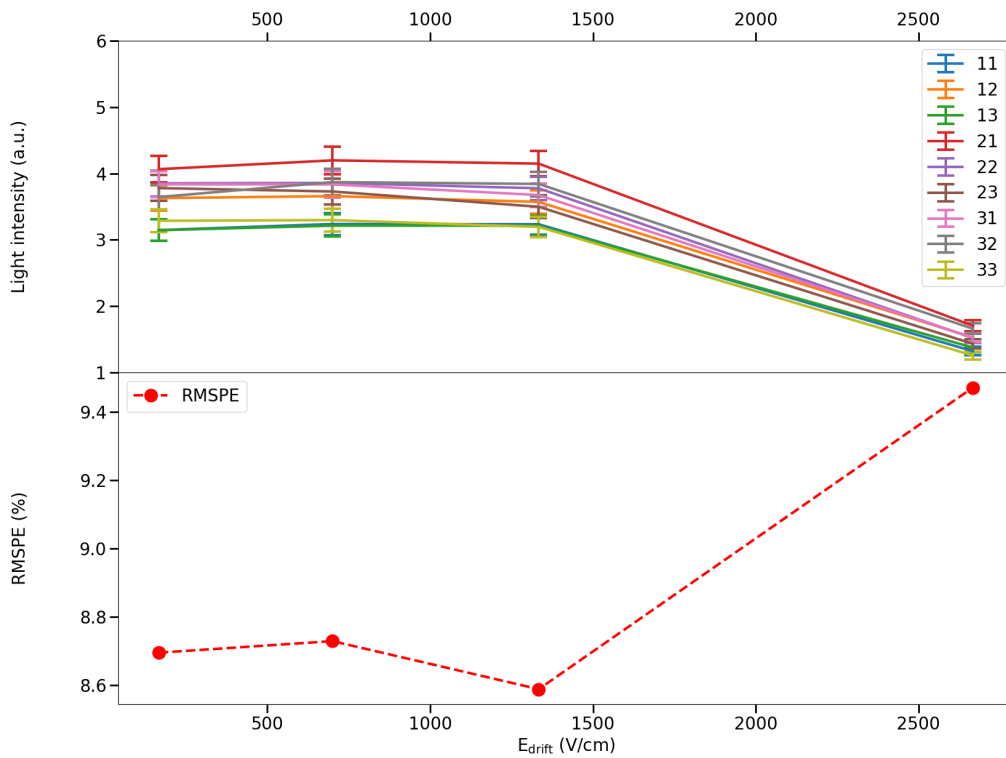


Figure 6.13: Total light intensity signal at different beam positions versus the drift field (top). Light intensity Root Mean Square Percentage Error (RMSPE) among the 9 beam positions as a function of the drift field (bottom). The light intensity signal shows a uniformity better than 10% among the detector active zone. The Micromegas detector is equipped with the beta mesh, the lens aperture is set to  $f/0.95$ , the beam energy is 6 keV and the amplification field is 43 kV/cm.



### 6.2.3 . Optical aberrations

As a second step, the shape of the PSF has been studied for different beam positions with a beta mesh glass Micromegas detector. As shown on Figure 6.14, the response to the beam spot shows a different profile depending on the image space. In fact, the signal shows a blur directed away from the optical axis. In other words, this deformation presents an axial symmetry with respect to the optical axis. This phenomenon is known as the Coma lens aberration which grows quadratically with the distance of the source from the optical axis, as explained in Sec. 4.5. The light intensity scale in Figure 6.14 is logarithmic, allowing to visualize the total light response, while there are several order of magnitude between the center of the PSF and the borders. Figure 6.14 (center) illustrates the ratio of light recorded at different distances from the center of the PSF profile. It shows that about 80 % of the total light amount is being recorded within a radius of 600  $\mu\text{m}$  around the beam center.

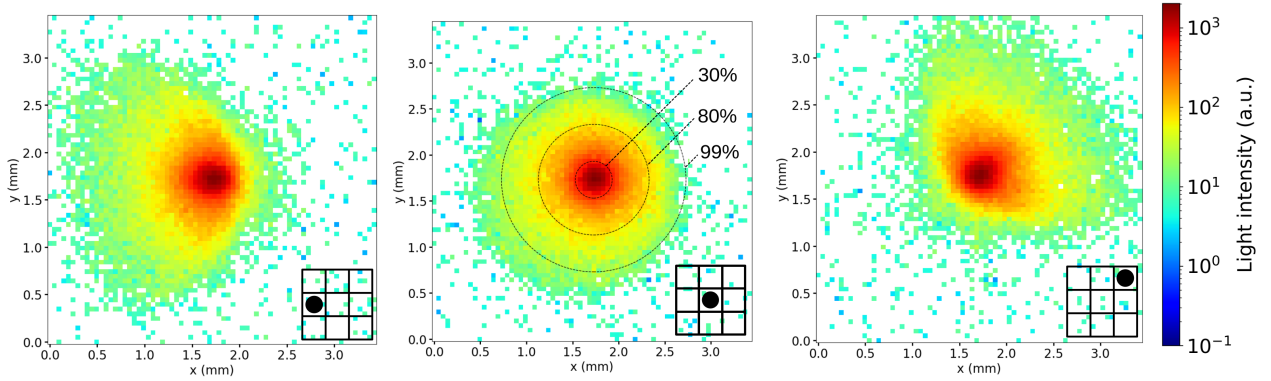


Figure 6.14: 2D profiles of a point-like beam located at the center left "21" (left), center "22" (middle) and top right "13" (right) of the image plane. Percentage of the total light amount among several distances from the beam axis (center). The Micromegas detector is equipped with the beta mesh, the lens aperture is  $f/0.95$ , the beam energy is at 6 keV, the drift field is 350 V/cm and the amplification field is 47 kV/cm. The colour scale is logarithmic. The optical aberrations with an asymmetric shape are visible.

A first method has been developed to extract the spatial resolution from the PSF and to be able to compare PSF profiles between configurations. One can extract the vertical and horizontal 1D profiles of the previous images and perform an appropriate fit. As shown on Figure 6.15, the horizontal 1D profile shows a Gaussian shape with an asymmetric component characteristic of the aberration. This asymmetry can be fitted by another Gaussian distribution shifted from the first one. Hence, the 1D distributions are fitted by the function  $f$  detailed in equation (6.8) where  $\mu_1$ ,  $\mu_2$ ,  $\sigma_1$  and  $\sigma_2$  are the mean and the standard deviation values and  $c$  the ratio between the amplitudes of the two Gaussian functions. The spatial resolution is generally related to the standard deviation of a distribution, which is expressed by the formula (6.9) for a distribution following a sum of  $N$  Gaussian functions. In the current situation, a simple distribution with  $N = 2$  is chosen and described in equation (6.10).

$$f = A \cdot \left( c \cdot \exp\left(-\frac{(x - \mu_1)^2}{2 \cdot \sigma_1^2}\right) + (1 - c) \cdot \exp\left(-\frac{(x - \mu_2)^2}{2 \cdot \sigma_2^2}\right) \right) \quad (6.8)$$

$$\sigma^2 = \sum_{i=1}^N c_i^2 \cdot \sigma_i^2 + \sum_{i=1}^{N-1} \sum_{j=i+1}^N c_i \cdot c_j \cdot (\sigma_i^2 + \sigma_j^2 + (\mu_i - \mu_j)^2) \quad (6.9)$$

$$\sigma_{Final}^2 = c \cdot \sigma_1^2 + (1 - c) \cdot \sigma_2^2 + c \cdot (1 - c) \cdot (\sigma_1^2 + \sigma_2^2 + (\mu_1 - \mu_2)^2) \quad (6.10)$$

The asymmetry and the Coma aberration are mainly driven by the lens aperture as shown in Sec. 4.5 and on Figure 5.24. The PSF has been measured at three different lens aperture values in order to assess the impact of the aperture value on the spatial resolution. The average of the

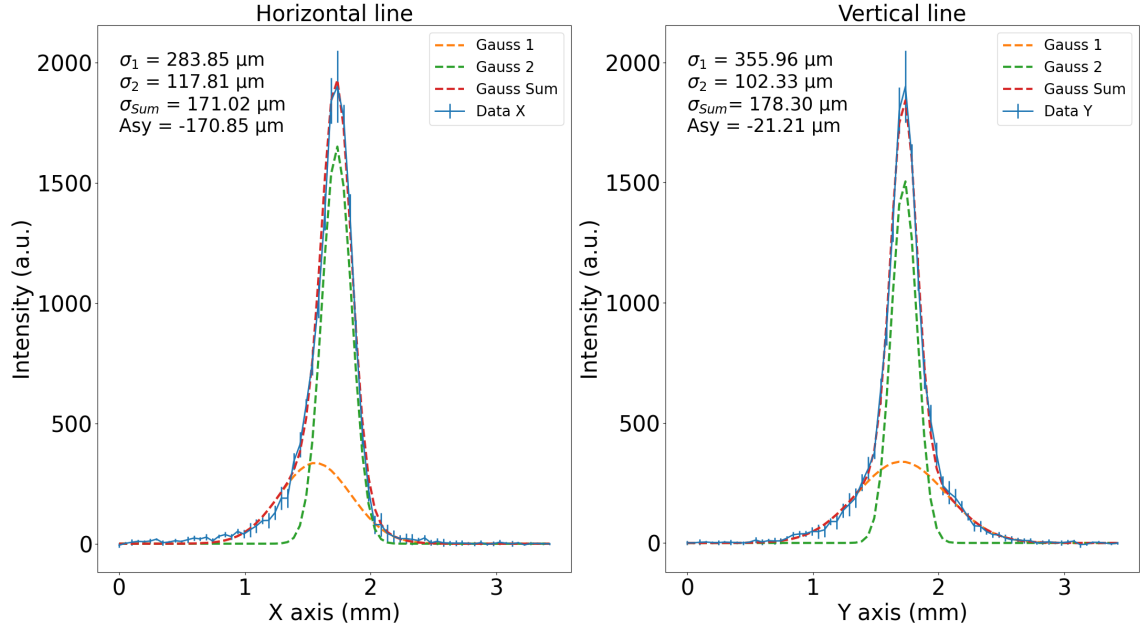


Figure 6.15: 1D horizontal and vertical lines profiles of the PSF displayed in Figure 6.14 at the position 21 (center left beam position). On the horizontal profile (left), the Gaussian distribution 1 (orange line) is shifted to the second one (green line). This shift is implemented in the variable  $Asy$  which is the different between the first and the second distributions' mean values. The Micromegas detector is equipped with the beta mesh, the lens aperture is  $f/0.95$ , the beam energy is at 6 keV, the drift field is 350 V/cm and the amplification field is 47 kV/cm.

standard deviations ( $\sigma_{Final}$ ) of the horizontal and vertical profiles is displayed on Figure 6.16 (top) for three different beam positions on the detector. The  $\sigma_{Final}$  value is decreasing at larger f-number and remains almost unchanged for different beam locations. By decreasing the aperture size, the marginal photons are not interacting with the lens periphery. Light rays are then crossing the lens only in its central part, where aberrations are less pronounced (Sec. 4.5). This result shows the influence of the lens aperture on the signal spreading, decreasing by about 37% for apertures from 0.95 to 2.8. While the shape of the aberrations depends on the beam position, it has almost no impact on the overall signal spreading. Increasing the aperture also decreases the light intensity, following a  $\frac{1}{(f/\#)^2}$  distribution (Sec. 4.4), as shown in Figure 6.16 (bottom).

#### 6.2.4 . Light reflection

The noise induced by the scintillation light reflection was found to be of significant contribution to the reconstructed image when integrating a large amount of light on the camera sensor. To minimize reflections, the most internal components of the leak tight chamber have been covered by a black mat layer, like the cathode, as explained in Sec. 6.1.2. The mesh being behind the avalanche from the point of view of the camera, it reflects back stray light that is emitted isotropically from the avalanche. Even if the mesh is made of shiny stainless steel, this reflection has been observed only with large X-ray flux and large detector gain, when the amount of statistics is sufficient to see this effect, which is about 2 orders of magnitude lower than the main central light signal. Figure 6.17 shows PSF profiles with a beta and a standard mesh in high amplification field conditions. It is clear that the reflection pattern is correlated to the mesh geometry (Sec. 5.1), recording a signal with a hexagonal-like shape for the beta mesh and a cross-like shape for the standard mesh.

In conclusion, in large aperture conditions, the aberrations are dominating any signal spreading contributions and involve a position dependant blur. However, at large amount of light accumulated in the camera sensor (high detector gain and large amount of statistics), the signal blurring is characteristic of the mesh reflection. In both cases, the PSF shows an asymmetry by revolution.

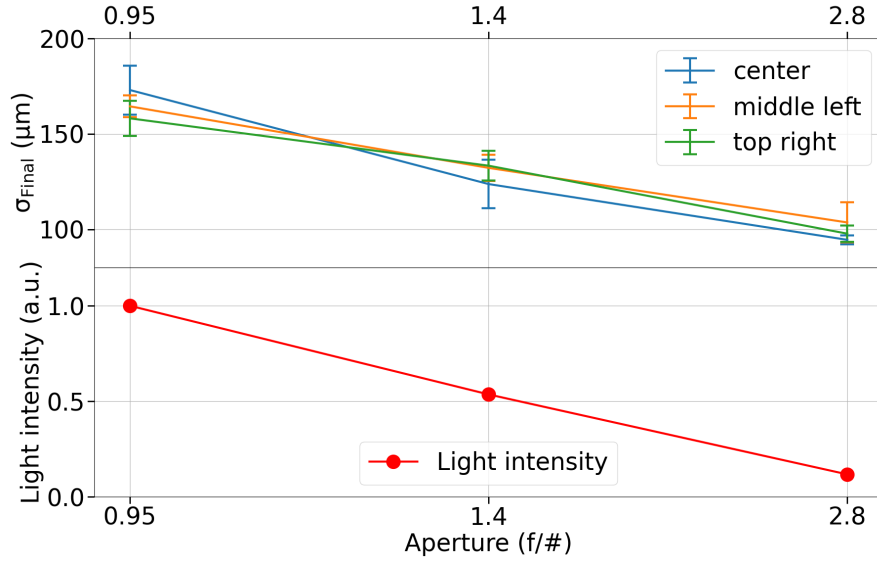


Figure 6.16: Standard deviation (top) extracted from the fit of the PSF shown in Figure 6.15 where  $\sigma_{Final}$  stands for the average of the vertical and horizontal standard deviations described in (6.10).  $\sigma_{Final}$  decreases with the lens aperture size. Total light intensity (bottom) that varies in  $\frac{1}{(f/\#)^2}$  with  $f/\#$  the aperture. The lens aperture values  $f/0.95$ ,  $f/1.4$ , and  $f/2.8$  are tested for three beam positions. The Micromegas detector is equipped with the beta mesh, the beam energy is at 6 keV, the drift field is 350 V/cm and the amplification field is 47 kV/cm.

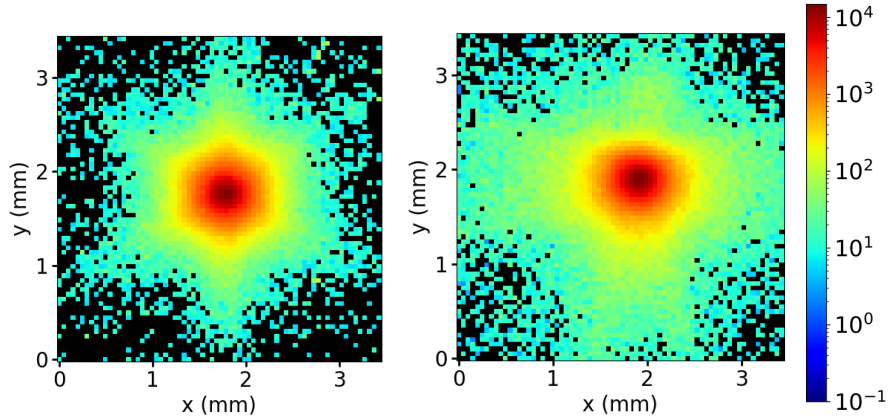


Figure 6.17: 2D profiles with a standard mesh (left) and a beta mesh (right). The detector is irradiated with a point-like beam source in the center of the image space. The amplification field is 59 kV/cm with the beta mesh where the amplification gap is 75  $\mu\text{m}$  thick, and 41 kV/cm with the standard mesh where the gap is 128  $\mu\text{m}$  thick. The lens aperture is  $f/1.4$ , the drift field is 350 V/cm and the beam energy is at 6 keV. The colour scale is logarithmic. Different reflection patterns are observed depending on the mesh geometry.

### 6.2.5 . PSF 2D modelization

In the following study, a new approach has been chosen to characterize the PSF based on a two dimensional fit of the overall beam signal rather than one dimensional fits on slice profiles. A 2D model is indeed more reliable since the fitted PSF profile shows an axial asymmetry, due to reflections and aberrations.

The establishment of an explicit model is a prior condition to fit the beam signal. This task is well known in astrophysics and has been greatly studied for stellar images of point sources at an infinite distance, registered by a telescope coupled with a CCD device [90]. However, in the present study, the source is extended, at a finite distance from the optical system and surrounded by reflecting surfaces, which involves more blurring than stellar imaging. The light reflection and aberration are described by complex models that depend on the source position, the detector and lens geometry. On the other hand, the particle range and charge diffusion in the gas are well known mechanisms that can be simulated without further difficulty.

The PSF is the consequence of these different contributions, which are adding up by a convolution operation. One way to illustrate the convolution operation is depicted in Figure 6.18. It is described by the following mechanism: the positions of the secondary electrons produced in the conversion gap by ionization are determined by the multiple scattering trajectory of the primary electrons (particle range contribution). Each secondary electron then diffuses transversally during their drift towards the mesh. Their final position results in the convolution of both their range and diffusion distributions. Scintillation light is produced at the location where these secondary electrons are ionizing the gas during the avalanche multiplication process. The light signal is further spread out by reflections, and optical aberration mechanisms into the lens. Hence, the 2D profile of the PSF is described by the expression (6.11) where  $f_R$ ,  $f_D$ ,  $f_L$  and  $f_A$  are the distributions describing the electron range, the electron diffusion, the light reflection and the optical aberration contributions respectively. Since the standard deviations of convolved functions that are independent add up quadratically, the standard deviation of the PSF is given by the formula (6.12).

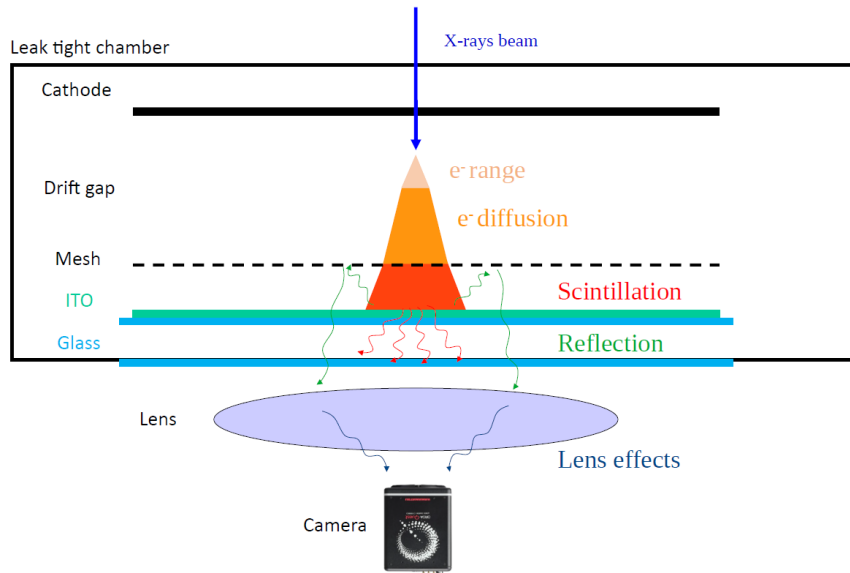


Figure 6.18: Signal's spreading mechanisms in the glass Micromegas detector during SOLEIL synchrotron test campaign. The different contributions to the PSF are illustrated: the electron range (beige colour), the diffusion (orange colour), the light reflection (green arrows) and the lens optical effects (blue arrows).

$$\text{PSF}(x, y) = f_R * f_D * f_L * f_A (x, y) \quad (6.11)$$

$$\sigma_{\text{PSF}} = \sqrt{\sigma_R^2 + \sigma_D^2 + \sigma_L^2 + \sigma_A^2} \quad (6.12)$$

Rather than modeling all the contributions and computing their convolution, PSFs are ordinarily fitted with well-known functions that provide a fair representation of an impulse response [67]. Among these models, the Gaussian distribution, the Moffat distribution (6.13) and the Lorentzian distribution (6.13) ( $\beta = 1$ ) have been implemented to fit the PSF. Moffat distributions are especially well suited for PSF fitting as they are sharply peaked and have heavier wings than Gaussian distributions, providing a better description of the light dispersion away from the center. While their mathematical expression is simple, the additional parameter  $\beta$  grants better versatility. The sum of two Gaussian distributions has also been implemented (6.14) as it is a good representation of the optical aberration in the 1D case (Figure 6.15).  $\mu_x, \mu_y, \sigma_x$  and  $\sigma_y$ , are the distributions mean and standard deviation values on the horizontal and vertical axes respectively. These variables have the indexes 1 and 2 for the first and second Gaussian distributions in the expression (6.14).  $A$  is the amplitude of the function and  $c$  is the ratio between the two Gaussian distributions.

$$\text{Moffat}(x, y) = \frac{A}{\pi\sigma_x\sigma_y} \left( 1 + \left( \frac{x - \mu_x}{\sigma_x} \right)^2 + \left( \frac{y - \mu_y}{\sigma_y} \right)^2 \right)^{-\beta} \quad (6.13)$$

$$\text{GaussSum}(x, y) = A \cdot c \cdot e^{-\left(\frac{x - \mu_{x1}}{\sigma_{x1}}\right)^2} e^{-\left(\frac{y - \mu_{y1}}{\sigma_{y1}}\right)^2} + A \cdot (1 - c) \cdot e^{-\left(\frac{x - \mu_{x2}}{\sigma_{x2}}\right)^2} e^{-\left(\frac{y - \mu_{y2}}{\sigma_{y2}}\right)^2} \quad (6.14)$$

The beam signal, the different models' 2D distributions and the residuals of the fit are displayed in Figure 6.19. The lens aperture is set at  $f/1.4$  while the amplification and drift fields are settled to 47 kV/cm and 350 V/cm respectively. The fit is evaluated by the  $\chi^2$  test and by the residuals profile. Reduced  $\chi^2$  values of about 0.3 were obtained for the simple Gaussian and Lorentzian distributions while the Moffat and double Gaussian distributions achieved  $\chi^2$  values of about 0.15. According to the residuals maps, the double Gaussian distribution shows a lower dispersion from the PSF. A standard deviation of  $135 \pm 1.58 \mu\text{m}$  was measured with the double Gaussian model using the relation (6.10).

### 6.2.6 . Comparison of the blurring contributions and electron diffusion

Aiming at correcting the light aberration contribution, PSFs were first compared using different lens' apertures. When operating in the same conditions (beams size, energy and flux are identical,  $E_{\text{Drift}} = 350 \text{ V/cm}$ ,  $E_{\text{Amp}} = 47 \text{ kV/cm}$ ) with a smaller lens aperture of  $f/2.8$ , the signal is much sharper, measuring a standard deviation of  $108 \pm 2.8 \mu\text{m}$ , in comparison to a lens aperture  $f/1.4$  ( $\sigma_{\text{PSF}} = 135 \pm 1.58 \mu\text{m}$ ). This difference shows the substantial contribution of the aberrations at a  $f/1.4$  aperture (Figure 6.20).

It is assumed that at lens aperture of  $f/2.8$ , the aberration contribution is negligible (Sec. 5.3.2) and that  $\sigma_{f/2.8}$  contains all the signal spreading contributions, except the lens aberration. Knowing that the standard deviation values of convolved distributions add up quadratically, one can express the standard deviation issued from the lens effects at  $f/1.4$  as  $\sigma_A^2 = \sigma_{f/1.4}^2 - \sigma_{f/2.8}^2$  with  $\sigma_{f/1.4}$  and  $\sigma_{f/2.8}$  the total measured standard deviations at lens apertures of  $f/1.4$  and  $f/2.8$  respectively. In the current conditions, with a lens aperture of  $f/1.4$ , a value  $\sigma_A = 81 \pm 2.3 \mu\text{m}$  has been derived.

As described in Sec. 3.1.2, the electron diffusion strongly depends on the electric drift field. To evaluate the influence of the diffusion on the signal blurring, the PSF has been measured for different drift field values. In Figure 6.21, the standard deviation is extracted from the PSF fit for five different drift fields, from 100 V/cm to 1000 V/cm, at an amplification field of 47 kV/cm, for a lens aperture of  $f/1.4$  and a beam energy at 6 keV. The aberration contribution is also corrected so that  $\sigma^2 = \sigma_{f/1.4}^2 - \sigma_A^2$ . The diffusion has been simulated on Magboltz [11] as described in Sec. 6.2.8, for a 2 mm drift gap, and is also represented in this figure. The sigma value variation presents a trend characteristic of the simulated diffusion, with a minimum value around 350 V/cm. The diffusion standard deviation in

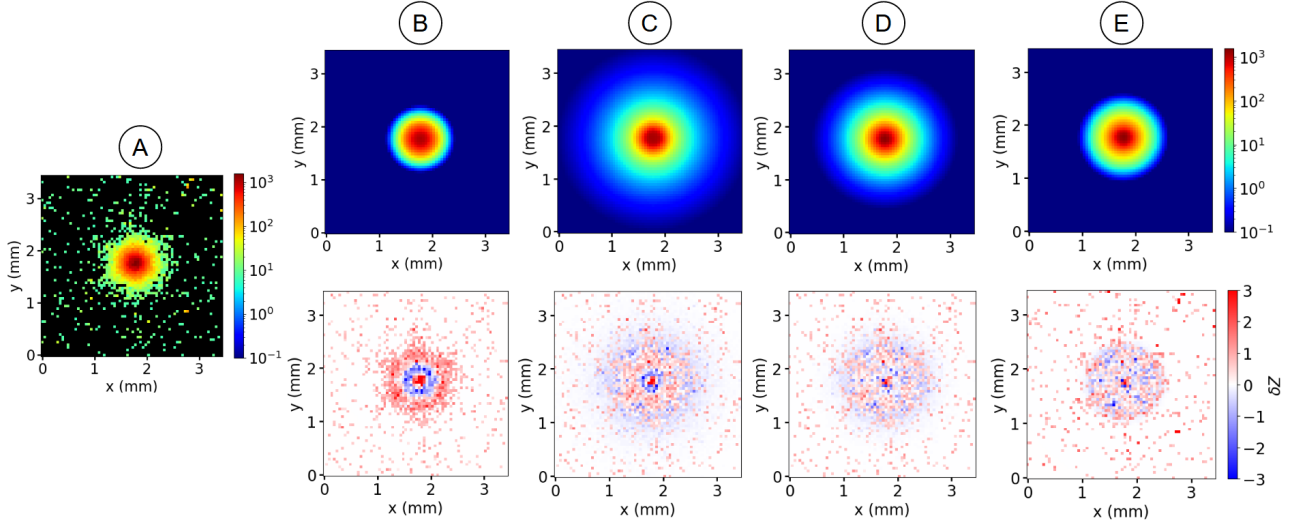


Figure 6.19: PSF of a point-like beam source in the center of the image space (A). The fitting models (top) are represented (the colour scale is logarithmic). The difference between the signal and the fit is represented (bottom) and the colour scale is normalized by the RMS of each pixels' intensity  $\delta Z$ . Single Gaussian distribution (B), Lorentzian distribution (C), Moffat distribution for  $\beta = 2.9$  (D) and double Gaussian distribution (E). The Micromegas detector is equipped with the beta mesh, the lens aperture is  $f/1.4$ , the beam energy is at 6 keV, the drift field is 350 V/cm and the amplification field is 47 kV/cm. The standard deviation extracted from the double Gaussian fit is  $135 \pm 1.58 \mu\text{m}$ .

the  $75 \mu\text{m}$  thick amplification gap at an electric field of 47 kV/cm is about  $15 \mu\text{m}$ . Since the diffusion contribution in the drift gap is much larger ( $\sigma_D^2 \gg 15^2 \mu\text{m}^2$ ), the diffusion in the amplification gap is negligible.

According to the equation (6.12), subtracting the aberration and diffusion contributions allows to extract the residual contributions stemming from the electron range and light reflection contributions, such that:

$$\sigma_{Res}^2 = \sigma_{PSF}^2 - \sigma_D^2 - \sigma_A^2 = \sigma_R^2 + \sigma_L^2 \quad (6.15)$$

From Figure 6.21, the quadratic subtraction between the standard deviation at a 2 mm drift gap thickness (corrected from the aberrations) and the simulated diffusion has been computed and averaged among the drift field values. A residual of  $\sigma_{Res} = 75.5 \pm 4.3 \mu\text{m}$  has been measured. At an amplification field of 47 kV/cm, the light intensity is relatively low and the reflection from the mesh are negligible compared to the other contributions. Thus, the assumption  $\sigma_{Res}^2 \approx \sigma_R^2$  is made in low gain conditions.

Finally, by calculating the ratio between the squared standard deviations of the three main contributions  $\sigma_R$ ,  $\sigma_D$  and  $\sigma_A$ , one can compute the average weight of each contribution for a lens aperture of  $f/1.4$ , a drift gap thickness of 2 mm, a 6 keV X-rays beam and an amplification field 47 kV/cm. While the aberration contribution is 36 %, similar contributions of 32 % was computed for the electron range and electron diffusion.

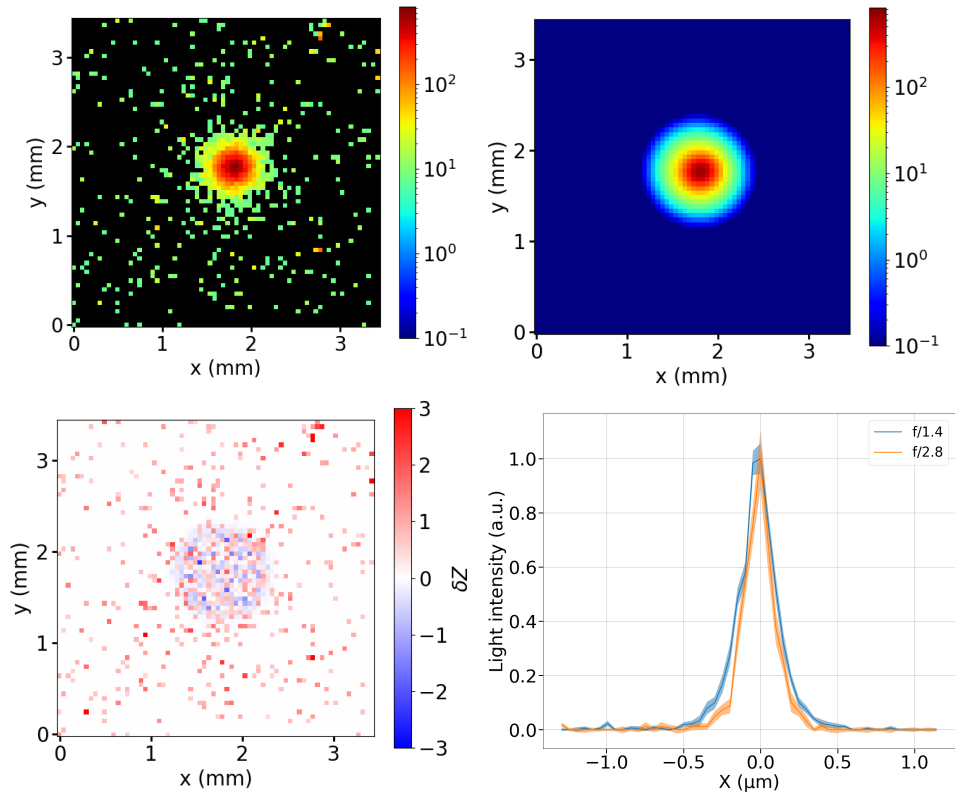


Figure 6.20: PSF of a point-like beam source in the center of the image space. The settings are identical to the previous figure but the lens aperture is  $f/2.8$ , minimizing the optical aberrations. The raw beam signal (top left) and the fitting model (top right) are represented (the colour scale is logarithmic). The difference between the signal and the fit is represented (bottom left) and the colour scale is normalized by the pixels intensity error. The standard deviation extracted from the fit is  $108 \pm 2.8 \mu\text{m}$ . 1D intensity line profiles (bottom right) for lens apertures at  $f/1.4$  and  $f/2.8$  are represented for better visualization. The profiles are normalized and centered.

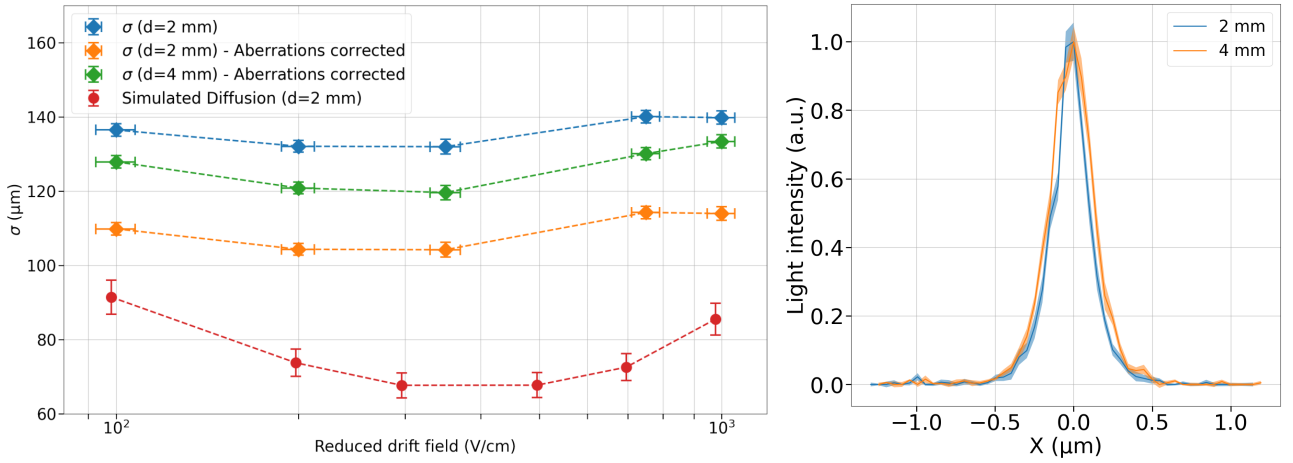


Figure 6.21: Left: Distribution among five drift field values of the extracted standard deviation from the fit for a 2 mm drift gap thickness (orange markers) and 4 mm drift gap thickness (green markers). The optical aberrations have been corrected such that  $\sigma^2 = \sigma_{f/1.4}^2 - \sigma_A^2$  with  $\sigma_A^2 = \sigma_{f/1.4}^2 - \sigma_{f/2.8}^2$  at  $E_{\text{drift}} = 350 \text{ kV/cm}$  and  $E_{\text{Amp}} = 47 \text{ kV/cm}$ . Standard deviation from the fit for a 2 mm drift gap thickness (blue markers) without the correction of the optical aberrations. The errors on  $\sigma$  are computed by error propagation from the fit parameters uncertainty. Simulated diffusion standard deviation, described in Sec. 6.2.8 for a 2 mm drift gap (red markers). The errors on the electric field are computed from the uncertainty on the cathode planarity that brings an error on the drift length  $d$ , involved in the diffusion standard deviation:  $\sigma_D \propto \sqrt{d}$ . Right: 1D intensity line profiles for drift gap thicknesses of 2 mm and 4 mm are represented for better visualization.



Since the diffusion standard deviation varies with  $\sqrt{d}$ , where  $d$  is the drift gap thickness, the PSF has been measured at a drift gap thickness of 4 mm instead of 2 mm as before (Figure 6.21), in order to analyse the impact of an increased diffusion on the signal broadening. The signal spreading involved by the diffusion should then increase by a factor  $\sqrt{\frac{4}{2}} \approx 1.41$ . The measured standard deviation at a 4 mm drift gap thickness is  $\sigma = 145.5 \pm 2.3 \mu\text{m}$  instead of  $135 \pm 1.58 \mu\text{m}$  for a 2 mm gap, at  $E_{\text{drift}} = 350 \text{ kV/cm}$  and  $E_{\text{Amp}} = 47 \text{ kV/cm}$ . In order to compute the diffusion contribution at a 4 mm gap, the correction of the aberration and electron range contributions is applied such that

$$\sigma_D(4 \text{ mm}) = \sqrt{\sigma_{\text{PSF}}^2 - \sigma_A^2 - \sigma_R^2} = \sqrt{145.5^2 - 81^2 - 75.5^2} = 94.4 \mu\text{m}$$

assuming that the electron range and light reflection contributions are similar at drift gaps of 2 mm and 4 mm. The contribution from the diffusion becomes larger, reaching 38 % while the optical contribution is 32 % and the electron range contribution is 30 %. A value  $\sigma_D(2 \text{ mm}) = 67.5 \mu\text{m}$  at a drift field of 350 V/cm has been obtained from simulations (Figure 6.21). The ratio between the diffusion contributions measured at 4 mm and simulated at 2 mm drift gap thickness is  $\sim 1.40$ , at a drift field of 350 V/cm. Hence, such similitude with the expected value of  $\sim 1.41$  confirms that the degradation of the spatial resolution when widening the drift gap thickness from 2 mm to 4 mm is due to the enlargement of the diffusion.

### 6.2.7 . Electron range

The photoelectron range strongly depends on the X-ray beam energy as mentioned in Sec. 2.1.2. Indeed, the photoelectron is emitted in the gas with an energy equal to the photon energy minus the Argon K-shell energy in most cases (binding energy of about 3.2 keV, Sec. 2.2). At larger X-ray energy, the photoelectron energy increases and its range in the gas scales up. Thus, the size of the ionizing cloud due to the photoelectrons multiple scattering is expected to grow with the photon energy. In order to study the effect of the electron range on the signal blurring, the PSF has been measured for X-rays energy ranging from 6 keV to 28 keV. The drift gap thickness is scaled up to 4 mm to avoid that the photoelectrons hit the Micromegas bulk before all their energy has been converted by gas ionization. In order to protect the camera from high-energy X-rays, that will degrade the sensor, a mirror was included in the set-up to bring the camera out of the X-rays beam axis. In fact, during data taking at a 28 keV X-rays beam, while the camera was aligned with the detector, as shown in Figure 6.10, few pixels were temporarily hitting up and emitting continuous signal while no light was sent to the camera sensor.

The Figure 6.22 (top) depicts PSF profiles at X-ray beam energies of 6 keV, 10 keV, 18 keV and 28 keV, that shows that the PSF width increases with the beam energy. The PSFs' standard deviation in the horizontal and vertical directions are displayed on Figure 6.22 (bottom) as a function of the X-ray beam energy. The optical aberrations have been corrected such that  $\sigma^2 = \sigma_{f/1.4}^2 - \sigma_A^2$  with  $\sigma_A^2 = \sigma_{f/1.4}^2 - \sigma_{f/2.8}^2$  at  $E_{\text{drift}} = 350 \text{ kV/cm}$  and  $E_{\text{Amp}} = 47 \text{ kV/cm}$ . The standard deviation without mirror, at a beam energy of 6 keV, is also represented (Figure 6.22, bottom, red marker). This illustrates the influence of the mirror on the signal blurring. The width of the PSFs increases with the beam energy by a factor  $\sim 14 \mu\text{m/keV}$  while the horizontal standard deviation is larger by 15 % in average than the vertical one. The lengthening in the horizontal direction exhibited by the PSF might correspond to the SOLEIL X-ray beam polarization that is known to be 100 % polarized horizontally [91]. However, further investigation and resources are needed to conclude on this behaviour.

Having in mind that most photoelectrons are issued from the Argon K-shell with a binding energy of about 3.2 keV, for 6 keV X-rays, the photoelectron has an energy of 2.8 keV and the Auger electron of 3.2 keV (Sec. 2.2). Hence, similar effect on the spatial resolution are expected from X-rays source of energies ranging from 6 keV to 28 keV, and an electrons source of energies from 2.8 keV to 24.8 keV. The main difference is that photoelectrons are produced among 3.2 keV Auger electrons and photons from fluorescence (mostly escape the gas volume). These results show the impact that the energy of incident particles has on the detector spatial resolution.

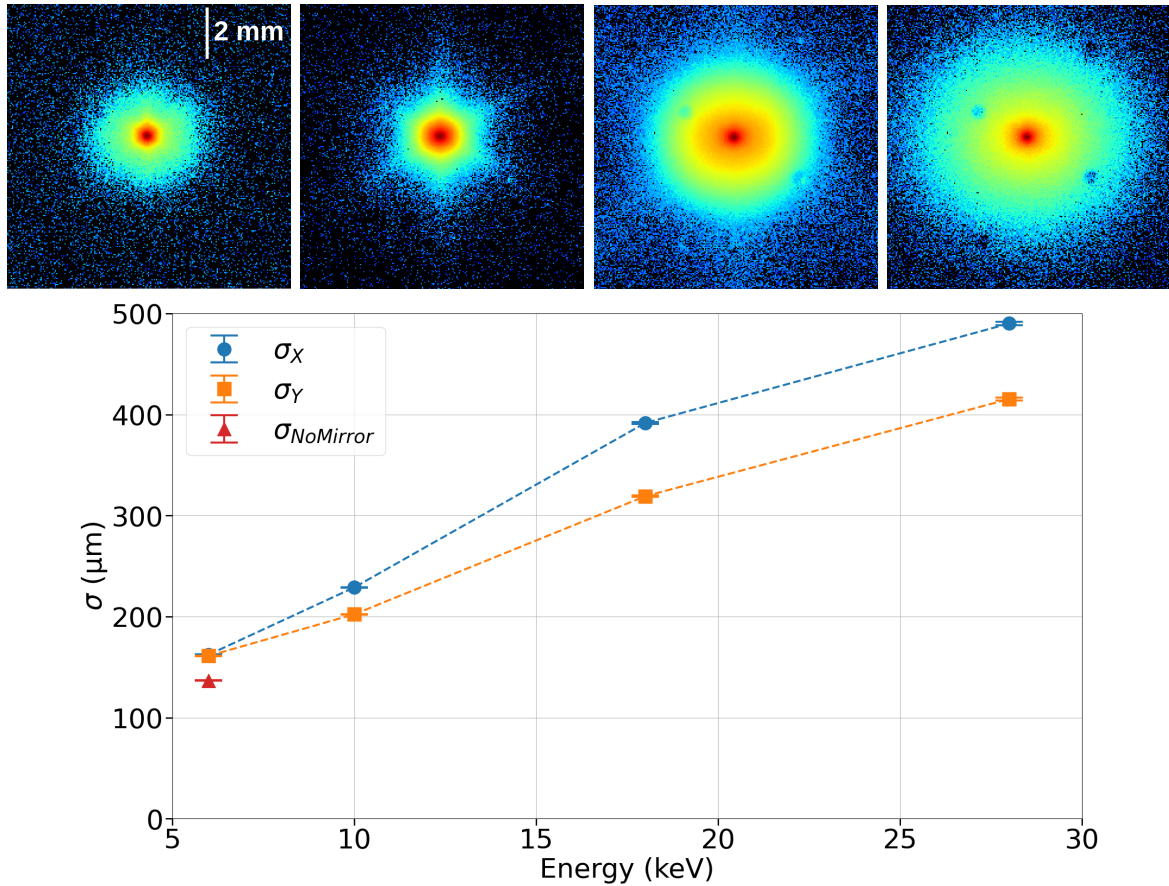


Figure 6.22: PSF profiles of the X-ray source at X-ray beam energies of 6 keV, 10 keV, 18 keV and 28 keV from left to right (top). Standard deviations extracted from PSF fit for four different X-ray beam energies in the horizontal ( $\sigma_X$ ) and vertical ( $\sigma_Y$ ) orientations (bottom) after correction of the optical aberration contribution. A mirror with a  $90^\circ$  orientation is used. Standard deviation (mean of the horizontal and vertical values) without mirror at a 6 keV X-ray beam energy (red marker), in the same conditions: The lens has a 25 mm focal length, the amplification and drift fields are of 59 kV/cm and 350 V/cm respectively. The mesh reflection pattern is visible especially, at a 10 keV beam. The pillars are noticeable at 18 keV and 28 keV X-rays beams.

### 6.2.8 . Simulation of the electrons range and diffusion

The impact of the electron diffusion (Sec. 6.2.6) and mean range (Sec. 6.2.7) on the PSF profile has been studied in the previous sections. The dependence of the diffusion on the drift field and the drift gap thickness especially was shown. The increase of the mean range with the beam energy has also been revealed. Because of their low mass, electrons undergo a large number of scattering processes and their trajectory is no longer straight. The motion of electrons in gas follows a statistical model, where electrons are scattered by inelastic collisions and Coulomb scattering. This motion depends on the initial kinetic energy of the electrons and on the electric field that reigns into the gaseous detector. The Magboltz simulation tool [11] integrates the models which govern the electrons motion and will be used to contrast the data exposed in the previous sections. The simulation code is based on a development by David Attié and Maxence Vandenbroucke. The goal of this study is to extract the mean distance of scattered electrons from their location of emission, which is a good description of the size of the electron cloud in the gas.

A simple detector geometry has been defined, with two parallel electrodes at a distance of 4 mm from each other. The detector is  $8 \times 8 \text{ cm}^2$  wide and is filled with a gas mixture of Argon/ $\text{CF}_4$  (90%/10%). A uniform drift field is applied between to two electrodes with an adjustable field weight. The motion of electrons from an initial photoelectron of 15 keV is shown in Figure 6.23, for a drift field of 350 V/cm. This figure illustrates the different mechanisms leading to the electron cloud spreading. The photoelectron first scatters in every directions, ionizing the gas on its path. The mean distance of the photoelectron from its initial position, weighted by the number of secondary electrons and projected on the readout plane ( $x, y$ ), is defined as the mean range. The motion of the initial electron reaches the millimeter scale. The drift of the electrons due to the electric field force involves an electron vertical motion towards the bottom electrode. Electrons simultaneously diffuse perpendicularly to the drift direction.

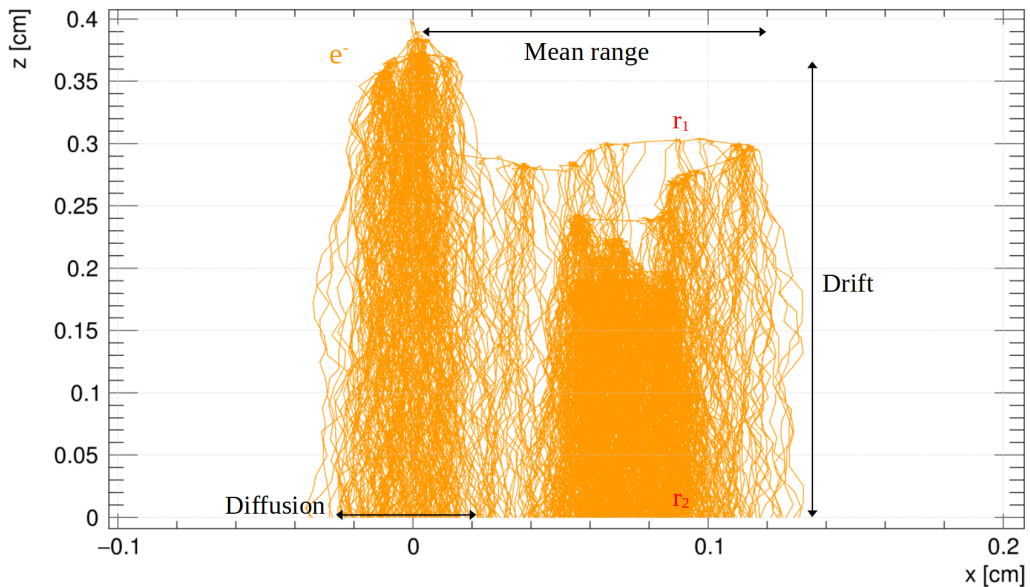


Figure 6.23: Plot of the electrons motion in the drift gap, projected on the ( $x, z$ ) plan. The horizontal movement of the initial, high kinetic energy electron is visible. The drift and diffusion of the secondary electrons are also identified.  $r_1$  and  $r_2$  stand for the initial and final secondary electrons' coordinates respectively. The initial electron energy is 15 keV and the electric field is 350 V/cm. The gas mixture is Argon/ $\text{CF}_4$  (90%/10%).

## Diffusion

The simulation provides the secondary electrons' initial position  $r_1 = (x_1, y_1, z_1)$  and final position  $r_2 = (x_2, y_2, z_2)$ , where they reach the bottom anode. The diffusion distribution is directly obtained by computing the subtraction  $dr = r_2 - r_1$ . The depth of the initial electron is fixed at the top electrode location ( $z_0 = 4$  mm) and the initial energy is close to 0 eV ( $e_0 \approx 0$  eV) for the convenience of the calculation. The distribution  $dr$  is projected on the readout plan and weighted by the secondary electron energy. The diffusion distribution ( $dx, dy$ ) is displayed on Figure 6.24. A Gaussian fit of the distribution is performed to extract the standard deviation of the diffusion. The standard deviation is expected to be similar in the  $x$  and  $y$  coordinates, which corresponds to the transverse diffusion standard deviation  $\sigma_T$ . This parameter is depicted for different gas mixtures and drift fields in Sec. 3.1.2.

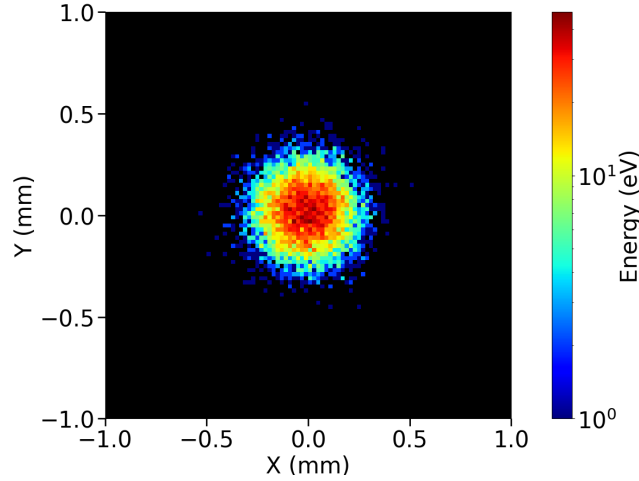


Figure 6.24: 2D diffusion profile at a drift field of 350 V/cm in Argon/CF<sub>4</sub> (90%/10%). A transverse diffusion coefficient of  $\sigma_T = 205 \mu\text{m} / \sqrt{\text{cm}}$  has been computed.

## Mean range

The contribution to the signal spreading issued from the photoelectron range derives from the distribution of the secondary electrons' initial position. These coordinates are directly accessible by the coordinates  $r_1$ . As shown in Figure 6.25, the length of the path of the photoelectron and the number of the secondary electrons increase with the energy of the photoelectron.

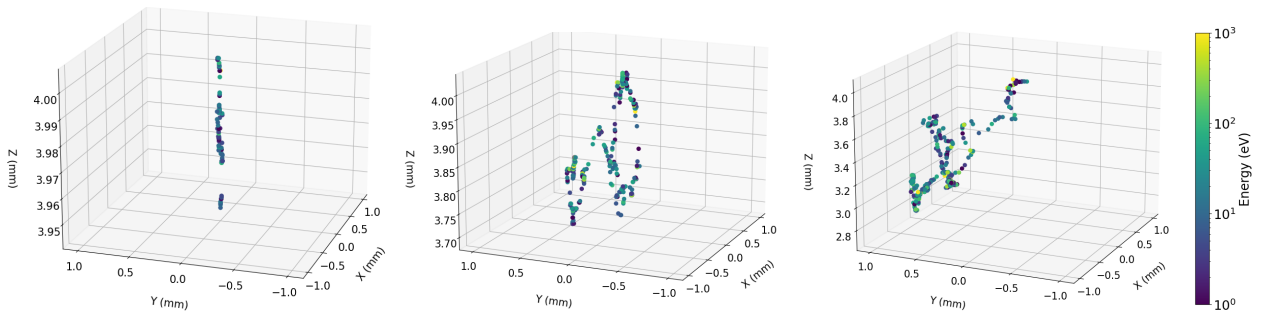


Figure 6.25: 3D distributions of a single photoelectron coordinates as a function of the deposited energy, at each ionization step. Initial energies of the photoelectron of 3 keV (left), 15 keV (middle) and 25 keV (right) are being computed. The range of the photoelectron increases with its initial energy.

Careful consideration must be given to the position, direction and energy of the initial photoelectron to be in adequacy with the measurements performed at the SOLEIL synchrotron in Sec. 6.2.7. The initial position of the photoelectron corresponds to the position of the absorption of the X-ray photon in the drift gap. According to Sec. 6.2.1, the beam profile follows a Gaussian distribution centered

in  $(0,0)$  with a standard deviation of  $7\mu\text{m}$ . For a 4 mm drift gap thickness, the X-ray longitudinal absorption in the gas is considered as uniform. Hence, the initial coordinates of the photoelectron follows a cylindrical distribution given in (6.16) (left). The initial coordinates  $r_1$  of the secondary electrons are displayed in Figure 6.26 (left) for 1000 photoelectrons of 15 keV. The deformation of the initial cylindrical shape is due to the photoelectron range.

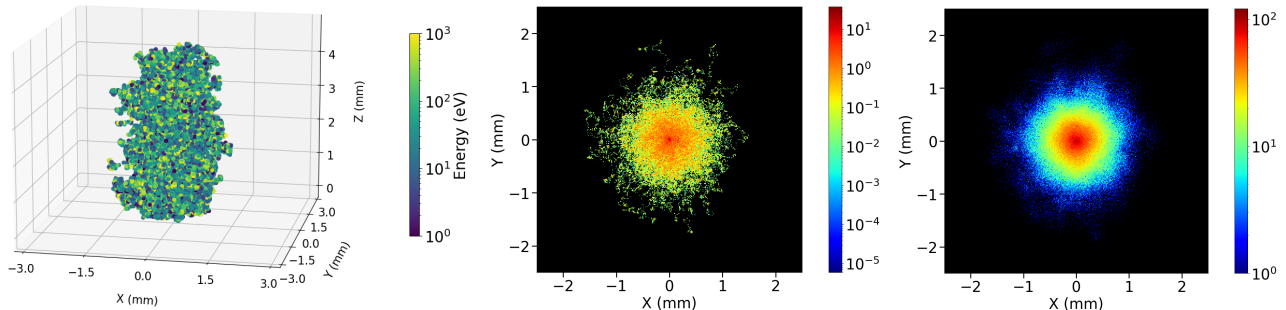


Figure 6.26: 3D distribution of the coordinates of 1000 accumulated photoelectrons of 15 keV, as a function of their deposited energy at each ionization step (left). The initial cylindrical beam absorption shape is deformed by the photoelectrons range. Projection on the  $(x, y)$  plan of the  $r_1$  distribution (secondary electrons initial coordinates) weighted by the secondary electrons energy in eV (middle). Projection on the  $(x, y)$  plan of the  $r_2$  distribution (secondary electrons coordinates after the drift and diffusion) weighted by the counts of secondary electrons (right).

The distribution of the variable  $r_2$  is the convolution of the variable  $r_1$  and the diffusion distribution, such that  $r_2 = r_1 * dr$ . The 2D distributions of  $r_1$  and  $r_2$  are shown in Figure 6.26 (middle, right). The distributions of  $r_1$  and  $dr$  are Gaussian and their convolution is also a Gaussian function. Hence, the mean positions  $(\mu_X, \mu_Y)$  and standard deviations  $(\sigma_X, \sigma_Y)$  of the distribution  $r_2$  can be extracted with a Gaussian fit.

Additionally, the direction of emission of the photoelectron must be modeled in conformity with the conditions at the synchrotron. The initial direction of the photoelectron is rapidly lost by multiple scattering. However, at large energy, it has an influence on the electrons mean range. To validate that the photoelectron direction has an impact on the mean range, photoelectrons of 15 keV were emitted with a momentum  $dx = 1$  (Figure 6.27, left) and  $dy = -1$  (Figure 6.27, middle). In the first case, a lengthening of the Gaussian shape in the  $x$  orientation and a displacement in the positive  $x$  direction is observed:  $\sigma_X = 360\mu\text{m}$ ,  $\sigma_Y = 342\mu\text{m}$ ,  $\mu_X = 93\mu\text{m}$  and  $\mu_Y = -3\mu\text{m}$ . A similar behaviour has been observed in the second case:  $\sigma_X = 351\mu\text{m}$ ,  $\sigma_Y = 371\mu\text{m}$ ,  $\mu_X = -11\mu\text{m}$  and  $\mu_Y = -125\mu\text{m}$ .

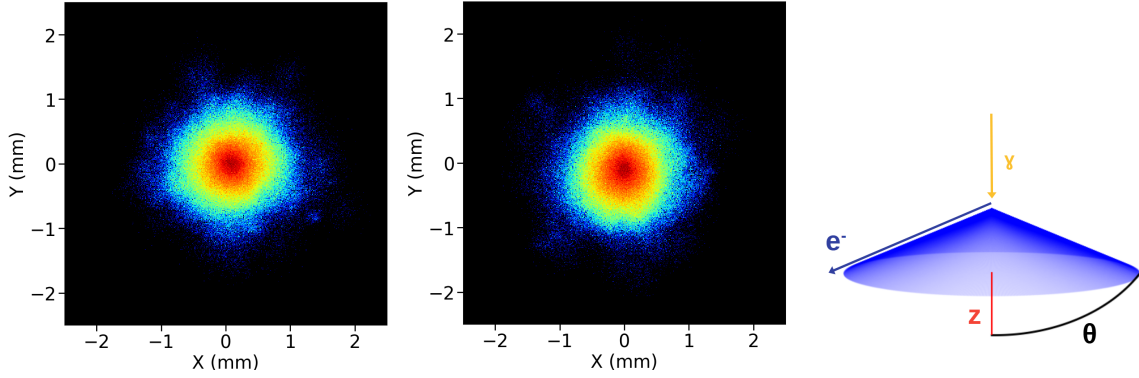


Figure 6.27: 2D distributions of the secondary electrons after drifting from 15 keV photoelectrons with a momentum  $dx = 1$  (left) and  $dy = -1$  (middle). Cartoon of the angular distribution of the photoelectron ( $e^-$ ) with a conical shape, oriented to the opposite direction of the  $z$  axis, with an opening angle  $\theta$ .

According to [8, 91], the angular distribution of the photoelectron depends on the X-ray energy. Especially, the opening angle  $\theta$  of the photoelectron conical emission (Figure 6.27, right) depends on the X-ray energy. At energies close to 0 keV, the angle tends to  $\theta = 90^\circ$  and at high energy, it tends to  $\theta = 0^\circ$ . At X-rays energies between 6 keV and 30 keV, the angle distribution is centered around  $\theta = 60^\circ$ . Hence, in the simulation, the momentum of the photoelectron has been defined following (6.16) (right) with  $\phi$  the angle of revolution of the cone. One should mention that the photoelectric effect largely dominates the Compton effect at such X-rays' energy range (Sec. 2.2.2). In the case of polarized X-rays beam, the revolution angle  $\phi$  is not uniform between 0 and  $2\pi$  but depends on the direction of polarization. This aspect has not been taken into account in the current simulation.

$$\left\{ \begin{array}{l} x_0 = \text{Gaus}(0, 7 \mu\text{m}) \\ y_0 = \text{Gaus}(0, 7 \mu\text{m}) \\ z_0 \in [0, 4 \text{ mm}] \end{array} \right. \quad \left\{ \begin{array}{l} \theta = 60^\circ \\ \phi \in [0, 2\pi] \\ dx = \sin(\theta) \cos(\phi) \\ dy = \sin(\theta) \sin(\phi) \\ dz = -\cos(\theta) \end{array} \right. \quad (6.16)$$

Finally, the energy of the photoelectron depends on the gas mixture and on the energy of the X-rays beam, as explained in Sec. 5.2.1. For Argon, hard X-rays mostly eject, by photoelectric effect, an electron from the K-shell of binding energy  $E_K=3.2\text{keV}$ . Thus, the photoelectron has an energy  $e_0 = h\nu - 3.2\text{keV}$ . In 85% of the cases, an Auger electron of 3.2 keV is emitted along with the photoelectron, at the X-ray absorption's location. In the other cases, a fluorescence photon is emitted, with a large absorption range and almost no contribution to the PSF. Therefore, for an X-rays beam of energy  $h\nu$ , two populations of electrons are generated: the photoelectrons of energy  $e_0 = h\nu - 3.2\text{keV}$ , and an addition of 85% of Auger electrons of energy  $e_0 = 3.2\text{keV}$ . For 1000 photoelectrons simulated, 850 Auger electrons are additionally generated, with an isotropical emission.

The distributions issued from the photoelectrons and the Auger electrons are not convolved, but overlapped. Accordingly, it has been observed that a sum of two Gaussian distributions instead of a single Gaussian offers a better fit. This specific distribution is detailed in (6.14). This argument supports the choice of the a sum of Gaussian distributions to fit the data in Sec. 6.2.5. The fit of the simulated distribution  $r_2$  allows to extract the standard deviation, following the relation (6.10). The average standard deviation is displayed in Figure 6.28 as a function of the X-ray beam energy. The standard deviation of the secondary electrons distribution clearly increases with the X-rays beam energy. The standard deviations on the  $x$  and  $y$  orientations, measured in Sec. 6.2.7, are also displayed, after correction of the signal spreading involved by the optical aberrations and mirror effects. The standard deviation measured at the synchrotron is then  $\sigma^2 = \sigma_{Mirror}^2 - \sigma_M^2 - \sigma_A^2$  with  $\sigma_M^2 = \sigma_{Mirror}^2 - \sigma_{NoMirror}^2$ .  $\sigma_M$  is the standard deviation describing the signal blurring due to the presence of the mirror on the optical axis.  $\sigma_A$  stands for the optical aberration contribution.

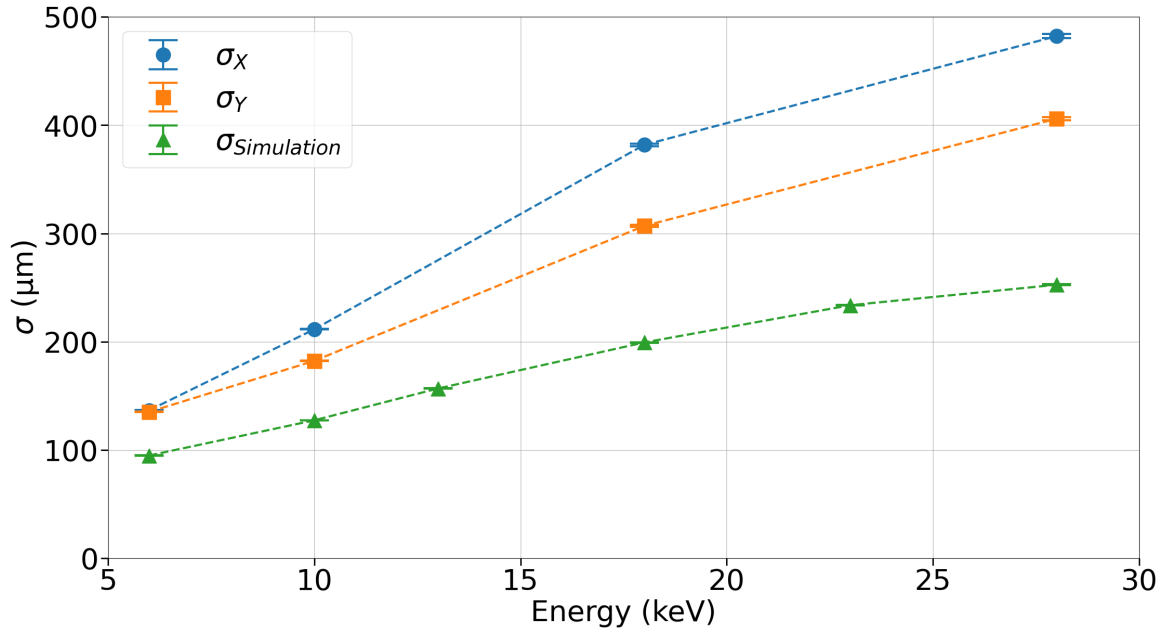


Figure 6.28: Standard deviation of the simulated secondary electrons distribution, after drifting (green markers). Measured standard deviations from the PSF fit (Sec. 6.2.7) in the  $x$  (blue plot) and  $y$  (orange plot) orientations, after correction of the lens aberration and mirror blurring effects. X-rays beam energies from 6 keV to 28 keV were investigated.

A common trend of the width of the signal as a function of the beam energy is observed on both measurements and simulations. The mean range from the simulation increases by a factor  $\sim 7 \mu\text{m}/\text{keV}$ . A coefficient of the same order of magnitude of  $\sim 14 \mu\text{m}/\text{keV}$  has been measured at the synchrotron. This similarity shows that the PSF is dominated by the photoelectron range at large beam energies. The gap between the simulation and the measurement most probably comes from the light reflection on the mesh that has not been rectified. The correction of the mirror and aberration effects has been performed at a beam energy of 6 keV, which might bring uncertainties on the corrections at higher beam energies. Besides, while the simulated beam range is symmetrical by revolution, the measured PSF shows an elongation in the  $x$  orientation. This different might derive from the fact that the X-rays beam polarization is not integrated in the simulation.

### 6.2.9 . set-up configurations comparison

The PSFs' standard deviation from different configurations of the imaging device were compared, changing either the Micromegas features or the optical components. The Figure 6.29 shows the standard deviation extracted from the fit of the PSF for different detector configurations. The first study relates to the Micromegas mesh type that is either flat and thin (beta mesh) or thicker and woven (standard mesh) as shown in Sec. 5.1. The lens has a 25 mm focal length and the aperture is  $f/1.4$ . The drift field is 350 V/cm while the amplification field is 59 kV/cm for the beta mesh and 41 kV/cm for the standard mesh, which corresponds to almost identical gains because of the different amplification gap thicknesses of  $75 \mu\text{m}$  and  $128 \mu\text{m}$  respectively. The light intensity is maximized at such gain in order to be sensitive to light reflection effects. The PSF's standard deviation is almost identical for both meshes although their reflection pattern are different (Figure 6.17).

The second group of measurements involves a mirror in the optical axis to remove the camera from the beam axis. Using a mirror is a critical aspect of the optical readout Micromegas detector because it prevents from damaging the readout device in case of high-energy and high flux particle beam. The detector is operated at high gain value ( $\sim 10^4$ ) to maximize the amount of light and to be sensitive to light reflection effects. The drift field is 350 V/cm and the amplification field of 59 kV/cm with the beta mesh. This measurement shows that the spatial resolution is highly degraded by the mirror in



conditions with intense scintillation light. The quality of the mirror, that involves its elements purity and flatness, might indeed cause light reflection and diffusion.

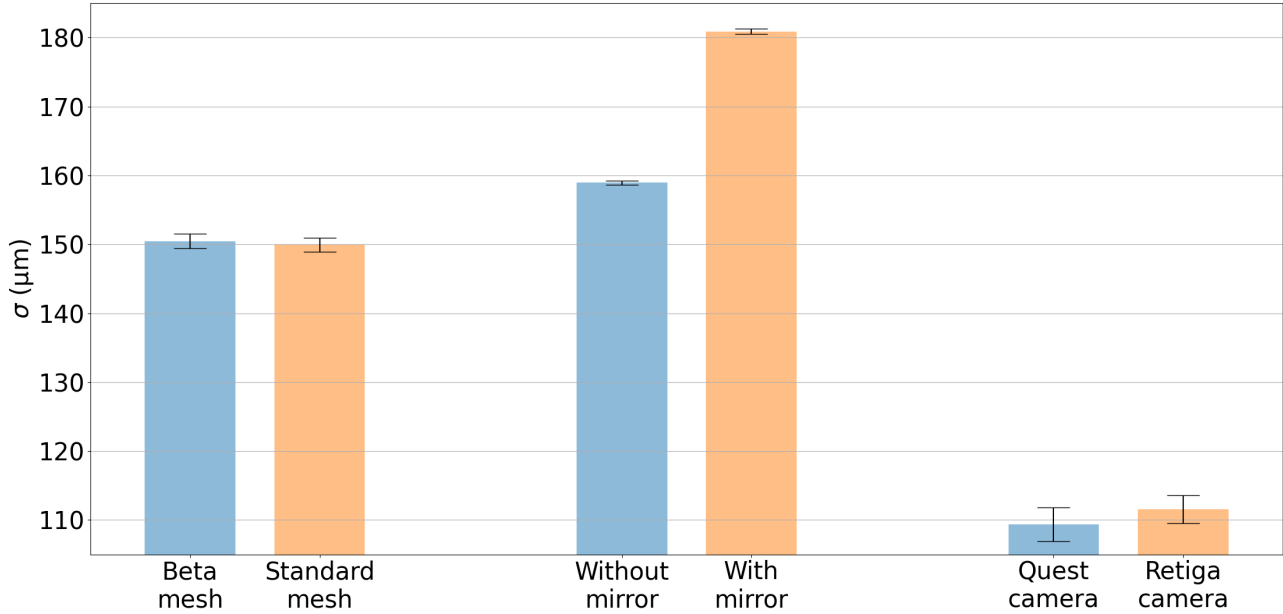


Figure 6.29: Comparison of the total standard deviation value extracted from the fit of the PSF, without any corrections. All settings are identical for each group of measurement, varying only the targeted parameter for a fair comparison.

Finally, in addition to the Orca-Quest camera described in Sec. 5.3.1, a Retiga R6 camera [92] has been tested. This camera has a lower sensitivity, providing a readout noise of  $5.7e^-$  RMS, while the QE and the pixel size is similar to the qCMOS camera. For a fair comparison, the dark images from the Retiga camera are used to compute the pedestals and common noise (Sec. 5.4) for the analysis of both cameras images. The width of the PSFs are similar for the Retiga camera and the Orca-Quest camera. It shows that high spatial resolution is achieved with a cost saving camera of lower sensitivity, as long as the signal to noise ratio is high enough, which is satisfied in large particle flux conditions. The 25 mm focal length lens has been used with a  $f/1.4$  aperture. The drift field is 350 V/cm and the amplification field of 62 kV/cm with the beta mesh.

### 6.2.10 . Study of the Micromegas pillar and mesh effects

Thanks to the magnification of  $\sim 1$  of the 50 mm focal length lens, the scintillation light emitted in the pillars and mesh holes vicinity is depicted with high accuracy. Since the light is emitted where the avalanche takes places, optical readout allows to study the shape and location of the avalanche at specific locations in the Micromegas detector structure.

At first, the beam shape has been analyzed while crossing a pillar with a  $17 \times 17 \mu\text{m}^2$  FWHM X-ray beam of 6 keV. Pillars are located between the mesh and the anode, with a pitch of 6 mm as detailed in Sec. 5.1. The Figure 6.30 (top) shows the beam profile at different heights of the detector and positions of the beam relatively to a pillar. One can notice that, even at a full overlap of the beam with a pillar (right image), a proportion of the signal remains, forming an eclipse-like shape around the pillar. Before the electron amplification, the electron cloud standard deviation is maximum  $100 \mu\text{m}$  because of the electrons range and diffusion, for a 2 mm drift gap thickness. Hence, above a diameter of  $4\sigma = 400 \mu\text{m}$ , less than 5 % of the signal should remain for a Gaussian distribution describing the beam spreading profile. However, at the bottom of Figure 6.30, the total light amount (blue line) drops by only 70 % where the beam is fully covered by the pillar, at a beam height  $Y = 600 \mu\text{m}$ . By linearity of the light yield, this means that at least 30 % of the electrons that drift towards a pillar are being transmitted to the amplification gap thanks to the field lines curvature around the pillar. While a fraction of the

light emitted close to the pillar is being reflected or absorbed by the pillar itself, a portion of the X-ray signal is also lost by the scintillation light. Hence, the loss of electron due to the presence of the pillar is over-estimated.

This effect is not related to light reflections or lens effects because the light signal is produced only in the amplification gap, after that the electrons have crossed the pillar. Moreover, the beam signal RMS (red line) raises as the beam overlapping by the pillar progresses, meaning that the enlargement is due to the pillar and not to regular effects (electron range and diffusion, light reflection and aberration). The curvature of the field lines around a dielectric spacer is a known phenomenon that has been simulated in the past in [93].

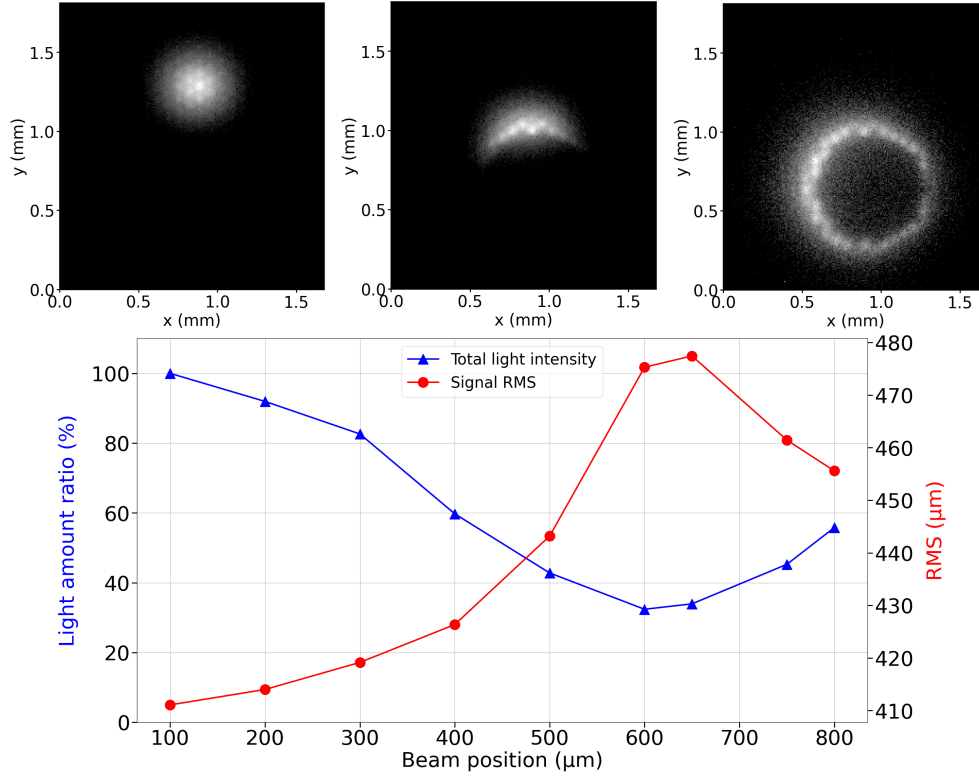


Figure 6.30: Beam profile at different heights  $Y$  of the detector while the beam stays still. On the top left, the beam is out of the pillar ( $Y = 100 \mu\text{m}$ ), on the top center, the pillar covers a section of the beam ( $Y = 400 \mu\text{m}$ ) and on the top right, the beam is fully covered by the pillar ( $Y = 600 \mu\text{m}$ ) (the gray scale is logarithmic and steady for every images). The figure at the bottom represents the normalized total signal light amount (blue line) and the total signal RMS (red line). 30% of the light amount remains while the beam and a pillar overlap, and light signal profile is enlarged by 15%.

A similar measurement was performed with a  $1 \times 1 \text{ mm}^2$  beam in order to compare the avalanche distribution for two different kind of meshes. Figure 6.31 shows the light intensity distribution for a beta mesh and a standard mesh, which are described in Sec. 5.1. On the left, the avalanche seems to be well localized in the beta mesh holes (red regions) for  $x$  and  $y$  values at  $0.7 \pm 0.3 \text{ mm}$  while light is being reflected on the holes edges, away from the beam. For the standard mesh on the right, high intensity zones with a square shape are visible although the mesh holes are harder to identify in comparison to the beta mesh. Light reflection is also identified on the mesh edges away from the beam. Because of the high reflectivity of the mesh, no conclusion can be done on the origin of the blurring, which can come either from the mesh reflectivity or from the field lines structure. However, this measurement might be an indication of a poorer signal sharpness for the standard mesh compared to the beta mesh.

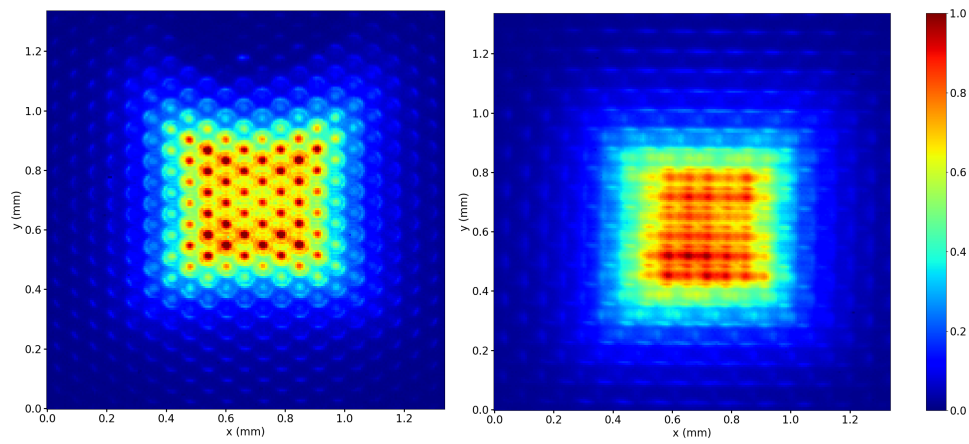


Figure 6.31: Light intensity profile with a beta mesh (left) and with a standard mesh (right). The lens has a 50 mm focal length and high gain is settled for both meshes.

### 6.2.11 . Conclusion

At CERN, high-intensity X-rays from an X-ray tube were used to optimize the detector's response. Initial tests revealed issues like non-uniform stretching and reflectivity of the aluminized Mylar foil cathode, which were mitigated using a Diamond-Like Carbon (DLC) layer on Kapton foil. Detailed radiographs of objects such as a deceased bat and lead target demonstrated the detector's capability to produce high-resolution images over large surfaces in real-time, with further improvements achieved through deconvolution algorithms like the Richardson–Lucy method. In the future, deconvolution techniques will be further studied, extending their use to neutron radiography.

At the SOLEIL synchrotron, precise PSF measurements identified key factors affecting spatial resolution. Optical aberrations were found to degrade signal quality, particularly at larger apertures. By reducing the lens aperture from  $f/1.4$  to  $f/2.8$ , the signal sharpness improved considerably, with the standard deviation decreasing to  $108 \pm 2.8 \mu\text{m}$ . This indicates that minimizing optical aberrations is crucial for enhancing spatial resolution. The PSF was studied at different positions, revealing that the PSF profile is space-dependent due to aberrations, while the detector gain uniformity is below 10%. New lenses will be required to reduce lens aberrations in large luminosity conditions. Using large diameter lens allows to cut the edges, decreasing aberrations, while the lens' speed remains high. In addition, aspheric lenses are known to significantly reduce aberrations.

Reflections from the mesh significantly contributed to signal blurring, especially under high light conditions (high gain and high particle flux), underscoring the importance of controlling reflections to maintain image sharpness. Glass Micromegas bulk detectors with black DLC coated mesh have already been built and will be tested for reflection moderation.

Modeling of the PSF in two dimensions was undertaken to find an optimal fit for the data. Further efforts will be invested in simulating the electron range, reflections and optics aberration to obtain a better model fitting the PSF. Instead of mathematical models, empirical models may also be used, providing a better representation of the PSF and better fitting.

Electron diffusion was another major factor, with its width varying depending on the electric drift field. PSF measurements across different drift fields showed a characteristic trend with a minimum blurring around 350 V/cm in Argon/CF<sub>4</sub> (90%/10%) gas mixture, consistent with simulated diffusion characteristics. Increasing the drift gap was observed to increase diffusion, thereby affecting spatial resolution. In future detector development phase, drifting negative ions instead of electrons may be explored, significantly reducing the transverse diffusion.

Electron range was also a critical factor, contributing to signal blurring, especially at higher X-ray beam energies, where the PSF width increased with the beam energy. Implementing amplification in the drift gap will be investigated in a following chapter to compensate particle range in the gas. Increasing the gas pressure might also be a solution to reduce the particle range and will be investigated for future developments. In addition, the impact of X-ray beam polarization will be further explored to demonstrate the potential of the glass Micromegas detector for polarimetry. Specifically, the shape of the PSF will be analyzed using high-energy X-rays at various detector rotation angles to separate the PSF elongation from the intrinsic effects of the detector.

The study provided insights into the relative weight of each contribution in specific scenarios, enhancing our understanding of how to optimize the detector for better performance. To summarize, the different contributions to the PSF and the parameters regulating them are depicted in Figure 6.32.

<b>Contribution</b>	<b>Parameters</b>
Electron diffusion	Drift field strength / drift gap
Electron range	X-rays beam energy
Lens aberration	Lens aperture
Light reflection	Mesh geometry and coating

Figure 6.32: Summary table of the contributions to the PSF and parameters that have been modified to study the contributions dependency on the experimental set-up.

Comparative studies of different detector configurations highlighted the impact of Micromegas mesh types and optical components on PSF characteristics. Measurements with different mesh types (beta mesh vs. standard mesh) showed comparable PSF standard deviations, despite variations in reflection patterns and amplification gap thicknesses. The introduction of a mirror in the optical axis revealed a degradation in spatial resolution under intense scintillation light conditions, underscoring the importance of optical component purity and flatness. Furthermore, the comparison between different cameras revealed that high spatial resolution can be attained with cost-effective, lower sensitivity cameras, as long as adequate signal-to-noise ratios are maintained under high particle flux conditions.

In-depth analysis of Micromegas pillar and mesh effects elucidated the role of pillar structures in shaping scintillation light distribution. Additionally, analyzing the scintillation shape near the pillars has provided valuable insights into the behavior of field lines near the pillars and the electronic transmission in their vicinity. Studies with X-ray beams of varying sizes and mesh types highlighted differences in light intensity distribution and reflection patterns, influencing overall signal sharpness.

Overall, by dissecting the individual contributions to signal blurring and comparing experimental results with simulations using Magboltz, the study provides key findings for optimizing the imaging device and improving spatial resolution. This study contributes to a better understanding of signal blurring mechanisms and optimization strategies for gaseous detectors in imaging applications. This expertise extends beyond X-rays to encompass a wide range of particle types.

## 7 - $\beta$ imaging

This chapter is dedicated to the development of a new imaging device for  $\beta$  particles detection with precise counting capability and high sensitivity. The requirements of the  $\beta$  imager are driven by the development of new drugs to treat cancer and by the analysis of their behaviour at the single tumor cell level. First, the biological context and goals are stated and an overview of autoradiography is given. The experimental setups with charge and optical readout are then described. Energy spectra issued from the interaction of  $\beta$  particles with the gaseous detector are measured and compared with simulated data with the Geant4 simulation tool [6]. The detection capability and localization of sub-becquerel activity samples as well as the activity measurement of such elements are finally exposed. The performance of the Micromegas based  $\beta$  imager has been compared to other imagers from the industry and the scientific community.

### 7.1 . Biological context and autoradiography

Cancer has remained one of the most severe diseases for decades, with diagnoses increasing while curability stagnates. Cancer, among other diseases like cardiovascular or infectious disorders, are mostly not cured because of a late diagnosis of the disease, detected only after physiological symptoms. While the diseases are investigated at the molecular and tissue level, the late diagnosis is caused by a lack of understanding of the disease at a cellular level. Understanding when, why and how cells deviate from a healthy ageing to the disease trajectory will lead to better detection and successful treatment of disorders. This new approach falls within the Lifetime Initiative that aims to study complex diseases at the single cell level [94]. In fact, research in oncology has indicated that tumors are composed by different types of tumor cells, both between and among tumors. This involves a more complex representation of a tumor driven by cells gene expression, proliferation and metastatic potential and affects the efficiency of drugs that were formerly developed from the tumor scale perspective [95].

Improving the success rate of treatments also sets in a strategy where the drug development is accelerated by decreasing the substantial drug development failure rate and cost. The study *ex vivo* of the drug behaviour and failure with the aim of killing cancer cells is a key aspect of this approach. In particular, the goal is to analyze if the drug reaches the targeted cell and if it effectively treats it [96]. Drug tagging has been achieved with fluorescence techniques [97] although the fluorescent groups are large molecules that affect the chemical dynamics and skew the measurement. That is why radioactive labelling is preferred, conserving the drug molecule structure by replacing H, C, F or S atoms by their radioisotopes. Such isotopes are  $\beta$  emitters, allowing for position reconstruction and drug concentration measurement by counting the isotopes activity.  $^{18}\text{F}$  and  $^{35}\text{S}$  still interfere with the metabolic mechanisms and  $^{18}\text{F}$  has a short lifetime (1.8 h half-time) which is inconvenient for experimental purposes. On the other hand,  $^3\text{H}$  and  $^{14}\text{C}$  have very long lifetimes (12.3 years and 5.7 years respectively) and their  $\beta$  spectra show a mean energy of 6 keV and 49 keV respectively, which are above the Micromegas detector sensitivity threshold. However, the radio-labelled samples must be inside the detector gas volume, or the low-energy  $\beta$  electrons would not go through the detector walls. The labelling technique based on bioanalytical methods is described in [98].

In opposition to radiography, where the radioactive source is behind the scanned object, in autoradiography, the sample contains the radioactive source. By putting an imaging device in contact with the samples, the distribution of the radioactive source within the samples is assessed. Historically, photographic emulsions (based on silver ions conversion) and phosphor screens (based on  $\text{F}^{2+}$  fluorescence in the UV region) were mainly used to perform autoradiography with good spatial resolution and quantification capability [99]. Nowadays, autoradiography is mainly performed with particle counting imaging systems based on gaseous detector technology, allowing for real time imaging and accurate counting. Parallel plates proportional chamber coupled with light readout was developed by Georges

Charpak [100, 101]. The  $\beta$  imager 2000 (now renamed Biospace tRACER) [43] derived from Charpak works, uses vapor of triethyl amine (TEA) to produce UV light that is intensified by a Microchannel plate (MCP) [42] and readout by a CCD camera. A  $\beta$  decay produces a spot of light that is counted, and the center of gravity of the spot light gives the position of emission of the  $\beta$  particle.  $\beta$  imaging has also been achieved with the Parallel Ionization Multiplier (PIM) detector [102], based on a parallel micro-meshes structure with multiple amplification gaps and a segmented readout anode of  $10^4$  pixels. The PIMager device [103] has shown high spatial resolution in autoradiography and demonstrated simultaneous detection of  $^3\text{H}$  and  $^{14}\text{C}$  with an efficient discrimination [104]. Finally, the Micromegas detector has first been implemented in an imaging device based on charge readout, with 1D strips for a proof a concept of autoradiography on sub-becquerel activity tritiated samples [105]. The Micromegas  $\beta$  imager with both charge and optical readout has been developed in collaboration with biologist (CEA/DRF/JOLIOT/DMTS/SIMOS) and microfluidicist (CEA/DRF/IRAMIS/NIMBE) teams. The radiolabeling of the tumor cells/glucose and the cellular culture have indeed been taken over by the biologists [98] (Figure 7.1 A and B) while the microfluidicists researchers are developing a system to isolate single tumor cells (Figure 7.1 C) [106, 107].

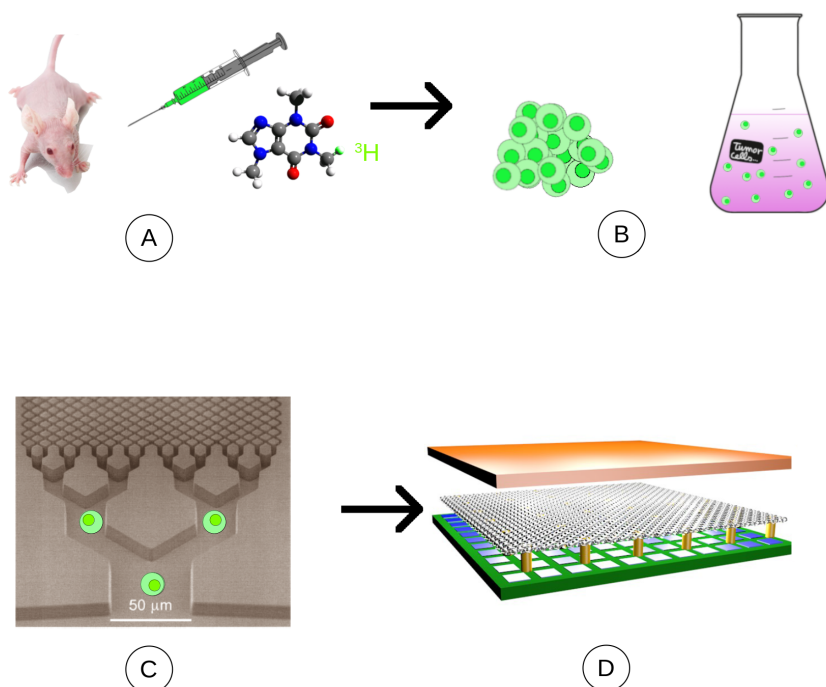


Figure 7.1: Illustration of the steps to perform an autoradiography of unique tumor cells. The tumor is first tagged with tritium with radiolabelling techniques and tumors cells are collected from the animal (A). The tumor cells are then grown in a cellular culture (B). The two first steps are carried out by the biology team. The microfluidics team then isolate the tumor cells by microfluidics techniques (C). Finally, the samples are placed in the Micromegas detector gas volume and autoradiography is performed by the detector developers (D).

The work presented in this thesis is dedicated to the design and test of a new  $\beta$  imager based on a glass Micromegas detector and a CMOS camera. The goal is to achieve simultaneous autoradiography on an extended number of tritiated samples with an individual activity of the order of a tenth of a Becquerel. The quantification of several samples at once, without reference of known activity, will be demonstrated. The measurements are performed both with a reconstruction algorithm in single event mode and without heavy data processing in light integration mode.

## 7.2 . Setups description and samples preparation

The glass Micromegas, which is used for the  $\beta$  imager, as well as the lens and the camera, are described in Sec. 5.1. The beta mesh is implemented with a  $75\ \mu\text{m}$  amplification gap and the cathode, which is also the sample holder, is made of a  $1.1\ \text{mm}$  thick glass of  $8 \times 8\ \text{cm}^2$  coated with  $150\ \text{nm}$  of ITO. The gas is composed of a mixture of Argon and either 20% of  $\text{CF}_4$  or 5% of Isobutane. As shown on Figure 7.2 (left), the Micromegas detector and the camera are vertically aligned to keep the samples on a holder facing upwards. While the isolation of single tumor cells has not been achieved yet, measurements are performed on tritiated glucose samples in which  $^3\text{H}$  activity is well controlled. The sample holder is kept horizontal as a precaution to avoid any fall of tritiated glucose into the mesh. However, all the liquid of the sample has dried at the moment of the measurement, and the sample is expected to remain unchanged. Labelling with  $^3\text{H}$  especially has been targeted for this project, regarding the low mean energy of its  $\beta$  spectrum (Figure 2.6) and the short range of the  $\beta$  electrons, a better spatial resolution is expected. The maximum reachable activity of a tritiated cell has been estimated to  $0.3\ \text{Bq}$  [108], and an appropriate tritium activity for the glucose samples has been chosen. The detection principle is very similar to the X-ray imaging, although the  $\beta$  emitters are inside the gas volume: the  $\beta$  electrons issued from the  $^3\text{H}$  ionize the gas along their path of less than  $100\ \mu\text{m}$  length in general, depending on their energy (Figure 7.2, right). The secondary electrons issued from the gas atoms ionization, then drift towards the mesh and visible light is produced during the amplification process.

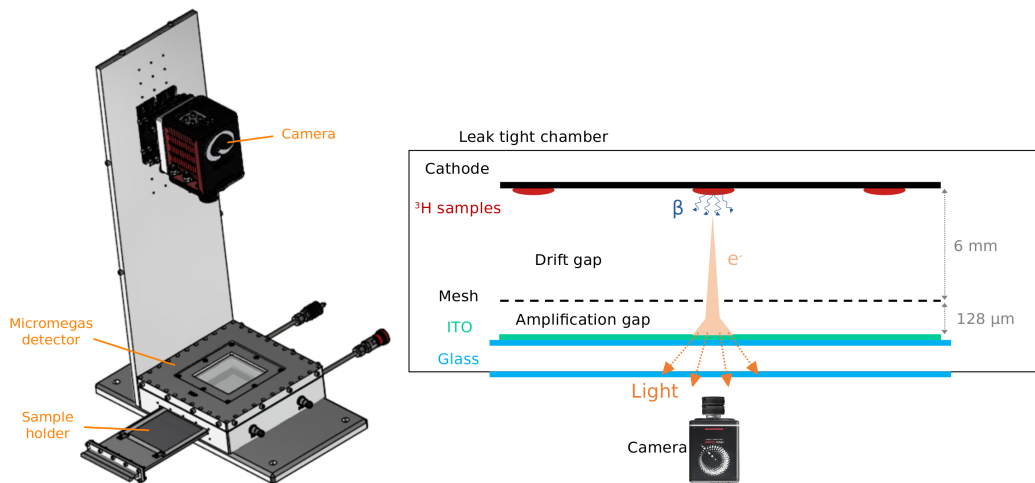


Figure 7.2:  $\beta$  imager overview (left) and principle of operation (right).

The glucose drops have a volume of  $1\ \mu\text{L}$  and are deposited by hand with a pipette with a unique plastic tip per sample to minimize the uncertainty on the drop volume (Figure 7.3, left). The activity of the tritiated glucose is measured by liquid scintillation counting [109] on a  $100\ \mu\text{L}$  container and constitutes the reference for the activity quantification tests. In the following sections, measurements are performed on samples with expected activities of  $0.1\ \text{Bq}$ ,  $1\ \text{Bq}$  and  $10\ \text{Bq}$ . 12 samples of each activity are deposited on the cathode, following the pattern shown in Figure 7.3 (right).

The real activity and reference of each group of samples was measured at  $0.09\ \text{Bq}$ ,  $1.05\ \text{Bq}$  and  $9.8\ \text{Bq}$  by liquid scintillation counting. Mainly due to the deposition by hand of the  $1\ \mu\text{L}$  drops, an uncertainty of  $\sigma = 10\%$  is taken into account for these references. In parallel, autoradiography is performed with an industrial  $\beta$  imager (BetaIMAGER™ tRACER) [110] on glucose drops of the same solutions. The results from the industrial  $\beta$  imager and the Micromegas  $\beta$  imager are being compared in this chapter. The tritiated glucose solution sampling and measurements are illustrated in Figure 7.4.



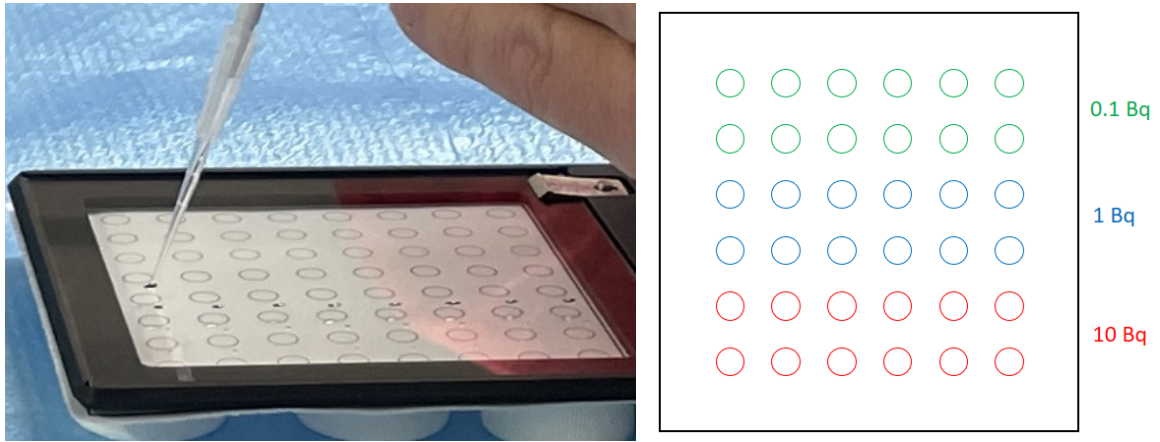


Figure 7.3: Picture of a tritiated drops deposition on the cathode (left). Sketch of the samples layout deposited on the cathode with their expected activities (right). There is a step of 1 cm between each sample.

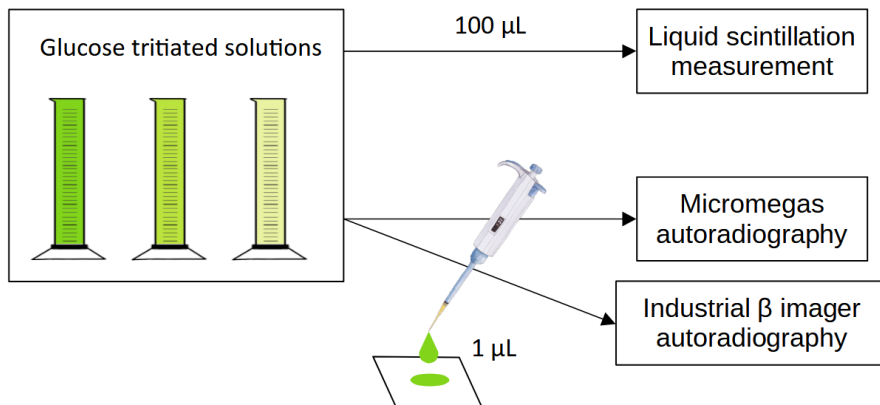


Figure 7.4: The tritiated glucose solutions of different activities are prepared by dissolution of the tritiated glucose. The solutions' activity of reference is measured by liquid scintillation counting.  $1 \mu\text{L}$  drops are deposited on sample holders and measured by the Micromegas and industrial  $\beta$  imagers.

### 7.3 . Autoradiography simulation

In a first instance, a simple simulation was computed on Geant4 [6] to study how the  $\beta$  particles are detected in our specific detector geometry, based on a development by F.J Iguaz Gutiérrez [111]. In particular, the  $^3\text{H}$  spectrum and the range of the  $\beta$  electrons are being calculated. Only the gas volume, the cathode, and a glucose sample are implemented in the simulation. The gas volume is made of a mixture of Argon, with either 5% of Isobutane or 20% of  $\text{CF}_4$ . It is  $8 \times 8 \text{ cm}^2$  wide and 6 mm thick. The cathode is made of 1.1 mm of glass coated with 150 nm of ITO and the sample is made of pure 2-Deoxy-d-glucose ( $\text{C}_6\text{H}_{12}\text{O}_5$ ). The sample is in direct contact with the ITO. By observation with a microscope, after drying, the sample shows a circular shape with a  $500 \mu\text{m}$  diameter. The equivalent volume of 1 Bq of tritiated glucose is  $633 \times 10^{-12} \text{ mm}^3$  according to the supplier. Given a surface of  $0.2 \text{ mm}^2$  and assuming that the glucose is uniformly distributed in a cylinder of  $500 \mu\text{m}$  diameter, the thickness of the sample is estimated at 3.2 nm. An initial  $\beta$  electron has an energy randomly picked from the  $^3\text{H}$  spectrum that has been computed by hand. The initial position of emission of the  $\beta$  particle is uniformly distributed inside the sample cylinder. The direction of emission of the initial electron follows a random distribution in the spherical coordinates such that  $\theta$  and  $\varphi$  are randomly picked in the intervals  $[0, \pi]$  and  $[0, 2\pi]$  respectively. The physics list *emlivermore* is used [112] for this simulation with a low energy production cut of 1 keV, a cut value of 1 nm and an ionization step of 0.1% of the  $\beta$  electron initial energy.

#### 7.3.1 . Energy spectrum simulation

To compute the detected energy spectrum, the total deposited energy by ionization in the gas is stored in a histogram for each  $\beta$  decay. Two effects on the detected energy are investigated, the edge effect from the cathode, and the auto-absorption of the glucose sample. Different geometries are implemented and shown in the Figure 7.5 (left) and the corresponding energy spectrum is displayed (right). In the first case (A), the electrons are produced in a large gas volume, and they interact only with the gas. The measured spectrum is identical to the emitted energy distribution. In the second case (B), the cathode only, made of glass and coated with 150 nm of ITO, is implemented. Some electrons will end up in the cathode made of high density materials and be fully absorbed. In these cases, either the event is not detected at all if the electron does not cross the gas, or the electron energy is partially detected if it crosses the gas before ending up in the cathode. The corresponding spectrum shows a shift towards the low energies and 53% of the initial events are detected. In the third case (C), the sample is implemented with a cylindrical geometry of dimensions  $500 \mu\text{m} \times 500 \mu\text{m} \times 3 \text{ nm}$ . A fraction of the electron energy is absorbed in the sample before it reaches the gas. For this sample thickness, the spectrum remains almost identical and 52% of the events are detected. In the last case (D) for a 50 nm thick sample, the spectrum undergoes a drop for energies below 5 keV, with a detection rate of 46%. To sum up, the edge effect of the cathode causes a significant modification of the spectrum shape with a drop of the number of detected events. The sample self-absorption induces a drop of the detection rate depending on the sample thickness, mainly for events of energies below 5 keV.

#### 7.3.2 . Electron range simulation

The range of the electrons in the gas is also computed to assess its influence on the spatial resolution. In this study, the range is defined as the maximum distance between ionizations along the path of a  $\beta$  electron. The Figure 7.6 (top) represents a histogram of the range as a function of the detected energy for the case C with a 3 nm thick sample. A linear correlation is clearly visible between the electron deposited energy and its range. This agrees with the Bethe–Bloch expression given in Sec.3.1.2 that shows the linearity between the particle variation of energy and range. One can notice a vertical distribution below 1 keV that corresponds to the energy shift to low energies coming from the cathode edge effect and sample self-absorption. A maximum range of several millimeters is reached in these conditions. However, it does not mean that the spatial resolution is affected by this same factor. The mean range is defined as the standard deviation of the total ionization position distribution around

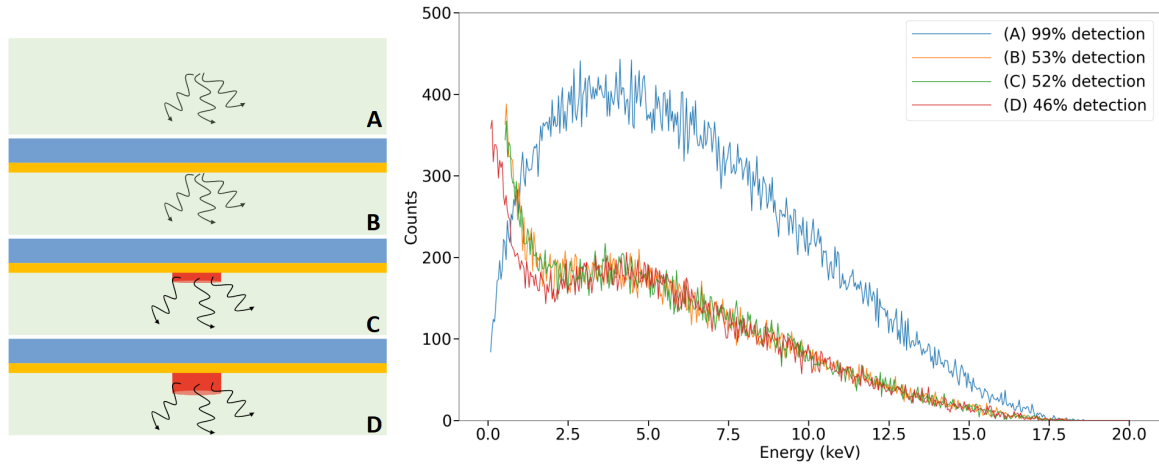


Figure 7.5: Sketches of the simulated geometry in four different cases (left). The gas volume (green), the electrons path (black), the cathode glass (blue), the ITO (yellow) and the sample (red) are represented. The distances are not to scale. Simulated energy distribution in the gas volume for four different cases (right) and for  $10^5$  initial particles in an Argon/Isobutane (95%/5%) gas mixture. The run name and detection ratio are shown in the legend.

the sample, weighted by the deposited energy at each ionization step. It expresses the degradation of the spatial resolution due to the electron range. The Figure 7.6 (bottom left) displays the distribution of the gas ionization position for a 1 nm thick and 1 nm wide sample. A point-like source has been simulated to assess the absolute mean range of  $\beta$  particles from  $^3\text{H}$ , without being impacted by the sample size. It is, in fact, shown that a maximum range above 1 mm is reached although it is also visible that the majority of the electrons are ionizing at a much shorter range. By fitting the 2D distribution on Figure 7.6 (bottom right), a standard deviation of  $52\ \mu\text{m}$  (FWHM =  $123\ \mu\text{m}$ ) has been measured. Hence, a degradation of the spatial resolution is observed due to the electron range.

#### 7.4 . $\beta$ detection with charge readout

To compute the total activity of all the samples shown in Figure 7.3, the energy spectrum is measured by reading out the charge signal from the mesh, as shown in Sec. 5.2.1. The total activity is computed by summing all the counts of the spectrum and dividing it by the total acquisition duration. The Figure 7.7 shows the measured energy spectrum in an Argon and Isobutane (5%) gas mixture with a beta mesh glass Micromegas detector (Sec. 5.1). The detector was operated at a gain close to  $10^5$ , where the energy threshold is estimated to 450 eV by extracting the noise level on the measured spectrum. The simulated spectrum from Sec. 7.3 is also represented for a sample thickness of 3 nm, and it is convolved by a resolution of 22%, which corresponds to the detector energy resolution in the current experimental conditions. A reasonable agreement of the measured and simulated spectra is observed, confirming the decrease in the detected energy due to the cathode edge effect and the sample self-absorption.

The measured spectrum is fitted with a polynomial function to smooth the curve fluctuations and to extrapolate the counts below the detection limit. The area below the fit is integrated to get the total number of counts and divided by the acquisition time, which gives a total activity of 74 Bq. According to the simulation conducted in Sec. 7.3, only 52% of the events are detected. The measured total activity corrected by the detection efficiency is then 142.3 Bq. This matches the total reference activity measured by liquid scintillation of  $131.28 \pm 12$  Bq within an error of one  $\sigma = 10\%$ . One method of sample activity quantification by optical readout, which will be described in the following sections, consists in using this total activity measured by charge readout as a normalization factor.

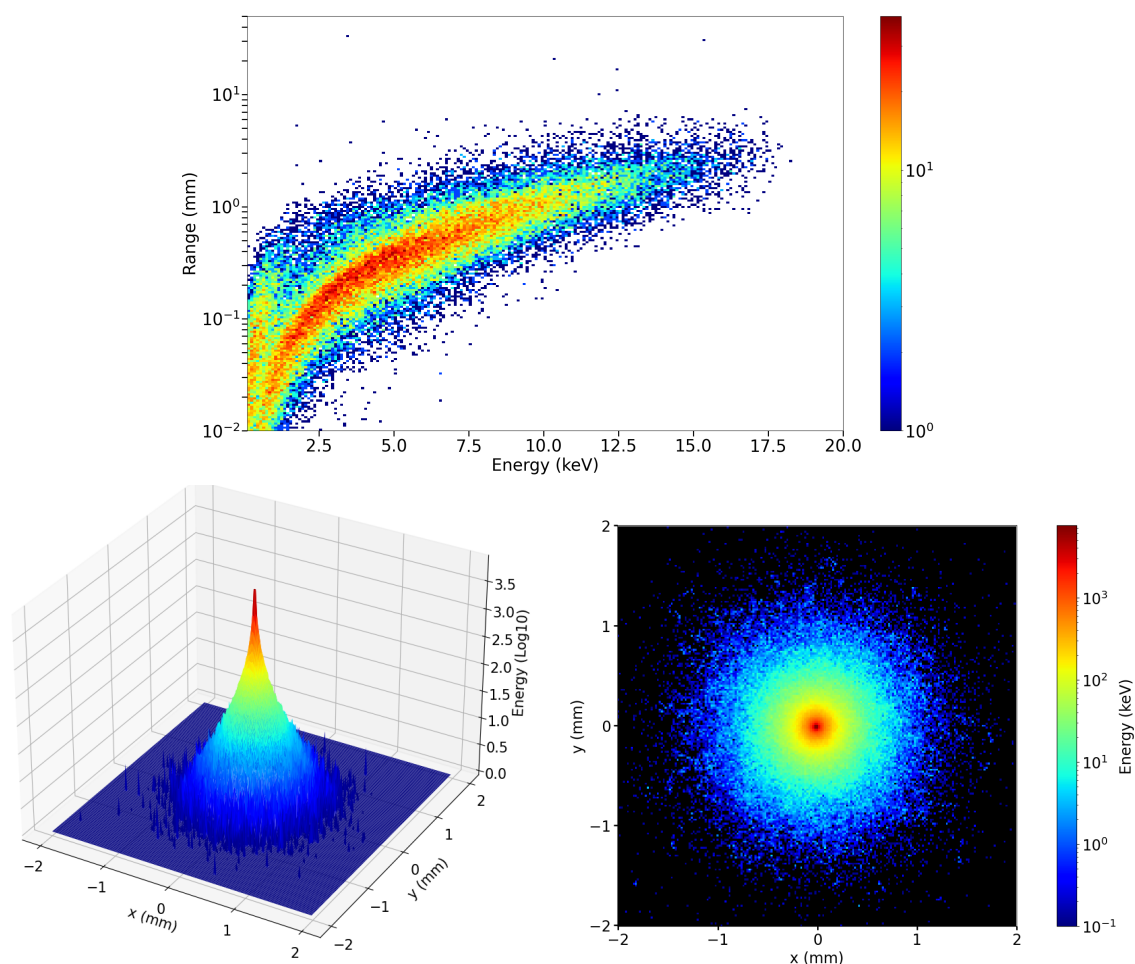


Figure 7.6: 2D histogram of the electrons maximum range as a function of the total electrons deposited energy (top). Both the vertical axis and the colour scale are logarithmic. 3D histogram of the positions of ionization in the gas (bottom left). The vertical axis represents counts and is in logarithmic scale. 2D histogram of the positions of ionization in the gas projected on the detection plane (bottom right). It is the projection over the vertical axis of the 3D histogram at the bottom left of the figure. A FWHM of  $123\ \mu\text{m}$  has been measured. The colour is in logarithmic scale.

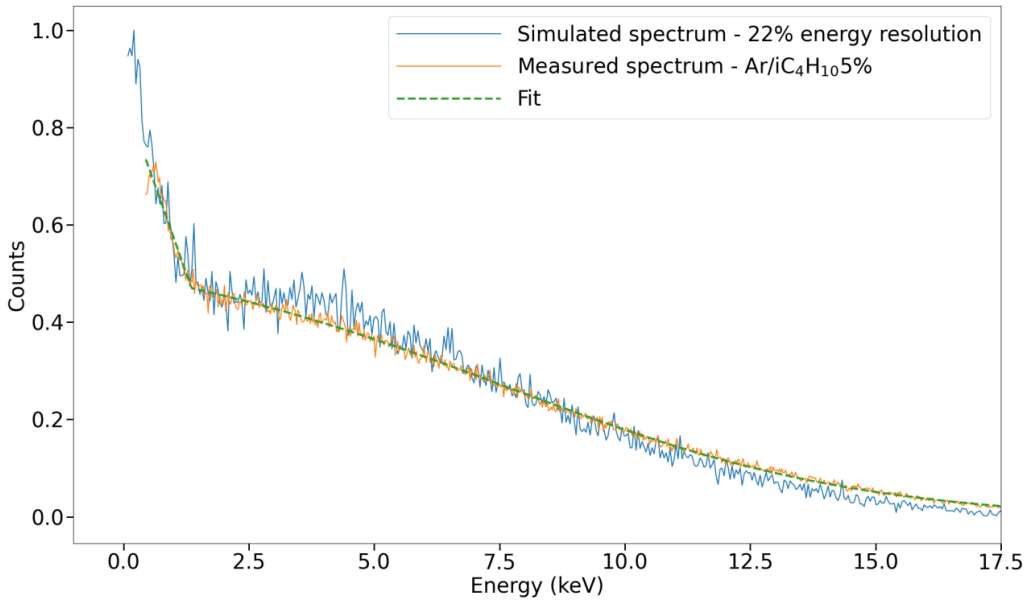


Figure 7.7: Measured energy spectrum (yellow line) of the tritiated samples in an Argon and 5% Isobutane gas mixture with a beta mesh glass Micromegas detector. The gain is close to  $10^5$  and the energy resolution 22% FWHM. The spectrum is fitted (green dotted line) with a polynomial function above 2 keV and with a linear function below 2 keV. The simulated spectrum (blue line) from Sec. 7.3 for a 3 nm thick sample and convolved by a 22% resolution is represented. The spectra are normalized by their maximum count value.

## 7.5 . $\beta$ detection with optical readout

The imaging of the samples shown in Figure 7.3 has been performed by optical readout, allowing precise position reconstruction and activity quantification in real time. The aim is to compute the light signal emitted per sample and to correlate it to the individual sample's  $^3\text{H}$  activity. The measurements are performed at a lens aperture of  $f/0.95$ , covering a field of view of  $10 \times 10 \text{ cm}^2$ . The gas mixture is composed of Argon/ $\text{CF}_4$  (80%/20%). The detection and activity quantification of sub-becquerel activity samples require significant detection efficiency to separate such low signal from the background. Moreover, the accuracy of the activity measurement and the shortening of the total duration of the measurement constitute major goals.

Considering the number of photons produced per unit of energy deposited in the gas, the geometrical acceptance, and the experimental setup detection efficiency (Sec. 5.2.2), the expected number of photons captured per pixel, following the energy distribution of the  $^3\text{H}$   $\beta$  spectrum, has been computed in Figure 7.8. The total noise of the camera has also been computed and plotted for comparison. The SNR (7.1), detailed in Sec. 4.3.1, has been assessed and plotted versus the number of photons per pixel, with  $N_*$ ,  $N_D$  and  $\sigma_R$  the number of photons per pixel, the number of dark current electrons per pixel and the readout noise respectively. Thanks to the low readout noise of the camera ( $0.27 \text{ e}^- \text{ RMS}$ ), most of the  $\beta$  events present high enough SNR to be detected. Two different modes of operation will be tested: a single event mode, where short acquisition time frames are acquired and single light clusters are captured, and an integration mode, where the events' light signals are accumulated through long integration time frames.

$$\text{SNR} = \frac{N_*}{\sqrt{N_* + N_D + \sigma_R^2}} \quad (7.1)$$

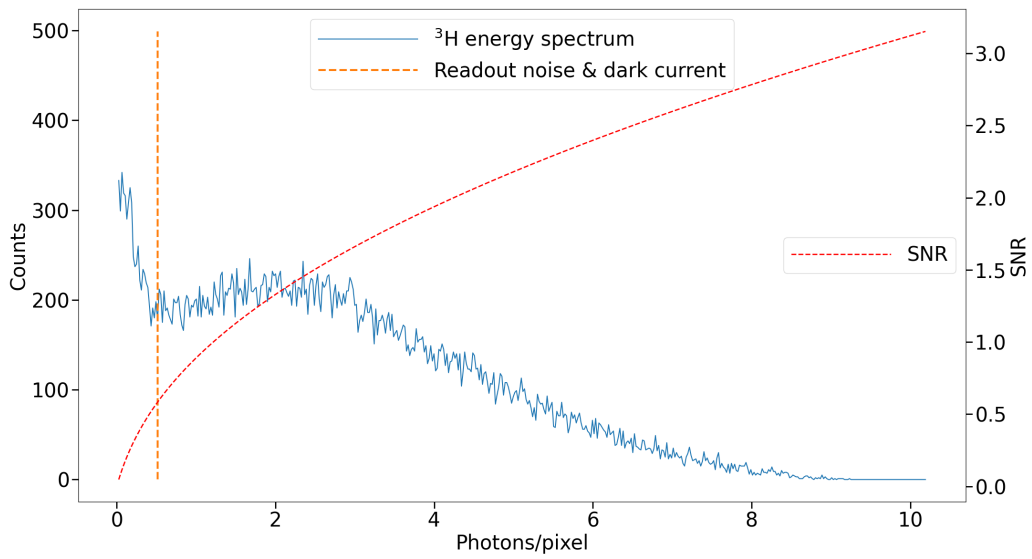


Figure 7.8:  $^3\text{H}$   $\beta$  energy distribution (blue line) converted in photons per pixel after computation of the Micromegas light yield, geometrical acceptance and detection efficiency. qCMOS camera readout noise ( $\sigma_R$ ) and dark current variance ( $N_D$ ) for a 5 s exposure time (yellow line) summing up following the expression  $\sqrt{N_D + \sigma_R^2}$ . Signal-to-noise ratio (SNR) as a function of the number of photons per pixel (red line).

### 7.5.1 . Single event mode

The detection of single events by recording short integration time frames is the first method that has been explored. It is also the process implemented in other industrial  $\beta$  imagers based on optical readout, like the  $\beta$  imager 2000 [110]. This method allows the quantification of the samples' activity by counting the number of clusters that have been recorded. Computing the center of gravity of each cluster, to reconstruct the  $\beta$  electron mean position, provides an enhanced spatial resolution. The lens aperture is settled to the maximum aperture ( $f/0.95$ ). The camera was operated in Ultra Quiet mode, reaching a suitable sensitivity (readout noise of  $0.27 e^-$  RMS), necessary to the imaging of single low-energy events. Due to the Ultra Quiet mode, and accessing to  $2048 \times 2048$  pixels<sup>2</sup>, the minimum integration time is 200 ms. Such long shutter opening period involves a probability of having an overlapping of events, especially for the 10 Bq samples. According to the Poisson statistics, the probability of recording  $k$  events for a mean detection rate  $\lambda$  is given by  $P(X = k)$  with  $X$  the number of detected events during a 200 ms period. The probability of having an overlap  $P(overlap)$  is given by the expressions:

$$P(X = k) = \frac{\lambda^k}{k!} e^{-\lambda}$$

$$P(overlap) = \frac{P(X > 1)}{P(X > 0)}$$

For a detection efficiency of 52% and an acquisition time of 200 ms,  $\lambda = A \times 0.52 \times 0.2$  with  $A$  the samples activity from the liquid scintillation reference in Becquerel. Hence, there is a probability of overlapping of 42.5% for the 10 Bq samples, 5.4% for the 1 Bq samples and 1% for the 0.1 Bq samples. The quantification of the 10 Bq samples especially is expected to be under estimated because of the high overlap probability.

The clustering algorithm is detailed in Sec. 5.4 and illustrated in Figure 5.27 for  $\beta$  decays from  $^3\text{H}$ . For each cluster, a Gaussian fit is performed to extract the center of gravity, and its total light intensity is recorded. The distribution of the cluster's position is shown in Figure 7.9 after 1 h of measurement. The positions of the samples are clearly identified, even for the low activity ones. To compute the activity per sample, square areas of  $8 \times 8 \text{ mm}^2$  are defined around each sample. Each of these boxes is expected to contain all the detected clusters emitted from a sample. The counts contained in a box are summed up and saved for every sample.

To quantify the activity of each sample and thus to correlate counts and activity, three different normalisation methods are investigated:

- The samples of 9.8 Bq activity are used as a reference. A calibration factor expressed in Becquerel per counts is obtained for these specific conditions (area size, integration time, gain, ...). The activity of the other two categories of sample, of expected activities 1 Bq and 0.1 Bq, are then measured by multiplying their counts by the calibration factor.
- The spectrum measured in Sec. 7.4 gives a total activity of 142.3 Bq. The counts' distribution map is normalized by the overall activity measured by charge readout. This method does not require preparing and analyzing a calibration sample like in the previous method, which constitutes a significant advantage for industrialized applications.
- The activity per sample is obtained by adding up the number of counts per sample and dividing it by the total duration of the measurement. It is then corrected by the overlap probabilities calculated above.

The mean activity for each group of activity was measured by the three methods previously explained and is plotted on Figure 7.10 versus the reference by scintillation counting. The linearity between the measured and reference activity is maintained. This is possible thanks to the Micromegas detector high stability, that can operate at a significant gain when exposed to high activity samples. Besides, it is sensitive enough to detect the low activity samples. The method consisting in counting

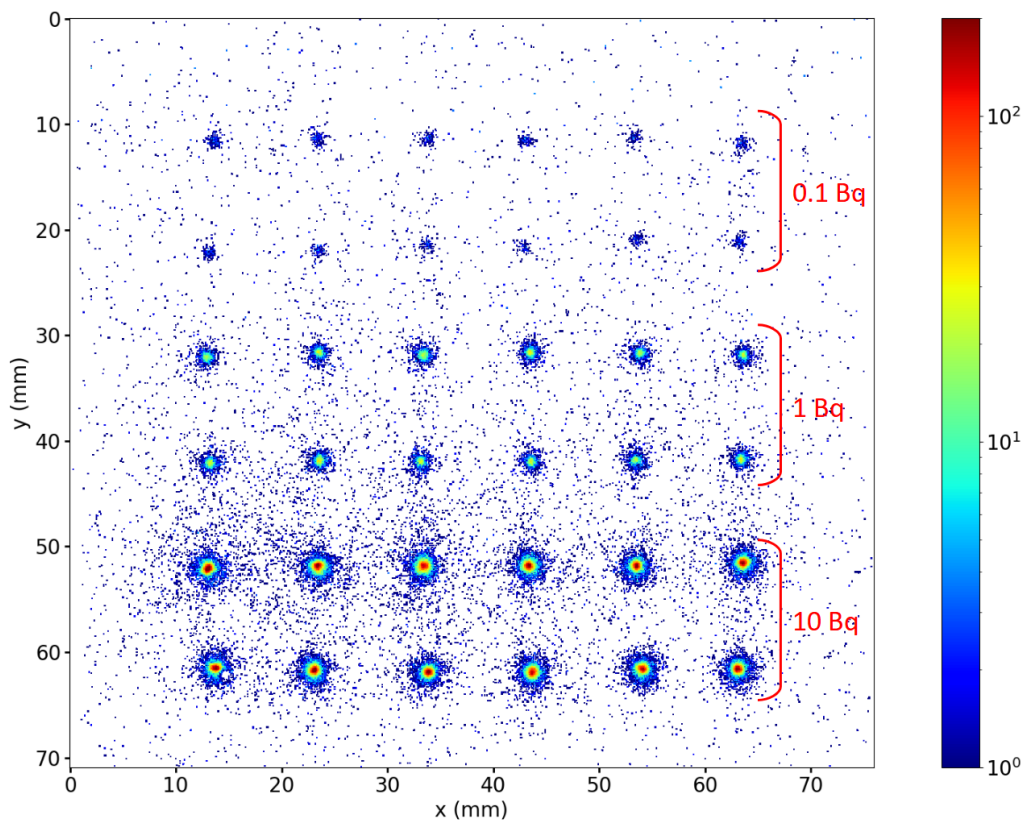


Figure 7.9: 2D histogram of the cluster's center of gravity after 1 h of measurement with 200 ms frames. The colour scale is logarithmic, and the bins are weighted by the cluster counts. The gas mixture is made of Argon and  $\text{CF}_4$  (20%) and a beta mesh is used with a  $75\ \mu\text{m}$  amplification gap thickness. The drift field is  $700\ \text{V}/\text{cm}$ , the amplification field of  $69\ \text{kV}/\text{cm}$  and the gain at about  $3 \times 10^4$ .



the clusters shows a better concordance with the reference and agrees within a  $1.5 \sigma$  error for the lowest activities. The gap with the reference increases to  $2 \sigma$  for the 10 Bq group which probably comes from the events overlapping remaining error. The other two methods concur and agree within a  $2.5 \sigma$  and  $3.5 \sigma$  error with the reference for the 0.1 Bq and 1 Bq samples respectively. The approach by charge normalisation fits the reference with a  $0.5 \sigma$  deviation only for the 10 Bq group. There is no trivial explanation for the larger deviation from the reference for the 1 Bq samples, compared to the 0.1 Bq sample, but it is potentially issued from a flawed measurement of the reference. However, the method by charge readout normalisation has the advantage of being self-consistent, and does not require a reference sample of known activity, or to compute the probability of overlapping for specific activities.

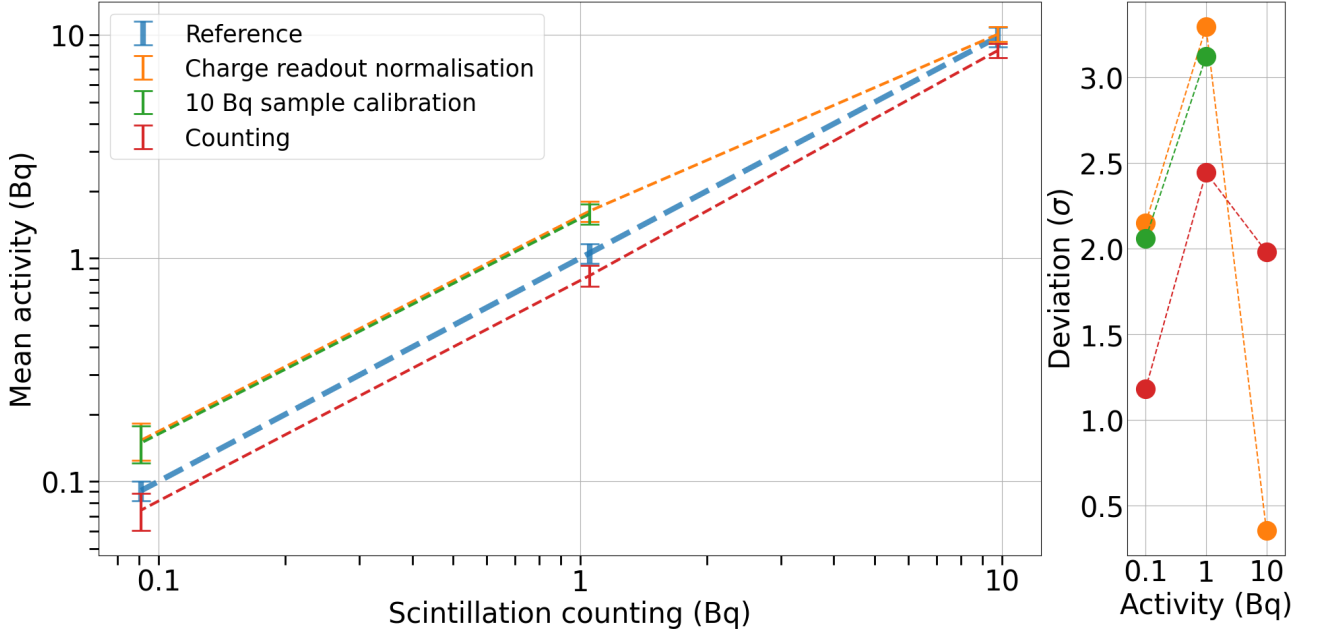


Figure 7.10: Comparison of the activities measured by the three measurement methods with the liquid scintillation reference (left). The activities measured for the 12 samples of each group are averaged, and the error bar is defined by the standard deviation ( $\sigma$ ) of each group. The reference is plotted for better clarity (blue line) as  $y = x$  with a 10% error due to the  $1 \mu\text{L}$  drop volume uncertainty. The activity measurement performed by charge readout calibration (yellow line), by using the 10 Bq sample as a reference (green line) and by counting of the clusters and correcting the overlaps (red line) are shown. On the right plot, the difference between the measurement and the reference, called the deviation and expressed as a factor of the error  $\sigma$ , is represented for all methods with the same colour code. The drift field is  $700 \text{ V/cm}$ , the amplification field of  $69 \text{ V/cm}$  and the gain at about  $3 \times 10^4$ .

### 7.5.2 . Integration mode

Recording short integration time frames and counting single clusters allows indeed to perform accurate quantification and position reconstruction of event. However, it requires processing a large amount of data and developing complex analysis algorithms. On the other hand, integrating the light from long integration time frames does not involve such constraints and also provides activity quantification with an acceptable spatial resolution. The detection sensitivity (Figure 7.8) remains the same for any sample activity in the single event mode because only one event is captured per frame (2 or 3 events occasionally happen per frame for the 10 Bq samples). On the other hand, in the integration mode, more than 10 events are stacking in one frame for the 10 Bq samples and only 1 event is recorded per frame for the 0.1 Bq samples in general. The noise being also integrated, lower SNR values are expected for the low activity samples.

For these measurements, 5 s exposure time frames are acquired during one hour in total. The lens aperture is set to  $f/0.95$  for an optimal sensitivity although the image sharpness is affected. The gas

is a mixture of Argon and 20% of  $\text{CF}_4$ . To enhance the sensitivity, images are binned by merging pixels 4 by 4, having an intensity per pixel 16 times larger. A moving average filter is also applied to each frame, assigning to each pixel the averaged value of the 9 neighbors. As explained in Sec. 5.4, the background image is subtracted for every frame and a threshold of  $3\sigma$  is applied. The frames are finally added up, giving the image shown in Figure 7.11 (top). The samples pattern depicted in Figure 7.3 and the activity groups are well identified since the light intensity is proportional to the sample activity. Hence, a relative measurement of the activity is provided for 36 samples at once, with few data processing. For this purpose, regions of interest (ROI) of  $8 \times 8 \text{ mm}^2$  are defined for all samples and the light intensity that a ROI contains is summed up. The ROI light intensity is then subtracted by the intensity of a background ROI located outside the Micromegas detector active area (Figure 7.11, bottom). This operation removes the noise counts that comes from a potential light leak of the chamber, remaining camera noise or natural background signals.

To obtain an absolute measurement of the samples activity, a correlation between light amount and activity is required. Two types of normalization methods are explored and were already used in the previous section on single event reconstruction:

- The samples of 9.8 Bq activity are used as a reference. The activity of the two other categories of sample of expected activities 1 Bq and 0.1 Bq are then measured by multiplying their light intensity by the calibration factor.
- The spectrum measured in Sec. 7.4 gives a total activity of 142.3 Bq. The light intensity map that gives a relative activity measurement for all the samples is then normalized by the overall activity measured by charge readout. Once again, this method does not require a calibration sample like in the other method.

The Figure 7.12 shows the averaged activity measured for each activity group for the two methods detailed above. The reference measured by liquid scintillation is drawn on the horizontal axis to assess the precision of the activity quantification. This measurement confirms the linearity between the measured activity by the Micromegas detector and by the scintillation counting reference. While the measurement at 10 Bq is in adequacy with the reference, the other low activities show a rough agreement within an error. While both methods are comparable in terms of precision, the calibration by charge readout is self-consistent since no additional sample for calibration is required. The overall activity measurement by charge readout and the optical readout measurement are performed in parallel with the same gas mixture and does not imply additional investment of time.

The time of acquisition required to perform activity quantification also represents a major aspect of the Micromegas  $\beta$  imager. The activity has been measured every 30 s for one sample of each group and displayed on Figure 7.13 (top). The aim is to reach an accurate quantification in the shortest time possible. It is shown that 10 minutes of acquisition are enough to converge toward a steady solution for any group of activity. As mentioned earlier, the measured samples activities agree within an error with the references. The Figure 7.13 (bottom) represents the difference between the measured activity and the reference, normalized by the standard deviation along time. After 10 minutes, the 10 Bq, 1 Bq and 0.1 Bq activities are assessed within a  $0.5\sigma$ ,  $2.5\sigma$  and  $1.5\sigma$  error respectively. The error on the 1 Bq samples quantification is yet again larger than the error on the 0.1 Bq samples. A similar anomaly was observed applying the single event method, studied in Sec. 7.5.1. Having the same effect for different methods of activity quantification confirms that there is an additional error from the scintillation counting reference for the 1 Bq group.

## 7.6 . Comparison with other $\beta$ imagers

The glass Micromegas  $\beta$  imager has demonstrated high performance in terms of low activity samples sensitivity and activity quantification. These results lie in the industrial context of pharmaceutical research for the development of new cancer treatment drugs and have proven that the Micromegas  $\beta$

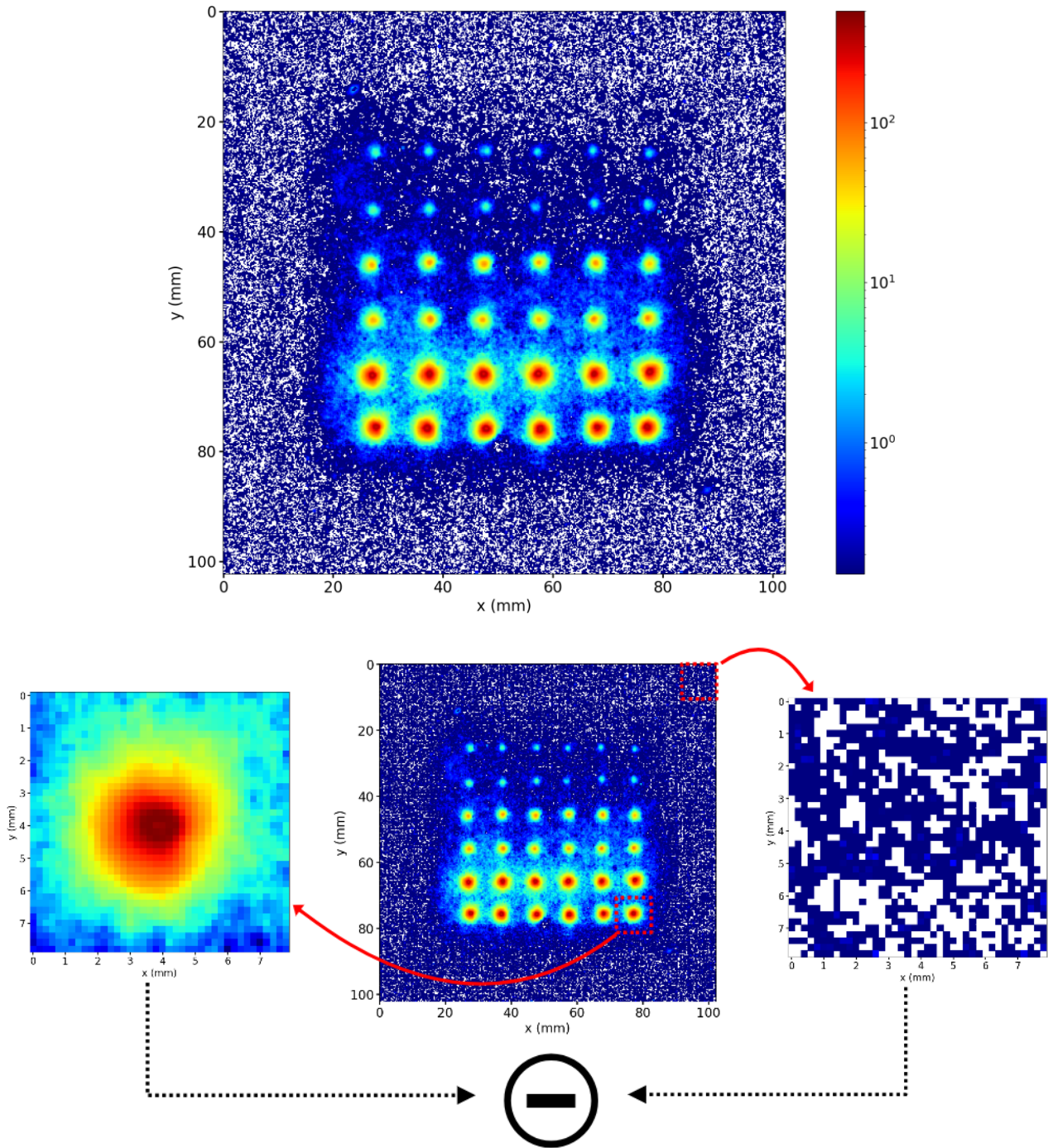


Figure 7.11: Light intensity frame of tritiated samples of expected activities of 10 Bq, 1 Bq and 0.1 Bq. 5 s acquisition-time frames are background subtracted with a  $3\sigma$  threshold and added up for a total of 1 h acquisition. The gas mixture is made of Argon and  $\text{CF}_4$  (20%) and a beta mesh is used with a  $75\ \mu\text{m}$  amplification gap thickness. The drift field is  $700\ \text{V}/\text{cm}$ , the amplification field is  $69\ \text{V}/\text{cm}$  and the gain is at about  $3 \times 10^4$ . The colour scale is logarithmic. Illustration of the ROI delimitation and light integration for a tritiated sample signal and a background signal (bottom). The signal from the sample is then subtracted by the background signal.

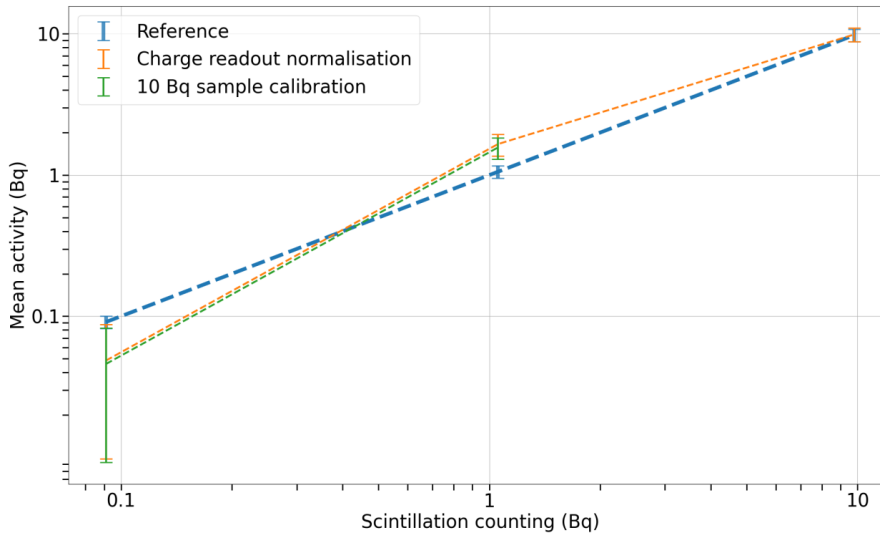


Figure 7.12: Comparison of the activities measured by the two calibration methods with the liquid scintillation reference. The activities measured for the 12 samples of each group are averaged, and the error bar is defined by the standard deviation of each group. The reference is plotted for better clarity (blue line) making a curve of equation  $y = x$  with a 10% error due to the  $1\ \mu\text{L}$  drop volume uncertainty. The activity measurement performed by charge readout calibration (yellow line) and the one performed by using the 10 Bq sample as a reference (green line) are shown. The drift field is 700 V/cm, the amplification field of 69 V/cm and the gain at about  $3 \times 10^4$ .

imager is already competitive compared to other  $\beta$  imagers. This section is dedicated to the state of the art of different imagers and to their comparison.

### 7.6.1 . Biospace $\beta$ Imager 2000 comparison to Micromegas

The BetaIMAGER tRACER [101, 43] has demonstrated simultaneous detection and discrimination of  $^3\text{H}$  and  $^{14}\text{C}$  with quantification of the sample's activity [98]. Real-time measurement with high accuracy has been performed and the relation of linearity between measured activity and reference activity measured by liquid scintillation has been confirmed. The high sensitivity and energy resolution of the BetaIMAGER was achieved thanks to the combination of a proportional avalanche chamber with a double amplification structure and a highly intensified charge coupled device camera. It provides a spatial resolution down to  $50\ \mu\text{m}$  for  $^3\text{H}$  and covers an active area of  $20 \times 25\ \text{cm}^2$ . To compare the quantification of the BetaIMAGER and the glass Micromegas detector, the measurements performed in Sec. 7.5 have also been done with the BetaIMAGER in similar conditions.

Triated glucose samples of activity 9.8 Bq, 1.05 Bq and 0.09 Bq were integrated to the BetaIMAGER for a 1 h measurement for quantification. The activity measured for each sample group and its deviation with the scintillation counting reference is shown in Figure 7.14, after correction of a 52% detection efficiency (according to Sec. 7.3). The data from Sec. 7.5 is also shown, representing the results from the single event mode (clusters counting method) and the integration mode (charge readout calibration). While the quantification with the glass Micromegas detector agrees with the reference within a  $3\sigma$  error, the BetaIMAGER shows a constant offset of at least 50% with the reference. Moreover, the quantification with the glass Micromegas detector is self-calibrated, meaning that no calibrated sample is required.

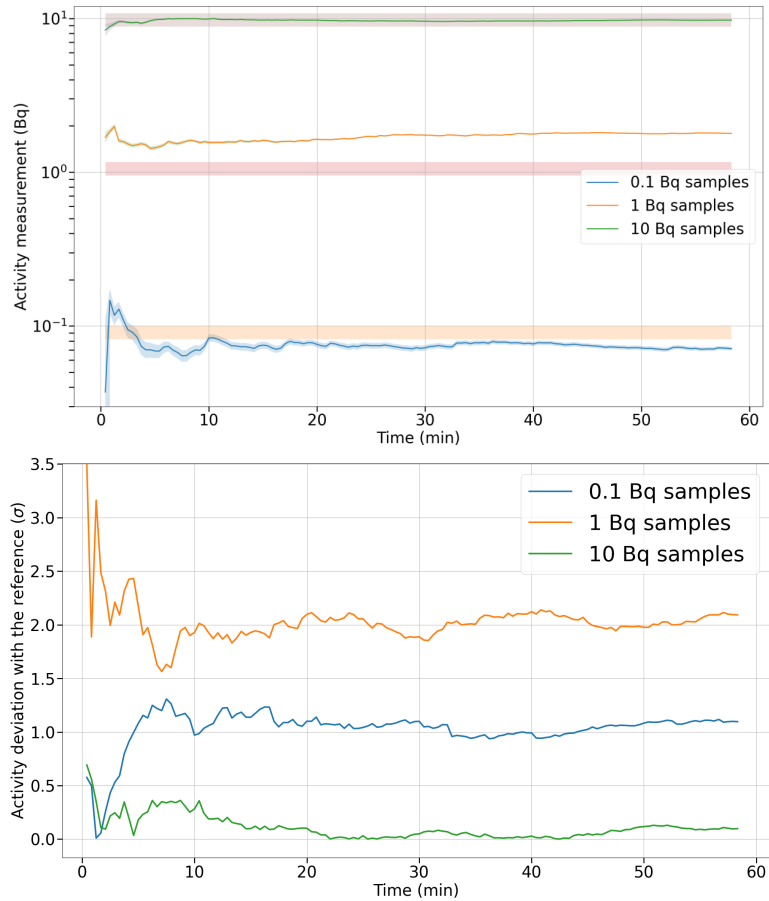


Figure 7.13: Distribution of the measured activity by charge readout calibration along time for a single sample for each activity group (top). The 0.1 Bq (blue line), 1 Bq (yellow line) and 10 Bq (green line) are represented. Semi-transparent bands indicate the liquid scintillation reference for each group of activity with a 10% error. The vertical axis is in logarithmic scale. The difference between the measured activity and the reference expressed as a factor of the error  $\sigma$  (standard deviation among 12 samples from each group) is represented along time (bottom).

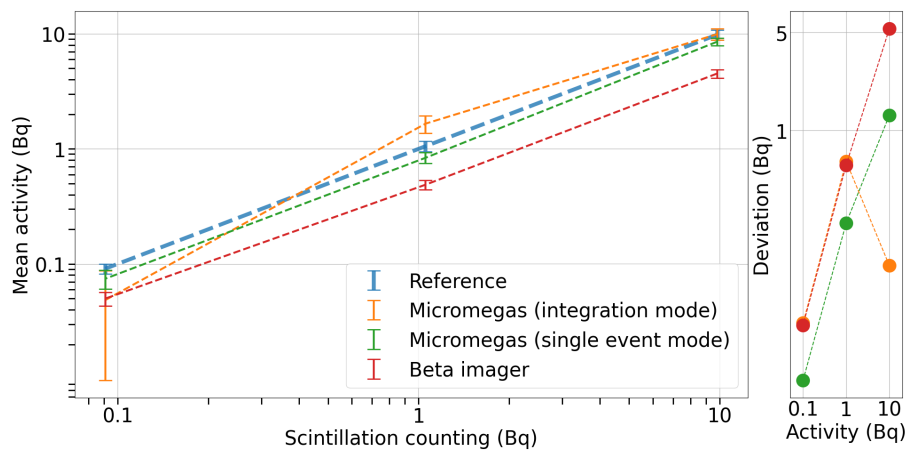


Figure 7.14: Comparison of the activities measured by the BetaIMAGER and the glass Micromegas detector with the liquid scintillation reference. The activities measured for the 12 samples (3 for the BetaIMAGER) of each group are averaged and the error bar is defined by standard deviation of each group. The reference is plotted for better clarity (blue line). The activity measurement performed by the Micromegas detector in integration mode (yellow line) and in single event mode (green line) are shown. The results from the quantification with the BetaIMAGER is shown in red. On the right hand side of the figure, the difference of the measurements with the reference is represented.

### 7.6.2 . The PIMager

Autoradiography has been performed with the PIMager [104, 103] detector with a spatial resolution of  $22\ \mu\text{m}$  (FWHM) on  $^3\text{H}$  gelatin samples as shown in Figure 7.15 (right). Simultaneous detection and discrimination of  $^3\text{H}$  and  $^{14}\text{C}$  have also been demonstrated. Such spatial resolution was obtained thanks to the double amplification structure of the PIMager that exposes the  $\beta$  particles that are close to their position of emission to a higher gain. The uncertainty on the spatial resolution brought by the electron range in the gas is drastically reduced.

To determine the spatial resolution of the glass Micromegas detector in similar conditions, a clusters 2D distribution was computed on a 10 Bq sample from the images obtained in Sec. 7.5.1. The profile shown in Figure 7.15 (left) corresponds to a spatial resolution of  $260\ \mu\text{m}$  given by the following expression, where the glucose drop is  $500\ \mu\text{m}$  wide and  $\sigma$  is the standard deviation extracted from the fit of the drop image.

$$\text{FWHM} = \sqrt{(2.355 \cdot \sigma)^2 - 500^2} = 260\ \mu\text{m}$$

In fact, in the glass Micromegas  $\beta$  imager, no amplification is performed in the drift gap and the spatial resolution is highly degraded by the electron range in the gas. Moreover, the spatial resolution in integration mode (Sec. 7.5.2) is even more degraded by the electron diffusion and the optical effects. However, the glass Micromegas  $\beta$  imager was developed for high sensitivity performances from the perspective of quantifying sub-becquerel tritiated samples. In the current experimental setup, the samples are well separated by a known distance and a spatial resolution of few hundred  $\mu\text{m}$  is sufficient. This technology gives the advantage of being of simple use and reduced cost. It avoids charge readout that involves thousands of channels and electronic cards which are of poor availability, high complexity and less reliable than optical readout. Nevertheless, for any application requiring high spatial resolution, the glass Micromegas detector can be easily adapted with the preamplification mode, which will be demonstrated in Sec. 8.4.

The performance of the glass Micromegas detector in terms of spatial accuracy has been further investigated in Appendix. A.1, using extended tritiated sources.

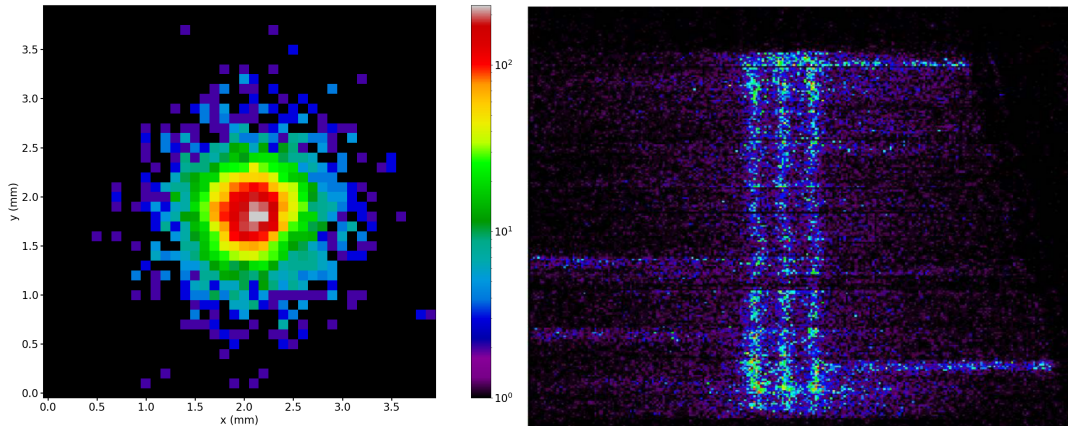


Figure 7.15: Imaging in single event mode of a 10 Bq tritiated sample of  $500\ \mu\text{m}$  width recorded by the glass Micromegas detector from Sec. 7.5.1 (left). 2D imaging of  $^3\text{H}$  gelatin slits imaged by the PIMager detector from [104] (right). The bars have a  $20\ \mu\text{m}$  width and are separated by  $50\ \mu\text{m}$ .

## 7.7 . Conclusion

This thesis contributes to the  $\beta$  imaging field by developing and testing a new beta imager based on a glass Micromegas detector coupled with a CMOS camera. This system enables simultaneous autoradiography of multiple tritiated samples with activities as low as a tenth of a Becquerel, offering both single event mode with reconstruction algorithms and light integration mode for simplified data processing.

Simulation studies illustrated the impact of detector design and sample properties on performance. The proximity of the cathode to the sample significantly affects the detection efficiency and the detected energy spectrum. The simulations also highlighted the influence of sample self-absorption, which depends on the sample thickness. Moreover, it was shown that the range of electrons in the gas degrades the spatial resolution, a key consideration for optimizing detector design.

The Micromegas detector demonstrates robust sensitivity and stability, successfully detecting both low and high activity samples. Several calibration methods were tested, including one that does not require a reference sample, which simplifies the process and enhances the practicality of the system for various applications. The ability to perform accurate quantification through two distinct methods; single event mode and light integration mode, showcases the detector's versatility.

In single event mode, individual beta events are detected and reconstructed, allowing precise quantification and spatial resolution. In light integration mode, the detector sums light intensity over longer periods, providing a simplified yet effective means of quantification. Both methods maintain a high level of accuracy, with the integration method achieving stable results within a few minutes, even for low activity samples. This rapid convergence towards a low deviation from the reference activity underscores the efficiency and reliability of the glass Micromegas beta imager.

A significant aspect of this technology is its simplicity and cost-effectiveness. This contrasts with charge readout systems, which necessitate intricate electronic setups and are generally more challenging to implement.

Overall, the glass Micromegas beta imager offers a robust, cost-effective, and user-friendly approach to beta imaging. Its capability to accurately quantify a wide range of activities with minimal setup and rapid convergence to reference values makes it a valuable tool for applications such as pharmaceutical research and beyond.

This work has paved the way for the development of an instrument that enables us to pursue research driven by biologists and microfluidists. This includes the quantification of drugs radiolabeled by  $^3\text{H}$  and  $^{14}\text{C}$  acting on various types of single cells.

In future developments, simultaneous detection of  $^3\text{H}$  and  $^{14}\text{C}$  will be investigated, requiring enhanced energy resolution and mitigation of the large range of the  $\beta$  particles issued from  $^{14}\text{C}$ . Implementation of a double amplification stage will be investigated to compensate the  $\beta$  particles' large range and improve the spatial resolution. Further simulations are required to study the impact of the drift gap thickness on the detection of  $^{14}\text{C}$ : the  $\beta$  electrons are expected to be partially detected because of their range shortening. Increasing the gas pressure is expected to reduce the  $\beta$  particles' range; towards enhanced spatial resolution and energy reconstruction. Additionally, investing in new lenses to decrease the distance of the lens from the detector will improve the solid-angle and the signal-to-noise ratio.

To summarize, the integration mode is well suited for the quantification of well localized tritiated cells, over a large surface of detection, with no risk of events overlapping. On the other hand, the single event mode is required for the double detection of  $^3\text{H}$  and  $^{14}\text{C}$ , accessing energy information. For future studies, increasing the gain, in order to improve the energy resolution, can be achieved by the hybridisation of the Micromegas detector with a GEM detector.

# 8 - Neutron radiography

## 8.1 . Context and applications

Neutron radiography has been considered as a reliable and non destructive imaging technique for the testing of the internal structure of different equipments. Photographic films and imaging plates have been a widespread and high spatial resolution technique for radiography for decades. However, they require significant time of film development. Most recent methods based on the coupling of a digital camera with a scintillator paved the way to tomography and dynamic neutron imaging thanks to a better handling of the data and timing resolution [113]. In parallel, MPGD technologies based on the GEM detector were developed using  $^3\text{He}$  as a converter. The coupling with a CCD camera has also been implemented to record the visible light emitted from the  $\text{CF}_4$  based gas mixture for neutron imaging [114]. Due to the shortage and price increase of  $^3\text{He}$ ,  $^{10}\text{B}$  solid converter was implemented with MPGD detectors based on the GEM, Micromegas and  $\mu\text{RWELL}$  technologies for neutron radiography and tomography [114, 115, 116, 117].

Neutron radiography covers a large scope of applications, from the examination of industrial components (battery, fuel cells, etc) to the direct support for research in many fields (physics, material science, biology, etc) [118]. Traditional methods of imaging, like X-ray radiography, are inappropriate for the investigation of objects covered by metal layers because of the large cross-section of X-rays with high atomic number atoms. In fact, X-rays interact with the electronic structure of the atom and are scattered or fully absorbed, leading to a reorganisation of the electronic layers (Figure 8.1, left). On the other hand, neutrons mostly interact with the nucleus of the atom (Figure 8.1, right) and have a large penetration depth. While the cross-section for X-rays interaction strongly depends on the number of electrons of an atom, the cross-section for neutron has no correlation with the atomic number and happens to be much larger for H than Al, Fe or Pb atoms (Figure 8.2). Even for isotopes like hydrogen and deuterium, the neutron probability of interaction is quite different. Hence, neutron radiography enables high contrasted imaging of H based materials and metals and is well suited for the examination of fluids flow in metal bulk, synthetic elements or any metal mechanic piece.

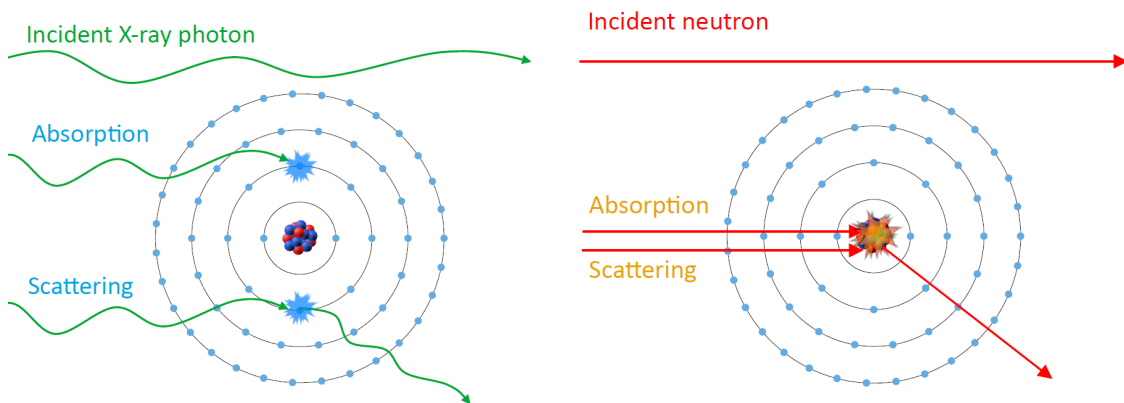


Figure 8.1: Sketch of the interaction of X-rays (left) and neutrons (right) with an atom.

The variation in space of the elements cross-section and materials density leads to an attenuation of the neutron beam intensity, which generates a contrasted image. The radiography is obtained by placing the object between the neutron source and the detector (Figure 8.3). The beam neutron intensity at a distance  $x$  from the source along the beam axis follows the Beer-Lambert law (8.1). Its solution (8.2) has a negative exponential distribution that depends on the incident beam flux  $I_0$ , the material density  $n$  (number of atom per  $\text{cm}^{-3}$ ) and the cross section  $\sigma$ . The cross section has two



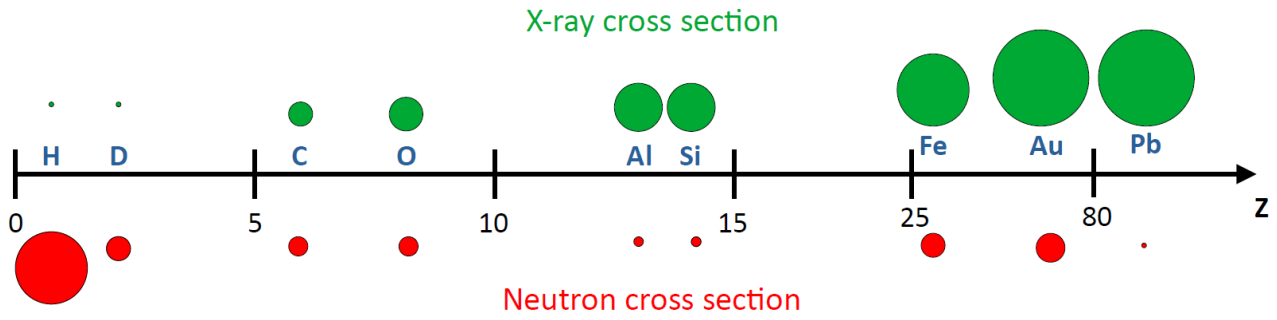


Figure 8.2: Relative cross section for X-rays (green) and thermal neutrons (red) being proportional to the size of the circles. The atoms symbol (blue) and their atomic number (black) are represented. Adapted from [119].

main contributions such that  $\sigma = \sigma_A + \sigma_S$  with  $\sigma_A$  and  $\sigma_S$  the absorption and scattering cross-sections respectively.

$$I(x + dx) = I(x) \cdot (1 - n\sigma dx) \quad (8.1)$$

$$I(x) = I_0 \cdot e^{-n\sigma x} \quad (8.2)$$

For any application, spatial resolution and detector sensitivity are the two main criteria for neutron radiography. Spatial resolution basically describes the sharpness of the image and the accuracy with which the object is reconstructed, both for radiography and tomography. Sensitivity is the ability to capture high-quality images in the shortest possible time. In order to improve the sensitivity, both the efficiency and the signal-to-noise ratio (SNR) matter. The efficiency contributes to increase the detection rate and to lower the statistical error while the SNR enhance the image contrast. It is shown in this chapter that the glass Micromegas detector fulfills both conditions, having a spatial resolution of about  $400 \mu\text{m}$  and a large SNR.

In comparison, classical neutron imagers are mostly solid states detector which achieve high detection efficiency and spatial resolution [113]. The best spatial resolution is achieved by photographic, X-rays films, and imaging plates ( $\sim 20 \mu\text{m}$ ). However, several minutes of exposure are required to obtain an image of good quality with films. Post-treatment of the film and imaging plates with a scanner is also time-consuming. Scintillators being coupled with a digital camera, the data treatment is instantaneous and spatial resolution below  $100 \mu\text{m}$  is usually achieved. The amount of light generated per neutron is nevertheless low, and long exposure duration is generally required. Image intensifier [120] are coupled to the camera to increase the amount of light, reducing the field of view and increasing the cost per pixel. On the other hand, the amplification structure of the Micromegas detector and high light yield allows short exposure time. Thus, it provides real-time imaging capacity and the possibility to perform radiography on moving objects [121]. Unlike solid state detectors, gaseous detectors involve high gamma discrimination and allow for neutron radiography in highly radioactive environment.

Besides, the Micromegas coupled with a digital camera provides an unlimited and linear dynamic range and tomography capability. It is scalable to an active area of the order of  $50 \times 50 \text{ cm}^2$ , has a high radiation hardness ( $> 10^6$  neutrons/s/cm) and gamma rejection ( $10^{-6}$ ) [122]. The radiation hardness, the gamma rejection and the dynamic range especially are key parameters to perform neutron radiography in high-radiation environments. In fact, nuclear waste and nuclear fuel characterization by neutron radiography involves the discrimination of the high gamma background of such object [123]. Moreover, the digital camera implemented in the Micromegas imaging system is out of the neutron beam axis and can be shielded in high-radiation environment. Thanks to the low hydrogen amount in the glass Micromegas detector, low detector activation probability is expected after neutron examination. All these benefits make the Micromegas detector suitable for the direct imaging of highly

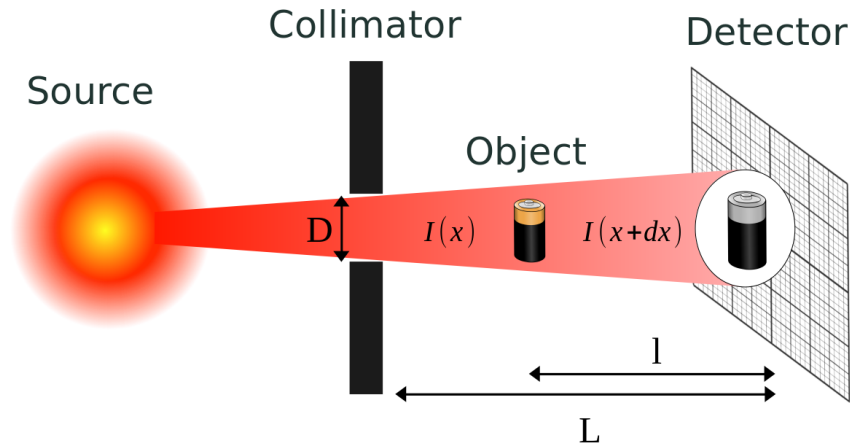


Figure 8.3: Scheme of the neutron radiography principle with a source collimated by a pinhole of diameter  $D$ , irradiating at a distance  $L$  between the pinhole and the detector plan. The object is at a distance  $l$  from the imaging plan.

radiating objects, such as irradiated fuel rods and nuclear wastes. The characterization of the spatial resolution and sensitivity of the glass Micromegas detector for neutron imaging is presented in this chapter.

## 8.2 . Setup description and $^{10}\text{B}_4\text{C}$ converter

Most of the elements of the neutron imager based on the coupling of a glass Micromegas detector and a digital camera are described in Sec. 5.1. The gas is a mixture of Argon and  $\text{CF}_4$  with either 10 % or 20 % of  $\text{CF}_4$ . For this instrument, a mirror is aligned in the optical axis, between the camera lens and the Micromegas detector, to reflect the scintillated light with a  $90^\circ$  angle and to take the camera out of the neutron beam axis (Figure 8.4).

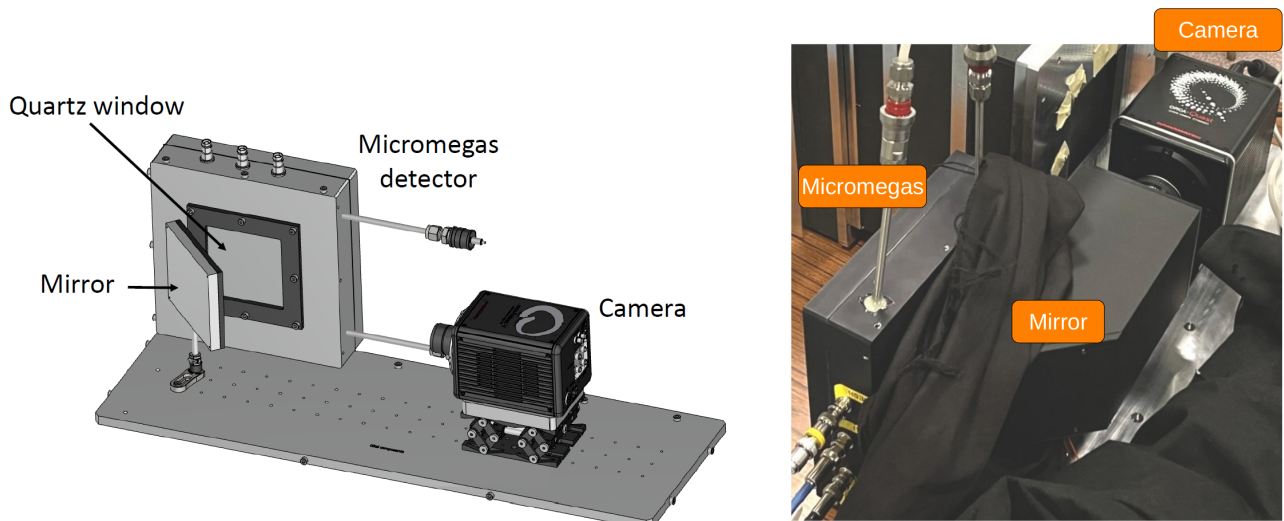


Figure 8.4: 3D drawing of the Micromegas neutron imager (left). Picture of the Micromegas neutron imager (right).

The cathode is one of the main features of this detector, being coated with a neutron-to-charged particle converter which mainly defines the detection efficiency of the detector. The cathode itself is a 5 mm thick piece of aluminium of  $8 \times 8 \text{ cm}^2$  being as flat and polished as possible. To adjust the

gap thickness between the mesh and the cathode, PCB spacers are used to support the cathode. The Figure 8.5 (left) shows a picture of the glass Micromegas detector settled in the leak tight chamber where the PCB spacers rest on the Micromegas walls. The neutron converter is a  $1.5\ \mu\text{m}$  thick layer of  $^{10}\text{B}_4\text{C}$  ( $>95\%$  enriched) deposited by evaporation on the cathode by the ESS Detector Coatings Workshop in Linköping, Sweden [124]. As shown in Figure 8.5 (right), the neutrons cross the aluminium cathode and are converted by the neutron capture  $^{10}\text{B}(n,\alpha)^7\text{Li}$  (Sec. 2.3) detailed in the equation (8.3):

$$n + ^{10}\text{B} = \begin{cases} \alpha (1.47\ \text{MeV}) + ^7\text{Li} (0.84\ \text{MeV}) + \gamma (0.48\ \text{MeV}), 94\% \\ \alpha (1.78\ \text{MeV}) + ^7\text{Li} (1.02\ \text{MeV}), 6\%. \end{cases} \quad (8.3)$$

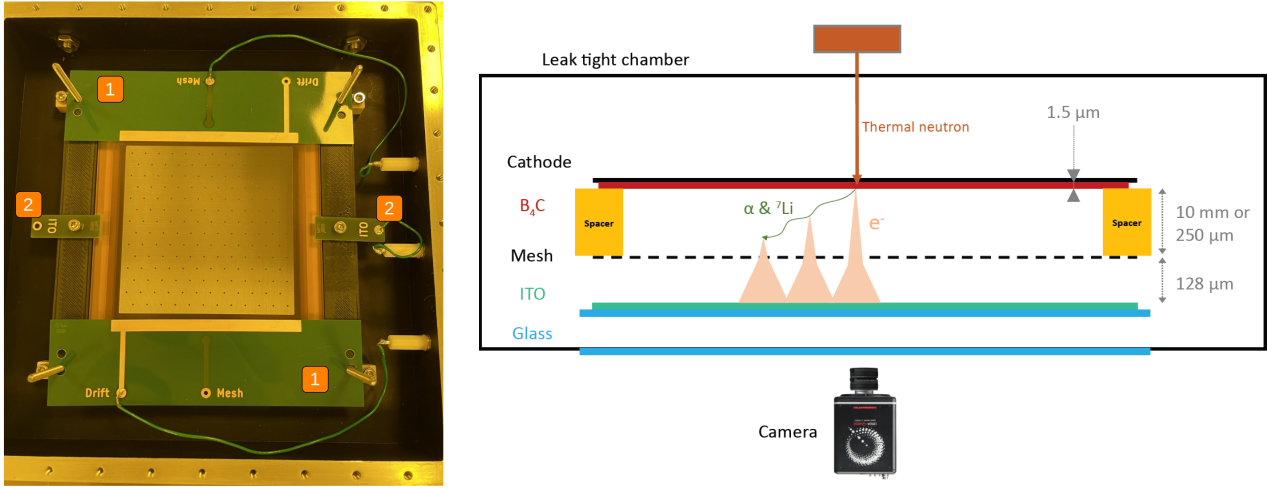


Figure 8.5: Picture of the glass Micromegas detector (left) fixed in the leak tight chamber by the PCB spacers (1) and the anode electrode contacts (2). Scheme of the glass Micromegas neutron imager (right). The thermal neutrons (brown arrow) are converted in the  $^{10}\text{B}_4\text{C}$  neutron-to-charge converter (red layer) into  $\alpha$  and  $^7\text{Li}$  fragments (green arrow). The drift gap thickness is defined by the PCB spacers (yellow boxes). The fragments ionize the gas and produce electrons that are drifted and amplified (pale red). The visible light is produced after the mesh in the amplification gap and is captured by the camera after crossing the ITO (green) and glass (blue) layers.

The  $\alpha$  and  $^7\text{Li}$  fragments are emitted back-to-back from the  $^{10}\text{B}_4\text{C}$  because of the momentum conservation. Thus, only one fragment reaches the gas volume per neutron conversion while the other fragment is lost in the cathode. Increasing the converter layer thickness increases the detection efficiency. However, the range of the fragments in the  $^{10}\text{B}_4\text{C}$  layer does not exceed few microns and the fragments are losing a large amount of their kinetic energy in the converter at larger thickness. There is thus an optimum detection efficiency of 4.5% for a converter thickness of about  $2.5\ \mu\text{m}$  and 3.5% at  $1.5\ \mu\text{m}$  thickness, for 25 meV neutrons according to [125].

Yet, cold neutrons are usually provided at neutron radiography facilities and the energy is  $\sim 3\ \text{meV}$  at the Paul Scherrer Institut (PSI) Morpheus beam line [126], where measurements were performed for this thesis. The neutron capture cross-section scales as  $1/\sqrt{E}$ : it is 3837 barn at 25 meV and about three times larger at 3 meV according to [7]. Since the detection efficiency is directly proportional to the cross-section, it scales up from 3.5% at 25 meV neutrons to about 10% at 3 meV neutrons, for a  $1.5\ \mu\text{m}$  thickness  $^{10}\text{B}$  layer.

According to [122], the signal amplitude induced in a Micromegas detector by gammas of energy above 1 MeV is well below the thermal neutrons signal. Because of the low interaction probability of gammas in gas, the gamma energy signal is indeed much lower than the neutron induced signal. The photoelectrons produced by the interaction of gammas with the detector solid materials have a large energy and low  $dE/dX$  in the gas. This separation is a key factor for the contrast between the neutron induced light signal from the gamma induced background.

### 8.3 . Single event study

A core element of the glass Micromegas neutron imager is the spatial resolution that is mainly affected by the visible light optical effects and the charges diffusion and range in the gas as detailed in Sec. 6.2. While the optical effects are similar to X-rays and  $\beta$  particles detection, the signal broadening induced by the electrons diffusion and the fragments range in the gas are worth studying. This section is dedicated to the characterization of single events from thermal neutrons detected by the glass Micromegas detector.

As presented in [127, 128], a first measurement was performed at the CERN Gas Detector Development (GDD) laboratory on an Americium–Beryllium source producing fast neutrons. The neutron source was contained in a block of polyethylene for thermalisation and a detection rate of about 4 counts/s was observed. The polyethylene block was placed as close as possible to the detector with no object between them (Figure 8.6). A mirror was included in the set-up to bring the camera out of the neutron flux and avoiding the camera degradation. For this first measurement, the drift gap is set to 10.5 mm to avoid that the fragments hit the Micromegas bulk before all their energy has been converted by gas ionization. A standard mesh has been used and an amplification field of 44.5 kV/cm was applied. Several 5 s exposure time frames were acquired and background subtracted.

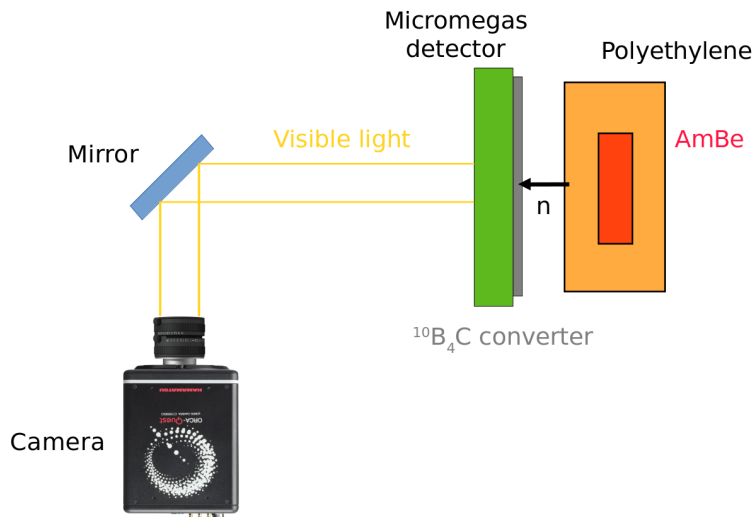


Figure 8.6: Sketch of the neutron imager exposed to neutrons emitted from a AmBe source and thermalized by a polyethylene block.

#### 8.3.1 . Fragments length measurement

The tracks from the fragments gas ionization shown in Figure 8.7 (A) were identified by the DB-SCAN clustering algorithm, after correction of the noise background (Sec. 5.4). The length of the recorded tracks were computed by extracting the norm of the vector defined by the two most separated coordinates of a cluster. The total light intensity of each track has also been measured by summing up the cluster pixels intensity. The length of about  $10^5$  tracks and their intensity is shown in Figure 8.8. The length of the projected fragments on the readout plane reaches several millimeters (3.6 mm in average and up to 8 mm). This illustrates that the fragments range brings uncertainty on the neutrons position assessment and significantly limits the detector spatial resolution. While there is a clear relation between the tracks light intensity and their length, no conclusion can be done on the fragments range dependency on their energy. In fact, the real fragments range can not be computed from the range of the projected fragments on the readout plane without the information on depth of the fragment interaction in the drift gap. Two distributions of the tracks' length are expected: one corresponding to the  $\alpha$  fragments and another at lower values for the  $^7\text{Li}$  fragments.

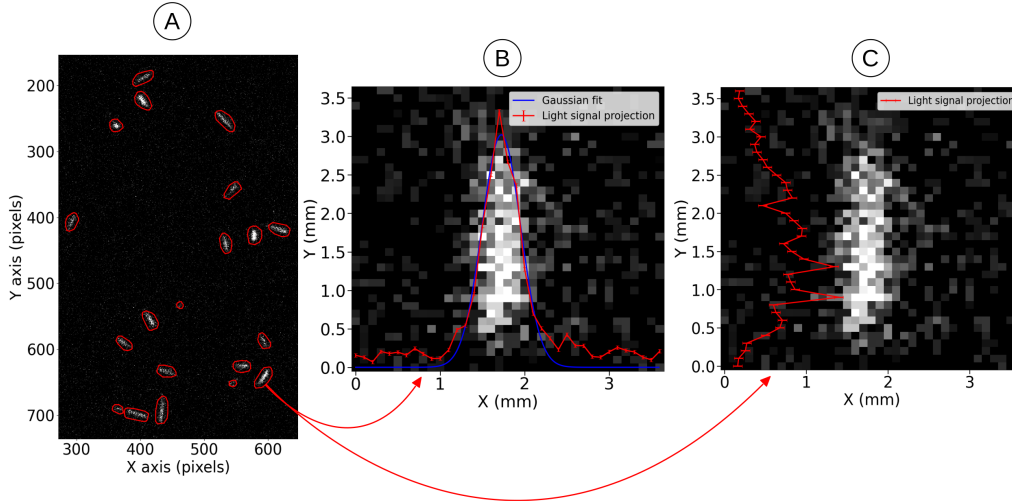


Figure 8.7: 2D light intensity profile of fragments from the neutron conversion from a 5 s exposure time frame (A). The  $\alpha$  and  ${}^7\text{Li}$  tracks are identified by the DBSCAN algorithm and encircled in red. Example of a track width measurement by vertical projection of the light intensity profile to a 1D profile and Gaussian fit (B). 1D horizontal profile of a track showing the non-uniform energy deposition along the track travelled distance (C).

A projection on the longitudinal track orientation allows to visualize the deposited energy as a function of the travelled distance in the gas (Figure 8.7, C). One can notice that more energy is deposited on one side on the track. This eventually corresponds to the Bragg peak of an  $\alpha$  fragment, illustrating that it loses more energy at the end of the track. However, according to [125], while  $\alpha$  fragments from the  ${}^{10}\text{B}_4\text{C}$  layer indeed generate more ionization at the end of the track, more energy is deposited at the beginning of the track for  ${}^7\text{Li}$  fragments. Such difference between the fragments strongly limits the reconstruction of the interaction position of the neutron with the converter. This reconstruction would be possible with the information on the depth of the fragment interaction in the drift gap, achievable with timing resolution [51].

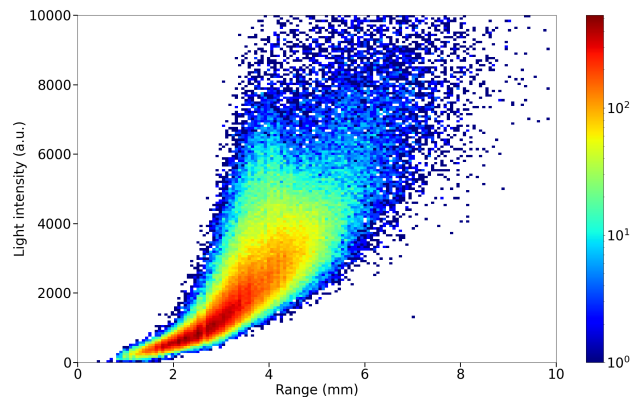


Figure 8.8: 2D histogram of the tracks light intensity versus their length. The projected fragments range reaches several millimeters length with an average value of 3.6 mm. The track light intensity and therefore the fragment energy increases with the track length.

### 8.3.2 . Fragments width measurement

While the spatial uncertainty is mainly brought by the fragments long range, the diffusion in the gas also contributes. Each track light intensity signal was rotated to a vertical orientation and projected on its vertical orientation giving a 1D profile (Figure 8.7, B). Fitting this profile with a Gaussian distribution allows to extract the width of the track. The width of the tracks is mainly determined by the electron diffusion in the drift gap. Moreover, the diffusion strongly depends on the electric drift field. The widths of about 1000 tracks have been extracted for three drift fields of 50 kV/cm, 840 kV/cm and 2100 kV/cm in a 10.5 mm drift gap. The mean tracks width ( $\sigma_{\text{Track}}$ ) was computed and displayed in Figure 8.9 for each drift field. The diffusion width ( $\sigma_{\text{Diff}}$ ) computed in Sec. 6.2.8 for a 20% CF<sub>4</sub>/Ar gas mixture has also been represented for comparison. It is first noticed that the measured tracks width follows the simulated diffusion trend with a minimum track width at 800 kV/cm that corresponds to the minimum of diffusion. The diffusion width was computed such that  $\sigma_{\text{Diff}} = D_T \times \sqrt{x}$  with  $D_T$  the transverse diffusion coefficient and  $x$  the drift distance. Because of the fragments range, ionization mostly occurs at a distance from the mesh smaller than the drift gap thickness ( $x \leq d = 10.5$  mm). According to the computations in Sec. 8.3 and to [125], the mean fragments range projected on the drift direction (which is equivalent to the range projected on the readout plane) is approximately 3.5 mm. Hence, the drift distance ranges from 10.5 mm to 7 mm in average (Figure 8.9, blue band). This study shows that the recorded tracks width are mainly determined by the electrons diffusion.

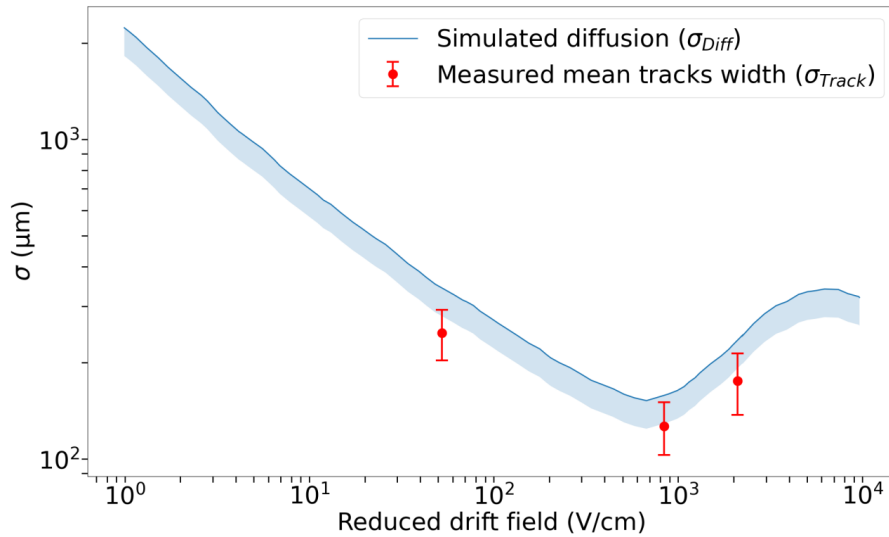


Figure 8.9: Average tracks width ( $\sigma_{\text{Track}}$ ) extracted from Figure 8.7 for drift fields of 50 kV/cm, 840 kV/cm and 2100 kV/cm (red dots). Simulated transverse diffusion ( $\sigma_{\text{Diff}} = D_T \times \sqrt{d}$ ) for a maximum drift distance  $d = 10.5$  mm (blue line). Transverse diffusion taking into account the fragment range and the reduced drift distance such that  $7 \text{ mm} \leq x \leq 10.5 \text{ mm}$  (blue band).

## 8.4 . Test at PSI

High spatial resolution neutron radiography requires specific conditions in terms of neutron flux, parallelism and energy. Low-energy neutrons are indeed advantageous for neutron imaging because of their larger probability of conversion in matter. There are mainly two categories of neutron sources: the experimental fission reactors and the spallation source, which is expanding nowadays. In spallation sources, protons are generally accelerated by a LINAC and they produce neutrons by hitting a tantalum or tungsten target. Then, neutrons are slowed down to thermal or cold energies and can have their energy selected by monochromators.

For this project, measurements were conducted at the Swiss Spallation Neutron Source [129] at the Paul Scherrer Institut (PSI) where the Morpheus beam line provides cold neutrons ( $5 \text{ \AA} \simeq 3 \text{ meV}$ ). A

neutron flux of  $2.3 \times 10^6$  neutrons/s was measured on a  $5 \times 6 \text{ cm}^2$  wide beam with the nBLM detector [122], coupled with a  $1.5 \mu\text{m}$  thick  $^{10}\text{B}$  converter of 10% efficiency. Thus, the absolute neutron flux is approximately  $2.3 \times 10^6 / (5 \times 6) / 0.1 = 7.6 \times 10^5$  neutrons/s/cm<sup>2</sup>. The neutron conversion cross-section in  $^{10}\text{B}$  is about 11500 barn at this energy. High neutron flux allows to record large amount of data in a short time and is preferable to perform good quality neutron radiography. The beam parallelism is a key factor to achieve sharp imaging since it prevents from the parallax effect and blurring (Figure 6.2). Beam parallelism is made possible by having the detector far from the source and by collimation of the source. The beam parallelism and its effect on the spatial resolution is computed in Sec. 8.4.3. The experimental setup is illustrated in Figure 8.10.

Different configurations of the Micromegas detector were explored and the response uniformity of the detector and its spatial resolution were measured for each of them. Two different drift gap thicknesses of 2.25 mm and 250  $\mu\text{m}$  were tested at different electric fields.

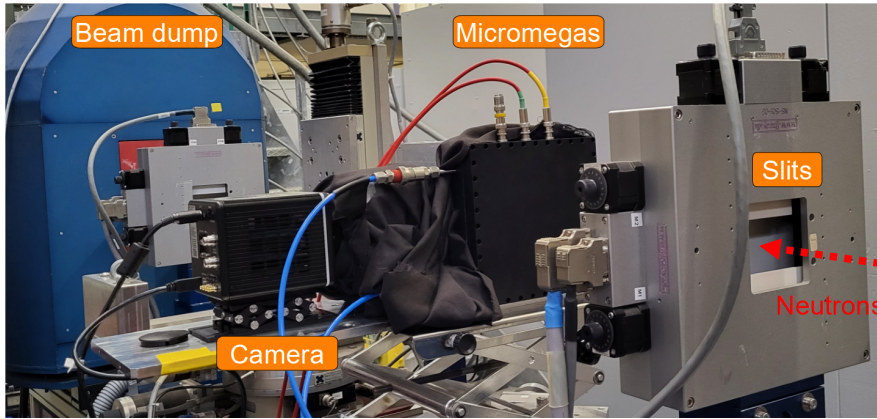


Figure 8.10: Picture of the Micromegas detector setup for neutron radiography at PSI.

#### 8.4.1 . Reduced drift gap and pre-amplification

One alternative to mitigate the spatial uncertainty brought by the fragments range is to decrease the conversion gap thickness to a few hundred microns. Then, the range of the fragments would be limited to a few hundred microns and the spatial resolution would be improved by the same order. As illustrated in Figure 8.11, the  $\alpha$  and  $^7\text{Li}$  fragments hit the mesh structure (or the anode) and are absorbed. The diffusion is also drastically reduced by reducing the drift gap thickness: the transverse diffusion width  $\sigma_T$  indeed follows a  $\sqrt{d}$  distribution with  $d$  the drift gap. For an optimal diffusion coefficient of  $209 \mu\text{m} / \sqrt{\text{cm}}$  at a drift field of about 400 kV/cm in a Ar/CF<sub>4</sub> (90%/10%) gas mixture, the diffusion drops from  $\sigma_T = 100 \mu\text{m}$  for a 2.25 mm gap to  $\sigma_T = 33 \mu\text{m}$  for a 250  $\mu\text{m}$  gap. Moreover, for short gap distances, it is possible to implement pre-amplification in the drift gap [116, 130]. This allows to enhance the signal near the neutron conversion position, while the signal away from the neutron conversion is smaller. As shown in Figure 8.11, due to the angle of the fragments track with respect to cathode plan, the primary electrons close to the neutron conversion are being further amplified. The number of secondary electrons  $n_{e^-}$  increases with the drift distance  $x$  ( $x \in [0, d]$ ) such that  $n_{e^-} \propto n_0 e^{\alpha x}$  with  $n_0$  the number of primary electrons and  $\alpha$  the Townsend coefficient (Sec. 3.2).

Decreasing the drift gap by one order of magnitude also contributes to the separation of the neutron signal from the gamma background in highly radioactive environment. The conversion probability of the gammas in the gas indeed scales with the width of the conversion gap as  $e^{-\mu x}$  with  $\mu$  the gamma attenuation coefficient. Even after the conversion of the gamma, the high-energy photoelectron most probably escapes the conversion gap with very low energy loss.

Pre-amplification has already been implemented with a Micromegas detector [131] and has showed stable operation at high gain values. The uniformity of the amplification depends on the stability of the drift gap thickness and is highly dependent on the cathode flatness and planarity. Thin PCB

spacers stand on the edges of the bulk glass Micromegas and support the cathode, defining a distance between the mesh and the cathode of about  $250\ \mu\text{m}$  (Figure 8.5, left). These different configurations were experimented at the PSI neutron facility. The results are presented in the following sections.

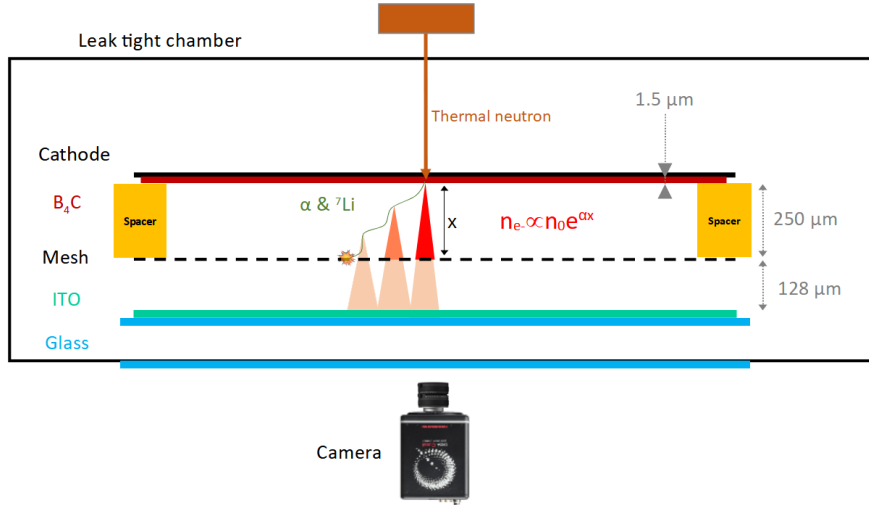


Figure 8.11: The glass Micromegas detector in pre-amplification mode for neutron imaging. The main elements of the schema are detailed in Figure 8.5. The drift gap is  $250\ \mu\text{m}$  thick and the electric field is high enough to perform amplification. The primary charges generated at a distance  $x$  from the mesh undergo a multiplication process generating  $n_{e^-} \propto n_0 e^{\alpha x}$  secondary electrons.

#### 8.4.2 . Flat beam irradiation

Besides the spatial resolution, the response uniformity and dynamic range of the detector are key parameters. The digital image uniformity is generally affected by several contributions: the beam flatness, lens optical effects such as vignetting [70] or detector anomalies like the gain uniformity. Images of a flat beam without any object in front were acquired at PSI to analyze the response uniformity of the detector in single and double amplification modes. Figure 8.12 represents the flat beam in single amplification mode ( $d = 250\ \mu\text{m}$ ,  $E_{\text{drift}} = 480\ \text{V/cm}$ ,  $E_{\text{Amp}} = 37\ \text{kV/cm}$ ). A dome-like shape is observed, which is mainly due to beam non-flatness and lens vignetting effect. The pillars acting like dead zones, also contribute to the non-uniformity of the detector signal. A uniformity of 31% was computed using the Root Mean Square Percentage Error (RMSPE) [87].

Secondly, a flat beam image in pre-amplification mode ( $d = 250\ \mu\text{m}$ ,  $E_{\text{drift}} = 24\ \text{kV/cm}$ ,  $E_{\text{Amp}} = 27\ \text{kV/cm}$ ) is represented in Figure 8.13 (left). In this case, amplification occurs in the drift gap and the gain uniformity is sensitive to any asperity of the gap, like cathode flatness. The flat beam is obtained after Flat Fielding (FF) using the frame in Figure 8.12. The signal after FF is computed by the expression

$$S_{\text{FF}} = \frac{S_{\text{PA}}}{S_{\text{A}}} \quad (8.4)$$

where  $S_{\text{PA}}$  is the flat beam with pre-amplification and  $S_{\text{A}}$  in single amplification mode. This operation helps to remove the beam and optics related non-uniformities. The remaining irregularities hence come from the cathode asperities. The cathode has been examined with a high precision microscope [132] that measures the piece height at several positions. The cathode height distribution is shown in Figure 8.13 (middle, right). A pattern with diagonal lines of higher height is visible and matches the higher gain regions of Figure 8.13 (left). The hollows are most probably issued from the fabrication of the cathode aluminium piece. However, the flat beam FF allows to remove such non-uniformity after radiographic image processing.

In high neutron flux, the detector stability, high dynamic range and linearity are necessary to avoid detector saturation and malfunction. The cumulative light intensity signal has been measured every



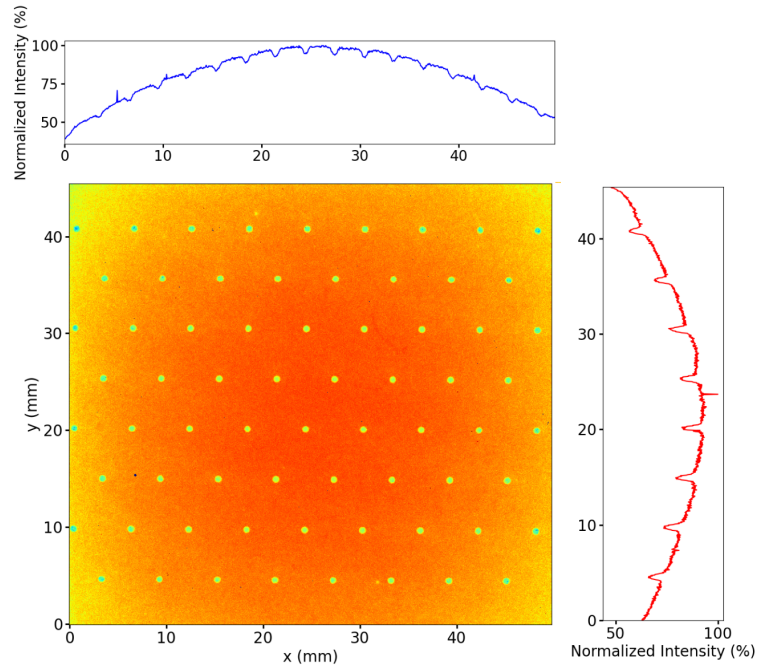


Figure 8.12: Light intensity distribution of a flat beam image at  $E_{\text{drift}} = 480 \text{ V/cm}$ ,  $E_{\text{Amp}} = 37.5 \text{ kV/cm}$ . 1D normalized projections on the vertical (blue plot) and horizontal (red line) axes. The dome like shape and the pillars are visible. A 31% uniformity has been computed.

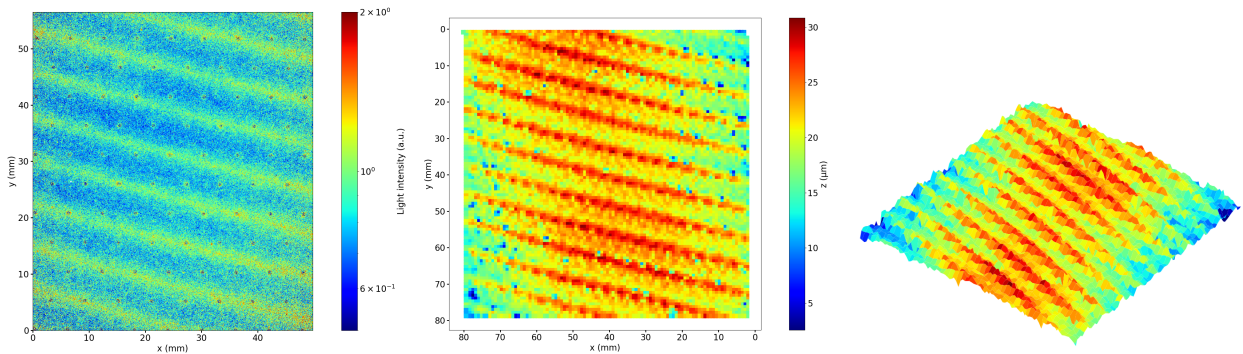


Figure 8.13: Beam flat profile in pre-amplification mode ( $d = 250 \mu\text{m}$ ,  $E_{\text{drift}} = 24 \text{ kV/cm}$ ,  $E_{\text{Amp}} = 27 \text{ kV/cm}$ ) after Flat Fielding (left). Diagonal lines are visible, resulting from the cathode non planarity. The uniformity is 23%. Cathode planarity map obtained by height scanning ( $4 \mu\text{m}$  planarity) (middle, right).

30 s for 50 min under a neutron detection rate of  $7.6 \times 10^4$  neutrons/s/cm<sup>2</sup>. The Figure 8.14, shows that the light signal is linear to the number of detected neutrons and does not show any saturation of the signal after 50 min of consecutive measurement.

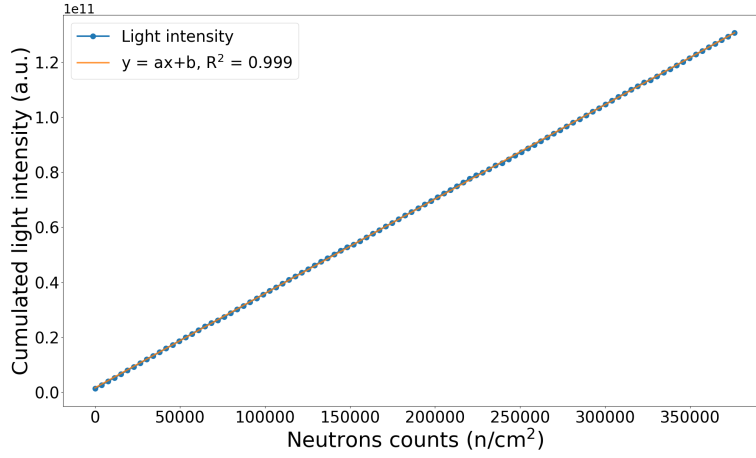


Figure 8.14: Cumulative light signal as a function of the number of detected neutrons. A good linearity is measured during 50 mn of measurement in a row.  $a=3.4 \times 10^5 \text{ n}^{-1}\text{cm}^2$  and  $b = 1.6 \times 10^9 \text{ a.u.}$

### 8.4.3 . Spatial resolution measurement

This section is dedicated to the spatial resolution measurement of the glass Micromegas neutron imager using the thermal neutron beam of the PSI facility. Different targets were placed in front of the detector at a distance  $l = 20$  mm, as shown in Figure 8.3. The ratio  $L/D$  is 1700/3 giving a geometrical unsharpness  $U_g = l \times D/L = 35 \mu\text{m}$  with  $D$  the collimator diameter and  $L$  the distance from the collimator to the imaging plan [133]. The geometrical unsharpness  $U_g$  is the minimum achievable spatial resolution.

Three methods to compute the spatial resolution were tested using two different targets: a slit of  $200 \mu\text{m}$  width in a  $1.7$  mm thick cadmium plate and a  $2.5 \mu\text{m}$  thick gadolinium target with patterns of different spatial frequencies. For each set of measurements, 20 images of 5 s exposure time were acquired, background subtracted and added up. No image filter was applied to the images. The methods are described and the results are given and compared.

### Line Spread Function fit

The first method consists in using the light intensity profile from the slit target radiography to generate a Line Spread Function (LSF). The Figure 8.15 (left) shows the 2D LSF that is first rotated to an optimum parallelism with the vertical axis and projected over 100 pixels on its vertical direction to obtain a 1D LSF (Figure 8.15, right). The spatial resolution is commonly described by the Full Width at Half Maximum (FWHM) of the LSF profile, that corresponds to the minimum distance between two objects to be distinguished by the imaging system. The function  $f$  described in (8.6) was chosen to fit the LSF. It is a convolution of two main distributions: a rectangle function that describes the slit width  $w$  centered in  $\mu$  and two Gaussian functions of standard deviation  $\sigma$  [116]. This method allows to extract the spatial error of the system without being biased by the slit width. The spatial resolution is computed as:

$$\text{FWHM} = 2\sqrt{2 \ln 2} \sigma \quad (8.5)$$

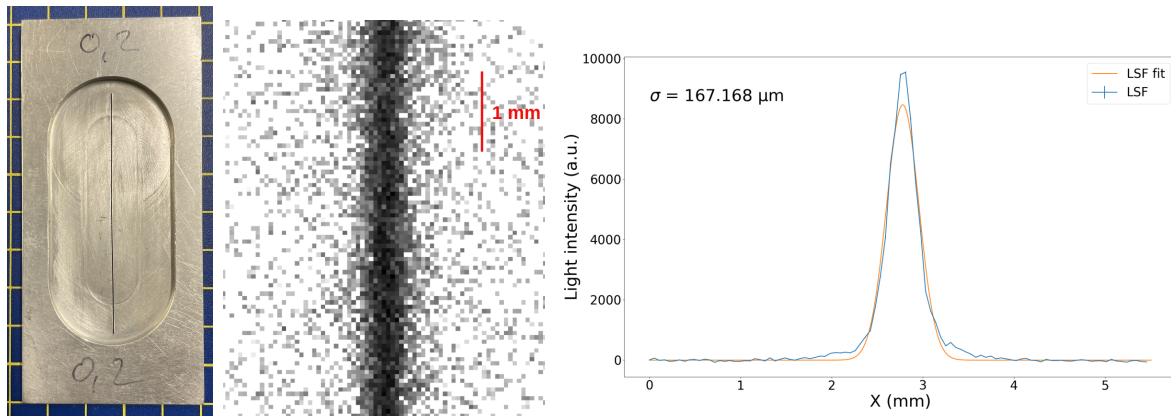


Figure 8.15: Light intensity image of the 200  $\mu\text{m}$  thick cadmium slit (left) with a gray level in logarithmic scale. Line Spread Function from the slit image (right). The LSF is fitted with the distribution described in equation (8.6) and a width of  $\sigma = 167\mu\text{m}$  was obtained.  $E_{\text{Drift}} = 27.2\text{ kV/cm}$  and  $E_{\text{Amp}} = 18.8\text{ kV/cm}$ .

$$\left\{ \begin{array}{l} \alpha_1 = \frac{\frac{w}{2} + (x - \mu)}{\sigma\sqrt{2}} \\ \alpha_2 = \frac{\frac{w}{2} - (x - \mu)}{\sigma\sqrt{2}} \\ \text{erf}(x) = \frac{2}{\sqrt{\pi}} \int_0^x e^{-t^2} dt, \end{array} \right. \quad f(x) = A \times [\text{erf}(\alpha_1) + \text{erf}(\alpha_2)] \quad (8.6)$$

### MTF measurement with the slit target

The second method also involves the slit target from which the LSF is computed. However, the MTF is used to define the spatial resolution in this case as it is usually the case for any imaging system [134, 135]. The Fast Fourier Transform (FFT) of the LSF is computed to convert the LSF spatial response into a frequency response. Thus, the normalized MTF is expressed by the expression:

$$\text{MTF}(v) = \frac{|L(v)|}{|L(0)|} \quad (8.7)$$

with  $L(v) = F(l(x))$  the FFT of the LSF with  $F$  the FFT operator,  $l(x)$  the LSF signal,  $x$  the distance and  $v$  the frequency [136]. The MTF is drawn as a function of the frequency in Figure 8.16. The spatial resolution corresponds to the inverse of the frequency at which the MTF reaches 10%:

$$\frac{1}{v_{(\text{MTF}=10\%)}} = 433\mu\text{m}$$

### MTF by contrast measurement

The last method consists in using a gadolinium target with line patterns of different spatial frequencies as shown in Figure 8.17.

The black dots are the pillars dead zones and the alternative bright and dark vertical lines are from the target image. The MTF is computed by another process where the contrast is measured for all spatial frequencies. The contrast is given by the expression:

$$C(v) = \frac{L_B - L_D}{L_B + L_D} \quad (8.8)$$

where  $L_B$  and  $L_D$  are the maximum bright and dark line intensity respectively (Figure 8.18).

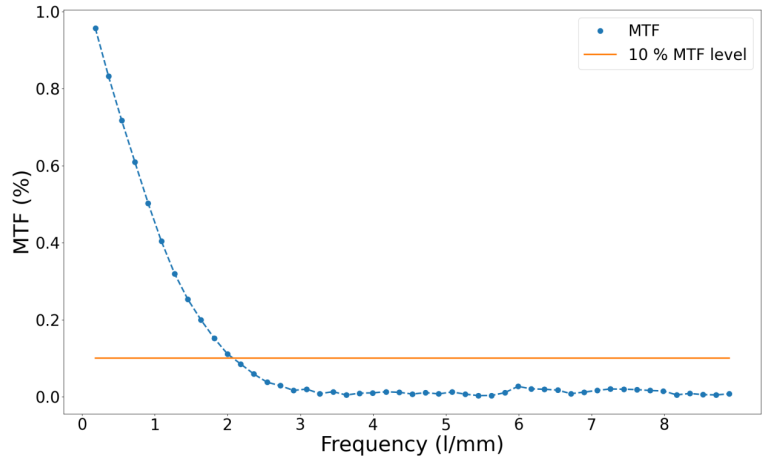


Figure 8.16: Normalized Modular Transfer Function (MTF) obtained from the Fast Fourier Transform (FFT) of the LSF shown in Figure 8.15. A spatial resolution of  $433 \mu\text{m}$  is obtained by taking the inverse of the spatial frequency at which the MTF is 10%.  $E_{\text{Drift}} = 27.2 \text{ kV/cm}$  and  $E_{\text{Amp}} = 18.8 \text{ kV/cm}$ .

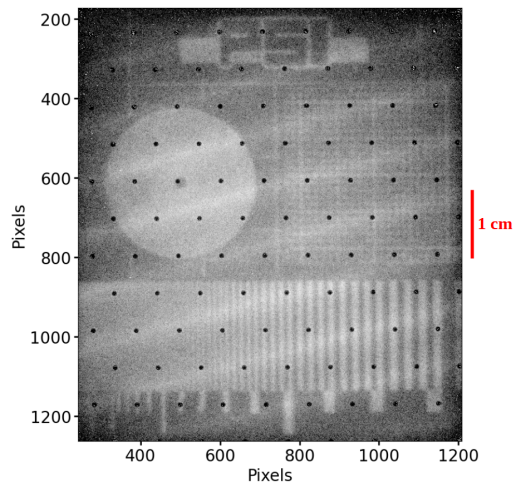


Figure 8.17: Light intensity image of the gadolinium target after background subtraction and frames summation. Only the line pattern is selected in a area of  $5 \times 1 \text{ cm}^2$  for the MTF measurement.

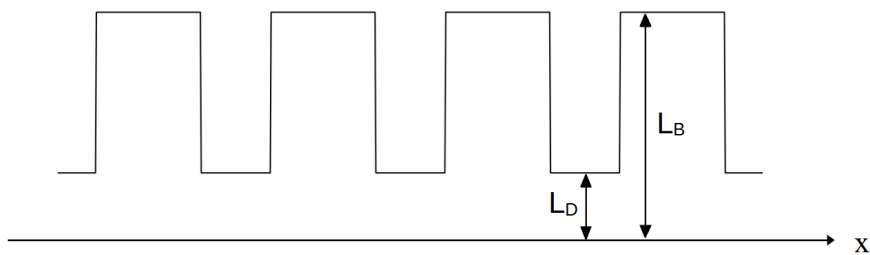


Figure 8.18: Cartoon of alternative bright and dark lines where the variables  $L_B$  and  $L_D$  involved in the contrast computation are shown.

The Figure 8.19(b) represents the 1D projection of the 2D figure (a) after rotating it to an optimized parallelism of the lines with the vertical axis. The curvature of the baseline comes from the neutron beam non-uniformity (Sec. 8.4.2) and must be corrected by Flat Fielding to measure the contrast. Hence, the image in Figure 8.19 (c) is produced showing more uniformity and a smoothing of the pillars. The projection of the FF image (Figure 8.19, d) shows a flat profile of the consecutive lines where the maximum and minimum amplitudes have been computed. On the gadolinium target, the gap between bright and dark lines; the spatial frequency decreases every four consecutive lines. Four contrast values are then averaged per frequency and displayed in Figure 8.19 (e). Similarly to Figure 8.16, the spatial resolution corresponds to the inverse of the frequency at which the contrast equals 10%.

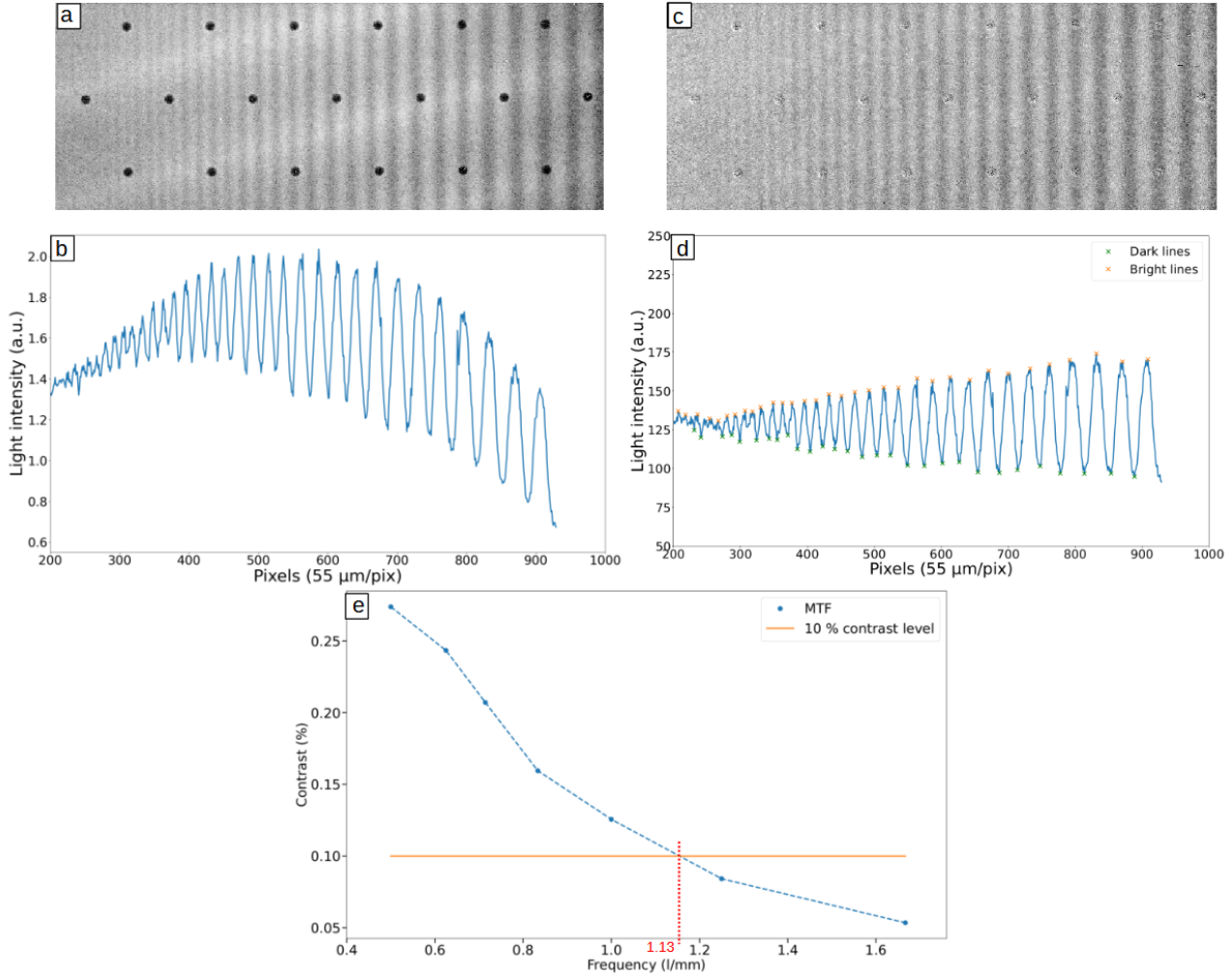


Figure 8.19: a) Light intensity image of the gadolinium target's line pattern after background subtraction and frames summation b) Vertical projection of the image c) Image after Flat Fielding (FF) d) Vertical projection of the FF image e) Contrast measured for each spatial frequency (blue plot) and 10% contrast level (orange line).  $E_{\text{Drift}} = 27.2 \text{ kV/cm}$  and  $E_{\text{Amp}} = 18.8 \text{ kV/cm}$ .

## Methods and amplification modes comparison

The spatial resolution obtained from the three methods is compared in Figure 8.20. Additionally, four different amplification structures of the Micromegas detector are compared. The modes from left to right in the figure are numbered from 1 to 4 in the Table 8.1 where the drift gap thickness and electric fields are described.

The two methods based on the slit target radiography are in good agreement. This validates that the fit of the LSF with the function (8.3) is reliable. In fact, the MTF calculation from the LSF is a well

known and trustful method including the contrast as variable. On the other hand, the MTF computed from the alternative lines target shown in Figure 8.19 shows a large divergence with the two other techniques. This degradation of the spatial resolution is most probably due to the low thickness of  $2.5\ \mu\text{m}$  and cross-section of the Gadolinium substrate in comparison to the Cadmium target. At  $3\ \text{meV}$  neutrons, the Gadolinium target shows an absorption of  $56\ \%$ , and about  $100\ \%$  for the Cadmium target [137]. It involves indeed a small difference of neutron penetration between bright and dark zones and then a poor input contrast to the detector.

The comparison between the amplification setups allows to assess the influence of the double amplification stage and small drift gap thickness on the spatial resolution. All the spatial resolution computation methods agrees on the following results:

- Decreasing the drift gap thickness from  $2.25\ \text{mm}$  to  $250\ \mu\text{m}$  improves the spatial resolution by  $\sim 60\ \%$ , according to the LSF measurements. According to Sec. 8.4.1, the improvement stems from the reduction of the  $\alpha$  and  ${}^7\text{Li}$  fragments range in the drift gap. The transverse diffusion ( $210\ \mu\text{m}/\sqrt{\text{cm}}$ ) drops from  $100\ \mu\text{m}$  to  $33\ \mu\text{m}$ .
- The implementation of a double amplification stage improves the spatial resolution by  $25\ \%$  in average. According to Sec. 8.4.1, the gain in the conversion gap is larger at the beginning of the  $\alpha$  and  ${}^7\text{Li}$  fragments tracks, enhancing the neutron conversion position.
- Having high electric field in the drift gap, even higher than in the amplification gap, improves the spatial resolution. In fact, the gain in the drift gap is higher close to the neutron conversion position while it is even in the amplification gap.

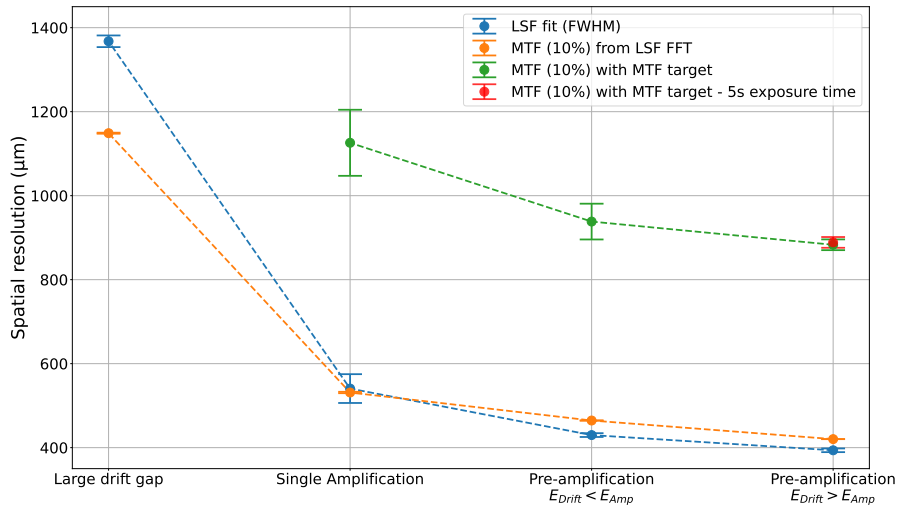


Figure 8.20: Spatial resolution measured for different amplification configurations with three methods. Full Width at Half Maximum of the Line Spread Function (LSF) fit (blue plot). The error bars are computed from the error propagation on the fit parameters for the first method. Inverse of the space frequency at 10% of the MTF from the Fast Fourier Transform of the LSF (orange plot). Inverse of the space frequency at 10% of the MTF from contrast measurements (green line) and with 5 s exposure time only (red marker). The drift gap thickness and electric field configurations are shown in Table 8.1.

The latest results were obtained from a stack of 20 frames of 5 s exposure time. However, the spatial resolution has been computed by contrast measurement with a single frame of 5 s exposure only and displayed on Figure 8.20 (red marker) for the second pre-amplification mode. It shows a similar spatial resolution to the 100s measurement (green line). Hence, 5 s of measurement is enough to perform

neutron radiography with high spatial resolution in a  $7.6 \times 10^4$  neutrons/cm<sup>2</sup>/s neutron beam. The image though is noisy at short exposure time because of a lack of statistics. This demonstrates the high detection sensitivity and efficiency of the detector issued from the Micromegas high gain and the <sup>10</sup>B conversion efficiency.

Mode No.	1	2	3	4
Mode name	Large drift gap	Single amplification	$E_{\text{drift}} < E_{\text{amp}}$	$E_{\text{drift}} > E_{\text{amp}}$
Drift gap ( $\mu\text{m}$ )	2250	250	250	250
$E_{\text{drift}}$ (kV/cm)	0.445	0.480	20.0	27.2
$E_{\text{amp}}$ (kV/cm)	28.1	37.5	33.6	18.8

Table 8.1: Table of the amplification configurations with the corresponding drift gap thickness, drift field and amplification field.

While there is significant deviation of the process based on lines pattern contrast measurement from the two other techniques, the trend is similar and it is considered reliable for relative spatial resolution measurement. It has been utilized to assess the behaviour of the spatial resolution as a function of the pre-amplification field (Figure 8.21). The spatial resolution improves as a function of the drift field by a factor  $7.1 \mu\text{m}/\text{kV}/\text{cm}$  in average. No asymptotic behaviour has been observed so far. While increasing the drift field further was causing instabilities, decreasing the drift gap thickness and improving the cathode flatness would allow to reach higher drift field.

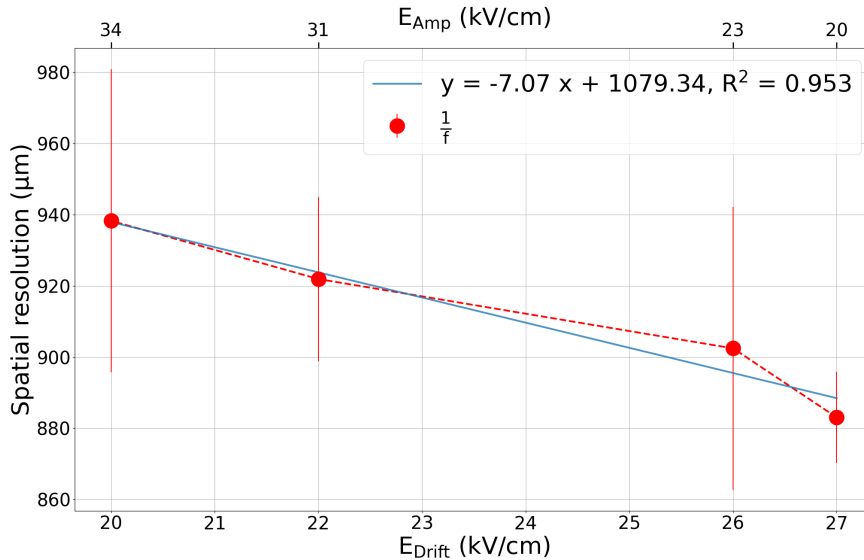


Figure 8.21: Spatial resolution measured for different amplification configurations. Inverse of the space frequency at 10% of the MTF computed from contrast measurement (red plot). The electric field in the drift gap is shown on the bottom horizontal axis and the electric field in the amplification gap is shown on the top axis. Linear regression (blue plot). The spatial resolution improves by increasing the pre-amplification field.

#### 8.4.4 . Fragments energy loss simulation

The  $\alpha$  and  ${}^7\text{Li}$  fragments energy loss in an Argon/ $\text{CF}_4$  (90%/10%) gas mixture has been simulated in Geant4 [6], based on a development by F.J Iguaz Gutiérrez [111]. The fragments issued from the conversion of thermal neutrons in  ${}^{10}\text{B}$  (8.3) are directly generated at random positions in a slit of  $200\ \mu\text{m}$  width in the  ${}^{10}\text{B}$  layer with an isotropic angle of emission (Figure 8.22, left). The energy loss of the fragments and their position at each step is recorded. The energy spectrum is represented in (Figure 8.22, right) for a 10 mm drift gap thickness. While the fragments are emitted at fixed energies, they first loose energy in the  $1.5\ \mu\text{m}$  thick  ${}^{10}\text{B}$  layer before reaching the gas, depositing a continuum of energy in the gas. The maximum energy loss for each fragment, which also corresponds to the fragments initial energy, is also represented.

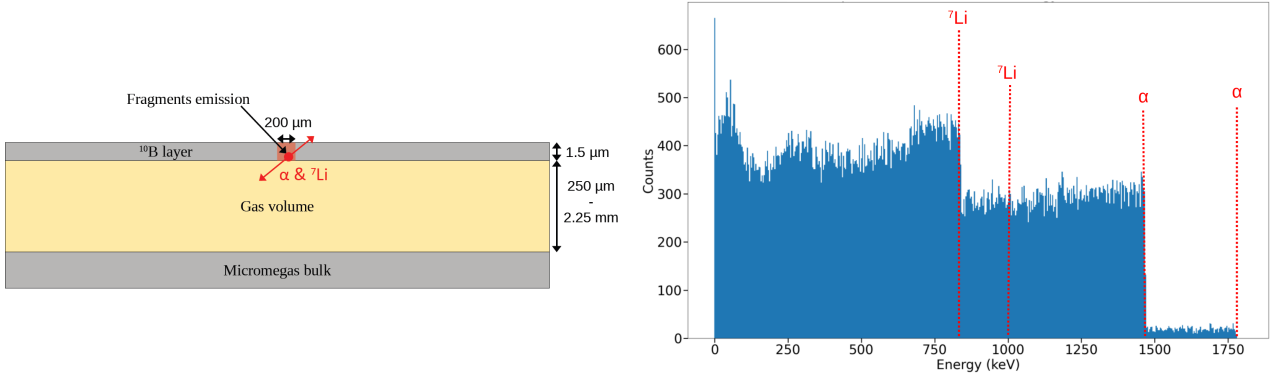


Figure 8.22: Sketch of the  $\alpha$  and  ${}^7\text{Li}$  fragments production in a  $1.5\ \mu\text{m}$  thick  ${}^{10}\text{B}$  layer and energy loss in gas (left). Distribution of the energy loss in the gas (right). The initial energy of the fragments are identified.

In addition, reducing the drift gap thickness is expected to shorten the fragments range and to reduce the amount of deposited energy in the gas. The energy spectrum has been computed for a drift gap thickness of  $2.25\ \text{mm}$  and  $0.25\ \text{mm}$  in Figure 8.23. For both gap thicknesses, the energy spectra are shifted towards lower energies, peaking at  $500\ \text{keV}$  and  $60\ \text{keV}$  for the  $2.25\ \text{mm}$  and  $0.25\ \text{mm}$  gap thicknesses respectively. Thus, even at very small drift gap thickness, the signal amplitude from a neutron event is expected to account for large SNR. To study the discrimination of gammas from neutron events, the interaction with the gas of  $1\ \text{MeV}$  gamma photons has also been simulated. The gammas are emitted uniformly and isotropically in the drift gap, and the energy spectra for a large ( $2.25\ \text{mm}$ ) and small ( $0.25\ \text{mm}$ ) gap thicknesses are shown in Figure 8.23. First, the gamma detection efficiency is only  $0.2\ \%$  for both drift gap thicknesses, due the low cross-section of gamma rays interaction with gas. More importantly, once they have converted into a photoelectron, which is quite energetic, it escapes the gas volume before that the large majority of its energy has been converted in the gas. These mechanisms result in a very small energy deposition in the gas from gamma events in comparison to neutron events. In fact, the gamma deposited energies are about two orders of magnitude smaller than the neutron fragments energies, for both drift gaps. These results corroborate with previous measurements performed with a Micromegas neutron detector, presented in [122].

To study the sensitivity of the glass Micromegas neutron imager, its SNR has been deduced from the mean deposited energy in the gas. From Figure 8.23, mean energies of  $94\ \text{keV}$  and  $520\ \text{keV}$  are delivered per neutron, for a  $0.25\ \text{mm}$  and a  $2.25\ \text{mm}$  drift gap respectively. A gain of about 700 and a light yield of about  $0.36\ \text{ph}/e^-$  were measured in Sec. 5.2.2, for an Argon/ $\text{CF}_4$  (90%/10%) gas mixture, a standard mesh and a  $37.5\ \text{kV}/\text{cm}$  amplification field. After computation of the geometrical acceptance [138], cluster size, projected pixel size, camera QE, lens and windows transmission,  $N_* = 34\ \text{ph}/\text{pixel}$  are detected in average from a neutron event, for a  $0.25\ \text{mm}$  drift gap. However, while for a  $2.25\ \text{mm}$  drift gap the mean energy is much larger, the cluster size is also much broader, spreading the photons among more pixels. A number  $N_* = 1.8\ \text{ph}/\text{pixel}$  has thus been calculated for a  $2.25\ \text{mm}$  drift gap.



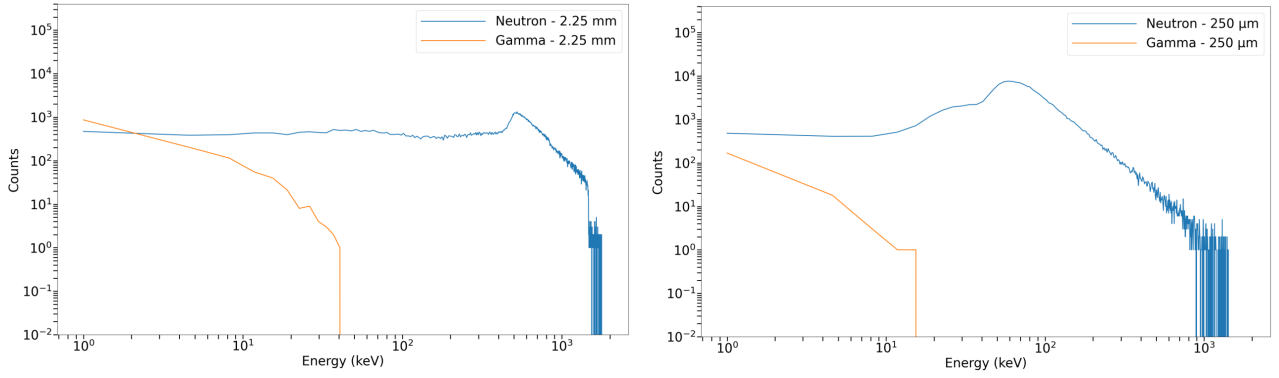


Figure 8.23: Energy spectra of the neutron’s fragments (blue plot) and 1 MeV gammas (yellow plot) in a Ar/CF<sub>4</sub> (90%/10%) gas mixture. The energy spectra were computed for a 2.25 mm (left) and a 0.25 mm (right) drift gaps.

The camera readout noise is  $\sigma_R = 0.27 e^-$  RMS and the dark current is  $N_D = 0.08 e^-/\text{pixel}$  for a 5 s exposure time. The SNR has been computed and displayed in Figure 8.24, according to the equation (8.9), for both gap thicknesses.

$$\text{SNR} = \frac{N_*}{\sqrt{N_* + N_D + \sigma_R^2}} \quad (8.9)$$

The SNR is larger at a drift gap of 0.25 mm compared to 2.25 mm by a factor of about 4.3. At the PSI neutron facility, with a neutron detection rate of  $7.6 \times 10^4$  neutrons/s/cm<sup>2</sup>, SNR exceeding 1000 is expected after few seconds. The SNR obtained with a glass Micromegas detector is expected to be much larger than typical solid-state scintillators coupled with a CCD camera, according to [139].

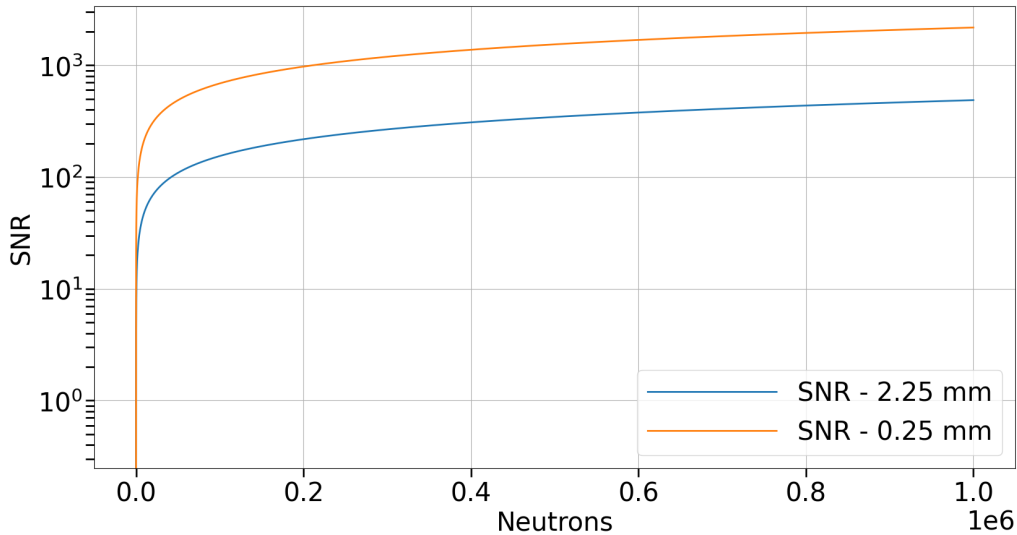


Figure 8.24: SNR computed from the formula (8.9) as a function of the number of detected neutrons, for an Argon/CF<sub>4</sub> (90%/10%) gas mixture. The SNR is larger for a drift gap of 0.25 mm (blue plot) compared to a drift gap of 2.25 mm (yellow plot).

The impact of the fragments range on the spatial resolution then has been studied for different drift gap thicknesses and electric field configurations, with a simplified simulation model. The energy losses per step are then projected on the readout plan and represented on Figure 8.25 for a 2.25 mm and 250  $\mu\text{m}$  gap thicknesses. The image of the slit is much broader for the large gap than for the short gap because of the reduction of the fragments range. The histogram is projected on the horizontal axis and the width of the profile is fitted with the function 8.6. A spatial resolution of 750  $\mu\text{m}$  has

been measured for the large gap and  $150\mu\text{m}$  for the small gap. Decreasing the drift gap thickness from  $2.25\text{ mm}$  to  $250\mu\text{m}$  improves the spatial resolution by about  $80\%$ . In comparison, a significant improvement of  $60\%$  has been measured in Figure 8.20.

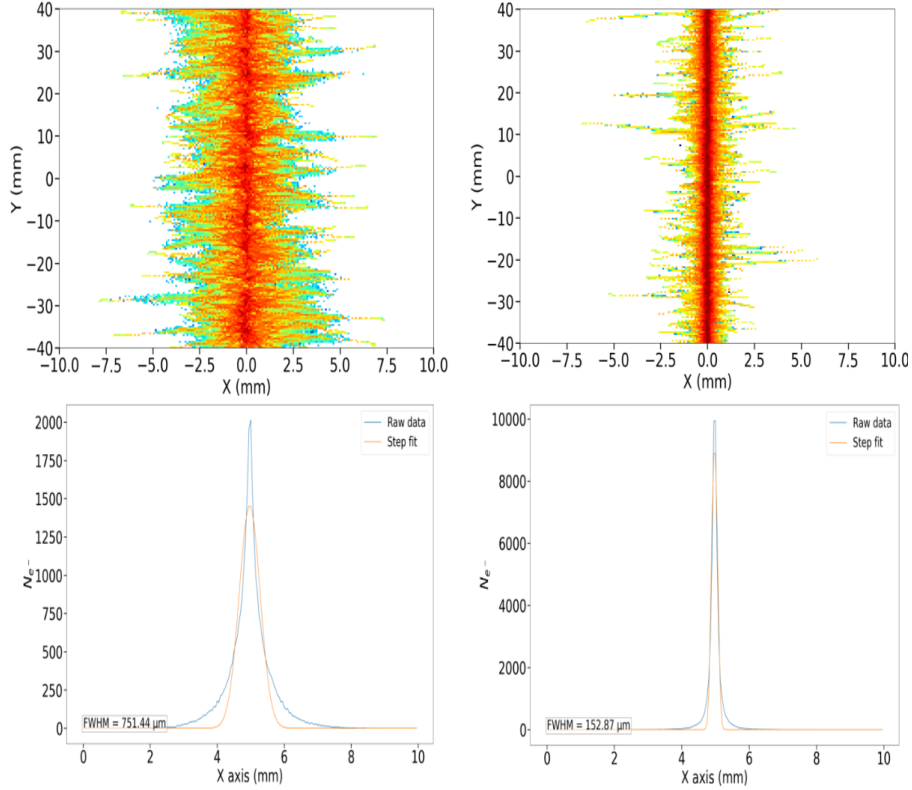


Figure 8.25: 2D histograms of the fragments energy loss position for a  $2.25\text{ mm}$  (left) and  $250\mu\text{m}$  (right) gap thicknesses. The bins' weight corresponds to the number of primary electrons produced at each step such that  $N_0 = W \times E_{step}$  with  $W$  the required energy per pair production and  $E_{step}$  the energy loss at each step. The vertical projections of the histograms and their fit with the function 8.6 are also represented.

To further study the impact of the pre-amplification on the spatial resolution, the number of secondary electrons generated at each step by the avalanche has been computed following the formula:

$$N_{e^-} = N_0 e^{(\alpha-\eta)x} \quad (8.10)$$

with  $\alpha$  the Townsend coefficient,  $\eta$  the attachment coefficient and  $x$  the amplification distance. The Townsend and attachment coefficients have been simulated on Magboltz [11] and are represented on Figure 8.26 (right) as a function of the electric field. The attachment coefficient is specifically high for  $\text{CF}_4$  although it is still much lower than the Townsend coefficient at high electric field. The effect of the attachment at lower electric field is studied in Sec. 3.2.

The spatial resolution has been measured with the method shown in Figure 8.25 for different electric fields, as shown in Figure 8.26 (left). The transverse diffusion has also been taken into account although it is significantly reduced at such gap thickness, being of  $41\mu\text{m}$  at  $20\text{ kV/cm}$  and  $34\mu\text{m}$  at  $30\text{ kV/cm}$  (Sec. 3.2). However, other effects such as optical aberrations, reflections, geometrical unsharpness or the camera noise are not included. The relative spatial resolution measured among the electric field configurations is hence more relevant than the absolute spatial resolution. This simulation shows a clear improvement of the spatial resolution by increasing the pre-amplification field of about  $4.5\mu\text{m} \cdot (\text{kV/cm})^{-1}$  (Figure 8.26, left). Nevertheless, the correlation between the spatial resolution and the electric field is well fitted by a negative exponential function. A similar spatial resolution improvement of  $7.1\mu\text{m} \cdot (\text{kV/cm})^{-1}$  has been measured in Figure 8.21. Both the measurement and the

simulation agree on the fact that increasing the pre-amplification electric field involves a clear but slow improvement of the spatial resolution with the field. The gap between measurements and simulation might be explained by optical effects, such as lens aberrations, light reflection and mirror defaults, which are not included in the simulation.

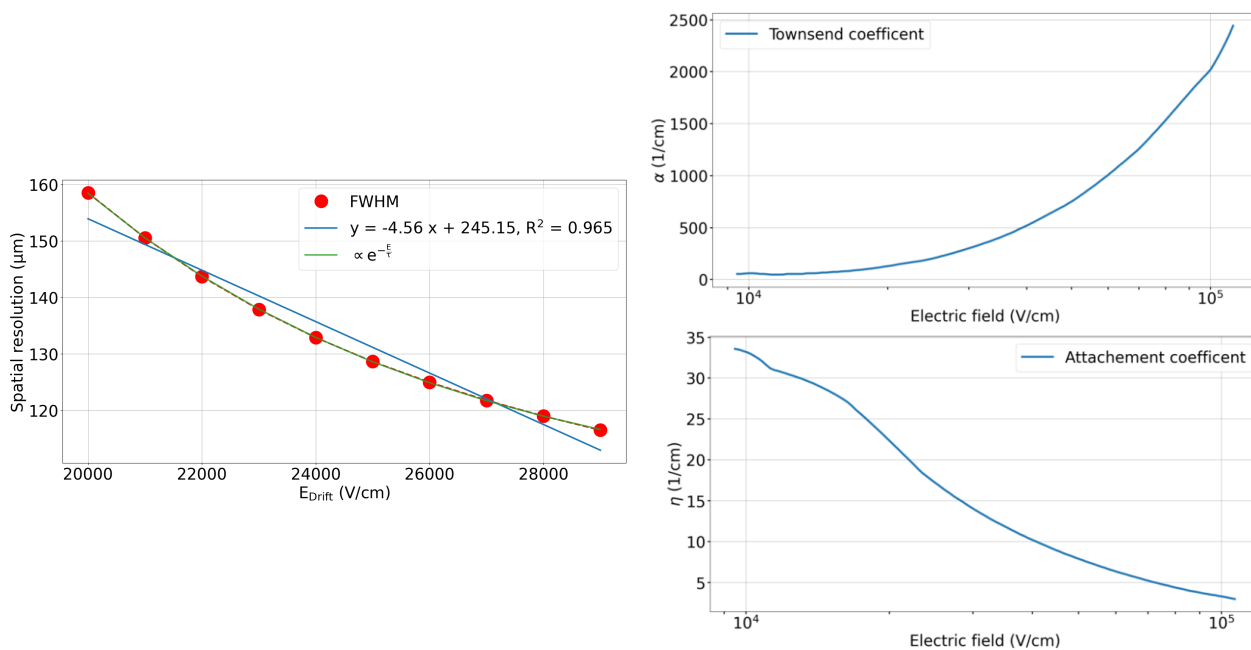


Figure 8.26: Spatial resolution (FWHM) as a function of the electric field (left). The spatial resolution is fitted with a linear function (blue) and a negative exponential function (green). Townsend coefficient (top right) and attachment coefficient (bottom right) as a function of the electric field in an Ar/CF<sub>4</sub> (90%/10%) gas mixture.

### 8.4.5 . Radiography

Neutron radiography has been also performed at the PSI neutron facility, under a neutron flux of  $7.6 \times 10^5$  neutrons/cm<sup>2</sup>/s. A larger maximum distance between the objects and the detection plan of 40 mm gives a geometrical unsharpness  $U_g = 70 \mu\text{m}$ . The largest beam dimension has been settled ( $5 \times 6 \text{ cm}^2$ ) and several objects were examined by radiography at once. Different sizes and elements were chosen, from plastic and silicone with high hydrogen composition (high neutron cross-section) to aluminium and iron metals (low neutron cross-section). Figure 8.27 (left) shows the radiography and a picture of the setup (right) with a 3D printed piece in plastic, two high-voltage (HV) connectors (brass with nickel plating) with Polytetrafluoroethylene (Teflon) and silicone, aluminium plates and a plastic hose clamp. High contrast is detected with plastic and silicone based materials, such as the "cea" sign, the plastic hose clamp and the silicone gasket of the HV connectors.

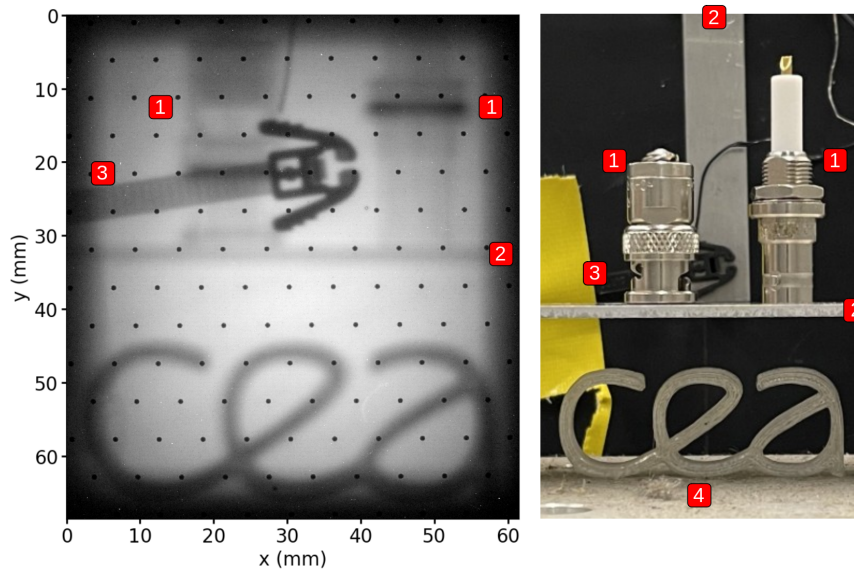


Figure 8.27: Neutron radiography (left) and picture (right) of plastic and metallic objects. 1) HV connectors 2) aluminium bands 3) plastic hose clamp 4) "cea" sign 3D printed in plastic. The plastic elements are contrasted while the metallic ones, like the HV connectors shell are transparent.  $E_{\text{drift}} = 480 \text{ V/cm}$ ,  $E_{\text{Amp}} = 37.5 \text{ kV/cm}$ . The lens has a 25 mm focal distance and an aperture of  $f/2.8$ . 30 images of 5s are accumulated. No FF is performed.

To further illustrate the capacity to examine objects that are inside a metallic container, with high contrast, a 5 mm thick iron cylinder is used, hiding the HV connectors (Figure 8.28, middle, right). The plastic hose clamp and a plastic wire are behind the cylinder from the point of view of the beam exit. The plastic elements and the silicone gasket inside the HV connectors are well resolved in the radiographic image (Figure 8.28, left).

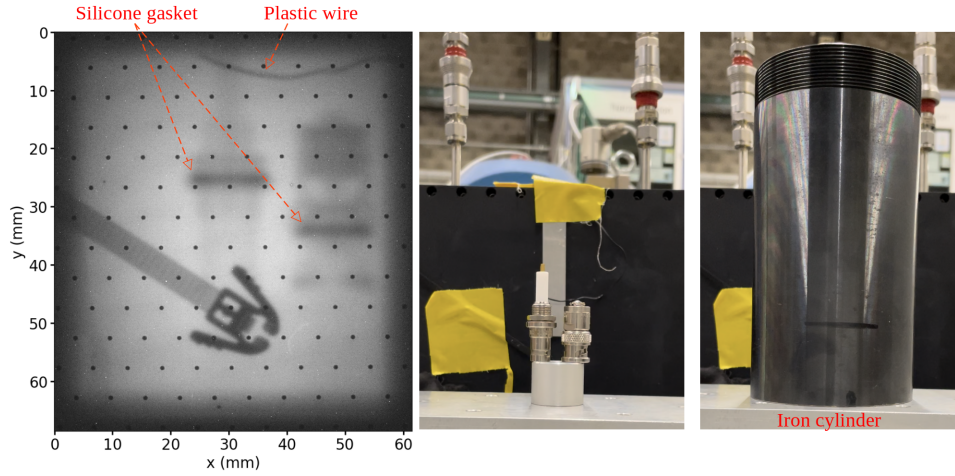


Figure 8.28: Neutron radiography (left) and pictures (middle) of objects with plastic, silicone and metal inside and behind a 5 mm thick iron cylinder (right).  $E_{\text{drift}} = 480 \text{ V/cm}$ ,  $E_{\text{Amp}} = 37.5 \text{ kV/cm}$ . The lens has a 25 mm focal distance and an aperture of  $f/2.8$ . 30 images of 5 s are accumulated. No FF is performed.

A Micromegas detector with its electronics from the nBLM project [122] has been examined by neutron radiography. Several zones of the detector were studied, from the HV wires (Figure 8.29, A), the electronic chip (B) and the Micromegas active area without the  $^{10}\text{B}$  converter (C). The internal structure of the wire and electronic components are revealed in A and B. Small white spots scattered among the images A and B correspond to holes in the PCB board. Moreover, the radiography of the nBLM Micromegas in C shows that the Pyralux pillars, present in its active area, are transparent to neutrons.

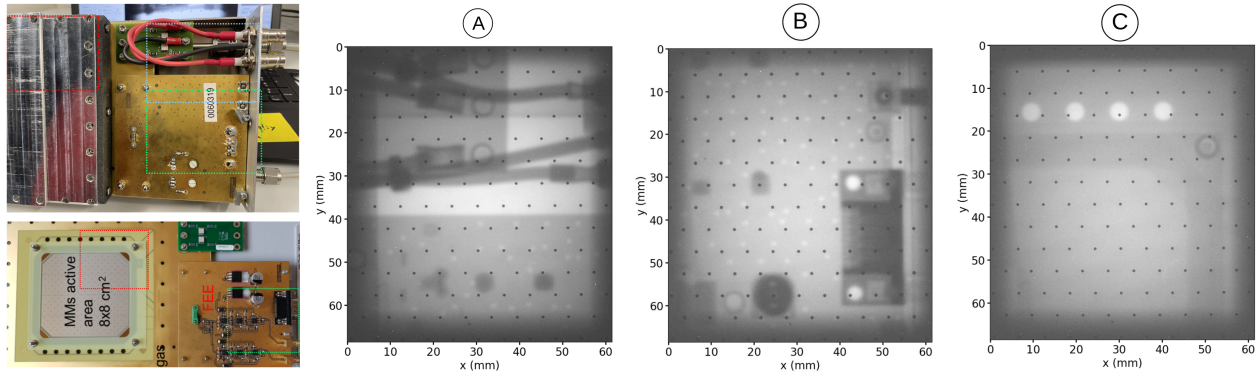


Figure 8.29: Neutron radiography of a bulk Micromegas detector built on PCB with its electronic chip. On the pictures on the left, the blue zone corresponds to the radiography A, the green zone to the B and the red zone to the C.  $E_{\text{drift}} = 480 \text{ V/cm}$ ,  $E_{\text{Amp}} = 37.5 \text{ kV/cm}$ . The lens has a 25 mm focal distance and an aperture of  $f/2.8$ . 30 images of 5 s are accumulated. No FF is performed.

## 8.5 . Conclusion

The study presented highlights the advantages and capabilities of the glass Micromegas detector for neutron imaging. The detector, characterized by its high spatial resolution, offers significant sensitivity thanks to the amplification structure, allowing for real-time imaging with short acquisition duration and tomography capability. Experiments at the Paul Scherrer Institut (PSI) with cold neutrons were conducted. A spatial resolution of  $\sim 400 \mu\text{m}$  (FWHM) has been reached in high particles flux, representing a milestone in the field of neutron radiography with gaseous detectors. This achievement brings us closer to the targeted spatial resolution of  $100 \mu\text{m}$ , which is the standard reached by traditional

scintillators in neutron radiography. In addition, the large gamma discrimination of the Micromegas detector opens the path to high resolution radiography and tomography of gamma emitting objects, such as irradiated fuel rods and nuclear waste. While gaseous detectors for neutron scattering experiments reach a typical spatial resolution of one millimeter [45, 140, 141], the glass Micromegas detector provides a resolution beyond this limit, while the efficiency and signal-to-noise ratio are expected to be similar to other MPGD detectors with a solid borated neutron converter.

The diffusion and the large  $\alpha$  and  $\text{Li}^7$  fragments range were identified as limiting factors of the spatial resolution. The capacity of the detector to depict the fragments Bragg curve has been demonstrated using the single event mode on low neutron flux sources. The reduction of the conversion gap thickness to few hundred microns provided a 60 % improvement of the spatial resolution. Implementation of a high electric field in the conversion gap allowed to perform a double amplification structure, enhancing the gain near the neutron conversion position. The spatial resolution has been refined by 25 % with this method. The dependency of the spatial resolution on the gap thickness and amplification structure have been confirmed by simulations on Geant4. The non-uniformity of the gain in the drift gap due to the cathode non planarity has been characterized and overcome by image flat fielding. The linearity of the detector's light response to high neutron fluxes and unlimited dynamic range have been assessed.

Three different spatial resolution measurement methods were investigated and compared at the PSI neutron facility using gadolinium and cadmium targets. These techniques involved direct fitting of a Line Spread Function (LSF) pattern, computation of the Modular Transfer Function (MTF) by Fast Fourier Transform of the LSF, and MTF determination by contrast measurements. Additionally, high contrast radiography of plastic and silicone-based materials, such as 3D printed pieces and HV connectors, was achieved. Thick metallic components appeared transparent, illustrating the detector's effectiveness in differentiating materials with varying neutron cross-sections.

Scaling up the detector active area to  $30 \times 30 \text{ cm}^2$  is envisioned for future detector designs and represents a significant advancement for large surface imaging. Enhanced gain uniformity can be achieved with improved cathode flatness and drift gap thickness uniformity, by performing better polishing (mirror polishing) of the cathode and refining the detector mechanics. Better spatial resolution will be obtained by further decreasing the drift gap thickness to reach higher pre-amplification fields and further reduce the fragments' range. Increasing the gas pressure of the detector might also be promising to shorten the fragments' range. Ensuring the quality and flatness of mirrors and improving optics also represent areas of improvement.

Additionally, understanding and enhancing the robustness of the Indium Tin Oxide (ITO) coating is essential to control the detector aging. Using an ITO layer thicker than 150 nm might strengthen it. Diversifying image processing techniques, such as flat field corrections, image denoising and pillar extrapolation by neural network algorithms are promising leads for image quality improvement. The measurement of the Point Spread Function of the Micromegas neutron imager would also conduct to a significant enhancement of the image sharpness using deconvolution algorithms, as foreseen in Sec 6.1.4. Finally, investigating the maximum achievable frame rate in neutron radiography would open the path to radiography of moving objects and high resolution tomography.



## 9 - Conclusion and perspectives

A new detector based on the coupling of a glass Micromegas detector with a digital camera has been designed and characterized. The combination of a modern digital camera and a magnifying lens allows scintillation light detection with high image quality and large active area. This approach has demonstrated high spatial resolution and sensitivity in X-ray,  $\beta$  and neutron imaging. Characterizing the detector's response under X-ray illumination has revealed weak points in the detector geometry along with physical mechanisms that lead to image quality deterioration. More specifically, computing the PSF of the detector provided a description of the effects degrading the spatial resolution and offered clear avenues for improving the imaging precision. In particular, the electron mean range and diffusion in the gas were characterized, and their impact on the spatial resolution was quantified. The dependence of these degrading effects on X-ray beam energy, drift field strength, and gap thickness was assessed. Lens aberrations and scintillation light reflections on the micro-mesh were found to significantly contribute to image blurring, depending on the lens quality and aperture, mesh coating and geometry.

The structure of the glass Micromegas detector was optimized by testing different glass substrate thicknesses and qualities, and micro-mesh types. A uniformity in response lower than 10% was obtained. With a gas mixture of Argon/ $\text{CF}_4$  (90%/10%), optimal detector gain and energy resolution of  $10^4$  and 34% were obtained with charge readout. A light yield of 0.38 ph/e<sup>-</sup> and energy resolution of 40% were measured with light readout. While such performances were achieved with a  $8 \times 8 \text{ cm}^2$  active area, a new design of the detector is envisioned, scaling up the active area to a surface of at least  $30 \times 30 \text{ cm}^2$ . With this larger area, radiography and tomography on large objects would be possible, with a maintained high spatial resolution of the order of 250  $\mu\text{m}$  for X-ray and 400  $\mu\text{m}$  (FWHM) for neutron radiography. Covering larger volume is also a precondition to use the glass Micromegas detector in large Optical TPCs. Coupled with a fast timing light detection device, such as a PMT, it can provide tracking capability at low cost per pixel.

Two different data acquisition approaches based on light integration and single event detection were developed. The light integration method has demonstrated high spatial resolution along with real-time imaging capability under high particle flux irradiation ( $>10^5 \text{ neutrons} \cdot \text{s}^{-1} \cdot \text{cm}^{-2}$ ). The method has also proven viable on very low activity  $\beta$  emitting samples thanks to the Micromegas high gain, light yield and stability. Single event detection provides valuable information about the particle interaction, such as its energy, location and direction of emission. The method is limited at higher particle flux, where pile-up and loss of information become appreciable due to saturation of occupancy. Using a camera with a larger frame rate would compensate for these effects at the cost of increasing the noise and degrading the signal-to-noise ratio (SNR) of the detector. MPGD technologies, such as multiple GEM or hybrid Micromegas and GEM detectors, offer higher gain and will be explored for this mode of operation. A camera with a higher rate ( $\sim 1 \mu\text{s}$ ) which can distinguish particle tracks in space and time is also envisioned, enabling a camera based TPC mode.

Spatial resolution and sensitivity of the glass Micromegas detector for both X-ray and neutron radiography has been demonstrated. The potential of deconvolution algorithms to improve spatial resolution in offline analysis has been proven, surpassing the limits of the detectors induced by physical processes. This justifies the expense of computing the Point Spread Function (PSF) of the neutron imager, which is required for deconvolution. This would significantly contribute to reducing the spatial resolution to 100  $\mu\text{m}$  and expanding the use of the glass Micromegas detector in neutron radiography.

In the context of PSF computation at the SOLEIL synchrotron facility, a methodology has been established to decompose the different contributions to the signal spreading in optical readout Micromegas detectors. It was found that the electron diffusion and range in the gas, as well as the optical aberration and light reflection accounted for contributions of the same order to spatial information uncertainty in light integration mode. These results testify to the importance of implementing this



approach for the development of future optical MPGDs for imaging. The PSF measurement campaign also provided a better description of the Micromegas function through direct imaging, especially of the structure of the field lines and the electronic transmission near the pillars. Using a higher magnification lens would enable visualization of the structure of the avalanche amplification in the mesh holes. Additionally, the ability to measure the average range and directionality of photoelectrons for high-energy X-rays has been demonstrated, paving the way for developing a detector suitable for polarimetry.

A high light yield value of  $0.38 \text{ ph/e}^-$  was obtained with a gas mixture of Argon and  $\text{CF}_4$  with proportion between 10% and 20%. However,  $\text{CF}_4$  is a greenhouse gas with high global warming potential and becoming less available. In the future, a gas recirculation system will be integrated into the optical readout detector to save  $\text{CF}_4$ .  $\text{CF}_4$  is one of the only gas able to provide stable operation at high gain, high light yield and low diffusion, making it difficult to replace. On the initiative of the CERN GDD laboratory, an alternative approach was explored, which employed a solid wavelength shifter (WLS), Tetraphenyl Butadiene (TPB), to shift the UV light produced by Argon into the visible region. Such a configuration allows the use of eco-friendly gasses such as hydrocarbons ( $\text{iC}_4\text{H}_{10}$ ,  $\text{C}_2\text{H}_6$  or  $\text{CH}_4$ ), which provide higher gain and energy resolution than  $\text{CF}_4$ . High compatibility is expected between the glass Micromegas and WLS, for which high light yield and spatial resolution are predicted. This would be a promising advancement for large size detectors like Optical TPCs, for which large gas volume is required.

A  $\beta$  imager capable of localizing and quantifying low activity tritiated samples in both integration and single event modes has been developed. 36 samples with activities ranging from 0.1 Bq to 10 Bq were simultaneously localized and quantified. Absolute activities were measured without requiring a calibrated sample of known activity, simplifying the measurement. An accuracy on the activity measurement better than an industrial  $\beta$  imager was achieved with only a few minutes of acquisition time. Integration mode is particularly well suited for imaging a large number of samples at the same time, and can quantify samples of high activity as well as samples with activity as low as 0.1 Bq. However, diffusion significantly degrades the spatial resolution in a drift gap of several millimeters. To enhance the position reconstruction accuracy in integration mode, adding amplification to the drift gap would decrease this diffusion. This is also valid for X-ray radiography, where a large drift gap is required for the efficient conversion of X-ray photons. The range of the  $\beta$  electrons and photoelectrons also worsen the spatial resolution. Pre-amplification would enhance the signal close to the initial point of interaction and compensate for the electron cloud spreading. A high pressure detector might also be investigated, which could limit the electrons' range. Finally, using drifting negative ions instead of electrons would lead to a significant reduction of the diffusion and improvement of the spatial resolution in a large drift gap configuration.

The ability to simultaneously quantify  $^3\text{H}$  and  $^{14}\text{C}$  in a single sample would be advantageous for biologists, allowing them to tag multiple cell types at once. Event-by-event mode is necessary for this purpose, as it provides information on the event's energy and the ability to distinguish different isotopes. Enhancing the energy resolution by optical readout thus becomes a priority. Implementing double amplification stages or coupling a GEM to the Micromegas would increase the maximum gain and improve the energy resolution with optical readout. The use of a high energy resolution gas like Isobutane in combination with a wavelength shifter is an attractive alternative for this application. Besides applications in biology, the  $\beta$  imager could be used in other fields such as water quality testing, where tritium and  $^{14}\text{C}$  quantification in a large number of samples over a short time is necessary in an industrialized process.

The potential of the glass Micromegas detector has been demonstrated for neutron radiography with competitive spatial resolution and sensitivity, enabling imaging with short measurement duration over a large active area. Specifically, it has been shown that reducing the drift gap thickness ( $250 \mu\text{m}$ ) significantly improves the spatial resolution, scoring a 60% better spatial resolution compared to the gap of 2 mm. Implementing a double stage amplification further improved the spatial resolution by 25%, and the improvement of the image sharpness with the pre-amplification electric field was

established. The ability to shorten the imaging time particularly limits the risk of material activation. In addition, Micromegas detectors show high discrimination of gamma background from the neutron signal. These characteristics make the optical Micromegas well suited for imaging in high radiation environments such as in the presence of nuclear waste and irradiated fuel rods. Short acquisition radiography also opens the path to tomography capability with short recording time. Reducing the acquisition rate to tens of milliseconds would provide the ability to record radiography of moving objects. Finally, the aptitude to locate a point-like neutron source is necessary for homeland security and radiation protection applications. Coupled with neutron optics like a coded mask or a pinhole, the glass Micromegas instrument paves the way to fast inspection and tracking of neutron sources with high angular resolution and wide field of view.

The feasibility of the glass Micromegas detector has been demonstrated during this thesis, and its properties have been thoroughly characterized. The large range of improvements of this detector and its suitability to meet needs in a wide range of applications assure its implementation in new projects ahead.



# A - Appendices

## A.1 . Extended tritiated source

In the continuity of the measurement performed on tritiated samples in Sec. 7, activity quantification has been performed on extended tritiated sources instead of point-like sources. This test, out of the scope of this thesis, allows to further investigate the position reconstruction of the glass Micromegas  $\beta$  imager on very low activity sources. Measurements were performed on 20  $\mu\text{m}$  thick slices of tritiated biological samples. Specifically, toxins labelled with tritium were injected in an adult rat. The concentration of tritium on slices of the placenta and embryo tissues are measured in order to study the penetrability of the toxin (pinnatoxin-G) across the placental barrier. The SIMOS laboratory (CEA/JOLIOT/DMTS) has demonstrated in [142] that this toxin is partially absorbed by the placenta and still reaches the embryo. This study warns about the harmfulness of this toxin for the bones of the embryo and for the risk that the pinnatoxin, found in contaminated shellfish, represents for seafood consumers.

These measurements were produced with the BetaIMAGER tRACER [110] for an acquisition of 24 h. Figure A.1 (left) shows the placenta and embryo slices deposited on an ITO coated glass slide. Figure A.1 (right) represents the activity distribution of the samples. High activity were measured on the placenta (large red zones) while the embryos record much lower activities (blue zones). However, larger concentration of the toxin was measured in the embryo tongue and spine.

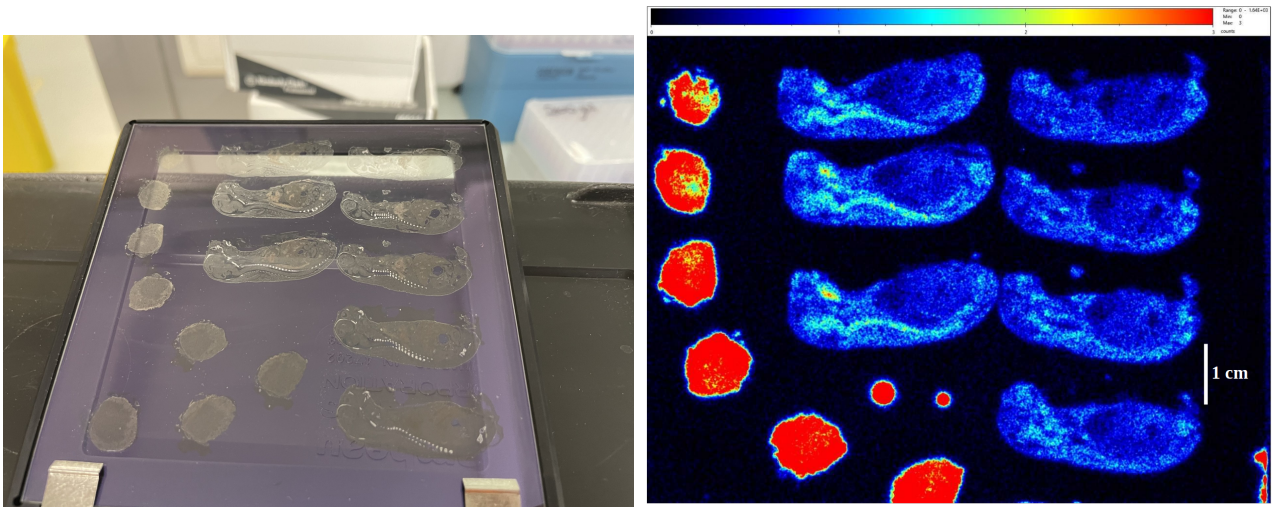


Figure A.1: Picture of the 20  $\mu\text{m}$  thick slices of placenta and embryo (left). Activity distribution of the placentas and embryos obtained with the industrial beta imager. The placentas (red large zones) account for large activities in comparison to the embryos (blue zones). Two glucose drops (small red disks) of known activity provide activity calibration.

This section is dedicated to the test the position reconstruction capability of the glass Micromegas beta imager and validating the findings of the biologists. Figure A.2 (left) represents the activity distribution of the same samples with the glass Micromegas detector in single event mode (Sec. 7.5.1). 500 ms frames were acquired for a total of 24 h with a  $f/0.95$  lens aperture. The detector was operated at a gain of about  $3 \times 10^4$  in Argon/ $\text{CF}_4$  (90%/10%). In comparison to the industrial imager, a smaller surface of  $5 \times 8 \text{ cm}^2$  was covered, providing recordings of two full placentas and embryos. Larger activities have been detected on the placentas compared to the embryos. The distribution map of the activity suffers from a lack of precision but the higher activity concentration at the level of the spine is distinguishable. Using the tritiated glucose calibration, mean activities of  $0.018 \text{ Bq/mm}^2$  and  $0.03 \text{ Bq/mm}^2$  were measured for embryos and placentas respectively.

The degradation of the image sharpness issued from the Micromegas detector compared to the industrial beta imager most probably comes from the range of  $\beta$  electrons in the gas. The beta imager indeed overcomes this difficulty thanks to its double amplification stage, which has not been implemented in the Micromegas detector during these measurements.

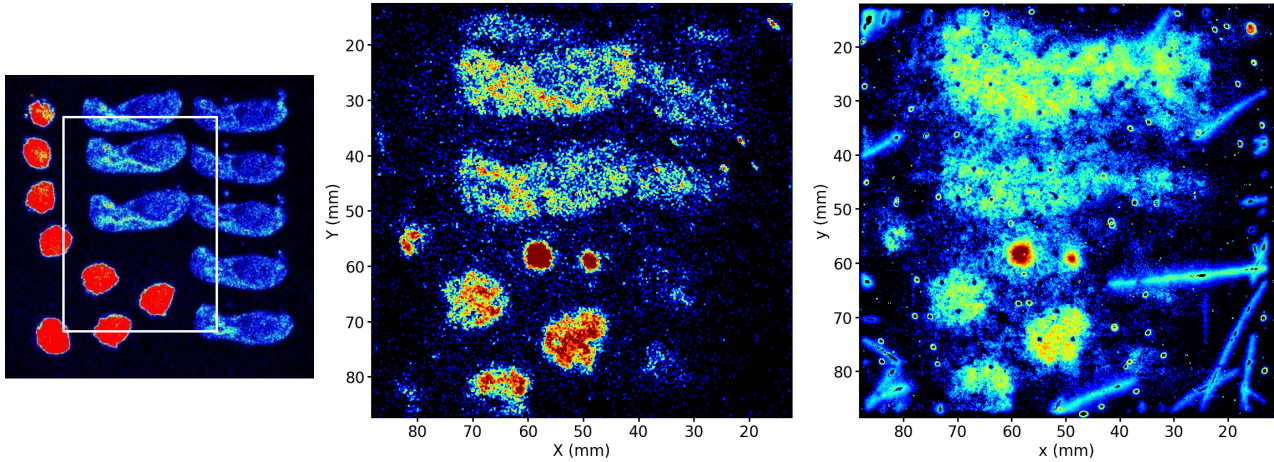


Figure A.2: Activity distribution obtained with the industrial beta imager where the white rectangle indicates the zone captured by the glass Micromegas detector (left). Activity distribution of embryo and placenta samples in single event mode (center) and integration mode (right) with the glass Micromegas detector.

In addition, Figure A.2 (right) depicts the samples' activity distribution acquired in light integration mode. The image sharpness is further degraded in this mode because of the light signal blurring induced by diffusion, light reflections and aberrations (Sec. 6.2). Such low activity samples require to accumulate statistics over 24h to separate the signal from the background. Thus, additional constraints due to detector instabilities and natural radioactive background interfere. The variation of the pressure and temperature during the night modifies the parameters of the gaseous detector and induces fluctuations of the gain, leading to discharges or reduced signal intensity. Moreover, natural radioactive elements, such as Radon, emit highly energetic  $\alpha$  particles at very low rate, which pollutes the measurement (Figure A.2 (right)). Further optimization of the detector's acquisition setup is required to regulate automatically the detector's gain regarding the temperature and pressure during long acquisitions. The image processing algorithm must be upgraded to discriminate unwanted events from natural background.

## A.2 . Solid wavelength shifter: towards the mitigation of greenhouse gases

Optically read out gaseous detectors are mostly used with a  $\text{CF}_4$  based gas mixture, because of its high light yield. It also allows detector stability at high gain and is convenient to use: it is not toxic nor flammable, and liquifies at very low temperature ( $-127^\circ\text{C}$ ). However,  $\text{CF}_4$  is a very strong greenhouse gas, with a global warming potential 7390 times larger than  $\text{CO}_2$  and an atmospheric lifetime of 50000 years [143]. This imposes to establish a strategy of low gas consumption, or replacement of  $\text{CF}_4$ . Improving the sealing of the detector allows to operate in seal mode [64]. However, the gas must be renewed to clean the impurities. The detector can also be operated in close loop, with a recycling system and filters that capture impurities ( $\text{N}_2$ ,  $\text{H}_2\text{O}$ ,  $\text{H}_2$  mostly). Though, a periodic input of clean gas is required to mitigate the impurities that strongly affect the gas scintillation properties [144]. Even if these alternatives allow to reduce the  $\text{CF}_4$  consumption, the supply of  $\text{CF}_4$  is still required. Because of its global warming potential and for geopolitical reasons,  $\text{CF}_4$  has become more expensive and hard to procure. While the total recycling of  $\text{CF}_4$  is hardly achievable, replacing  $\text{CF}_4$  represents an ideal solution. Other gases can be utilized to generate scintillation light in the visible band with large light

yield, like triethyl amine (TEA) [38]. Nevertheless, this type of gas involves detector instability at high gain, and is toxic, flammable, and liquid in normal pressure and temperature conditions.

On the initiative of Florian Brunbauer from the CERN GDD laboratory, an alternative approach based on the use of a solid wavelength shifter (WLS), Tetraphenyl Butadiene (TPB) [145], has been investigated to generate visible scintillation light without the need of  $\text{CF}_4$ . TPB has the specificity to shift UV light into visible light, at a wavelength of about 430 nm. Hence, the UV light scintillated by noble gases can be shifted to the visible region. For example, the UV scintillation spectrum of Argon shows an intense peak at about 126 nm with several other emission lines [59]. Instead of using pure Argon, the use of a quencher such as hydrocarbons ( $\text{iC}_4\text{H}_{10}$ ,  $\text{C}_2\text{H}_6$  or  $\text{CH}_4$ ) provides more stable operation at high gain. However, hydrocarbon gases are known to account for significant UV absorption cross-section. Hence, if the TPB layer is too far away from the avalanche multiplication, where the UV light is emitted, a large fraction of the UV light might be absorbed before reaching the TPB layer. Nevertheless, high proximity between the avalanche and the TPB layer has been implemented in the glass Micromegas detector.

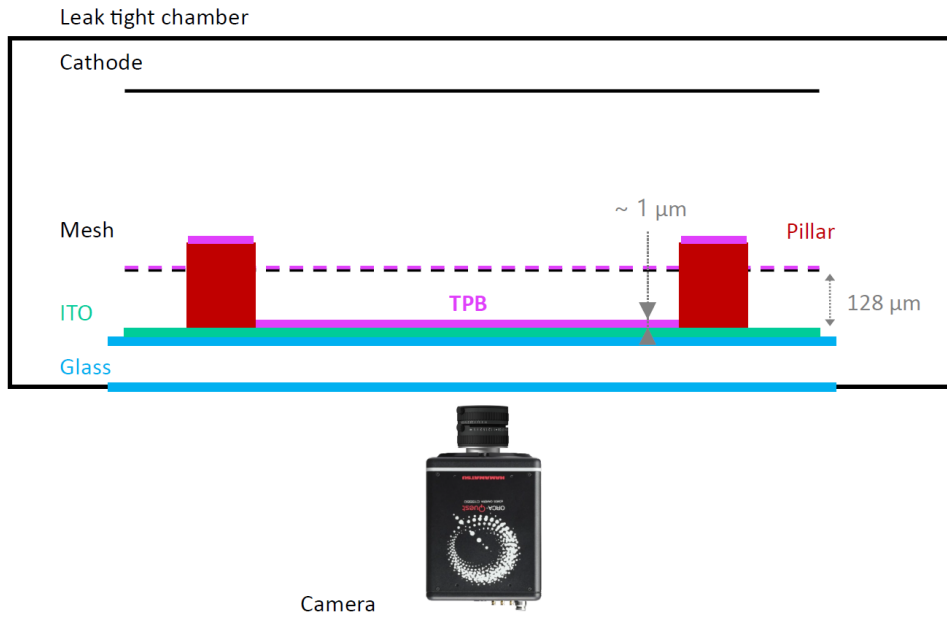


Figure A.3: Sketch of the glass Micromegas detector with a thin layer of TPB evaporated on the anode.

As shown in Figure A.3, a small amount of TPB has been evaporated on the glass Micromegas bulk, reaching the bulk anode by going through the mesh holes and forming a thin layer on the anode with a thickness of the order of one micron. The avalanche taking place below the mesh, at few tens of microns from the TPB, the UV light crosses a very short distance before being shifted by the TPB. The amount of UV scintillation light produced at a distance  $x$  from the mesh is actually proportional to the gain  $M$ , given by the formula (A.1).

$$M = e^{\alpha x} \quad (\text{A.1})$$

$\alpha$  is the Townsend coefficient,  $x \in [0, d]$  and  $d = 128 \mu\text{m}$  is the amplification gap thickness. In addition, the transmission of the UV light is given by the Beer-Lambert law (A.2):

$$I(x) = I_0 e^{-\sigma(d-x)} \quad (\text{A.2})$$

with  $\sigma$  the light absorption coefficient and  $I_0$  the initial photon flux. To render the high efficiency of the UV conversion in the glass Micromegas detector, the gain and UV light transmission have been calculated for a gas mixture of Argon/Isobutane (95%/5%). For an amplification field of about

37 kV/cm,  $\alpha \approx 750 \text{ cm}^{-1}$ . For a UV wavelength of 126 nm, the absorption coefficient is  $\sim 10 \text{ cm}^{-1}$  for Argon and  $\sim 50 \text{ cm}^{-1}$  for Isobutane. Hence  $\sigma \approx 12 \text{ cm}^{-1}$  for the 5% Isobutane gas mixture. The Figure A.4 represents the relative gain and UV light transmission as a function of the depth in the amplification gap.

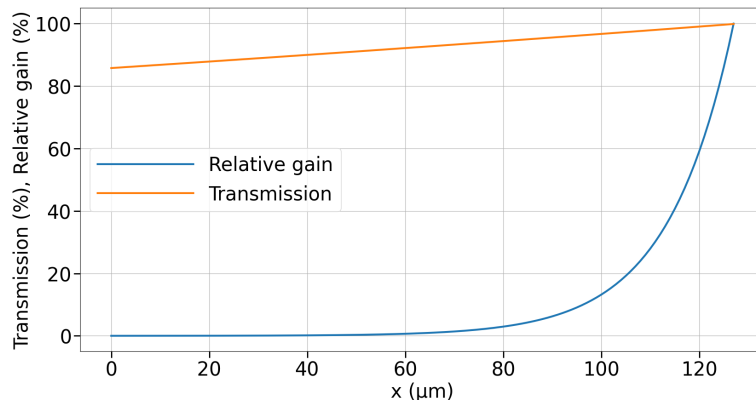


Figure A.4: Plot of the UV light (126 nm) relative transmission (orange plot) and relative gain (blue plot) as a function of the depth  $x$  in the amplification gap such that  $x \in [0, d]$ , with  $d = 128 \mu\text{m}$  the amplification gap thickness.

While the majority of the UV scintillation light is produced in the last tens of microns of the gap, this also corresponds to shorter distances crossed by the UV light, and thus smaller attenuation. This simple calculation offers insight into the suitability of the glass Micromegas detector for TPB based wavelength shifting.

A test has been performed to analyze the light produced by the TPB based glass Micromegas detector. Two different optical filters have been placed at the output window of the detector (Figure A.5, left). As shown on (Figure A.5, right), one filter is only transparent to the light scintillated by a  $\text{CF}_4$  based gas mixture (red plot), with a transmission peak at 630 nm (orange plot). The other filter is only transparent to the light scintillated by the TPB (green plot), with a transmission peak at 450 nm (blue plot). This way, if light crosses the 630 nm filter,  $\text{CF}_4$  is involved, and if it crosses the 450 nm filter, TPB is involved.

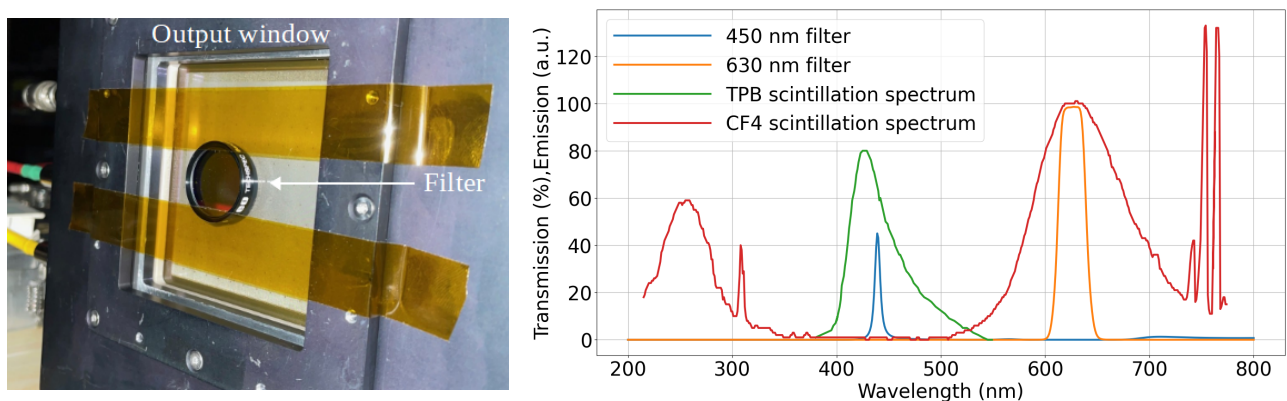


Figure A.5: Picture of the glass Micromegas detector front window with an optical filter (left). Scintillation spectrum of an Argon/ $\text{CF}_4$  based gas mixture (red plot) and TPB (green plot). 450 nm filter (blue plot) and 630 nm filter (orange plot) wavelength dependent transmissions.

The TPB based glass Micromegas detector has been tested with a standard mesh and a  $128 \mu\text{m}$  amplification gap thickness, using a  $^{55}\text{Fe}$  source, with a similar setup to the one in Sec. 5.2.2. First, the detector was operated with an Argon/ $\text{CF}_4$  (80%/20%) gas mixture at a amplification field of 49 kV/cm. As shown in Figure A.6 (left), only the 630 nm filter lets the light pass, indicating that the scintillation

light indeed comes from the  $\text{CF}_4$  based gas mixture. Then, the detector was operated with an Argon/Isobutane (95 %/5 %) gas mixture at a amplification field of 37 kV/cm. Inversely, only the 450 nm filter lets the light pass in Figure A.6, showing that the light comes from the TPB scintillation.

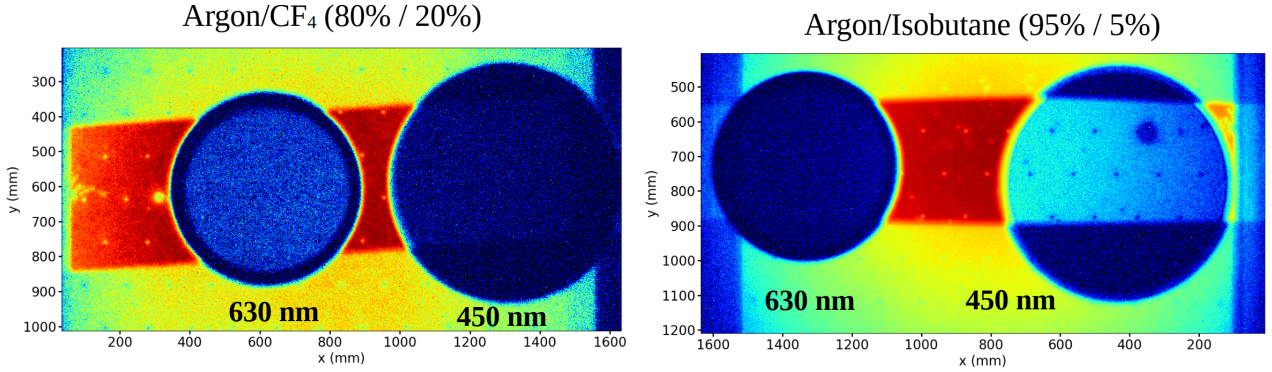


Figure A.6: Light intensity frames recorded with the qCMOS camera. The TPB based glass Micromegas is operated with an Argon/ $\text{CF}_4$  (80 %/20 %) gas mixture (left) and with an Argon/Isobutane (95 %/5 %) gas mixture (right). The 630 nm filter and the 450 nm filter are identified.

These results prove that the glass Micromegas detector allows scintillating in the visible by using TPB and an Argon/Isobutane (95 %/5 %) gas mixture. To quantify the amount of visible light produced by the WLS, a PMT has been used to measure the number of photons, and the charge signal from the detector's mesh has been measured in parallel. This configuration and the analysis process are described in the light yield measurement campaign in Sec. 5.2.2. The Figure A.7 (right) represents the scintillation spectrum of the TPB normalized by the windows' transmission and the PMT's QE. An efficiency of photodetection of 20.15 % has been calculated and a geometrical acceptance of 4.6 % was computed. The Figure A.7 (left) represents the light yield as a function of the electronic gain. The light yield is the ratio between the number of photons produced by the TPB, and the number of secondary electrons. A light yield of about 0.2 has been measured at a gain around  $10^4$ . In such gas mixture, the detector remains stable at gain values scaling up to  $10^5$ , and a small drop of the light yield is expected, as in Sec. 5.2.2. In comparison to the light yield and gain achieved in the Argon/ $\text{CF}_4$  gas mixture, the current configuration generates five times more photons. This method allows to take benefit from the Argon high UV light yield, from the high electronic gain in the Argon/Isobutane gas mixture, and from the expected high wavelength shifting efficiency of TPB.

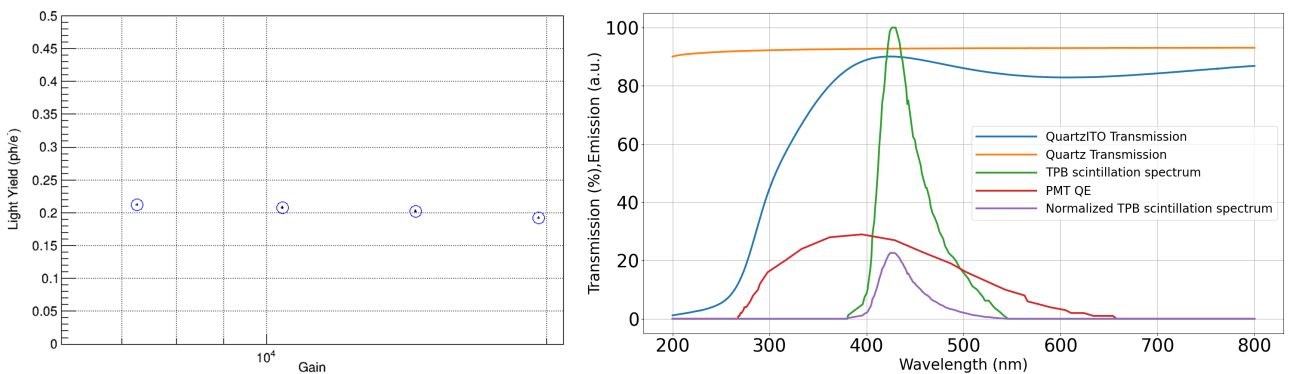


Figure A.7: Light yield obtained from the formula (5.12) as a function of the gain (left). The glass Micromegas detector is TPB coated and the gas is a mixture of Argon/Isobutane (95 %/5 %). The gain ranges from 7000 to 20000 in a 128  $\mu\text{m}$  amplification gap. Scintillation spectrum of the TPB normalized by the windows' transmission and the PMT's QE.

In these conditions where large light amount is emitted, more sensitivity with the camera and a better detection of single X-rays events are expected. The detector was operating with an Ar-



gon/Isobutane (95%/5%) gas mixture, at atmospheric pressure, at a gain around  $10^5$  and a drift field of 1000 V/cm. The lens was at about 20 cm from the ITO layer and the aperture was f/0.95. The detector was exposed to an  $^{55}\text{Fe}$  source and the X-rays flux was decreased to avoid pile-ups of clusters. The Figure A.8 (left) represents a 151 ms frame where the light clusters originating from single X-rays events are clearly distinguishable and well separated from the image background. The clusters were automatically located and their light intensity was registered following the method detailed in Sec. 5.4.2. Flat fielding was applied to each frame in order to correct the solid angle effect of the lens. The clusters' total light intensity have been stored in a histogram (Figure A.8, right) to reconstruct the  $^{55}\text{Fe}$  energy spectrum. The 5.9 keV peak has been fitted following the procedure in Sec. 5.2.1, and an energy resolution of 34.6% FWHM has been measured. Such energy resolution has been achieved by using only the camera thanks to the large light amount generated in the gas and in the WLS, and by means of the better energy resolution usually obtained in Argon/Isobutane gas mixture.

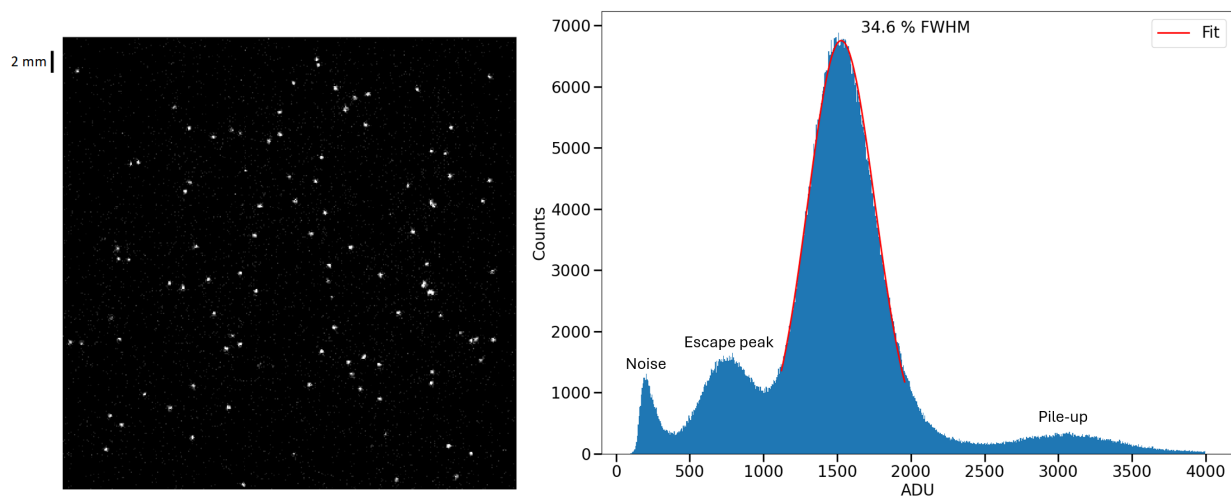


Figure A.8: 151 ms exposure frame with visible light clusters from X-rays events (left).  $^{55}\text{Fe}$  energy spectrum obtained by storing in a histogram the clusters' light intensity. An energy resolution of 34.6% FWHM has been obtained by fitting the 5.9 keV peak. The escape peak, typical of Argon, the pile-ups and the noise were also identified in the spectrum.

Future studies will be dedicated to the measurement of the detector light yield in different gas mixtures, with different WLS materials and detector gains. In addition, the energy resolution might be optimized by improving the flat fielding correction, by bringing the lens closer to the detector or by purchasing better quality lens. Finally, low degradation of the spatial resolution is envisioned, thanks to the proximity of the avalanche with the TPB, and to the low diffusion of the UV light before reaching the TPB.

## Résumé en français

Un nouveau concept de détecteur Micromegas a été développé, testé, et appliqué à l'imagerie de rayons-X, neutronique et bêta. Lorsqu'une avalanche électronique est déclenchée au sein du détecteur Micromegas, une importante quantité de lumière du domaine visible ( $\sim 630$  nm) est générée. En intégrant au détecteur une caméra couplée avec un objectif photographique, cette lumière peut être enregistrée (Figure 1).

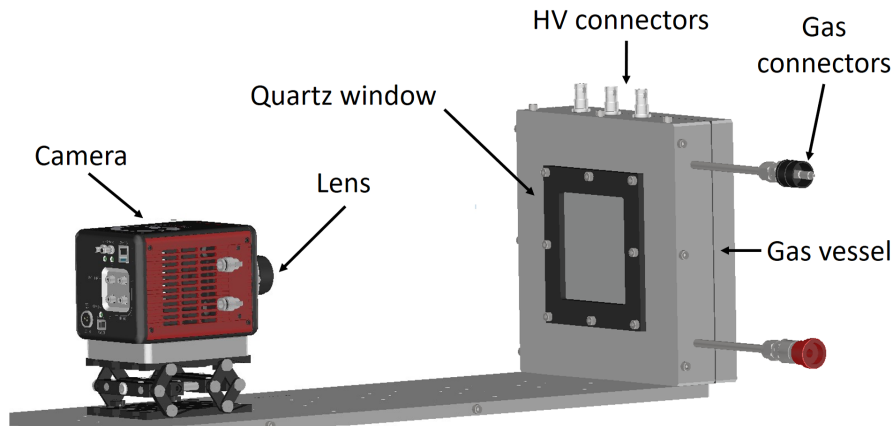


Figure 1: Schéma d'un détecteur Micromegas à lecture optique. La caméra CMOS fait face au plan de lecture et capture la lumière scintillée dans le gaz qui traverse la fenêtre en verre.

Cette méthode permet de localiser avec précision la position d'interaction d'une particule avec le détecteur Micromegas, tout en couvrant une large surface de détection. Cette technique permet en outre d'obtenir une image 2D pixelisée du détecteur, avec une taille de pixel de l'ordre de  $50\ \mu\text{m}$ , à faible coût par pixel, et avec la possibilité de réaliser une imagerie en temps réel. Pour ce faire, le détecteur Micromegas a été fabriqué sur une plaque de verre de 5 mm d'épaisseur avec un dépôt d'Oxyde d'indium-étain (ITO) de 150 nm d'épaisseur. L'ITO est transparent à la lumière visible et est conducteur, laissant la lumière scintillée dans le gaz atteindre la caméra, tout en maintenant un champ électrique dans l'espace d'amplification. Le détecteur Micromegas en verre est illustré par un schéma et par une photographie dans la Figure 2.

Au cours de cette thèse, la structure du détecteur Micromegas en verre a été optimisée pour obtenir une imagerie à haute résolution spatiale et sensibilité pour les rayons X, les particules bêta et les neutrons. En utilisant un mélange gazeux d'Argon et de  $\text{CF}_4$ , une résolution en énergie de 40 % au mieux et un gain de  $10^4$  des détecteurs Micromegas en verre ont été mesurés, avec différents substrats en verre et différentes géométries de micro-grille, en utilisant une source de  $^{55}\text{Fe}$ . L'uniformité de la réponse lumineuse du détecteur Micromegas en verre a été examinée au laboratoire de développement des détecteurs gazeux (GDD) du CERN, en utilisant un tube à rayons X. Une radiographie par rayons X a été effectuée sur un petit animal décédé et sur une cible en plomb pour étudier la résolution spatiale du détecteur (Figure 3). En utilisant un algorithme de déconvolution, une résolution spatiale de l'ordre de  $300\ \mu\text{m}$  a été mesurée.

La réponse lumineuse du détecteur est étudiée plus en détail en mesurant la Fonction d'Étalement du Point (PSF) du détecteur au synchrotron SOLEIL. La réponse du détecteur à un faisceau de rayons X d'une largeur de quelques micromètres fournit une description détaillée des facteurs qui affectent la résolution spatiale. La PSF est décrite comme une convolution de différents effets physiques, comme la diffusion, le parcours moyen des électrons dans le gaz, ou bien la réflexion de la lumière scintillée et les aberrations optiques, chacun étant étudié individuellement. Le profil de la PSF est illustré Figure 4, mettant en évidence l'étalement de l'image d'un point causé soit par des aberrations optiques (à

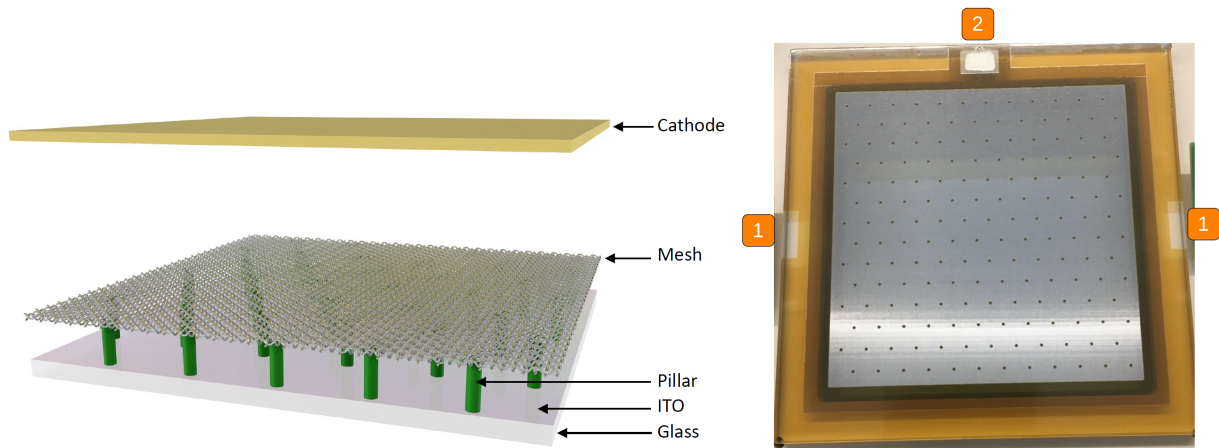


Figure 2: Dessin 3D du détecteur Micromegas en verre. Les différents éléments du détecteur, la dimension de l'espace d'amplification (épaisseur de  $128 \mu\text{m}$ ) et l'espace de dérive (épaisseur de quelques millimètres) sont montrés (à gauche). Photo du détecteur Micromegas en verre (à droite) avec les contacts des électrodes de l'anode en ITO (1) et de la micro-grille (2).

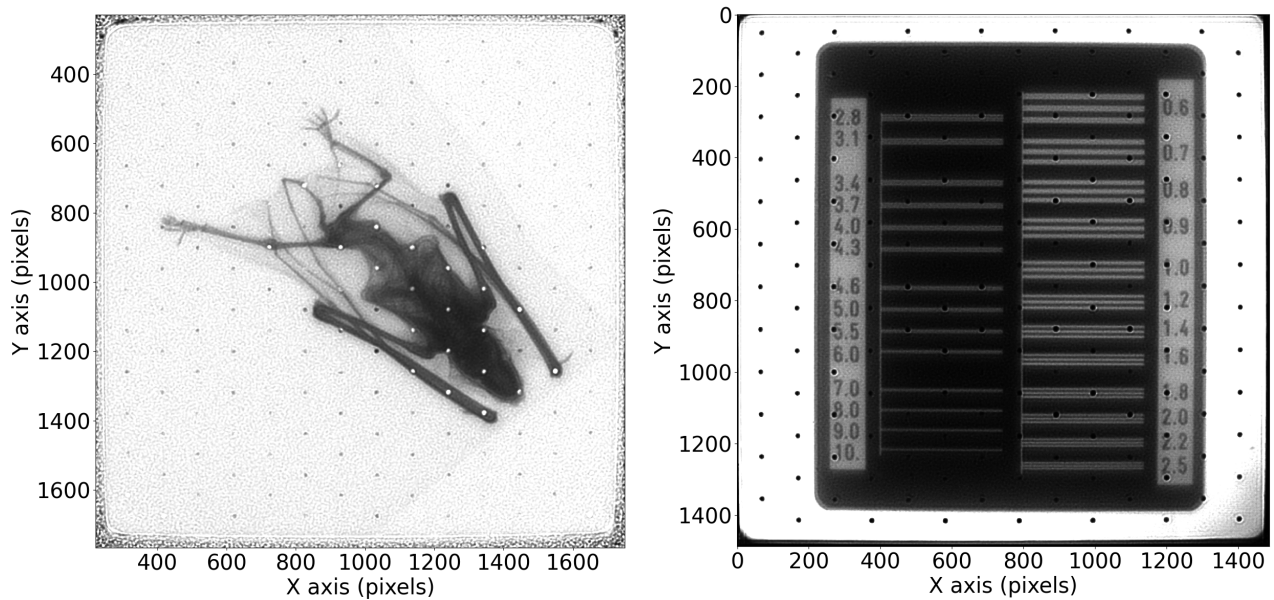


Figure 3: Radiographies d'une chauve-souris (à gauche) et d'une cible en plomb (à droite) utilisant l'algorithme de déconvolution de Richardson-Lucy avec 130 itérations. Le détecteur est utilisé avec un gain d'environ  $10^4$  et à une transmission maximale de la micro-grille.

gauche), la réflexion de la lumière sur la micro-grille (au centre), ou le parcours moyen des électrons dans le gaz (à droite). Le poids de leur contribution à la PSF a été évalué, fournissant une stratégie détaillée pour l'amélioration de la résolution spatiale du détecteur.

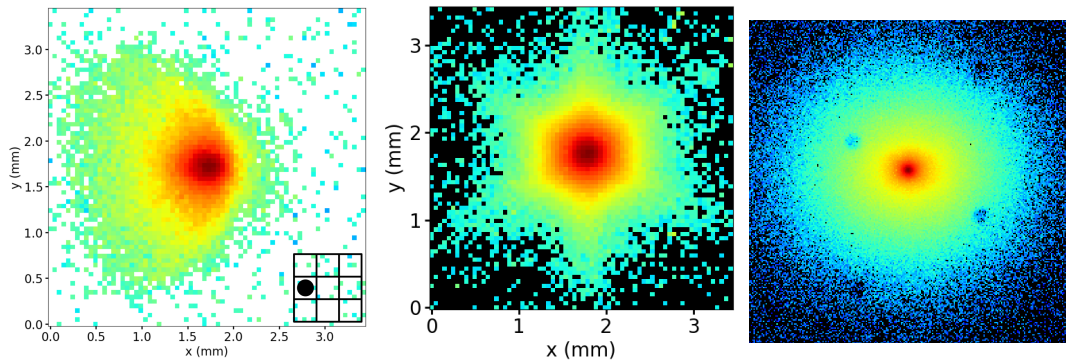


Figure 4: Profil 2D d'un faisceau ponctuel situé au centre gauche du plan de l'image (à gauche). Les aberrations optiques sont visibles. Profil 2D avec une micro-grille hexagonale (au centre), où le motif de réflexion de la micro-grille apparaît clairement. Profil de la PSF de la source de rayons X à une énergie de faisceau de rayons X de 18 keV (à droite). Le parcours moyen des électrons étale la PSF, et les piliers sont perceptibles.

Le potentiel du détecteur Micromegas en verre pour détecter, quantifier et localiser des échantillons tritiés a également été étudié en collaboration avec des biologistes et des experts en microfluidique dans le cadre de la recherche en oncologie. Ce système permet l'autoradiographie simultanée de plusieurs échantillons tritiés avec des activités aussi faibles qu'un dixième de Becquerel.

Le détecteur Micromegas a démontré une importante sensibilité et une stabilité, détectant avec succès des échantillons à faible et haute activité. La Figure 5 illustre la détection simultanée de 36 échantillons tritiés avec des activités allant de 0.1 Bq à 10 Bq. Plusieurs méthodes de calibration de la quantité de lumière en fonction de l'activité des échantillons ont été testées, dont une qui ne nécessite pas d'échantillon de référence, ce qui simplifie le processus et améliore la facilité d'utilisation du système. L'imagerie bêta avec un Micromegas en verre offre une approche robuste, économique et facile d'utilisation pour l'imagerie bêta. Sa capacité à quantifier avec précision une large gamme d'activités avec une simple géométrie de détecteur et une convergence rapide de la mesure de l'activité vers des valeurs de référence en fait un outil précieux pour des applications telles que la recherche pharmaceutique et au-delà.

Le détecteur Micromegas en verre a également été développé pour la radiographie neutronique à haute résolution spatiale. Le couplage du détecteur Micromegas en verre avec un convertisseur neutron-charge au  $^{10}\text{B}$  offre une haute sensibilité de détection des neutrons et une capacité d'imagerie en temps réel dans un environnement à haut flux de particules. Une résolution spatiale de  $400\ \mu\text{m}$  (FWHM) a été mesurée à l'Institut Paul Scherrer. L'importante discrimination gamma du détecteur Micromegas ouvre la voie à la radiographie et à la tomographie d'objets émettant des rayonnements gamma, tels que les barres de combustible irradié et les déchets nucléaires. Un schéma du principe de fonctionnement du détecteur à neutrons ainsi que des images de radiographie neutron sont illustrés Figure 6.

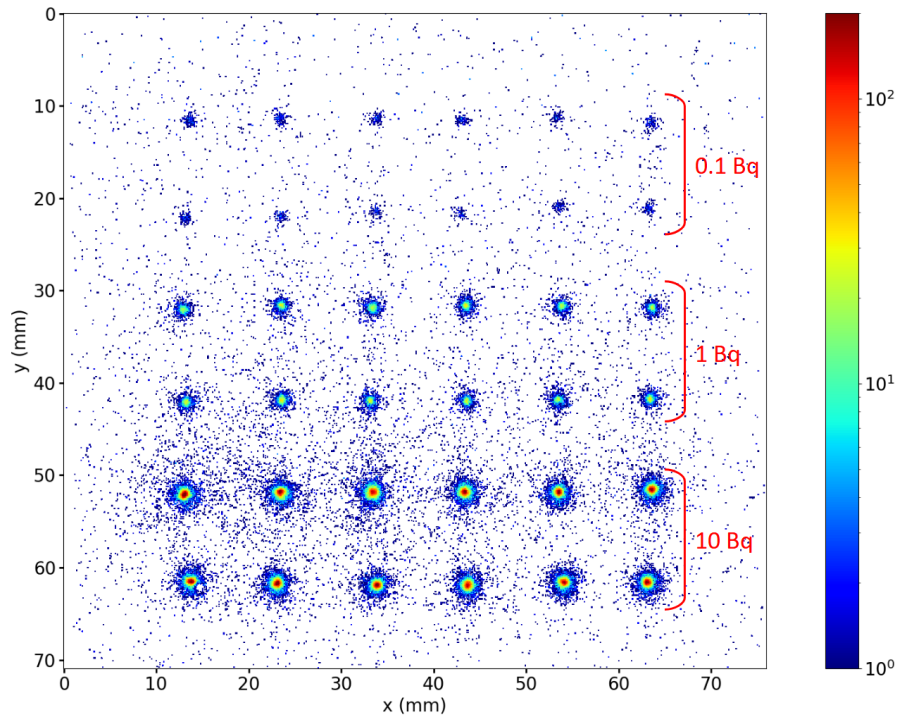


Figure 5: Histogramme 2D du centroïde des amas de lumière après 1 heure de mesure avec des images de 200 ms de temps d'exposition. L'échelle de couleur est logarithmique et le poids des bins est pondéré par le nombre d'amas. Le mélange gazeux est composé d'Argon et de  $\text{CF}_4$  (20%) et une épaisseur de la zone d'amplification de 75 microns est utilisée. Le champ de dérive est de 700 V/cm, le champ d'amplification de 69 kV/cm et le gain est d'environ  $3 \times 10^4$ .

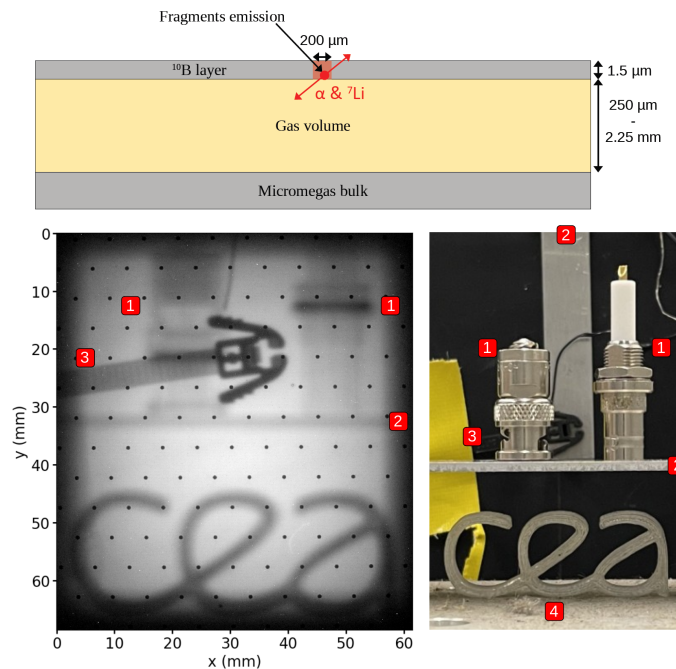


Figure 6: Schéma de la production de fragments  $\alpha$  et  ${}^7\text{Li}$  dans une couche de  ${}^{10}\text{B}$  épaisse de  $1.5\ \mu\text{m}$  intégrée sur un Micromegas en verre (au-dessus). Radiographie neutronique (en bas à gauche) et photo (en bas à droite) d'objets en plastique et métalliques. 1) Connecteurs haute tension 2) Bandes en aluminium 3) Collier de serrage en plastique 4) Signe 'cea' imprimé en 3D en plastique. Les éléments en plastique sont contrastés tandis que les éléments métalliques, comme l'enveloppe des connecteurs haute tension, sont transparents.

## Bibliography

- [1] Particle Data Group PDG. “Passage of particles through matter”. In: *Nuclear and Particle Physics*, vol. 33, no. 27, pp. 258-270 (2006). URL: <http://www.google.it/url?sa=t&source=web&cd=1&ved=0CBoQFjAA&url=https://docs.google.com/viewer?url=http%3A%2F%2Fpdg.lbl.gov%2F2006%2Freviews%2Fpassagerpp.pdf&ei=m3I3TevGBMadOuaHvfYD&usg=AFQjCNGEqYc4XyRNaSD1h09J3HTY3ZQA6w>.
- [2] “Andersen HH, Ziegler JF (1977) Stopping and ranges of ions in matter, vol 3. Pergamon Press, Elmsford, New York”. In: ().
- [3] “Lindhard J (1954) Kgl Danske Videnskab Selskab MatFys Medd 28:Nr. 8”. In: ().
- [4] William R. Leo. *Techniques for Nuclear and Particle Physics Experiments. A How-to Approach*. 2nd ed. Springer Berlin, Heidelberg, Feb. 25, 1994, pp. XVIII, 382. ISBN: 978-3-540-57280-0. DOI: <https://doi.org/10.1007/978-3-642-57920-2>. URL: <https://doi.org/10.1007/978-3-642-57920-2>.
- [5] M.J. Berger et al. “XCOM: Photon Cross Sections Database”. In: (). DOI: <https://dx.doi.org/10.18434/T48G6X>.
- [6] S. Agostinelli et al. “GEANT4—a simulation toolkit”. In: *Nucl. Instrum. Meth. A* 506 (2003), pp. 250–303. DOI: [10.1016/S0168-9002\(03\)01368-8](https://doi.org/10.1016/S0168-9002(03)01368-8).
- [7] IAEA. *Evaluated Nuclear Data File (ENDF)*. URL: <https://www-nds.iaea.org/exfor/endl.htm>.
- [8] F. Sauli. *Gaseous Radiation Detectors*. Cambridge Monographs on Particle Physics, Nuclear Physics and Cosmology. Cambridge University Press, Cambridge, 2014.
- [9] E. Oliveri F. Sauli. *GASEOUS DETECTORS HANDBOOK*. URL: <http://fabio.home.cern.ch/fabio/handbook.html>.
- [10] “Electron attachment, effective ionization coefficient, and electron drift velocity for CF4 gas mixtures”. In: *Nuclear Instruments and Methods in Physics Research Section A: Accelerators, Spectrometers, Detectors and Associated Equipment* 323.1 (1992), pp. 273–279. ISSN: 0168-9002. DOI: [https://doi.org/10.1016/0168-9002\(92\)90302-K](https://doi.org/10.1016/0168-9002(92)90302-K). URL: <https://www.sciencedirect.com/science/article/pii/016890029290302K>.
- [11] S. Biagi. *Magboltz — transport of electrons in gas mixtures*. (1995)–(2009). URL: <http://cern.ch/magboltz>.
- [12] H. Raethe. *Electron avalanches and breakdowns in gases*. Washington: Butterworths, 1964.
- [13] G. C. Montgomery and D. D. Montgomery. “Geiger–Mueller Counters”. In: *J. Franklin Inst.* 231, 447. (1941).
- [14] S. Ramo. “Currents Induced by Electron Motion”. In: *Proceedings of the IRE* 27.9 (1939), pp. 584–585. DOI: [10.1109/JRPROC.1939.228757](https://doi.org/10.1109/JRPROC.1939.228757).
- [15] Miyamoto S. Fukui S. “A new type of particle detector: the discharge chamber”. In: *Il Nuovo Cimento (1955-1965)*, 113 ,115,11,1827-6121 (1959). DOI: <https://doi.org/10.1007/BF02724913>.

- [16] D. Brinkmann et al. “Image data analysis for the NA35 streamer chamber”. In: *Nuclear Instruments and Methods in Physics Research Section A: Accelerators, Spectrometers, Detectors and Associated Equipment* 354.2 (1995), pp. 419–436. ISSN: 0168-9002. DOI: [https://doi.org/10.1016/0168-9002\(94\)01014-5](https://doi.org/10.1016/0168-9002(94)01014-5). URL: <https://www.sciencedirect.com/science/article/pii/0168900294010145>.
- [17] G. Charpak et al. “The use of multiwire proportional counters to select and localize charged particles”. In: *Nuclear Instruments and Methods* 62.3 (1968), pp. 262–268. ISSN: 0029-554X. DOI: [https://doi.org/10.1016/0029-554X\(68\)90371-6](https://doi.org/10.1016/0029-554X(68)90371-6). URL: <https://www.sciencedirect.com/science/article/pii/0029554X68903716>.
- [18] A. Breskin et al. “The multistep avalanche chamber: A new family of fast, high-rate particle detectors”. In: *Nuclear Instruments and Methods* 161.1 (1979), pp. 19–34. ISSN: 0029-554X. DOI: [https://doi.org/10.1016/0029-554X\(79\)90358-6](https://doi.org/10.1016/0029-554X(79)90358-6). URL: <https://www.sciencedirect.com/science/article/pii/0029554X79903586>.
- [19] A. Oed. “Position-sensitive detector with microstrip anode for electron multiplication with gases”. In: *Nuclear Instruments and Methods in Physics Research Section A: Accelerators, Spectrometers, Detectors and Associated Equipment* 263.2 (1988), pp. 351–359. ISSN: 0168-9002. DOI: [https://doi.org/10.1016/0168-9002\(88\)90970-9](https://doi.org/10.1016/0168-9002(88)90970-9). URL: <https://www.sciencedirect.com/science/article/pii/0168900288909709>.
- [20] S.F Biagi et al. “First experimental results from a microdot gas avalanche detector integrated onto a silicon wafer”. In: *Nuclear Instruments and Methods in Physics Research Section A: Accelerators, Spectrometers, Detectors and Associated Equipment* 366.1 (1995), pp. 76–78. ISSN: 0168-9002. DOI: [https://doi.org/10.1016/0168-9002\(95\)00687-7](https://doi.org/10.1016/0168-9002(95)00687-7). URL: <https://www.sciencedirect.com/science/article/pii/0168900295006877>.
- [21] Y. Giomataris et al. “MICROMEAS: a high-granularity position-sensitive gaseous detector for high particle-flux environments”. In: *Nuclear Instruments and Methods in Physics Research Section A: Accelerators, Spectrometers, Detectors and Associated Equipment* 376.1 (1996), pp. 29–35. ISSN: 0168-9002. DOI: [https://doi.org/10.1016/0168-9002\(96\)00175-1](https://doi.org/10.1016/0168-9002(96)00175-1). URL: <https://www.sciencedirect.com/science/article/pii/0168900296001751>.
- [22] F. Sauli. “GEM: A new concept for electron amplification in gas detectors”. In: *Nuclear Instruments and Methods in Physics Research Section A: Accelerators, Spectrometers, Detectors and Associated Equipment* 386.2 (1997), pp. 531–534. ISSN: 0168-9002. DOI: [https://doi.org/10.1016/S0168-9002\(96\)01172-2](https://doi.org/10.1016/S0168-9002(96)01172-2). URL: <https://www.sciencedirect.com/science/article/pii/S0168900296011722>.
- [23] *CERN Gaseous Detector Laboratory*. DOI: <https://gdd.web.cern.ch/gem>.
- [24] David Attié et al. “Current Status and Future Developments of Micromegas Detectors for Physics and Applications”. In: *Applied Sciences* 11.12 (2021). ISSN: 2076-3417. DOI: [10.3390/app11125362](https://doi.org/10.3390/app11125362). URL: <https://www.mdpi.com/2076-3417/11/12/5362>.
- [25] J. Derré and I. Giomataris. “Spatial resolution and rate capability of MICROMEAS detector”. In: *Nuclear Instruments and Methods in Physics Research Section A: Accelerators, Spectrometers, Detectors and Associated Equipment* 461.1 (2001). 8th Pisa Meeting on Advanced Detectors, pp. 74–76. ISSN: 0168-9002. DOI: [https://doi.org/10.1016/S0168-9002\(00\)01171-2](https://doi.org/10.1016/S0168-9002(00)01171-2). URL: <https://www.sciencedirect.com/science/article/pii/S0168900200011712>.
- [26] K Nikolopoulos et al. “Electron transparency of a Micromegas mesh”. In: *Journal of Instrumentation* 6.06 (June 2011), P06011. DOI: [10.1088/1748-0221/6/06/P06011](https://doi.org/10.1088/1748-0221/6/06/P06011). URL: <https://dx.doi.org/10.1088/1748-0221/6/06/P06011>.

- [27] “COMSOL”. In: (). DOI: <https://www.comsol.fr/>.
- [28] T Kawamoto et al. *New Small Wheel Technical Design Report*. Tech. rep. ATLAS New Small Wheel Technical Design Report. 2013. URL: <https://cds.cern.ch/record/1552862>.
- [29] I. Giomataris et al. “Micromegas in a bulk”. In: *Nuclear Instruments and Methods in Physics Research Section A: Accelerators, Spectrometers, Detectors and Associated Equipment* 560.2 (2006), pp. 405–408. ISSN: 0168-9002. DOI: <https://doi.org/10.1016/j.nima.2005.12.222>. URL: <https://www.sciencedirect.com/science/article/pii/S0168900205026501>.
- [30] T. Alexopoulos et al. “Performance studies of resistive-strip bulk micromegas detectors in view of the ATLAS New Small Wheel upgrade”. In: *Nuclear Instruments and Methods in Physics Research Section A: Accelerators, Spectrometers, Detectors and Associated Equipment* 937 (2019), pp. 125–140. ISSN: 0168-9002. DOI: <https://doi.org/10.1016/j.nima.2019.04.050>. URL: <https://www.sciencedirect.com/science/article/pii/S0168900219305194>.
- [31] T. Alexopoulos et al. “A spark-resistant bulk-micromegas chamber for high-rate applications”. In: *Nuclear Instruments and Methods in Physics Research Section A: Accelerators, Spectrometers, Detectors and Associated Equipment* 640.1 (2011), pp. 110–118. ISSN: 0168-9002. DOI: <https://doi.org/10.1016/j.nima.2011.03.025>. URL: <https://www.sciencedirect.com/science/article/pii/S0168900211005869>.
- [32] N. Abgrall et al. “Time projection chambers for the T2K near detectors”. In: *Nuclear Instruments and Methods in Physics Research Section A: Accelerators, Spectrometers, Detectors and Associated Equipment* 637.1 (2011), pp. 25–46. ISSN: 0168-9002. DOI: <https://doi.org/10.1016/j.nima.2011.02.036>. URL: <https://www.sciencedirect.com/science/article/pii/S0168900211003421>.
- [33] A. Acker et al. “The CLAS12 Micromegas Vertex Tracker”. In: *Nuclear Instruments and Methods in Physics Research Section A: Accelerators, Spectrometers, Detectors and Associated Equipment* 957 (2020), p. 163423. ISSN: 0168-9002. DOI: <https://doi.org/10.1016/j.nima.2020.163423>. URL: <https://www.sciencedirect.com/science/article/pii/S0168900220300280>.
- [34] F Gautheron et al. *COMPASS-II Proposal*. Tech. rep. Geneva: CERN, 2010. URL: <http://cds.cern.ch/record/1265628>.
- [35] D Attié et al. “Towards smaller gap microbulks”. In: *Journal of Instrumentation* 9.04 (Apr. 2014), p. C04013. DOI: [10.1088/1748-0221/9/04/C04013](https://doi.org/10.1088/1748-0221/9/04/C04013). URL: <https://dx.doi.org/10.1088/1748-0221/9/04/C04013>.
- [36] P Abbon et al. “The Micromegas detector of the CAST experiment”. In: *New Journal of Physics* 9.6 (June 2007), p. 170. DOI: [10.1088/1367-2630/9/6/170](https://doi.org/10.1088/1367-2630/9/6/170). URL: <https://dx.doi.org/10.1088/1367-2630/9/6/170>.
- [37] M. Chefdeville et al. “An electron-multiplying ‘Micromegas’ grid made in silicon wafer post-processing technology”. In: *Nuclear Instruments and Methods in Physics Research Section A: Accelerators, Spectrometers, Detectors and Associated Equipment* 556.2 (2006), pp. 490–494. ISSN: 0168-9002. DOI: <https://doi.org/10.1016/j.nima.2005.11.065>. URL: <https://www.sciencedirect.com/science/article/pii/S0168900205021418>.



- [38] M.M.F.R. Fraga et al. “The GEM scintillation in He–CF<sub>4</sub>, Ar–CF<sub>4</sub>, Ar–TEA and Xe–TEA mixtures”. In: *Nuclear Instruments and Methods in Physics Research Section A: Accelerators, Spectrometers, Detectors and Associated Equipment* 504.1 (2003). Proceedings of the 3rd International Conference on New Developments in Photodetection, pp. 88–92. ISSN: 0168-9002. DOI: [https://doi.org/10.1016/S0168-9002\(03\)00758-7](https://doi.org/10.1016/S0168-9002(03)00758-7). URL: <https://www.sciencedirect.com/science/article/pii/S0168900203007587>.
- [39] J. Derré et al. “Spatial resolution in Micromegas detectors”. In: *Nuclear Instruments and Methods in Physics Research Section A: Accelerators, Spectrometers, Detectors and Associated Equipment* 459.3 (2001), pp. 523–531. ISSN: 0168-9002. DOI: [https://doi.org/10.1016/S0168-9002\(00\)01051-2](https://doi.org/10.1016/S0168-9002(00)01051-2). URL: <https://www.sciencedirect.com/science/article/pii/S0168900200010512>.
- [40] M Byszewski and J Wotschack. “Resistive-strips micromegas detectors with two-dimensional readout”. In: *Journal of Instrumentation* 7.02 (Feb. 2012), p. C02060. DOI: [10.1088/1748-0221/7/02/C02060](https://doi.org/10.1088/1748-0221/7/02/C02060). URL: <https://dx.doi.org/10.1088/1748-0221/7/02/C02060>.
- [41] S. Bouteille et al. “A Micromegas-based telescope for muon tomography: The WatTo experiment”. In: *Nuclear Instruments and Methods in Physics Research Section A: Accelerators, Spectrometers, Detectors and Associated Equipment* 834 (2016), pp. 223–228. ISSN: 0168-9002. DOI: <https://doi.org/10.1016/j.nima.2016.08.002>. URL: <https://www.sciencedirect.com/science/article/pii/S0168900216308166>.
- [42] Joseph Ladislav Wiza. “Microchannel plate detectors”. In: *Nuclear Instruments and Methods* 162.1 (1979), pp. 587–601. ISSN: 0029-554X. DOI: [https://doi.org/10.1016/0029-554X\(79\)90734-1](https://doi.org/10.1016/0029-554X(79)90734-1). URL: <https://www.sciencedirect.com/science/article/pii/0029554X79907341>.
- [43] N Barthe et al. “Recent technologic developments on high-resolution beta imaging systems for quantitative autoradiography and double labeling applications”. In: *Nuclear Instruments and Methods in Physics Research Section A: Accelerators, Spectrometers, Detectors and Associated Equipment* 527.1 (2004). Proceedings of the 2nd International Conference on Imaging Technologies in Biomedical Sciences, pp. 41–45. ISSN: 0168-9002. DOI: <https://doi.org/10.1016/j.nima.2004.03.014>. URL: <https://www.sciencedirect.com/science/article/pii/S0168900204003614>.
- [44] E. Aprile et al. “The XENON100 dark matter experiment”. In: *Astroparticle Physics* 35.9 (Apr. 2012), pp. 573–590. ISSN: 0927-6505. DOI: [10.1016/j.astropartphys.2012.01.003](https://doi.org/10.1016/j.astropartphys.2012.01.003). URL: <http://dx.doi.org/10.1016/j.astropartphys.2012.01.003>.
- [45] A. Morozov et al. “A 2D gas scintillation detector for thermal neutrons”. In: *2012 IEEE Nuclear Science Symposium and Medical Imaging Conference Record (NSS/MIC)*. 2012, pp. 1572–1576. DOI: [10.1109/NSSMIC.2012.6551375](https://doi.org/10.1109/NSSMIC.2012.6551375).
- [46] K. et al. Bays. “Supernova relic neutrino search at super-Kamiokande”. In: *Phys. Rev. D* 85 (5 Mar. 2012), p. 052007. DOI: [10.1103/PhysRevD.85.052007](https://doi.org/10.1103/PhysRevD.85.052007). URL: <https://link.aps.org/doi/10.1103/PhysRevD.85.052007>.
- [47] Gabriella Sciolla and the DMTPC Collaboration. “The DMTPC project”. In: *Journal of Physics: Conference Series* 179 (July 2009), p. 012009. ISSN: 1742-6596. DOI: [10.1088/1742-6596/179/1/012009](https://doi.org/10.1088/1742-6596/179/1/012009). URL: <http://dx.doi.org/10.1088/1742-6596/179/1/012009>.
- [48] G. Mazzitelli et al. “A high resolution TPC based on GEM optical readout”. In: *2017 IEEE Nuclear Science Symposium and Medical Imaging Conference (NSS/MIC)*. 2017, pp. 1–4. DOI: [10.1109/NSSMIC.2017.8532631](https://doi.org/10.1109/NSSMIC.2017.8532631).

- [49] M. Pomorski et al. “Proton spectroscopy of  $^{48}\text{Ni}$ ,  $^{46}\text{Fe}$ , and  $^{44}\text{Cr}$ ”. In: *Phys. Rev. C* 90 (1 July 2014), p. 014311. DOI: [10.1103/PhysRevC.90.014311](https://doi.org/10.1103/PhysRevC.90.014311). URL: <https://link.aps.org/doi/10.1103/PhysRevC.90.014311>.
- [50] H.M. Araújo et al. “The MIGDAL experiment: Measuring a rare atomic process to aid the search for dark matter”. In: *Astroparticle Physics* 151 (2023), p. 102853. ISSN: 0927-6505. DOI: <https://doi.org/10.1016/j.astropartphys.2023.102853>. URL: <https://www.sciencedirect.com/science/article/pii/S0927650523000397>.
- [51] Florian M. Brunbauer et al. “Combined Optical and Electronic Readout for Event Reconstruction in a GEM-Based TPC”. In: *IEEE Transactions on Nuclear Science* 65.3 (2018), pp. 913–918.
- [52] F.M. Brunbauer et al. “Radiation imaging with glass Micromegas”. In: *Nuclear Instruments and Methods in Physics Research Section A: Accelerators, Spectrometers, Detectors and Associated Equipment* 955 (2020), p. 163320. ISSN: 0168-9002. DOI: <https://doi.org/10.1016/j.nima.2019.163320>. URL: <https://www.sciencedirect.com/science/article/pii/S0168900219315591>.
- [53] J. Bortfeldt. “Gaseous Detectors for Preclinical Proton Beam Monitoring, Characterization and Imaging”. In: URL: <https://indico.cern.ch/event/1219224/contributions/5130791/attachments/2568577/4428816/bortfeldt221216.pdf>.
- [54] E. Robert et al. “Time-resolved spectroscopy of high pressure rare gases excited by an energetic flash X-ray source”. In: *Optics Communications* 117.1 (1995), pp. 179–188. ISSN: 0030-4018. DOI: [https://doi.org/10.1016/0030-4018\(94\)00664-G](https://doi.org/10.1016/0030-4018(94)00664-G). URL: <https://www.sciencedirect.com/science/article/pii/003040189400664G>.
- [55] K. Saito et al. “Absolute number of scintillation photons emitted by alpha particles in rare gases”. In: *IEEE Transactions on Nuclear Science* 49.4 (2002), pp. 1674–1680. DOI: [10.1109/TNS.2002.801700](https://doi.org/10.1109/TNS.2002.801700).
- [56] L. G. Christophorou and J. K. Olthoff. “Electron Interactions With Plasma Processing Gases: An Update for  $\text{CF}_4$ ,  $\text{CHF}_3$ ,  $\text{C}_2\text{F}_6$ , and  $\text{C}_3\text{F}_8$ ”. In: *Journal of Physical and Chemical Reference Data* 28.4 (July 1999), pp. 967–982. ISSN: 0047-2689. DOI: [10.1063/1.556042](https://doi.org/10.1063/1.556042). eprint: <https://pubs.aip.org/aip/jpr/article-pdf/28/4/967/8183493/967\1\online.pdf>. URL: <https://doi.org/10.1063/1.556042>.
- [57] Müller U. et al. “Further studies of the continuous UV emission produced by electron impact on  $\text{CF}_4$ ”. In: *Zeitschrift für Physik D Atoms, Molecules and Clusters* (1992). DOI: <https://doi.org/10.1007/BF01426697>.
- [58] Kenji Furuya, Eri Koto, and Teiichiro Ogawa. “Fragment ion-photon coincidence investigation of carbon tetrafluoride by controlled electron impact”. In: *Journal of Physics B: Atomic, Molecular and Optical Physics* 34.8 (Apr. 2001), p. 1405. DOI: [10.1088/0953-4075/34/8/306](https://doi.org/10.1088/0953-4075/34/8/306). URL: <https://dx.doi.org/10.1088/0953-4075/34/8/306>.
- [59] P. Amedo et al. *Observation of strong wavelength-shifting in the argon-tetrafluoromethane system*. 2023. arXiv: [2306.09919](https://arxiv.org/abs/2306.09919) [id='physics.ins-det' full\_name='InstrumentationandDetection' Truealt\_name = Nonein\_archive = 'physics'is\_general = Falsedescription = 'InstrumentationandDetection']
- [60] Nobuaki Washida et al. “Emission spectra of  $\text{CF}_3$  radicals. IV. Excitation spectra, quantum yields, and potential energy surfaces of the  $\text{CF}_3$  fluorescences”. In: *The Journal of Chemical Physics* 78.3 (Feb. 1983), pp. 1025–1032. ISSN: 0021-9606. DOI: [10.1063/1.444902](https://doi.org/10.1063/1.444902). eprint: <https://pubs.aip.org/aip/jcp/article-pdf/78/3/1025/18940597/1025\1\online.pdf>. URL: <https://doi.org/10.1063/1.444902>.

- [61] Masaharu Tsuji et al. “Dissociative excitation of CF<sub>4</sub>, CCl<sub>4</sub>, and chlorofluoromethanes by collisions with argon and helium active species”. In: *The Journal of Chemical Physics* 97.1 (July 1992), pp. 245–255. ISSN: 0021-9606. DOI: [10.1063/1.463622](https://doi.org/10.1063/1.463622). eprint: [https://pubs.aip.org/aip/jcp/article-pdf/97/1/245/19000754/245\\\_1\\\_online.pdf](https://pubs.aip.org/aip/jcp/article-pdf/97/1/245/19000754/245\_1\_online.pdf). URL: <https://doi.org/10.1063/1.463622>.
- [62] Masaharu Tsuji et al. “Dissociative charge-transfer reactions of Ar<sup>+</sup> with CF<sub>n</sub>Cl<sub>4-n</sub> at thermal energy”. In: *The Journal of Chemical Physics* 96.5 (Mar. 1992), pp. 3649–3655. ISSN: 0021-9606. DOI: [10.1063/1.461918](https://doi.org/10.1063/1.461918). eprint: [https://pubs.aip.org/aip/jcp/article-pdf/96/5/3649/18997777/3649\\\_1\\\_online.pdf](https://pubs.aip.org/aip/jcp/article-pdf/96/5/3649/18997777/3649\_1\_online.pdf). URL: <https://doi.org/10.1063/1.461918>.
- [63] E. Seravalli. “A Scintillating GEM Detector for 2D Dose Imaging in Hadron Therapy. PhD thesis”. PhD thesis. Technische Universiteit Delft, 2008.
- [64] F. Brunbauer. “Dissertation Applications of gas scintillation properties in optically read out GEM-based detectors”. PhD thesis. 2018. DOI: <https://doi.org/10.34726/hss.2018.33748>.
- [65] V. Peskov et al. “Investigation of light emission from a parallel-plate avalanche chamber filled with noble gases and with TEA, TMAE, and H<sub>2</sub>O vapours at atmospheric pressure”. In: *Nuclear Instruments and Methods in Physics Research Section A: Accelerators, Spectrometers, Detectors and Associated Equipment* 277.2 (1989), pp. 547–556. ISSN: 0168-9002. DOI: [https://doi.org/10.1016/0168-9002\(89\)90788-2](https://doi.org/10.1016/0168-9002(89)90788-2). URL: <https://www.sciencedirect.com/science/article/pii/0168900289907882>.
- [66] Hamamatsu. *Technical note*. URL: [https://www.hamamatsu.com/content/dam/hamamatsu-photonics/sites/documents/99\\_SALES\\_LIBRARY/sys/SCAS0154E\\_C15550-20UP\\_tec.pdf](https://www.hamamatsu.com/content/dam/hamamatsu-photonics/sites/documents/99_SALES_LIBRARY/sys/SCAS0154E_C15550-20UP_tec.pdf).
- [67] STEVE HOWELL and Ali Tavackolimehr. *Handbook of CCD Astronomy*. Apr. 2019.
- [68] Albert J.P. Theuwissen. “CMOS image sensors: State-of-the-art”. In: *Solid-State Electronics* 52.9 (2008). Papers Selected from the 37th European Solid-State Device Research Conference - ESSDERC’07, pp. 1401–1406. ISSN: 0038-1101. DOI: <https://doi.org/10.1016/j.sse.2008.04.012>. URL: <https://www.sciencedirect.com/science/article/pii/S0038110108001317>.
- [69] Thomas H. Lee. *The Design of CMOS Radio-Frequency Integrated Circuits*. 2nd ed. Cambridge University Press, 2003. URL: <https://web.archive.org/web/20191209032130/https://web.stanford.edu/class/archive/ee/ee214/ee214.1032/Handouts/H02.pdf>.
- [70] Eugene hecht. *Optics*. Pearson Education © 2017, 2017. ISBN: 9780133977226.
- [71] *Ray Optics Simulation*. URL: <https://phydemo.app/ray-optics/>.
- [72] Hamamatsu. *SCAS0152E ORCA Quest concept brochure*. URL: [https://www.hamamatsu.com/content/dam/hamamatsu-photonics/sites/documents/99\\_SALES\\_LIBRARY/sys/SCAS0152E\\_ORCA-Quest\\_concept\\_brochure.pdf](https://www.hamamatsu.com/content/dam/hamamatsu-photonics/sites/documents/99_SALES_LIBRARY/sys/SCAS0152E_ORCA-Quest_concept_brochure.pdf).
- [73] dupont. URL: <https://www.dupont.com/electronics-industrial/pyralux-fr.html>.
- [74] Maxim Titov. *Gaseous Detectors: recent developments and applications*. 2010. arXiv: 1008.3736 [physics.ins-det].
- [75] Hamamatsu. URL: [https://www.hamamatsu.com/eu/en/product/optical-sensors/pmt/pmt\\_tube-alone/head-on-type/R6231-01.html](https://www.hamamatsu.com/eu/en/product/optical-sensors/pmt/pmt_tube-alone/head-on-type/R6231-01.html).

- [76] Glenn F. Knoll. *Radiation Detection and Measurement*. 3rd. New York: Wiley, 2000. ISBN: 978-0-471-07338-3.
- [77] schneiderkreuznach. URL: [https://schneiderkreuznach.com/application/files/5316/8422/6360/ONYX\\_095\\_25\\_C\\_0012101\\_datasheet.pdf](https://schneiderkreuznach.com/application/files/5316/8422/6360/ONYX_095_25_C_0012101_datasheet.pdf).
- [78] Ultimaker. URL: <https://ultimaker.com/fr/3d-printers/s-series/ultimaker-2-connect/>.
- [79] Martin Ester et al. “A Density-Based Algorithm for Discovering Clusters in Large Spatial Databases with Noise”. In: *Knowledge Discovery and Data Mining*. 1996. URL: <https://api.semanticscholar.org/CorpusID:355163>.
- [80] X-ray Hüttner. *Lead target for X-rays - Type 81*. URL: <https://www.xray-huettner.com/print.php?name=19>.
- [81] L. B. Lucy. “An iterative technique for the rectification of observed distributions”. In: *Astronomical Journal, Vol. 79, p. 745* (1974). DOI: [10.1086/111605](https://doi.org/10.1086/111605).
- [82] A. Cools et al. “X-ray imaging with Micromegas detectors with optical readout”. In: *Journal of Instrumentation* 18.06 (June 2023), p. C06019. DOI: [10.1088/1748-0221/18/06/C06019](https://doi.org/10.1088/1748-0221/18/06/C06019). URL: <https://dx.doi.org/10.1088/1748-0221/18/06/C06019>.
- [83] Mourad Idir et al. “Metrology and Tests Beamline at SOLEIL”. In: *AIP Conference Proceedings* 879.1 (2007), pp. 619–622. DOI: [10.1063/1.2436137](https://doi.org/10.1063/1.2436137). eprint: <https://aip.scitation.org/doi/pdf/10.1063/1.2436137>. URL: <https://aip.scitation.org/doi/abs/10.1063/1.2436137>.
- [84] Y. Ménesguen and M.-C. Lépy. “Characterization of the Metrology beamline at the SOLEIL synchrotron and application to the determination of mass attenuation coefficients of Ag and Sn in the range  $3.5 \leq E \leq 28$  keV”. In: *X-Ray Spectrometry* 40.6 (2011), pp. 411–416. DOI: <https://doi.org/10.1002/xrs.1366>. URL: <https://analyticalsciencejournals.onlinelibrary.wiley.com/doi/abs/10.1002/xrs.1366>.
- [85] *SOLEIL synchrotron scheme*. URL: [https://commons.wikimedia.org/wiki/File:Sch%C3%A9ma\\_de\\_principe\\_du\\_synchrotron.png](https://commons.wikimedia.org/wiki/File:Sch%C3%A9ma_de_principe_du_synchrotron.png).
- [86] AltaVision. URL: [http://www.altavision.com.br/Datasheets/Basler\\_EN/scA1300-32gm.html](http://www.altavision.com.br/Datasheets/Basler_EN/scA1300-32gm.html).
- [87] Prof. Tom Fomby. *SCORING MEASURES FOR PREDICTION PROBLEMS*. URL: [https://s2.smu.edu/tfomby/eco5385\\_eco6380/lecture/Scoring%20Measures%20for%20Prediction%20Problems.pdf](https://s2.smu.edu/tfomby/eco5385_eco6380/lecture/Scoring%20Measures%20for%20Prediction%20Problems.pdf).
- [88] L. Ambrosi et al. “Characterization of charge spreading and gain of encapsulated resistive Micromegas detectors for the upgrade of the T2K Near Detector Time Projection Chambers”. In: *Nuclear Instruments and Methods in Physics Research Section A: Accelerators, Spectrometers, Detectors and Associated Equipment* 1056 (2023), p. 168534. ISSN: 0168-9002. DOI: <https://doi.org/10.1016/j.nima.2023.168534>. URL: <https://www.sciencedirect.com/science/article/pii/S0168900223005247>.
- [89] A. Delbart. “Production and calibration of 9m2 of bulk-micromegas detectors for the readout of the ND280/TPCs of the T2K experiment”. In: *Nuclear Instruments and Methods in Physics Research Section A: Accelerators, Spectrometers, Detectors and Associated Equipment* 623.1 (2010). 1st International Conference on Technology and Instrumentation in Particle Physics, pp. 105–107. ISSN: 0168-9002. DOI: <https://doi.org/10.1016/j.nima.2010.02.163>. URL: <https://www.sciencedirect.com/science/article/pii/S0168900210004304>.

- [90] F. Diego. “STELLAR IMAGE PROFILES FROM LINEAR DETECTORS AND THE THROUGHPUT OF ASTRONOMICAL INSTRUMENTS”. In: *Publications of the Astronomical Society of the Pacific* 97.598 (Dec. 1985), p. 1209. DOI: [10.1086/131688](https://doi.org/10.1086/131688). URL: <https://dx.doi.org/10.1086/131688>.
- [91] Paul Serrano. “Caliste-MM : a new spectro-polarimeter for soft X-ray astrophysics”. Theses. Université Paris Saclay (COMUE), Oct. 2017. URL: <https://theses.hal.science/tel-01723432>.
- [92] TELEDYNE PHOTOMETRICS. *Retiga<sub>R6</sub>Datasheet*. URL: [https://www.photometrics.com/wp-content/uploads/2022/02/Retiga\\_R6\\_Datasheet-28-02-2022.pdf](https://www.photometrics.com/wp-content/uploads/2022/02/Retiga_R6_Datasheet-28-02-2022.pdf).
- [93] Purba Bhattacharya et al. “The effect of spacers on the performance of Micromegas detectors: A numerical investigation”. In: *Nuclear Instruments and Methods in Physics Research Section A: Accelerators, Spectrometers, Detectors and Associated Equipment* 793 (2015), pp. 41–48. ISSN: 0168-9002. DOI: <https://doi.org/10.1016/j.nima.2015.04.051>. URL: <https://www.sciencedirect.com/science/article/pii/S0168900215005549>.
- [94] Gorski S.A. et al. Rajewsky N. Almouzni G. “LifeTime and improving European health-care through cell-based interceptive medicine”. In: *Nature* 587 (2020), pp. 377–386. DOI: <https://doi.org/10.1038/s41586-020-2715-9>.
- [95] Almendro V Marusyk A and Polyak K. “Intra-tumour heterogeneity: a looking glass for cancer?” In: *Nature Reviews Cancer* 12 (2012), p. 323. DOI: <https://doi.org/10.1038/nrc3261>.
- [96] Claudio Vinegoni et al. “Advances in measuring single-cell pharmacology in vivo”. In: *Drug Discovery Today* 20.9 (2015), pp. 1087–1092. ISSN: 1359-6446. DOI: <https://doi.org/10.1016/j.drudis.2015.05.011>. URL: <https://www.sciencedirect.com/science/article/pii/S1359644615002196>.
- [97] Mahmood U. et al Weissleder R. Tung CH. “In vivo imaging of tumors with protease-activated near-infrared fluorescent probes”. In: *Nat Biotechnol* 17.9 (1999), pp. 375–378. URL: <https://doi.org/10.1038/7933>.
- [98] Héloïse Cahuzac et al. “Monitoring In Vivo Performances of Protein–Drug Conjugates Using Site-Selective Dual Radiolabeling and Ex Vivo Digital Imaging”. In: *Journal of Medicinal Chemistry* 65.9 (2022). PMID: 35500280, pp. 6953–6968. DOI: [10.1021/acs.jmedchem.2c00401](https://doi.org/10.1021/acs.jmedchem.2c00401). eprint: <https://doi.org/10.1021/acs.jmedchem.2c00401>. URL: <https://doi.org/10.1021/acs.jmedchem.2c00401>.
- [99] Nicole Barthe et al. “Chapter 9 - High-resolution beta imaging”. In: *Handbook of Radioactivity Analysis: Volume 2 (Fourth Edition)*. Ed. by Michael F. L’Annunziata. Fourth Edition. Academic Press, 2020, pp. 669–727. ISBN: 978-0-12-814395-7. DOI: <https://doi.org/10.1016/B978-0-12-814395-7.00009-X>. URL: <https://www.sciencedirect.com/science/article/pii/B978012814395700009X>.
- [100] Georges Charpak, Wojciech Dominik, and Nicolas Zaganidis. “Optical imaging of the spatial distribution of  $\beta$ -particles emerging from surfaces”. In: *Proc. Natl. Acad. Sci. U. S. A.* 86 (1989), pp. 1741–1745. URL: <https://cds.cern.ch/record/193334>.
- [101] Nicole Barthe et al. “Optimization of a New Scintillation Gas Detector Used to Localize Electrons Emitted by  $^{99m}\text{Tc}$ ”. In: *Journal of Nuclear Medicine* 40.5 (1999), pp. 868–875. ISSN: 0161-5505. eprint: <https://jnm.snmjournals.org/content/40/5/868.full.pdf>. URL: <https://jnm.snmjournals.org/content/40/5/868>.

- [102] D. Thers et al. “New prospects on particle detection with a Parallel Ionization Multiplier (PIM)”. In: *Nuclear Instruments and Methods in Physics Research Section A: Accelerators, Spectrometers, Detectors and Associated Equipment* 535.1 (2004). Proceedings of the 10th International Vienna Conference on Instrumentation, pp. 562–565. ISSN: 0168-9002. DOI: <https://doi.org/10.1016/j.nima.2004.07.281>. URL: <https://www.sciencedirect.com/science/article/pii/S0168900204017346>.
- [103] J. Donnard et al. “The PIMager: A new tool for high sensitive digital  $\beta$  autoradiograph”. In: *2009 IEEE Nuclear Science Symposium Conference Record (NSS/MIC)*. 2009, pp. 3672–3674. DOI: [10.1109/NSSMIC.2009.5401854](https://doi.org/10.1109/NSSMIC.2009.5401854).
- [104] J. Donnard et al. “High spatial resolution in  $\beta$ -imaging with a PIM device”. In: *2007 IEEE Nuclear Science Symposium Conference Record*. Vol. 6. 2007, pp. 4658–4661. DOI: [10.1109/NSSMIC.2007.4437146](https://doi.org/10.1109/NSSMIC.2007.4437146).
- [105] F. Jambon et al. “Medica-Plus: A Micromegas-based proof-of-concept detector for sub-becquerel tritium activity assessment at the service of oncological research”. In: *Nuclear Instruments and Methods in Physics Research Section A: Accelerators, Spectrometers, Detectors and Associated Equipment* 1027 (2022), p. 166332. ISSN: 0168-9002. DOI: <https://doi.org/10.1016/j.nima.2022.166332>. URL: <https://www.sciencedirect.com/science/article/pii/S0168900222000171>.
- [106] Elsa Mazari-Arrighi et al. “Construction of functional biliary epithelial branched networks with predefined geometry using digital light stereolithography”. In: *Biomaterials* 279 (2021), p. 121207. ISSN: 0142-9612. DOI: <https://doi.org/10.1016/j.biomaterials.2021.121207>. URL: <https://www.sciencedirect.com/science/article/pii/S0142961221005640>.
- [107] Nosayba Al-Azzam and Anas Alazzam. “Micropatterning of cells via adjusting surface wettability using plasma treatment and graphene oxide deposition”. In: *PLOS ONE* 17.6 (June 2022), pp. 1–14. DOI: [10.1371/journal.pone.0269914](https://doi.org/10.1371/journal.pone.0269914). URL: <https://doi.org/10.1371/journal.pone.0269914>.
- [108] A. Cools et al. “Medica-Plus: a Micromegas-based proof-of-concept detector for sub-becquerel tritium activity assessment in the context of oncological research, RD51 mini-week, June 6-9, 2016, CERN, Geneva, Switzerland”. In: URL: <https://indico.cern.ch/event/1110129/timetable/?view=standard>.
- [109] National Diagnostics Laboratory Staff. *Principles and Applications of Liquid Scintillation Counting*. URL: [https://web.archive.org/web/20110406115218/http://www.ehs.psu.edu/radprot/LSC\\_Theory2.pdf](https://web.archive.org/web/20110406115218/http://www.ehs.psu.edu/radprot/LSC_Theory2.pdf).
- [110] *The BetaIMAGER™ tRACER*. URL: <https://biospacelab.com/products/>.
- [111] F Jambon et al. “Medica-Plus: a novel Micromegas detector for high-resolution  $\beta$  imaging for improved pharmacological applications”. In: *Journal of Physics: Conference Series* 1498.1 (Apr. 2020), p. 012046. DOI: [10.1088/1742-6596/1498/1/012046](https://doi.org/10.1088/1742-6596/1498/1/012046). URL: <https://dx.doi.org/10.1088/1742-6596/1498/1/012046>.
- [112] *Livermore low-energy electromagnetic models*. URL: <https://twiki.cern.ch/twiki/bin/view/Geant4/LoweMigratedLivermore>.
- [113] E.H. Lehmann et al. “The micro-setup for neutron imaging: A major step forward to improve the spatial resolution”. In: *Nuclear Instruments and Methods in Physics Research Section A: Accelerators, Spectrometers, Detectors and Associated Equipment* 576.2 (2007), pp. 389–396. ISSN: 0168-9002. DOI: <https://doi.org/10.1016/j.nima.2007.03.017>. URL: <https://www.sciencedirect.com/science/article/pii/S0168900207004950>.

- [114] F.A.F Fraga et al. “CCD readout of GEM-based neutron detectors”. In: *Nuclear Instruments and Methods in Physics Research Section A: Accelerators, Spectrometers, Detectors and Associated Equipment* 478.1 (2002). Proceedings of the ninth Int.Conf. on Instrumentation, pp. 357–361. ISSN: 0168-9002. DOI: [https://doi.org/10.1016/S0168-9002\(01\)01829-0](https://doi.org/10.1016/S0168-9002(01)01829-0). URL: <https://www.sciencedirect.com/science/article/pii/S0168900201018290>.
- [115] Takeshi Fujiwara et al. “Microstructured boron foil scintillating G-GEM detector for neutron imaging”. In: *Nuclear Instruments and Methods in Physics Research Section A: Accelerators, Spectrometers, Detectors and Associated Equipment* 838 (2016), pp. 124–128. ISSN: 0168-9002. DOI: <https://doi.org/10.1016/j.nima.2016.09.005>. URL: <https://www.sciencedirect.com/science/article/pii/S0168900216309275>.
- [116] S. Andriamonje et al. “Neutron imaging with a Micromegas detector”. In: *IEEE Symposium Conference Record Nuclear Science 2004*. Vol. 3. 2004, 1621–1625 Vol. 3. DOI: [10.1109/NSSMIC.2004.1462550](https://doi.org/10.1109/NSSMIC.2004.1462550).
- [117] Farinelli, R. et al. “ $\mu$ RANIA-V: an innovative solution for neutron detection in homeland security”. In: *EPJ Web Conf.* 253 (2021), p. 07009. DOI: [10.1051/epjconf/202125307009](https://doi.org/10.1051/epjconf/202125307009). URL: <https://doi.org/10.1051/epjconf/202125307009>.
- [118] M Strobl et al. “Advances in neutron radiography and tomography”. In: *Journal of Physics D: Applied Physics* 42.24 (Nov. 2009), p. 243001. DOI: [10.1088/0022-3727/42/24/243001](https://doi.org/10.1088/0022-3727/42/24/243001). URL: <https://dx.doi.org/10.1088/0022-3727/42/24/243001>.
- [119] K. Kihm et al. “Neutron Imaging of Alkali Metal Heat Pipes”. In: *Physics Procedia* 43 (2013). The 7th International Topical Meeting on Neutron Radiography (ITMNR-7), pp. 323–330. ISSN: 1875-3892. DOI: <https://doi.org/10.1016/j.phpro.2013.03.038>. URL: <https://www.sciencedirect.com/science/article/pii/S1875389213000527>.
- [120] Koichi Nittoh et al. “New feature of the neutron color image intensifier”. In: *Nuclear Instruments and Methods in Physics Research Section A: Accelerators, Spectrometers, Detectors and Associated Equipment* 605.1 (2009). ITMNR 08, pp. 107–110. ISSN: 0168-9002. DOI: <https://doi.org/10.1016/j.nima.2009.01.136>. URL: <https://www.sciencedirect.com/science/article/pii/S0168900209002587>.
- [121] Burkhard Schillinger, Johannes Brunner, and Elbio Calzada. “A study of oil lubrication in a rotating engine using stroboscopic neutron imaging”. In: *Physica B: Condensed Matter* 385-386 (2006), pp. 921–923. ISSN: 0921-4526. DOI: <https://doi.org/10.1016/j.physb.2006.05.250>. URL: <https://www.sciencedirect.com/science/article/pii/S0921452606011045>.
- [122] L. Segui et al. “Detector design and performance tests of the ESS-neutron Beam Loss Monitor detectors”. In: *Journal of Instrumentation* 18.01 (Jan. 2023), P01013. DOI: [10.1088/1748-0221/18/01/P01013](https://doi.org/10.1088/1748-0221/18/01/P01013). URL: <https://dx.doi.org/10.1088/1748-0221/18/01/P01013>.
- [123] Simon, E. and Guimbal, P. “Performance assessment of imaging plates for the JHR transfer Neutron Imaging System”. In: *EPJ Web Conf.* 170 (2018), p. 04021. DOI: [10.1051/epjconf/201817004021](https://doi.org/10.1051/epjconf/201817004021). URL: <https://doi.org/10.1051/epjconf/201817004021>.
- [124] Carina Höglund et al. “B4C thin films for neutron detection”. In: *Journal of Applied Physics* 111.10 (May 2012), p. 104908. ISSN: 0021-8979. DOI: [10.1063/1.4718573](https://doi.org/10.1063/1.4718573). eprint: [https://pubs.aip.org/aip/jap/article-pdf/doi/10.1063/1.4718573/15090184/104908\\_1\\_online.pdf](https://pubs.aip.org/aip/jap/article-pdf/doi/10.1063/1.4718573/15090184/104908_1_online.pdf). URL: <https://doi.org/10.1063/1.4718573>.

- [125] N.F.V. Duarte et al. “Improving position resolution of neutron detectors with ultra-thin B4C foils”. In: *Journal of Instrumentation* 17.03 (Mar. 2022), T03003. DOI: [10.1088/1748-0221/17/03/T03003](https://doi.org/10.1088/1748-0221/17/03/T03003). URL: <https://dx.doi.org/10.1088/1748-0221/17/03/T03003>.
- [126] SINQ. *Morpheus: Two-axes neutron diffractometer reflectometer*. URL: <https://www.psi.ch/en/sinq/morpheus/description>.
- [127] A. Cools et al. “Neutron and beta imaging with Micromegas detectors with optical readout”. In: *Nuclear Instruments and Methods in Physics Research Section A: Accelerators, Spectrometers, Detectors and Associated Equipment* 1048 (2023), p. 167910. ISSN: 0168-9002. DOI: <https://doi.org/10.1016/j.nima.2022.167910>. URL: <https://www.sciencedirect.com/science/article/pii/S0168900222012025>.
- [128] Cools, A. et al. “Neutron imaging with Micromegas detectors with optical readout”. In: *EPJ Web Conf.* 288 (2023), p. 07009. DOI: [10.1051/epjconf/202328807009](https://doi.org/10.1051/epjconf/202328807009). URL: <https://doi.org/10.1051/epjconf/202328807009>.
- [129] SINQ. *SINQ: The Swiss Spallation Neutron Source*. URL: <https://www.psi.ch/en/sinq>.
- [130] J. Bortfeldt et al. “PICOSEC: Charged particle timing at sub-25 picosecond precision with a Micromegas based detector”. In: *Nuclear Instruments and Methods in Physics Research Section A: Accelerators, Spectrometers, Detectors and Associated Equipment* 903 (2018), pp. 317–325. ISSN: 0168-9002. DOI: <https://doi.org/10.1016/j.nima.2018.04.033>. URL: <https://www.sciencedirect.com/science/article/pii/S0168900218305369>.
- [131] S. Andriamonje et al. “Preamplification structures based on Micromegas”. In: *IEEE Symposium Conference Record Nuclear Science 2004*. Vol. 1. 2004, 461–464 Vol. 1. DOI: [10.1109/NSSMIC.2004.1462234](https://doi.org/10.1109/NSSMIC.2004.1462234).
- [132] Mitutoyo. *QV ACTIVE 404*. URL: [https://shop.mitutoyo.fr/web/mitutoyo/fr\\_FR/mitutoyo/\\$catalogue/mitutoyoData/PR/363-110-30/datasheet.xhtml](https://shop.mitutoyo.fr/web/mitutoyo/fr_FR/mitutoyo/$catalogue/mitutoyoData/PR/363-110-30/datasheet.xhtml).
- [133] Reynaldo Pugliesi, Marco Stanojev Pereira, and Roberto Schoueri. “Method to evaluate the L/D Ratio of Neutron Imaging Beams”. In: *Brazilian Journal of Radiation Sciences* 5 (Apr. 2017). DOI: [10.15392/bjrs.v5i1.257](https://doi.org/10.15392/bjrs.v5i1.257).
- [134] Ehsan Samei, Michael J. Flynn, and David A. Reimann. “A method for measuring the presampled MTF of digital radiographic systems using an edge test device”. In: *Medical Physics* 25.1 (), pp. 102–113. DOI: <https://doi.org/10.1118/1.598165>. eprint: <https://aapm.onlinelibrary.wiley.com/doi/pdf/10.1118/1.598165>. URL: <https://aapm.onlinelibrary.wiley.com/doi/abs/10.1118/1.598165>.
- [135] T. Williams. *The Optical Transfer Function of Imaging Systems (1st ed.)*. Routledge, 1999. DOI: <https://doi.org/10.1201/9780203736296>.
- [136] I. A. Cunningham and B. K. Reid. “Signal and noise in modulation transfer function determinations using the slit, wire, and edge techniques”. In: *Medical Physics* 19.4 (1992), pp. 1037–1044. DOI: <https://doi.org/10.1118/1.596821>. eprint: <https://aapm.onlinelibrary.wiley.com/doi/pdf/10.1118/1.596821>. URL: <https://aapm.onlinelibrary.wiley.com/doi/abs/10.1118/1.596821>.
- [137] NIST. *Neutron activation and scattering calculator*. URL: <https://www.ncnr.nist.gov/resources/activation/>.
- [138] Davide Pinci - INFN Roma. “Optical and hybrid readout techniques, RD51 Micro Pattern Gaseous Detectors School, November 30, 2024, CERN, Geneva, Switzerland”. In: URL: <https://indico.cern.ch/event/1239595/timetable/>.



- [139] Helena Pleinert, Eberhard Lehmann, and Sonja Körner. “Design of a new CCD-camera neutron radiography detector”. In: *Nuclear Instruments and Methods in Physics Research Section A: Accelerators, Spectrometers, Detectors and Associated Equipment* 399.2 (1997), pp. 382–390. ISSN: 0168-9002. DOI: [https://doi.org/10.1016/S0168-9002\(97\)00944-3](https://doi.org/10.1016/S0168-9002(97)00944-3). URL: <https://www.sciencedirect.com/science/article/pii/S0168900297009443>.
- [140] Tao Yang et al. “A Novel Method to Improve the Spatial Resolution of GEM Neutron Detectors With a Stopping Layer”. In: *IEEE Transactions on Nuclear Science* 69.1 (2022), pp. 68–77. DOI: [10.1109/TNS.2021.3135929](https://doi.org/10.1109/TNS.2021.3135929).
- [141] M. Köhli et al. “Efficiency and spatial resolution of the CASCADE thermal neutron detector”. In: *Nuclear Instruments and Methods in Physics Research Section A: Accelerators, Spectrometers, Detectors and Associated Equipment* 828 (2016), pp. 242–249. ISSN: 0168-9002. DOI: <https://doi.org/10.1016/j.nima.2016.05.014>. URL: <https://www.sciencedirect.com/science/article/pii/S0168900216303722>.
- [142] Denis Servent et al. “First evidence that emerging pinnatoxin-G, a contaminant of shellfish, reaches the brain and crosses the placental barrier”. In: *Science of The Total Environment* 790 (2021), p. 148125. ISSN: 0048-9697. DOI: <https://doi.org/10.1016/j.scitotenv.2021.148125>. URL: <https://www.sciencedirect.com/science/article/pii/S004896972103196X>.
- [143] Intergovernmental Panel on Climate Change (IPCC). “Changes in Atmospheric Constituents and in Radiative Forcing”. In: *Fourth Assessment Report*. IPCC, 2007. Chap. 2.
- [144] L.M.S. Margato et al. “Effect of the gas contamination on CF<sub>4</sub> primary and secondary scintillation”. In: *Nuclear Instruments and Methods in Physics Research Section A: Accelerators, Spectrometers, Detectors and Associated Equipment* 695 (2012). New Developments in Photodetection NDIP11, pp. 425–428. ISSN: 0168-9002. DOI: <https://doi.org/10.1016/j.nima.2011.10.033>. URL: <https://www.sciencedirect.com/science/article/pii/S0168900211019838>.
- [145] M. G. Boulay et al. “Direct comparison of PEN and TPB wavelength shifters in a liquid argon detector”. In: *The European Physical Journal C* 81.12 (2021). ISSN: 1434-6052. DOI: [10.1140/epjc/s10052-021-09870-7](https://doi.org/10.1140/epjc/s10052-021-09870-7). URL: <http://dx.doi.org/10.1140/epjc/s10052-021-09870-7>.